Gravitational collapse, compact objects and gravitational waves in General Relativity and modified gravity

Roxana Roșca-Mead

Department of Applied Mathematics and Theoretical Physics
University of Cambridge

This dissertation is submitted for the degree of
Doctor of Philosophy

Newnham College

November 2019

I would like to dedicate this thesis to my beloved Mycroft …

Declaration

This dissertation is the result of my own work and includes nothing which is the outcome of work done in collaboration except as declared in the Preface and specified in the text. It is not substantially the same as any that I have submitted, or, is being concurrently submitted for a degree or diploma or other qualification at the University of Cambridge or any other University or similar institution except as declared in the Preface and specified in the text. I further state that no substantial part of my dissertation has already been submitted, or, is being concurrently submitted for any such degree, diploma or other qualification at the University of Cambridge or any other University or similar institution except as declared in the Preface and specified in the text.

Roxana Roșca-Mead
November 2019

Gravitational collapse, compact objects and gravitational waves in General Relativity and modified gravity

Roxana Roșca-Mead

Since the upgrade of the two LIGO Detectors it has been an exciting time for General Relativity (GR) research, as soon after they were upgraded to advanced status GW150914, the first gravitational wave signal from the inspiral and merger of two black holes was detected. The following consistent detections (9 further black hole binaries and one neutron star system) and the introduction of the European interferometer Virgo, as well as other planned detectors such as KAGRA and IndiGO mark the start of a new era of Gravitational Wave Physics and Astrophysics. This provides us with a window into the dynamics of strong gravity as well as the opportunity to test modified gravity and alternative theories in the strong regime, by confirming deviations from GR or constraining such theories. Why is General Relativity not enough though? It has passed all the tests so far with flying colors; in addition, the gravitational waves detected so far have demonstrated excellent agreement with GR's predictions. Despite all these successful tests, there are still important questions related to Dark Energy and Dark Matter left unexplained. As a consequence, a clearer understanding of modified gravity theories is needed as well as a catalogue of gravitational waves resulting from these theories that could be used in the analysis of interferometer data and for stochastic background and continuous wave searches. In this Thesis we provide source modelling for GR and one of the most popular candidates for modified gravity, Scalar Tensor (ST) theories, as well as look for smoking-gun signatures. We analyse the formation of compact objects from core collapse simulations of stars in massive ST theories over the astrophysically plausible range of stellar progenitor masses and metallicities, as well as a large part of the parameter space of this class of modified theories of gravity. Next we test the robustness of our results by expanding the simulations to ST theories with self-interacting potentials. Finally, we study the recoil resulting from black holes mergers by varying the orbital eccentricity in an attempt to amplify the kicks.

Acknowledgements

First and foremost I would like to thank my supervisor, Ulrich Sperhake, who has been there for me throughout these years and without whom this thesis would not have happened. He had confidence in me when I had none.

I have been fortunate to be able to meet and colaborate with some exceptional researchers during my time at Cambridge: Chris Moore, Michalis Agathos and Davide Gerosa, Emanuele Berti, Will Cook, Miren Radia, Robin Croft and Amelia Drew with whom I've had many interesting discussions about physics and numerics that helped me learn and grow along the way. I am thankful to my examiners Anne-Christine Davis and Vitor Cardoso for their helpful comments and suggestions for this thesis.

I am deeply indebted to my friends from Pavilion B: Miren, Fred, Owain, Philip, Wuhyun, Roland, Julija, João and Maeve, who have brighten the last few years of my PhD. I am especially thankful to my officemates Toby and Charles, for many productive discussions, that sometimes diverged into philosophy and politics. "Highest number" and "chair wars" will not be the same without them.

I would also like to thank my parents for their continuous support. And last but not least my husband, Mycroft, for being there for me throughout my entire PhD.

I am grateful for the opportunities I was given to visit the Yukawa Institute for Theoretical Physics in Kyoto, Kindai University in Osaka and University of Mississippi in Oxford, Mississippi, USA where part of the work for this thesis was performed. These visits were made possible as part of the European Union Horizon 2020 H2020-MSCA-RISE-2015 "StrongGrHEP" 690904 project.

The numerical work presented in this thesis was performed on the Cambridge Service for Data Driven Discovery clusters. Throughout my PhD I have been supported by a studentship from the Science and Technology Facilities Council. I have additionally received invaluable financial assistance from Newnham College, Cambridge and the Cambridge Philosophical Society.

Table of contents

List of figures

List of tables

Chapter 1

Introduction

The year 1915 remains a cornerstone in the scientific comunity as it was the year Albert Einstein published his now famous papers on General Relativity [1–3]. Einstein's theory puts time and space on equal footing by writing them covariantly and introduces the concept of curved spacetime. It helped explain some of the puzzling observations up to that point.

Before 1915, Sir Isaac Newton's laws of motion reigned supreme. One mystery for the astronomers of the day, however, was the shift they saw in Mercury's perihelion (the point closest to the Sun) after every orbit. In 1859 a French scientist, Urbain-Jean-Joseph Le Verrier, used Newton's law of gravitation to suggest that the shift may be caused by an undiscovered planet (later named Vulcan), closer to the Sun than Mercury. This was not outlandish to the scientific community as Le Verrier came to fame by similarly explaining the oddities in Uranus' orbit, which led to the discovery of Neptune. For the next decades many amateur astronomers (and even a few professional ones) reported seeing Vulcan. But the consistent lack of sightings by respected astronomers sowed doubts about the planet. The debate was closed and Vulcan's existence rejected once and for all when Einstein proposed his theory of General Relativity (GR). He proved that Mercury's orbit can be explained if one models gravity with GR rather than Newtonian theories [4].

Since then, GR has successfully passed numerous tests [5, 6] and, in the words of Ref. [7], "occupies a well-earned place next to the standard model as one of the two pillars of modern physics." And yet, the enigmatic nature of *dark energy* and *dark matter* evoked in the explanation of cosmological and astrophysical observations [8], as well as theoretical considerations regarding the renormalization of the theory in a quantum theory sense, indicate that GR may ultimately need modifications in the low- and/or high-energy regime [9].

Tests of GR have so far been largely limited to relatively weak fields. Besides Mercury's perihelion shift mentioned above, other examples include light deflection measurements and lunar laser ranging. In 1974, Hulse and Taylor detected the first binary pulsar system, PSR 1913+16, and the emission of gravitational radiation was indirectly inferred from the change in the period of the system's orbit. But in 2015 the first gravitational wave signal (GW150914) from the inspiral and merger of two black holes was detected by the Advanced Laser Interferometer Gravitational-Wave Observatory (LIGO) [10]. The recent breakthrough detection of gravitational waves (GWs) by LIGO has opened a new observational channel towards strong-field gravity.

Tests of Einstein's theory are a key goal of the new field of GW physics [11, 12]. Most GW-based tests either (i) construct a phenomenological parameterization of possible deviations from the expected physics and seek to constrain the different parameters, or (ii) model the physical system in the framework of a chosen alternative theory to see if it can better explain the observed data. As Vulcan's saga has taught us, it is important to remain open minded for different explanations of possible anomalies in the observations.

We need to further explore effects of GR, while building a wider knowledge on alternative theories to be sure we use the right templates in our detections. Many proposed modified gravity theories have been rejected due to the large deviations they predict in the weak field regime, where GR has been tested successfully. A screening mechanism is therefore needed that "turns off" the deviations at moderate to large length scales, but allows the theory to make predictions different from GR on small and cosmological ones.

Furthermore a mathematical understanding of the theory, in particular its well-posedness, is necessary for fully nonlinear simulations. One of the most popular candidate extensions of GR are Scalar Tensor (ST) theories of gravity [13, 14], adding a scalar sector to the vector and tensor fields of Maxwell GR. Scalar fields naturally arise in higher-dimensional theories including string theory and feature prominently in cosmology, and ST theories have a well-posed Cauchy formulation. ST theories also give rise to the most concrete example of a strong deviation from GR known to date: the *spontaneous scalarization* of neutron stars [15].

In this thesis, we study signatures for massive ST theories by modelling static neutron star solutions and the GW emission from stellar core collapse. We also contribute to the current understanding of GR phenomenology through the study of superkicks resulting from eccentric black hole mergers. Further motivations for our individual studies will be given in their respective chapters (especially 3 and 7).

We employ numerical relativity when Einstein's field equations cannot be solved analytically. One representative example is the two-body problem in GR, such as the collision of two black holes. Despite decades-long efforts the breakthrough simulation came as recently as 2005: Pretorius published results from his successful evolution of a binary composed of two equal mass, non-spinning black holes, through a single plunge-orbit, merger and ring down [16]. This was soon followed by the moving puncture breakthrough of the Brownsville and Goddard groups [17, 18].

We start with an introduction to Numerical Relativity in Chapter 2. We cover the 3+1 formulation of Einstein's equations, in particular the ADM and BSSNOK formalism. In Chapter 3 we introduce the theoretical aspects of Scalar Tensor theory with one scalar field. We obtain the corresponding field equations in spherical symmetry and the wave equation for the scalar field. We rewrite the equations as a first-order system and cast the matter evolution equations in flux conservative form which is needed for the core collapse code. We discuss the scalar parameters we use in this thesis and the constraints set on them by Solar System tests. Finally, we derive a semi-analytic formula for propagating a wave signal to galactic distances taking into account the dispersive nature of the mass term. In Chapter 4 we explore the static neutron star solutions in massive ST theory and their stability. In Chapter 5 we cover the results from solving the full dynamical system of equations in spherical symmetry. We test the code and discuss the astrophysical initial data used to start our simulations. We present the phenomenology of the scalarization for different stellar progenitors, ST parameters and EOSs. Finally, we consider the scope for observing the resulting scalar GWs with present and future GW detectors. In Chapter 6 we expand the scalar potential to include self-interacting terms and study how these additional parameters influence the GWs. Finally, in Chapter 7 we simulate eccentric merging black holes with initially anti-parallel spins lying in the orbital plane and study the recoil of the remnants.

Chapter 2

Numerical Relativity

In this chapter we introduce the different formalisms we use in our numerical studies to write Einstein's equations. Henceforth, we use geometrical units $G = c = 1$, and only reintroduce these factors on a few occasions for clarity.

2.1 Notation

By definition, a spacetime is described by a manifold $\mathcal{M}$ with Lorentzian metric $g_{\alpha\beta}$. We consider the spacetime metric signature $(-1, +1, +1, +1)$ and use the following conventions for related geometrical quantities.

$$\text{Christoffel symbol:} \quad \Gamma^{\mu}_{\nu\lambda} = \frac{1}{2} g^{\mu\rho} \left(\partial_{\nu} g_{\rho\lambda} + \partial_{\lambda} g_{\rho\nu} - \partial_{\rho} g_{\nu\lambda} \right) \,, \tag{2.1}$$

$$\text{Covariant derivative:} \quad \nabla_{\alpha} X^{\beta} = \partial_{\alpha} X^{\beta} + X^{\mu} \Gamma^{\beta}_{\alpha\mu} \,, \tag{2.2}$$

$$\text{Riemann curvature tensor:} \quad R^{\alpha}{}_{\beta\mu\nu} = \partial_{\alpha\mu} \Gamma^{\alpha}_{\beta\nu} - \partial \Gamma^{\alpha}_{\beta\mu} + \Gamma^{\alpha}_{\rho\mu} \Gamma^{\rho}_{\beta\nu} - \Gamma^{\alpha}_{\rho\nu} \Gamma^{\rho}_{\beta\mu} \,, \tag{2.3}$$

$$\text{Ricci curvature tensor:} \quad R_{\mu\nu} = R^{\lambda}{}_{\mu\lambda\nu} \,, \tag{2.4}$$

$$\text{Ricci scalar:} \quad R = R^{\mu}_{\mu} \,, \tag{2.5}$$

$$\text{Einstein tensor:} \quad G^{\mu\nu} = R^{\mu\nu} - \frac{1}{2} g^{\mu\nu} R \,, \tag{2.6}$$

$$\text{Lie derivative along } X_{\alpha} : \quad \mathcal{L}_X g_{\alpha\beta} = \nabla_{\alpha} X_{\beta} + \nabla_{\beta} X_{\alpha} \,, \tag{2.7}$$

$$\text{Einstein's equation:} \quad G_{\alpha\beta} = 8\pi T_{\alpha\beta} + \Lambda g_{\alpha\beta} \,, \tag{2.8}$$

$$\text{Index range:} \quad \alpha,\ \beta \ldots \text{ from } 0 \text{ to } 3 \,, \tag{2.9}$$

$$i,\ j, \ldots \text{ from } 1 \text{ to } 3 \,. \tag{2.10}$$

2.2 3+1 formalism

The covariant formulation of Einstein's equation is beautiful and elegant but sometimes a split into space and time is needed, particularly if we want to study the time evolution of a gravitational field around massive objects numerically. Thus the field equations need to be split in a way that allows us to set certain initial data from which to calculate the evolution of the gravitational field [19]. Though there are many formulations to achieve this goal, we shall here employ the 3+1 formalism which splits spacetime into 3D space and time. In the next sections we will be using the notation as presented in [19].

2.2.1 Spacetime foliation

We assume we are dealing with a globally hyperbolic[1] spacetime with metric $g_{\alpha\beta}$ (in order to be able to formulate an initial value problem). We can foliate a hyperbolic spacetime by hypersurfaces Σ_t parametrized by a global time function, $t(x^\alpha)$ [20]. We denote the unit normal vector field to Σ_t as n^α.

The spacetime metric $g_{\alpha\beta}$ induces a spatial metric (a 3D Riemannian metric) $\gamma_{\alpha\beta}$ on each hypersurface Σ_t given by [20]

$$\gamma_{\alpha\beta} = g_{\alpha\beta} + n_\alpha n_\beta \,. \tag{2.11}$$

The lapse of proper time between two hypersurfaces Σ_t and Σ_{t+dt} as measured by an observer moving along the direction normal to the hypersurface (this is called an Eulerian observer) is [19]

$$d\tau = \alpha(t, x^i)dt \,, \tag{2.12}$$

where α is known as the lapse function and x^i labels points inside Σ_t.

The relative deviation β_i between the Eulerian observers and the lines of constant spatial coordinates is

$$x^i_{t+dt} = x^i_t - \beta^i(t, x^j)dt \tag{2.13}$$

---

[1] A spacetime $(\mathcal{M}, g_{\alpha\beta})$ is hyperbolic if it admits a Cauchy surface (a spacelike hypersurface Σ in $\mathcal{M}$ such that each timelike or null curve without endpoint intersects Σ exactly once [20]).

This is more commonly referred to as the shift vector. The way in which we foliate spacetime is not unique; α and β_i are arbitrary functions that represent the coordinate or gauge freedom of GR.

The line element then can be written as

$$ds^2 = (-\alpha^2 + \beta_i\beta^i)dt^2 + 2\beta_i dt dx^i + \gamma_{ij}dx^i dx^j \,, \tag{2.14}$$

or, equivalently, the metric is given by

$$g_{\mu\nu} = \begin{pmatrix} -\alpha^2 + \beta_k\beta^k & \beta_i \\ \beta_j & \gamma_{ij} \end{pmatrix} . \tag{2.15}$$

In this coordinate system the normal unit vector is

$$n^\mu = (1/\alpha, -\beta^i/\alpha), \qquad n_\mu = (-\alpha, 0) \,. \tag{2.16}$$

Here, β^i is written as a 3D vector, but, we can expand it to a 4-vector $\beta^\mu = (0, \beta^i)$ and use it to construct the time vector

$$t^\mu = \alpha n^\mu + \beta^\mu \,, \tag{2.17}$$

which is tangent to the lines of constant spatial coordinates. Thus we notice that the shift β^μ is the projection of the time vector onto the spatial hypersurface $\beta^\nu = P^\nu_\mu t^\mu$, where

$$P^\alpha_\beta = \delta^\alpha_\beta + n^\alpha n_\beta \,, \tag{2.18}$$

is the projection operator, which in this case is equal to the spatial metric $\gamma_{\alpha\beta} := P^\mu_\alpha P^\nu_\beta g_{\mu\nu} = g_{\alpha\beta} + n_\alpha n_\beta$.

Another quantity that will prove important is the extrinsic curvature $K_{\alpha\beta}$ which measures the change of the normal vector under parallel transport [19]. This can be defined using the projection operator

$$K_{\mu\nu} = -P^\alpha_\mu \nabla_\alpha n_\nu = -(\nabla_\mu n_\nu + n_\mu n^\alpha \nabla_\alpha n_\nu) \,. \tag{2.19}$$

or, equivalently, in terms of the Lie derivative of the spatial metric with respect to the normal vector n

$$K_{\mu\nu} = -\frac{1}{2}\mathcal{L}_n \gamma_{\mu\nu} \,. \tag{2.20}$$

By expanding the Lie derivative, we can write the definition of the extrinsic curvature as an evolution equation for γ_{ij}:

$$\partial_t \gamma_{ij} = -2\alpha K_{ij} + D_i \beta_j + D_j \beta_i , \text{ where } D_\mu = P^\alpha_\mu \nabla_\alpha \alpha \, . \tag{2.21}$$

We have now all the definitions to rewrite Einstein's equations.

2.2.2 ADM formalism

We reformulate Einstein's equations as evolution equations and constraints for γ_{ij} and K_{ij} by calculating all possible projections of the Einstein equations onto Σ_t and its normal n^α [19]. We notice that with Eq. (2.21), part of our job is done. For the second evolution equation, we start with the various projections of the energy-momentum tensor:

$$\begin{aligned} \rho &= n^\mu n^\nu T_{\mu\nu} \, , & (2.22)\\ j^\alpha &= -P^{\alpha\mu} n^\nu T_{\mu\nu} \, , & (2.23)\\ S_{\mu\nu} &= P^\alpha_\mu P^\beta_\nu T_{\alpha\beta} \, , & (2.24) \end{aligned}$$

which are the energy density, momentum density and spatial stress tensor, respectively, as measured by Eulerian observers.

Next we project the Riemann tensor. Two of these projections give us the Gauss-Codazzi and Codazzi-Mainardi equations

$$\begin{aligned} P^\delta_\alpha P^\kappa_\beta P^\lambda_\mu P^\sigma_\nu R_{\delta\kappa\lambda\sigma} &= \mathcal{R}_{\alpha\beta\mu\nu} + K_{\alpha\mu} K_{\beta\nu} - K_{\alpha\nu} K_{\beta\mu} \, , & (2.25)\\ P^\delta_\alpha P^\kappa_\beta P^\lambda_\mu n^\nu R_{\delta\kappa\lambda\nu} &= D_\beta K_{\lambda\mu} - D_\alpha K_{\beta\mu} \, , & (2.26) \end{aligned}$$

where $\mathcal{R}$ is the Riemann tensor associated with the spatial metric $\gamma_{\mu\nu}$. From Eq. (2.25) we obtain by contraction

$$P^{\alpha\mu} P^{\beta\nu} R_{\alpha\beta\mu\nu} = \mathcal{R} + K^2 - K_{\mu\nu} K^{\mu\nu} \, , \tag{2.27}$$

where $K = K^\mu_\mu$ is the trace of the extrinsic curvature. We also notice that

$$\begin{aligned} P^{\alpha\mu} P^{\beta\nu} R_{\alpha\beta\mu\nu} &= (g^{\alpha\mu} + n^\alpha n^\mu)(g^{\beta\nu} + n^\beta n^\nu) R_{\alpha\beta\mu\nu} \, ,\\ &= 2 n^\mu n^\nu G_{\mu\nu} \, . & (2.28) \end{aligned}$$

Combining the last two expressions together with Einstein's equations yields the **Hamiltonian constraint**

$$\mathcal{R} + K^2 - K_{\mu\nu}K^{\mu\nu} = 16\pi\rho\,. \tag{2.29}$$

We note that a mixed contraction of the Einstein tensor can be written in terms of the Ricci tensor

$$P^{\alpha\mu}n^\nu G_{\mu\nu} = P^{\alpha\mu}n^\nu R_{\mu\nu}\,, \tag{2.30}$$

which, together with Eq. (2.26) contracted over α and μ, implies

$$\gamma^{\alpha\mu}n^\nu G_{\mu\nu} = D^\alpha K - D_\mu K^{\alpha\mu}\,. \tag{2.31}$$

Combining this with the Einstein field equations and Eq. (2.23), we obtain the **momentum constraints**

$$D_\mu(K^{\alpha\mu} - \gamma^{\alpha\mu}K) = 8\pi j^\alpha\,. \tag{2.32}$$

We note that these are not evolution equations but constraints that must be satisfied on each hypersurface.

We still have the projection of the Riemann tensor contracted twice with the normal n^α which gives us the Ricci equation

$$P^\delta_\mu P^\kappa_\nu n^\lambda n^\sigma R_{\delta\lambda\kappa\sigma} = \mathcal{L}_n K_{\mu\nu} + K_{\mu\lambda}K^\lambda_\nu + \frac{1}{\alpha}D_\mu D_\nu\alpha\,. \tag{2.33}$$

By contracting Eq. (2.25) over α and μ, we obtain

$$P^\delta_\mu P^\kappa_\nu(n^\lambda n^\sigma R_{\delta\lambda\kappa\sigma} + R_{\delta\kappa}) = \mathcal{R}_{\mu\nu} + KK_{\mu\nu} - K_{\mu\lambda}K^\lambda_\nu\,, \tag{2.34}$$

which, together with Eq. (2.33) yields

$$\mathcal{L}_t K_{\mu\nu} - \mathcal{L}_\beta K_{\mu\nu} = -D_\mu D_\nu\alpha + \alpha\left(-P^\delta_\mu P^\kappa_\nu R_{\delta\kappa} + \mathcal{R}_{\mu\nu} + KK_{\mu\nu} - 2K_{\mu\nu}K^\lambda_{\mu\lambda\nu}\nu\right)\,. \tag{2.35}$$

Using the Einstein equations and replacing the Lie derivatives, the spatial components of the result gives us the evolution equation for the extrinsic curvature

$$\begin{aligned}\partial_t K_{ij} = \quad & \beta^k\partial_k K_{ij} + K_{ki}\partial_j\beta^k + K_{kj}\partial_i\beta^k - D_iD_j\alpha \\ & +\alpha\left[\mathcal{R}_{ij} + KK_{ij} - 2K_{ik}K^k_j\right] + 4\pi\alpha\left[\gamma_{ij}(S-\rho) - 2S_{ij}\right]\,,\end{aligned} \tag{2.36}$$

where $S = S^{\mu}_{\mu}$.

In numerical relativity the evolution equations (2.21) and (2.36) are known as the ADM equations and were proposed by Arnowitt, Deser and Misner in 1959 [21].

2.2.3 BSSNOK formalism

The ADM equations are weakly hyperbolic [19], therefore in our study of BH recoil we employ the BSSNOK formalism, a strongly hyperbolic reformulation of the 3+1 formalism suitable for numerical evolutions. Note also that we are free to manipulate the ADM equations by adding the constraints as formally zero extra source terms to the right hand side of the evolution equations for γ_{ij} and K_{ij} .

For the BSSNOK formulation we start by considering a conformal rescaling of the spatial metric

$$\tilde{\gamma}_{ij} = \psi^{-4} \gamma_{ij} \,, \tag{2.37}$$

such that the new metric has unit determinant, i.e. $\psi = \gamma^{1/12}$. In addition, we require this to remain true throughout the evolution. The evolution equation of the spatial metric γ_{ij} (Eq. 2.21) gives us the evolution equation for the determinant

$$\partial_t \gamma = -2\gamma(\alpha K - \partial_i \beta^i) + \beta^i \partial_i \gamma \,, \tag{2.38}$$

which, in turn, implies

$$\partial_t \psi = -\frac{1}{6} \psi(\alpha K - \partial_i \beta^i) + \beta^i \partial_i \psi \,. \tag{2.39}$$

As suggested in [17] evolving $\chi = 1/\psi^4 = e^{-4\phi}$ is better for BH simulations as ψ has a $1/r$ singularity (ϕ a logarithmic singularity) and χ is a C^4 function. We also separate the extrinsic curvature K_{ij} into its trace K and its tracefree part

$$A_{ij} = K_{ij} - \frac{1}{3} \gamma_{ij} K \,, \tag{2.40}$$

which we also conformally rescale

$$\bar{A}_{ij} = \psi^{-4} A_{ij} = \chi A_{ij} \,. \tag{2.41}$$

In addition, we consider three auxiliary variables refered to as the conformal connection functions [19]

$$\tilde{\Gamma}^i = \tilde{\gamma}^{jk}\tilde{\Gamma}^i_{jk} = -\partial_j\tilde{\gamma}^{ij}\,, \tag{2.42}$$

where $\tilde{\Gamma}^i_{jk}$ is the Christoffel symbol associated with $\tilde{\gamma}_{ij}$.

By rewriting the ADM equations as evolution equations for K, $\psi, \tilde{\gamma}_{ij}$ and $\tilde{A}_{ij}$ we obtain the BSSNOK (Baumgarte, Shapiro, Shibata, Nakamura, Oohara and Kojima) equations [22–24]

$$\begin{aligned}
\frac{d}{dt}\tilde{\gamma}_{ij} &= -2\alpha\tilde{A}_{ij}\,, && (2.43)\\
\frac{d}{dt}\phi &= -\frac{1}{6}\alpha K\,, && (2.44)\\
\frac{d}{dt}\tilde{A}_{ij} &= \chi\left[-D_iD'_j\alpha + \alpha\mathcal{R}_{ij} + 4\pi\alpha\left(\gamma_{ij}(S-\rho) - 2S_{ij}\right)\right]^{TF} \\
&\quad +\alpha\left(K\tilde{A}_{ij} - 2\tilde{A}_{ik}\tilde{A}^k_j\right)\,, && (2.45)\\
\frac{d}{dt}K &= -D_iD^i\alpha + \alpha\left(\tilde{A}_{ij}\tilde{A}^{ij} + \frac{1}{3}K^2\right) + 4\pi\alpha(\rho+S)\,, && (2.46)\\
\frac{d}{dt}\tilde{\Gamma}^i &= \tilde{\gamma}^{jk}\partial_j\partial_k\beta^i + \frac{1}{3}\tilde{\gamma}^{ij}\partial_j\partial_k\beta^k - 2\tilde{A}^{ij}\partial_j\alpha \\
&\quad +2\alpha\left(\tilde{\Gamma}^i_{jk}\tilde{A}^{jk} + 6\tilde{A}^{ij}\partial_j\phi - \frac{2}{3}\tilde{\gamma}^{ij}\partial_jK - 8\pi\tilde{j}^i\right)\,, && (2.47)
\end{aligned}$$

where $d/dt \equiv \partial_t - \mathcal{L}_t$, $\tilde{j}^i = \frac{1}{\chi}j^i$ and TF denotes the trace-free quantity in the brackets. For our BH simulations we use the χ version together with the moving puncture gauge [17, 18].

2.3 Formulation for spherically symmetric neutron star collapse

In this thesis we study core collapse in Scalar Tensor theory of massive stars. We assume spherical symmetry, which simplifies the equations considerably. We use the 3+1 formulation described above with polar time slicing, a subcategory of maximal slicing (which has vanishing mean curve $K = 0$). Polar slicing is defined in spherical coordinates $(x^i) = (r, \theta, \phi)$ by [25]

$$K^\theta_\theta + K^\phi_\phi = 0\,. \tag{2.48}$$

In addition, we choose to fix the coordinate freedom by using the radial gauge: r is the areal radius and our spatial metric takes the form:

$$\gamma_{ij}dx^i dx^j = X^2(t,r)dr^2 + r^2(d\theta^2 + \sin^2\theta d\phi^2)\,. \tag{2.49}$$

Polar slicing can be shown to imply a zero shift vector in spherical symmetry [25] which reduces the spacetime metric to

$$g_{\alpha\beta}dx^\alpha dx^\beta = -\alpha^2(r,t)dt^2 + r^2(d\theta^2 + \sin^2\theta d\phi^2)\,. \tag{2.50}$$

One particular feature of polar slicing is the collapse of the lapse function (i.e. $\alpha \to 0$) during the evolution as a black hole forms through gravitational collapse [25].

Chapter 3

Scalar Tensor Theories from a theoretical point of view

In this chapter we review the formalism for ST theories with one scalar field and write the equations of motion in flux conservative form; next we discuss the chosen scalar functions and the constraints imposed on their parameters; and finally we present the procedure for calculating the GW signals propagated to astrophysically large distances.

This chapter and Appendix B is based on material published in [26] in collaboration with Ulrich Sperhake, Christopher J. Moore, Michalis Agathos, Davide Gerosa and Christian D. Ott, as well as a paper in preparation. The analytic wave propagation was researched by C. Moore and U. Sperhake and independently verified by the author. The numerical wave propagation was performed by U. Sperhake and C. Moore. All remaining theoretical calculations were done independently by the author.

3.1 Introduction

In spite of the tremendous success of GR in explaining a plethora of phenomena in the observable universe [5, 6], theoretical considerations as well as persistent puzzles in observational astronomy may ultimately require Einstein's theory to be extended or modified [9]. The new era of gravitational wave (GW) astronomy, marked by LIGO's detection of GW150914 [10] and twelve further events identified in the data of the LIGO [27] and Virgo [28] detectors (ten from O2 and two from O3), has now opened up qualitatively new opportunities to probe GR in the strong-field regime [29]. First tests using GW observations have resulted in valuable constraints on deviations from GR, including constraints on the post-Newtonian coefficients and on the propagation of the dipole radiation from compact binaries [12, 11, 30], but more comprehensive tests will require more systematic efforts on the modelling of sources of GWs in modified theories of gravity.

This effort faces considerable challenges. First, there should exist a well-posed [31] initial value formulation of the theory under consideration to ensure that solutions are unique and depend continuously on the initial data. This aspect has been explored for a few candidate theories (see eg [31–35]) but largely remains an open issue which is further complicated by the fact that the question of well-posedness is, in general, gauge dependent. The difficulties associated with the potential lack of well-posedness may be bypassed through a perturbative expansion of the theory around GR and truncating this series at some order in the expansion parameter. Such an effective-field theory approach has been used to compute deviations at linear order from GR in the inspiral of black-hole (BH) binaries in dynamical Chern-Simons theory [36, 37] and scalar Gauss-Bonnet gravity [38]. A second major challenge faced in the modelling of sources of GWs in modified gravity arises from the tremendous success of GR itself. Clearly, a serious candidate theory must be compatible with the wide range of observational tests GR has already passed. The challenge then is to identify theories that agree with GR in the weak-field regime but make concrete predictions in the strong-field regime that deviate sufficiently from GR such that they serve as a potential discriminant in observational tests [9].

The most concrete prediction of this type is the *spontaneous scalarization* of compact stars in ST theories identified by Damour and Esposito-Farèse [15]. Here, a second branch of strongly scalarized stars emerges over a significant subset of the parameter space of the theory and its members may be energetically favoured over their weakly scalarized, “GR like” counterparts. The onset of this strong scalarization has been observed in various simulations of collapsing stars and binary neutron star mergers in ST theory where it generates significant gravitational radiation in the form of scalar waves [39–46]. All of these studies, however, as well as recent analytical calculations of binary dynamics in ST theory to high post-Newtonian order [47, 48], are restricted to the case of *massless* ST gravity. In the massless case, the parameter space of the theory is already severely constrained through binary pulsar observations [49–51] and Doppler tracking of the Cassini spacecraft [52]. The surviving parameter regime of massless ST gravity barely allows for spontaneous scalarization to occur.

On the other hand, both the binary pulsar and Cassini constraints rely on observations of widely separated objects and therefore do not apply to theories where the scalar degree of freedom is effectively screened on the scales in question. Such a screening is provided by a scalar mass $\mu \gtrsim 10^{-19}\,\mathrm{eV}$ corresponding to a Compton wavelength $\lambda_c = (2\pi\hbar)/(\mu c)$ smaller than or comparable to the distances between the relevant objects [7, 53].

Massive ST gravity therefore remains a largely untested class of theories with considerable potential to generate strong-field deviations from GR in, as yet, unobserved regimes while passing all weak-field tests. The theory is furthermore manifestly well-posed by virtue of the equivalence of its description in the Einstein and Jordan frames [13, 54–56]. Recent years have accordingly seen a rising number of studies exploring potentially observable features of compact objects in this class of theories, such as the computation of static equilibrium models [53], the structure of uniformly or differentially rotating neutron stars and their inertia and quadrupole moment [57–59] and the generalisation of the spontaneous scalarization mechanism to a wider range of theories [60–63].

3.2 Formalism

We consider in this work the class of ST theories of gravity first studied by Bergmann [64] and Wagoner [65] which are characterised by the following properties. The theory is described by an action $S = S_{\mathrm{G}} + S_{\mathrm{M}}$, where S_{G} only contains the gravitational fields and S_{M} describes the matter fields and their interaction with gravity. Gravity is mediated by the (physical) spacetime metric $g_{\alpha\beta}$ and a single, non-minimally coupled real scalar field. Variation of the action S results in at most two-derivative field equations[1] that are diffeomorphism invariant and obey the weak equivalence principle.

Using the above principles we can formulate the action in the Jordan-Fierz frame [9]:

$$S = \int dx^4 \sqrt{-g} \left[\frac{F(\phi)}{16\pi G} R - \frac{1}{2} g^{\mu\nu} (\partial_\mu \phi)(\partial_\nu \phi) - V(\phi) \right] + S_m(\psi_m, g_{\mu\nu}) \,, \tag{3.1}$$

where $g_{\mu\nu}$ represents the metric (from now on refered to as the Jordan metric), g is its determinant, R is the Ricci scalar corresponding to $g_{\mu\nu}$, ϕ represents the scalar field, F and V are arbitrary functions of ϕ, and S_m represents the action of the matter fields ψ_m. The first term of the integral, $\sqrt{-g}\frac{F(\phi)}{16\pi G}R$, replaces the usual Einstein-Hilbert term and leads to the interaction between the scalar and tensor sectors of the geometry [14]. The matter fields do not interact directly with the scalar field, but are influenced indirectly through the metric $g_{\mu\nu}$.

---

[1] The word "two-derivative" implies that each term may involve at most two derivative operators, i.e. terms may be linear in second derivatives or quadratic in first derivatives but may not contain products such as $f_{,\alpha}\, f_{,\beta\gamma}$.

By varying action (3.1) with respect to the metric and scalar field we obtain the following equations:

$$
\begin{aligned}
G_{\alpha\beta} &= \frac{8\pi}{F}\left(T^{F}_{\alpha\beta} + T^{\phi}_{\alpha\beta} + T_{\alpha\beta}\right), && (3.2)\\
T^{F}_{\alpha\beta} &= \frac{1}{8\pi}(\nabla_\alpha\nabla_\beta F - g_{\alpha\beta}\nabla^\mu\nabla_\mu F), && (3.3)\\
T^{\phi}_{\alpha\beta} &= \partial_\alpha\phi\partial_\beta\phi - g_{\alpha\beta}\left[\frac{1}{2}g^{\mu\nu}\partial_\mu\phi\partial_\nu\phi + V(\phi)\right], && (3.4)\\
\Box\phi &= -\frac{1}{16\pi}F_{,\phi}R + V_{,\phi}. && (3.5)
\end{aligned}
$$

where $T_{\alpha\beta}$ is the energy momentum tensor obtained by varying the matter action S_m with respect to the metric:

$$T^{\alpha\beta} \equiv \frac{2}{\sqrt{-g}}\frac{\delta S_m}{\delta g_{\alpha\beta}}. \tag{3.6}$$

Further evolution equations arise from the conservation of the energy-momentum tensor and of the matter current density J^α in the physical (Jordan) frame:

$$
\begin{aligned}
\nabla_\beta T^{\beta}{}_{\alpha} &= 0\,, && (3.7)\\
\nabla_\alpha J^\alpha &= 0\,. && (3.8)
\end{aligned}
$$

This class of theories is conveniently described in the so-called Einstein frame, obtained from the physical or Jordan frame through a conformal transformation of the metric and a redefinition of the scalar degree of freedom. The physical Jordan metric $g_{\alpha\beta}$ is related to the Einstein metric $\bar{g}_{\alpha\beta}$ by the conformal factor:

$$g_{\alpha\beta} = a^2\bar{g}_{\alpha\beta} = \frac{1}{F}\bar{g}_{\alpha\beta}. \tag{3.9}$$

Both notations, using a and F, are found in the literature; in this thesis we shall be using only F. If we furthermore denote the scalar field in the Einstein frame as φ and relate it to ϕ as follows:

$$\frac{\partial\varphi}{\partial\phi} = \sqrt{\frac{3}{4}\frac{F_{,\phi}{}^2}{F^2} + \frac{4\pi}{F}}\,, \tag{3.10}$$

$$\frac{\partial\phi}{\partial\varphi} = \sqrt{\frac{4F^2 - 3F_{,\varphi}{}^2}{16\pi F}}\,, \tag{3.11}$$

then the action (3.1) for the scalar tensor theory in this new frame is:

$$S = \frac{1}{16\pi G}\int dx^4\sqrt{-\bar{g}}\left[\bar{R} - 2\bar{g}^{\mu\nu}(\partial_\mu\varphi)(\partial_\nu\varphi) - 4W(\varphi)\right] + S_m[\psi_m, \frac{\bar{g}_{\mu\nu}}{F(\varphi)}]\,. \tag{3.12}$$

This is the Einstein-Hilbert gravity minimally coupled to a scalar field. The two scalar potentials are related to each other by:

$$V(\phi) = \frac{F^2}{4\pi G}W(\varphi). \tag{3.13}$$

The algebra for the conformal transformation and the choice of the scalar field equations (3.10)-(3.11) is covered in Appendix A. The field equations obtained by varying the action (3.12) with respect to $g_{\alpha\beta}$ and φ are

$$\begin{aligned} \bar{G}_{\alpha\beta} &= 2\partial_\alpha\varphi\partial_\beta\varphi - \bar{g}_{\alpha\beta}\bar{g}^{\mu\nu}\partial_\mu\varphi\partial_\nu\varphi + 8\pi G\bar{T}_{\alpha\beta} - 2W(\varphi)\bar{g}_{\alpha\beta}, && (3.14)\\ \bar{\Box}\varphi &= -4\pi\alpha(\varphi)\bar{T} + W_{,\varphi}. && (3.15)\end{aligned}$$

where

$$\alpha\,(\varphi) = \frac{\partial\ln a}{\partial\varphi} = -\frac{1}{2}\frac{\partial\ln F}{\partial\varphi}\,. \tag{3.16}$$

Notationwise, all barred quantities refer to the metric from the Einstein frame, $\bar{g}_{\alpha\beta}$. The energy momentum tensor $\bar{T}^{\alpha\beta}$ is obtained from varying the matter action with respect to the Einstein metric

$$\bar{T}^{\alpha\beta} \equiv \frac{2}{\sqrt{-\bar{g}}}\frac{\delta S_m}{\delta\bar{g}_{\alpha\beta}} = \frac{1}{F(\varphi)^3}\frac{2}{\sqrt{-g}}\frac{\delta S_m}{\delta g_{\alpha\beta}} \equiv \frac{1}{F(\varphi)^3}T^{\alpha\beta}\,. \tag{3.17}$$

Thus, the conservation of the energy momentum tensor (3.7) translates in the Einstein frame to

$$\bar{\nabla}_\beta\bar{T}^{\beta\alpha} = -\frac{1}{2}\frac{F_{,\varphi}}{F}\bar{T}\bar{g}^{\alpha\beta}\bar{\nabla}_\beta\varphi\,. \tag{3.18}$$

Henceforth, we consider spherical symmetry and impose polar slicing and radial gauge in the Einstein frame, so that the line element takes on the form

$$\mathrm{d}s^2 = \bar{g}_{\mu\nu}\mathrm{d}x^\mu\mathrm{d}x^\nu = -F\nu^2\mathrm{d}t^2 + FX^2\mathrm{d}r^2 + r^2\mathrm{d}\Omega^2. \tag{3.19}$$

where ν, X are functions of (t, r). As a consequence the Jordan metric is given by

$$\mathrm{d}s^2 = g_{\alpha\beta}\mathrm{d}x^\alpha\mathrm{d}x^\beta = -\nu^2\mathrm{d}t^2 + X^2\mathrm{d}r^2 + \frac{r^2}{F}\mathrm{d}\Omega^2\,. \tag{3.20}$$

Following common practice, we introduce for convenience the potential $\Phi(t,r)$ and the mass function $m(t,r)$ through

$$F\nu^2 = e^{2\Phi}\,, \qquad FX^2 = \left(1 - \frac{2m}{r}\right)^{-1}\,. \tag{3.21}$$

Similarly to [66] we assume ideal hydrodynamics. Thus, the energy-momentum tensor and matter current density for a spherically symmetric perfect fluid with baryon density ρ, enthalpy h and 4-velocity u^α are given by

$$\begin{aligned} T_{\alpha\beta} &= \rho h u_\alpha u_\beta + P g_{\alpha\beta}\,, && (3.22)\\ J^\alpha &= \rho u^\alpha\,. && (3.23) \end{aligned}$$

The four velocity in spherical symmetry is

$$u^\alpha = \frac{1}{\sqrt{1-v^2}}\left[\frac{1}{\nu},\ \frac{v}{X},\ 0,\ 0\right]. \tag{3.24}$$

The velocity field v as well as the matter variables $\rho,\ P,\ h,\ \epsilon$ are functions of (t,r). By inserting the expressions of Eqs. (3.19),(3.21)-(3.24) into the field equations (3.8),(3.15),(3.18) and (3.14), we obtain the set of equations that govern the dynamics of spherically symmetric fluid configurations in Bergmann-Wagoner ST theory of gravity. In order to accurately model discontinuities arising through shock formation in the fluid profiles, however, we require high resolution shock capturing and, hence, a flux conservative form of the matter equations. This is achieved by converting the *primitive* variables (ρ, v, h) to their flux conservative counterparts [46, 66],

$$\bar{D} = \frac{\rho X F^{-3/2}}{\sqrt{1-v^2}}\,,\ \bar{S}^r = \frac{\rho h F^{-2}}{1-v^2}\,,\ \bar{\tau} = \frac{\bar{S}^r}{v} - \frac{P}{F^2} - \bar{D}\,. \tag{3.25}$$

Finally, we convert the wave equation (3.15) for the scalar field into a first order system by defining

$$\eta = \frac{1}{X}\partial_r\varphi\,, \qquad \psi = \frac{1}{\nu}\partial_t\varphi\,. \tag{3.26}$$

The PDEs arising from Einstein's tensor equation (3.14) are:

$$\begin{aligned}
\frac{\partial_r \nu}{\nu} &= X^2 F\left[\frac{m}{r^2} + 4\pi r\left(\bar{S}^r v + \frac{P}{F^2}\right) + \frac{r}{2F}\left(\eta^2+\psi^2\right)\right] - \frac{F_{,\varphi}}{2F}X\eta \\
&\quad -rFX^2W, &(3.27)\\
\frac{\partial_r X}{X} &= 4\pi r F X^2\left(\bar{\tau}+\bar{D}\right) + \frac{rX^2}{2}\left(\eta^2+\psi^2\right) - FX^2\frac{m}{r^2} - \frac{F_{,\varphi}}{2F}X\eta \\
&\quad +rFX^2W, &(3.28)\\
\frac{\partial_t X}{X} &= rX\alpha\left(\eta\psi - 4\pi F\bar{S}^r\right) - \frac{F_{,\varphi}}{2F}\nu\psi. &(3.29)
\end{aligned}$$

The wave equation for the scalar field takes the form:

$$\begin{aligned}
\partial_t\partial_t\varphi &= \frac{\nu^2}{X^2}\left[\partial_r\partial_r\varphi + \frac{2}{r}\partial_r\varphi + \left(\frac{\partial_r\nu}{\nu} - \frac{\partial_r X}{X}\right)\partial_r\varphi\right] + \left(\frac{\partial_t\nu}{\nu} - \frac{\partial_t X}{X}\right)\partial_t\varphi \\
&\quad +2\pi\nu^2\left(\bar{\tau} - \bar{S}^r v + \bar{D} - 2\frac{P}{F^2}\right)F_{,\varphi} - \nu^2 F W_{,\varphi}. &(3.30)
\end{aligned}$$

This can be rewritten in three first-order equations using (3.26):

$$\begin{aligned}
\partial_t\varphi &= \nu\psi\,, &(3.31)\\
\partial_r\eta &= -\eta\frac{\partial_t X}{X} + \frac{\nu}{X}\left(\partial_r\psi + \psi\frac{\partial_r\nu}{\nu}\right), &(3.32)\\
\partial_t\psi &= \frac{1}{r^2X}\partial_r\left(\nu r^2\eta\right) - \psi\frac{\partial_t X}{X} + 2\pi\nu\left(\bar{\tau} - \bar{S}^r v + \bar{D} - 3\frac{P}{F^2}\right)F_{,\varphi} \\
&\quad -\nu F W_{,\varphi}\,. &(3.33)
\end{aligned}$$

Finally, the matter evolution equations are written in flux conservative form as follows (this form is necessary for the high-resolution shock capturing techniques used in the time simulation code):

$$\partial_t\begin{pmatrix}\bar{D}\\ \bar{S}^r\\ \bar{\tau}\end{pmatrix} + \frac{1}{r^2}\partial_r\left[r^2\frac{\alpha}{X}\begin{pmatrix}f_{\bar{D}}\\ f_{\bar{S}^r}\\ f_{\bar{\tau}}\end{pmatrix}\right] = \begin{pmatrix}s_{\bar{D}}\\ s_{\bar{S}^r}\\ s_{\bar{\tau}}\end{pmatrix}, \tag{3.34}$$

or, equivalently,

$$
\begin{aligned}
\partial_t \bar{D} + \frac{1}{\sqrt{F} r^2}\partial_r \left(r^2 \frac{\nu}{X}\sqrt{F} f_{\bar{D}} \right) &= s_{\bar{D}} \, , & (3.35)\\
\partial_t \bar{S}^r + \frac{1}{r^2}\partial_r \left(r^2 \frac{\nu}{X} f_{\bar{S}^r} \right) &= s_{\bar{S}^r} \, , & (3.36)\\
\partial_t \bar{\tau} + \frac{1}{r^2}\partial_r \left(r^2 \frac{\nu}{X} f_{\bar{\tau}} \right) &= s_{\bar{\tau}} \, . & (3.37)
\end{aligned}
$$

where

$$
\begin{aligned}
f_{\bar{D}} &= \bar{D} v \, , & (3.38)\\
f_{\bar{S}^r} &= \bar{S}^r v + \frac{P}{F^2} \, , & (3.39)\\
f_{\bar{\tau}} &= \bar{S}^r - \bar{D} v \, , & (3.40)\\
s_{\bar{D}} &= -\bar{D}\frac{F_{,\varphi}}{2F}\nu\psi \, , & (3.41)\\
s_{\bar{S}^r} &= \left(\bar{S}^r v - \bar{\tau} - \bar{D} \right) \nu X F \left(8\pi \frac{P}{F^2} + \frac{m}{r^2} - \frac{F_{,\varphi}}{2F^2 X}\eta - rW \right) + \frac{\nu X}{F} P \frac{m}{r^2} & \\
&\quad - \frac{3}{2}\nu \frac{P}{F^2}\frac{F_{,\varphi}}{F}\eta - \frac{r}{2}\nu X \left(\eta^2 + \psi^2 \right) \left(\bar{\tau} + \frac{P}{F^2} + \bar{D} \right) \left(1 + v^2 \right) & \\
&\quad + 2\frac{\nu P}{r X F^2} - 2 r \nu X \bar{S}^r \eta \psi - r \nu X \frac{PW}{F} \, , & (3.42)\\
s_{\bar{\tau}} &= - \left(\bar{\tau} + \frac{P}{F^2} + \bar{D} \right) r \nu X \left[\left(1 + v^2 \right) \eta\psi + v \left(\eta^2 + \psi^2 \right) \right] & \\
&\quad + \frac{\nu}{2}\frac{F_{,\varphi}}{F} \left[\bar{D} v \eta + \left(\bar{S}^r v - \bar{\tau} + 3\frac{P}{F^2} \right) \psi \right] \, . & (3.43)
\end{aligned}
$$

3.3 Scalar parameters

3.3.1 Coupling function

Theories of gravity can be probed in the slow-motion, weak field limit which measures deviations from the flat space solution. In this approximation, known as the post-Newtonian (PN) limit, the spacetime metric $g_{\alpha\beta}$ predicted by nearly every metric theory of gravity has the same structure [5]: the PN limit can be written as an expansion about the Minkowski metric in terms of dimensionless gravitational potentials of varying degrees of smallness. The metrics differ from each other through the coefficients in front of these potentials.

The parametrized post-Newtonian (PPN) formalism inserts parameters in place of these coefficients, parameters whose values depend on the theory under study. The current version of the PPN formalism uses ten parameters. The Eddington-Robertson-Schiff parameters, which are used to describe "classical" tests of GR, are the only non-zero PPN parameters in ST theory [5]. They depend on the asymptotic value of $\ln F$ at spatial infinity and its derivatives

$$\begin{aligned} 1-\gamma &= \frac{2{\alpha_0}^2}{1+{\alpha_0}^2}, && (3.44)\\ \beta-1 &= \frac{\beta_0{\alpha_0}^2}{2(1+{\alpha_0}^2)^2}. && (3.45) \end{aligned}$$

where

$$\begin{aligned} \lim_{r\to\infty}\varphi &= \varphi_0\,, && (3.46)\\ \alpha_0 &= -\frac{1}{2}\frac{\partial \ln F}{\partial\varphi}\bigg|_{\varphi=\varphi_0}, && (3.47)\\ \beta_0 &= -\frac{1}{2}\frac{\partial^2 \ln F}{\partial^2\varphi}\bigg|_{\varphi=\varphi_0}. && (3.48) \end{aligned}$$

When $\beta_0 = 0$, we recover Brans-Dicke theory. If in addition $\alpha_0 = 0$, we recover General Relativity.

Furthermore, the effective gravitational constant betweeen two bodies, which is measured by a Cavendish experiment, is given by [67]

$$\bar{G} = G(1+{\alpha_0}^2)\,, \tag{3.49}$$

where G is the bare gravitational constant from our action.

Since α_0 and β_0 give the two leading order terms in the Taylor expansion of α, the standard choice in the literature to parametrize the conformal function F is

$$F(\varphi) = e^{-2\alpha_0(\varphi-\varphi_0)-\beta_0(\varphi-\varphi_0)^2}\,. \tag{3.50}$$

In the remainder of our study we will follow this choice and work with the conformal factor given by Eq. (3.50). The parameter α_0 determines the coupling of the scalar field to a GW detector far away from the source: a scalar wave of angular frequency Ω induces a total detector strain

$$h = 2\alpha_0\left[1-\left(\frac{\omega_*}{\Omega}\right)\right]\varphi \tag{3.51}$$

where $\omega_* = \mu/\hbar$ is the characteristic frequency introduced by the scalar mass μ. This will be studied in more detail in Sec. 5.8.

The φ_0 term is not an independent parameter, as we can redefine the scalar field $\bar{\varphi} \equiv \varphi - \varphi_0$, with the asymptotic value being $\bar{\varphi}_0 = 0$ and the coupling function $F(\varphi) = e^{-2\alpha_0\bar{\varphi}-\beta_0\bar{\varphi}^2}$ [67]. As a consequence, throughout this thesis we shall set $\varphi_0 = 0$ without loss of generality.

We shall explore the impact of both α_0 and β_0 on the theory. To the best of our knowledge, the nonzero α_0 case is barely covered in the literature on massive ST theory in both static cases and dynamic simulations.

3.3.2 Constraints

In massless ST theories we can constrain α_0 by measuring PPN deviations to GR in Solar System tests such as Mercury's perihelion shift [68], lunar laser ranging [69] and light deflection measurements. The most stringent constraint comes from time delay measurements from the Cassini spacecraft [52]:

$$\gamma - 1 = (2.1 \pm 2.3) \times 10^{-5}\,, \tag{3.52}$$

which limits the scalar parameter to $\alpha_0 < 3.4 \times 10^{-3}$

The β_0 parameter (also in massless ST theory) can be constrained using measurements from pulsars in close binaries. Their orbits shrink over time due to GW emission, but, in ST theory, the scalar field provides an additional radiative degree of freedom leading to more energy being lost and the orbits shrinking faster. The most stringent constraint obtained so far is based on the pulsar-white dwarf binary PSR J1738 0333 [49], which limits $\beta_0 > -4.5$.

In [42, 70], it has been shown that the least negative β_0 value which allows spontaneous scalarization to occur is ~ -4.35, though the exact value depends on the equation of state. This leaves little room for the phenomenon to occur in massless ST theory when taking into account the binary pulsar constraints.

3.3.3 Scalar potential

One way to circumvent the constraints put on massless ST theories is introducing a scalar potential and effectively giving the scalar field a mass [53] (temporarily restoring the asymptote φ_0):

$$W(\varphi) = \frac{1}{2}\mu^2(\varphi - \varphi_0)^2\,, \tag{3.53}$$

where μ acts as the scalar field mass parameter. The Compton wavelength of the field will then be $\lambda_c = (2\pi\hbar)/(\mu c)$. In massless ST, the asymptotic behaviour of φ at spatial infinity is given by [13]

$$\varphi(r \to \infty) = \varphi_0 + \frac{\varpi}{r} + O\left(\frac{1}{r^2}\right) , \tag{3.54}$$

where ϖ is the scalar charge, whereas in massive ST theory an assymptotic analysis of the scalar field wave equation yields for regular solutions an exponential decay of the form

$$\varphi(r \to \infty) = \varphi_0 + \frac{e^{\frac{-2\pi r}{\lambda_c}}}{r} + O\left(\frac{1}{r^2}\right) . \tag{3.55}$$

Again, we can set the asymptotic value of φ to 0.

To understand how the constraints are avoided, we follow the analysis in [53] by looking at the mechanism that leads to spontaneous scalarization. We return to the wave equation for the scalar field in the Einstein frame Eq. (3.15):

$$\bar{\Box}\varphi = -4\pi\alpha(\varphi)\bar{T} + W_{,\varphi} .$$

For our choice of a coupling function we have $\alpha(\varphi) = \alpha_0 + \beta_0\varphi$ and the trace of the energy-momentum tensor in the Einstein frame can be related to its Jordan frame counterpart:

$$\bar{T} = \bar{T}^{\alpha\beta}\bar{g}_{\alpha\beta} = \frac{1}{F^3}T^{\alpha\beta} \times F g_{\alpha\beta} = \frac{1}{F^2}T. \tag{3.56}$$

Thus, the wave equation becomes

$$\bar{\Box}\varphi = -4\pi(\alpha_0 + \beta_0\varphi) \times e^{4\alpha_0\varphi + 2\beta_0\varphi^2}T + \mu^2\varphi . \tag{3.57}$$

For this analysis we assume α_0 is negligibly small. By expanding perturbatively around the GR-like solution $\varphi = 0$ the wave equation reduces to:

$$\bar{\Box}\varphi \approx (-4\pi T\beta_0 + \mu^2)\varphi. \tag{3.58}$$

The trace of the energy-momentum tensor for a perfect fluid is $T = -\rho + 3P$. For non-relativistic matter we have furthermore $\rho \gg P$, leading to $T \approx -\rho$, in which case the wave equation reduces even further

$$\bar{\Box}\varphi \approx (4\pi\rho\beta_0 + \mu^2)\varphi . \tag{3.59}$$

For β_0 very negative, the whole term on the right hand side is negative, potentially giving rise to a tachyonic instability. Let us define $\omega_{\text{eff}}^2 = 4\pi\rho|\beta_0|$ and $\lambda_{\text{eff}} = 2\pi/\omega_{\text{eff}}$. We obtain exponentially growing modes if and only if β_0 is sufficiently negative such that $\lambda_{\text{eff}} < \lambda_c$. In this case, the Fourier modes $e^{-i(\omega t - kr)}$ with wavelengths satisfying:

$$\frac{1}{\lambda^2} < \frac{1}{\lambda_{\text{eff}}^2} - \frac{1}{\lambda_c^2} \implies \lambda > \frac{\lambda_{\text{eff}}}{\sqrt{1 - \left(\frac{\lambda_{\text{eff}}}{\lambda_c}\right)^2}}\,, \tag{3.60}$$

will experience a tachyonic instability. The increase is not indefinite: as the scalar field increases, the non-linear terms in (3.57) become important and will supress any further growth. We also need at least one of these modes to fit within the star (otherwise they will mostly experience $\rho = 0$), i.e. the wavelength of the shortest unstable mode has to be less than the stellar radius, $\lambda_{\text{eff}} < R$.

For a star, we have $\rho \sim \frac{M}{R^3} = \frac{C}{2R^2}$, where $M,\ R,\ C \equiv 2M/R$ are the mass, radius and compactness of the star. Thus, we obtain an approximate condition for scalarization

$$\lambda_{\text{eff}} \sim \frac{R}{\sqrt{C|\beta_0|}} \implies \frac{R}{\sqrt{C|\beta_0|}} \lesssim R \tag{3.61}$$

$$\implies \frac{1}{|\beta_0|} \lesssim C\,. \tag{3.62}$$

The compactness for a 1.4 $M_\odot$ neutron star ranges between 1/3 and 1/5, whereas for a white dwarf $C \sim 10^{-3}$ and for a main sequence star $C \sim 10^{-6}$ [53]. Thus, in order to obtain spontaneous scalarization within a neutron star, but assuming white dwarfs are not strongly scalarized, from Eq. (3.62) we obtain new bounds for β_0,

$$3 \lesssim -\beta_0 \lesssim 10^3. \tag{3.63}$$

But, in order for these values to generate strong scalarization through the tachyonic instability, we still need $\lambda_{\text{eff}} < \lambda_c$. A strict upper limit can be obtained by considering the smallest Compton wavelength the scalar field can have, or, equivalently, the smallest value of λ_{eff}. Since the latter depends on the structure of the star according to (3.61) we must consider a neutron star where $C|\beta_0|$ is maximal [53], i.e. $C \sim 1/3$ and $|\beta_0| = 10^3$ (from Eq. (3.63)); with $R \approx 10$ km for NSs, we obtain

$$\mu \lesssim 10^{-9}\ \text{eV}. \tag{3.64}$$

In order to circumvent the binary system pulsar constraints, we need the scalar field to decay exponentially with distance before it affects the orbit of the system, i.e. the scalar mass must be sufficiently large such that $\lambda_c \ll r_p$, where r_p is the periapse of the system's orbit. If we use the measurements from the pulsar-white dwarf binary PSR J1738 0333, $r_p \sim 10^{10}$ m, we obtain a lower limit for the scalar mass:

$$\mu \gg 10^{-16}\ \mathrm{eV}. \tag{3.65}$$

PPN parameters for massive ST theories have not been studied in as much detail as for the massless case. In [7] the authors calculate the Eddington parameters for massive Brans-Dicke theory of gravity. A first exploration of the PPN parameters in massive ST theory has been presented in [71], but the dependence of the PPN terms on the distance to the source makes the interpretation of observational data more complicated, so that rigorous bounds beyond the above considerations are, at present, not available to the best of our knowledge.

3.4 Wave propagation in massive ST theory

In this section the extraction of the scalar waveforms from the core collapse simulations is described along with a procedure for converting this into a prediction for the GW signal at astrophysically large distances which is potentially observable by LIGO/Virgo. The latter step is complicated by the dispersive nature of wave propagation for massive fields; it will be shown how this dispersion generically leads to an *inverse chirp*.

There are two natural lengthscales relevant to the problem: the gravitational radius associated with the mass of the star, $r_{\mathrm{G}} = GMc^{-2}$; and the reduced Compton wavelength for the massive scalar field, $\lambdabar_{\mathrm{C}} = c/\omega_*$ where

$$\omega_* = \mu c^2 \hbar^{-1}\,. \tag{3.66}$$

At large distance from the star ($r \gg r_{\mathrm{G}}$) the dynamics of the gravitational scalar are, to a good approximation, governed by the flat-space Klein-Gordon equation,

$$\partial_t^2 \varphi - \nabla^2 \varphi + \omega_*^2 \varphi = 0\,. \tag{3.67}$$

In spherical symmetry (using coordinates $\{t,\, r,\, \theta,\, \phi\}$) the field depends only on time and radius, $\psi = \psi(t; r)$, the Laplacian is given by $\nabla^2 \cdot = r^{-2}\partial_r(r^2\partial_r \cdot)$, and the rescaled field $\sigma \equiv r\varphi$ satisfies a 1D wave equation,

$$\partial_t^2 \sigma - \partial_r^2 \sigma + \omega_*^2 \sigma = 0\,. \tag{3.68}$$

Consider first the behaviour of a single Fourier mode, $\sigma \propto e^{-i(\omega t - kr)}$; Eq. (3.68) gives the *dispersion relation*

$$\omega^2 = k^2 + \omega_*^2\,. \tag{3.69}$$

The wavenumber k is real for high frequencies $|\omega| > \omega_*$ and the solution describes a propagating wave. For low frequencies $|\omega| < \omega_*$, including the static case $\omega = 0$, the wavenumber is imaginary leading to solutions which decay exponentially over a characteristic length $\lambda\!\!\!^{-}_{\rm C}$.

The critical frequency ω_*, associated with the scalar field mass, acts as a low frequency cutoff in the GW spectrum. For propagating solutions, the phase velocity ($v_{\rm phase} = \omega/k = [1 - (\omega_*/\omega)^2]^{-1/2}$) is superluminal, while the group velocity ($v_{\rm group} = {\rm d}\omega/{\rm d}k = [1 - (\omega_*/\omega)]^{+1/2}$) is subluminal.

In the massless case ($\mu = 0$) the general solution to Eq. (3.68) can be written as the sum of ingoing and outgoing pulses travelling at the speed of light c. This makes interpreting the output of core-collapse simulations particularly simple. First, one extracts the field as a function of time $\sigma(t; r_{\rm ex})$ at a fixed *extraction radius*, $r_{\rm ex}$. This radius must be sufficiently large that (i) the flat space Eq. (3.67) holds, and (ii) $r_{\rm ex}$ is in the wave zone so that the signal has decoupled from the source and is purely outgoing. In the massless case both (i) and (ii) are satisfied by choosing $r_{\rm ex} \gg r_{\rm G}$. Then, the signal as a function of time at some larger *target radius*, $\sigma(t; r)$, is simply obtained via $\sigma(t - [r - r_{\rm ex}]; r) = \sigma(t; r_{\rm ex})$. The only changes in the signal between $r_{\rm ex}$ and r are a time delay and an amplitude decay in the field φ proportional to $(r/r_{\rm ex})^{-1}$.

We seek an analogous method in the massive case ($\mu > 0$) for relating the signal at the extraction radius to the signal at the much larger target radius. The extraction radius is chosen to satisfy the two conditions as before, but now (ii) requires $r_{\rm ex} \gg \lambda\!\!\!^{-}_{\rm C}$. This is generally a stricter condition than $r_{\rm ex} \gg r_{\rm G}$; for $\mu = 10^{-14}\,{\rm eV}$ the Compton wavelength is $\lambda\!\!\!^{-}_{\rm C} \approx 10^7\,{\rm m}$ whereas the gravitational radius for a $12\,M_\odot$ is star $r_{\rm G} \approx 10^4\,{\rm m}$. In this thesis the extraction radius is taken to be in the range $= 3.0 \times 10^7 - 10^8$ m. The target radius, the distance of the supernova from Earth, is very much larger; e.g. $\sim 10\,{\rm kpc}$.

The remainder of this section describes two methods for evolving signals from the extraction radius out to large radii. Firstly, a numerical evolution of Eq. (3.68) in the time domain is described. This numerical method, while very accurate at short distance,

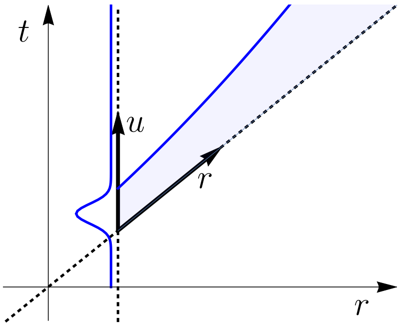

Fig. 3.1 A sketch plot of the coordinates used in the numerical evolution. The main axes show the standard $\{t, r\}$ coordinates and the inset arrows show the $\{u, r\}$ coordinates. The vertical blue line indicates the signal as a function of time at the extraction radius, $\sigma(t; r_{\text{ex}})$, and the shading indicates the region where the signal will propagate to (dispersively). A numerical grid based on null coordinates $\{u, r\}$ can cover the shaded region with less redundant space than one based on $\{t, r\}$.

is of limited use in practice because it struggles to cope with the very large astrophysical distances. Secondly, an analytic method for solving Eq. (3.68) in the frequency domain is described. The two methods are validated by comparing them against each other in the regime where both can be evaluated. Finally, the analytic method is used to study the asymptotic behaviour at large distances using the stationary phase approximation (SPA).

3.4.1 Numerical evolution in the time domain

Given suitable initial data it is possible to numerically evolve Eq. (3.68). Here it is necessary to evolve some given outgoing data on a timelike surface out to larger radii (see Fig. 3.1). Equation (3.68) is written in a manner that makes a $1+1$ dimensional split obvious using the coordinates $\{t, r\}$. However, these coordinates are not well adapted for signals travelling at, or near, the speed of light. Alternatively, and much more efficiently, a $1+1$ split can be implemented based on coordinates $\{u, r\}$, where $u \equiv t - r$ is the (null) retarded time coordinate. Using these coordinates the wave equation becomes

$$2\partial_u \partial_r \sigma - \partial_r^2 \sigma + \omega_*^2 \sigma = 0 \,. \tag{3.70}$$

By defining the conjugate momentum $\Pi_u \equiv \partial_u \sigma(u; r)$ Eq. (3.70) can be reduced to first order form.

Given an initial signal on the extraction sphere, $\sigma(u; r_{\text{ex}})$, it is straightforward to solve Eq. (3.70) using standard techniques; in our case a *method of line* integration with the *iterated Crank-Nicholson* scheme [72]. From this numerical solution, we directly extract the signal at some larger target radius, $\sigma(u; r)$.

3.4.2 Analytic evolution in the Fourier domain

For an analytic study, we now revert to coordinates $\{t, r\}$ in Eq. (3.68). With the convention

$$\tilde{\sigma}(\omega; r) = \int_{-\infty}^{\infty} \mathrm{d}t \; \sigma(t, r) e^{\mathrm{i}\omega t} \, , \tag{3.71}$$

$$\sigma(t; r) = \int_{-\infty}^{\infty} \frac{\mathrm{d}\omega}{2\pi} \; \tilde{\sigma}(\omega, r) e^{-\mathrm{i}\omega t} \, , \tag{3.72}$$

the Fourier transform of Eq. (3.68) yields the simple harmonic motion equation for $\tilde{\sigma}(\omega; r)$,

$$\partial_r^2 \, \tilde{\sigma}(\omega; r) = -\Big(\omega^2 - \omega_*^2\Big) \tilde{\sigma}(\omega; r) \, . \tag{3.73}$$

Defining $k^+ \equiv + \sqrt{\omega^2 - \omega_*^2}$ as the positive root of the dispersion relation in Eq. (3.69), the solution to Eq. (3.73) can be written in terms of two arbitrary functions,

$$\tilde{\sigma}(\omega; r) = A(\omega) \mathrm{e}^{\mathrm{i}k^+ (r - r_{\text{ex}})} + B(\omega) \mathrm{e}^{-\mathrm{i}k^+ (r - r_{\text{ex}})} \, . \tag{3.74}$$

The radial coordinate has been shifted to the extraction radius for later convenience. Taking the inverse Fourier transform to convert back into the time domain gives

$$\sigma(t; r) = \int_{-\infty}^{\infty} \frac{\mathrm{d}\omega}{2\pi} \left[A(\omega) \mathrm{e}^{\mathrm{i}k^+ (r - r_{\text{ex}})} + B(\omega) \mathrm{e}^{-\mathrm{i}k^+ (r - r_{\text{ex}})} \right] \mathrm{e}^{-\mathrm{i}\omega t} \, . \tag{3.75}$$

The fact that the field φ is real imposes some constraints on the otherwise arbitrary functions A and B;

$$\sigma(t; r) \in \mathbb{R} \;\Rightarrow\; \tilde{\sigma}(\omega; r) = \tilde{\sigma}^*(-\omega; r) \tag{3.76}$$

$$\Rightarrow \begin{cases} A(\omega) = B^*(-\omega) & \text{if } |\omega| > \omega_* \\ A(\omega) = A^*(-\omega) \text{ and } B(\omega) = B^*(-\omega) & \text{if } |\omega| < \omega_* . \end{cases}$$

A further constraint on the function B is obtained by imposing boundary conditions at infinity. The field φ must decay as $1/r$ (or faster) which implies that $\tilde{\sigma}(\omega; r)$ remains bounded at large radii. From Eq. (3.75), and recalling that k^+ is imaginary for $|\omega| < \omega_*$, we obtain the constraint

$$B(\omega) = 0 \quad \text{if } |\omega| < \omega_* \,. \tag{3.77}$$

The constraints (3.76) and (3.77) can be used to eliminate $B(\omega)$ in favour of $A(\omega)$. Furthermore, the symmetries implied by the constraint (3.76) allow the Fourier integral in Eq. (3.75) to be written over positive frequencies:

$$\begin{aligned}\sigma(t;r) = \int_0^\infty \frac{\mathrm{d}\omega}{2\pi} \Big[& A(\omega)\mathrm{e}^{\mathrm{i}k^+(r-r_{\mathrm{ex}})}\mathrm{e}^{-\mathrm{i}\omega t} + B(\omega)\mathrm{e}^{-\mathrm{i}k^+(r-r_{\mathrm{ex}})}\mathrm{e}^{-\mathrm{i}\omega t} \\ & + A(-\omega)\mathrm{e}^{\mathrm{i}k^+(r-r_{\mathrm{ex}})}\mathrm{e}^{\mathrm{i}\omega t} + B(-\omega)\mathrm{e}^{-\mathrm{i}k^+(r-r_{\mathrm{ex}})}\mathrm{e}^{\mathrm{i}\omega t}\Big] \,.\end{aligned} \tag{3.78}$$

Next, we split the integral into frequencies above and below ω_*:

$$\int_0^\infty = \int_0^{\omega_*} + \int_{\omega_*}^\infty \,.$$

The constraints (3.76) and (3.77) eliminate the B terms and replaces $A(-\omega)$ with $A^*(\omega)$ in the first integral,

$$\begin{aligned}\sigma(t;r) = & \int_0^{\omega_*} \frac{\mathrm{d}\omega}{2\pi} \Big[A(\omega)\mathrm{e}^{\mathrm{i}k^+(r-r_{\mathrm{ex}})}\mathrm{e}^{-\mathrm{i}\omega t} + A^*(\omega)\mathrm{e}^{\mathrm{i}k^+(r-r_{\mathrm{ex}})}\mathrm{e}^{\mathrm{i}\omega t}\Big] \\ & + \int_{\omega_*}^\infty \frac{\mathrm{d}\omega}{2\pi} \Big[A(\omega)\mathrm{e}^{\mathrm{i}k^+(r-r_{\mathrm{ex}})}\mathrm{e}^{-\mathrm{i}\omega t} + B(\omega)\mathrm{e}^{-\mathrm{i}k^+(r-r_{\mathrm{ex}})}\mathrm{e}^{-\mathrm{i}\omega t} \\ & \qquad + A(-\omega)\mathrm{e}^{\mathrm{i}k^+(r-r_{\mathrm{ex}})}\mathrm{e}^{\mathrm{i}\omega t} + B(-\omega)\mathrm{e}^{-\mathrm{i}k^+(r-r_{\mathrm{ex}})}\mathrm{e}^{\mathrm{i}\omega t}\Big] \,.\end{aligned} \tag{3.79}$$

while (3.76) can be used to replace the B terms in the second integral

$$\begin{aligned}\sigma(t;r) = & \int_0^{\omega_*} \frac{\mathrm{d}\omega}{2\pi} \Big[A(\omega)\mathrm{e}^{\mathrm{i}k^+(r-r_{\mathrm{ex}})}\mathrm{e}^{-\mathrm{i}\omega t} + A^*(\omega)\mathrm{e}^{\mathrm{i}k^+(r-r_{\mathrm{ex}})}\mathrm{e}^{\mathrm{i}\omega t}\Big] \\ & + \int_{\omega_*}^\infty \frac{\mathrm{d}\omega}{2\pi} \Big[A(\omega)\mathrm{e}^{\mathrm{i}k^+(r-r_{\mathrm{ex}})}\mathrm{e}^{-\mathrm{i}\omega t} + A^*(-\omega)\mathrm{e}^{-\mathrm{i}k^+(r-r_{\mathrm{ex}})}\mathrm{e}^{-\mathrm{i}\omega t} \\ & \qquad + A(-\omega)\mathrm{e}^{\mathrm{i}k^+(r-r_{\mathrm{ex}})}\mathrm{e}^{\mathrm{i}\omega t} + A^*(\omega)\mathrm{e}^{-\mathrm{i}k^+(r-r_{\mathrm{ex}})}\mathrm{e}^{\mathrm{i}\omega t}\Big] \,.\end{aligned} \tag{3.80}$$

Clearly the terms in the second half of both integrals are the complex conjugates of those in the first half. The general solution in Eq. (3.75) becomes

$$\begin{aligned}\sigma(t;r) = 2\Re\bigg\{ &\int_0^{\omega_*} \frac{\mathrm{d}\omega}{2\pi}\, A(\omega)\mathrm{e}^{\mathrm{i}k^+(r-r_{\mathrm{ex}})}\mathrm{e}^{-\mathrm{i}\omega t} \\ &+ \int_{\omega_*}^{\infty} \frac{\mathrm{d}\omega}{2\pi} \Big(A(\omega)\mathrm{e}^{\mathrm{i}k^+(r-r_{\mathrm{ex}})} + A^*(-\omega)\mathrm{e}^{-\mathrm{i}k^+(r-r_{\mathrm{ex}})} \Big) \mathrm{e}^{-\mathrm{i}\omega t} \bigg\}.\end{aligned} \tag{3.81}$$

From Eq. (3.81), and considering the sign of k^+, it can be seen that the high frequencies $A(\omega > \omega_*)$ represent outgoing modes, the large negative frequencies $A(\omega < -\omega_*)$ represent ingoing modes, and the intermediate frequencies $A(|\omega| < \omega_*)$ represent non-propagating modes.

It only remains to relate the unknown function $A(\omega)$ to the (purely outgoing) scalar profile at the extraction radius obtained from the core collapse simulation, $\sigma(t; r_{\mathrm{ex}})$. The function $A(\omega)$ is given by

$$A(\omega) = \begin{cases} 0 & \text{if } \omega \leq -\omega_* \\ \tilde{\sigma}(\omega; r_{\mathrm{ex}}) & \text{if } \omega > -\omega_* \end{cases} . \tag{3.82}$$

Substituting this into Eq. (3.81) results in

$$\begin{aligned}\sigma(t;r) = 2\Re\bigg\{ &\int_0^{\omega_*} \frac{\mathrm{d}\omega}{2\pi}\, \tilde{\sigma}(\omega; r_{\mathrm{ex}})\mathrm{e}^{\mathrm{i}k^+(r-r_{\mathrm{ex}})}\mathrm{e}^{-\mathrm{i}\omega t} \\ &+ \int_{\omega_*}^{\infty} \frac{\mathrm{d}\omega}{2\pi}\, \tilde{\sigma}(\omega; r_{\mathrm{ex}})\mathrm{e}^{\mathrm{i}k^+(r-r_{\mathrm{ex}})}\mathrm{e}^{-\mathrm{i}\omega t} \bigg\},\end{aligned} \tag{3.83}$$

and returning to writing the integral over both positive and negative frequencies, gives

$$\begin{aligned}\sigma(t;r) = &\int_0^{\omega_*} \frac{\mathrm{d}\omega}{2\pi} \Big[\tilde{\sigma}(\omega; r_{\mathrm{ex}})\mathrm{e}^{\mathrm{i}k^+(r-r_{\mathrm{ex}})}\mathrm{e}^{-\mathrm{i}\omega t} + \tilde{\sigma}^*(\omega; r_{\mathrm{ex}})\mathrm{e}^{\mathrm{i}k^+(r-r_{\mathrm{ex}})}\mathrm{e}^{\mathrm{i}\omega t} \Big] \\ &+ \int_{\omega_*}^{\infty} \frac{\mathrm{d}\omega}{2\pi} \Big[\tilde{\sigma}(\omega; r_{\mathrm{ex}})\mathrm{e}^{\mathrm{i}k^+(r-r_{\mathrm{ex}})}\mathrm{e}^{-\mathrm{i}\omega t} + \tilde{\sigma}^*(\omega; r_{\mathrm{ex}})\mathrm{e}^{-\mathrm{i}k^+(r-r_{\mathrm{ex}})}\mathrm{e}^{\mathrm{i}\omega t} \Big].\end{aligned} \tag{3.84}$$

Since σ is a real function, we have $\tilde{\sigma}^*(\omega; r_{\mathrm{ex}}) = \tilde{\sigma}(-\omega; r_{\mathrm{ex}})$ which implies

$$\begin{aligned}\sigma(t;r) = &\int_0^{\omega_*} \frac{\mathrm{d}\omega}{2\pi} \Big[\tilde{\sigma}(\omega; r_{\mathrm{ex}})\mathrm{e}^{ik^+(r-r_{\mathrm{ex}})}\mathrm{e}^{-\mathrm{i}\omega t} + \tilde{\sigma}(-\omega; r_{\mathrm{ex}})\mathrm{e}^{ik^+(r-r_{\mathrm{ex}})}\mathrm{e}^{\mathrm{i}\omega t} \Big] \\ &+ \int_{\omega_*}^{\infty} \frac{\mathrm{d}\omega}{2\pi} \Big[\tilde{\sigma}(\omega; r_{\mathrm{ex}})\mathrm{e}^{ik^+(r-r_{\mathrm{ex}})}\mathrm{e}^{-\mathrm{i}\omega t} + \tilde{\sigma}(-\omega; r_{\mathrm{ex}})\mathrm{e}^{-\mathrm{i}k^+(r-r_{\mathrm{ex}})}\mathrm{e}^{\mathrm{i}\omega t} \Big]\end{aligned} \tag{3.85}$$

$$\begin{aligned}\implies \sigma(t;r) = &\int_{-\omega_*}^{\omega_*} \frac{\mathrm{d}\omega}{2\pi}\,\tilde{\sigma}(\omega;r_{\mathrm{ex}})\mathrm{e}^{\mathrm{i}k^+(r-r_{\mathrm{ex}})}\mathrm{e}^{-\mathrm{i}\omega t} \\ &+\int_{\omega_*}^{\infty} \frac{\mathrm{d}\omega}{2\pi}\,\tilde{\sigma}(\omega;r_{\mathrm{ex}})\mathrm{e}^{\mathrm{i}k^+(r-r_{\mathrm{ex}})}\mathrm{e}^{-\mathrm{i}\omega t} + \int_{-\infty}^{\omega_*} \frac{\mathrm{d}\omega}{2\pi}\, + \tilde{\sigma}(\omega;r_{\mathrm{ex}})\mathrm{e}^{-\mathrm{i}k^+(r-r_{\mathrm{ex}})}\mathrm{e}^{-\mathrm{i}\omega t}\,.\end{aligned} \tag{3.86}$$

Thus we obtain

$$\sigma(t;r) = \int \frac{\mathrm{d}\omega}{2\pi}\,\tilde{\sigma}(\omega;r_{\mathrm{ex}}) \times \left\{\begin{matrix} \mathrm{e}^{-\mathrm{i}k^+(r-r_{\mathrm{ex}})} & \text{if } \omega \leq -\omega_* \\ \mathrm{e}^{+\mathrm{i}k^+(r-r_{\mathrm{ex}})} & \text{if } \omega > -\omega_* \end{matrix}\right\} \mathrm{e}^{-\mathrm{i}\omega t}\,. \tag{3.87}$$

This shows that the frequency domain signal at the target radius is related to that at the extraction radius via

$$\tilde{\sigma}(\omega;r) = \tilde{\sigma}(\omega;r_{\mathrm{ex}}) \times \left\{\begin{matrix} \mathrm{e}^{-\mathrm{i}k^+(r-r_{\mathrm{ex}})} & \text{if } \omega \leq -\omega_* \\ \mathrm{e}^{+\mathrm{i}k^+(r-r_{\mathrm{ex}})} & \text{if } \omega > -\omega_* \end{matrix}\right\}. \tag{3.88}$$

Note that the effect of the dispersion enters only in the complex phase of the Fourier transform. Therefore, the effect of the dispersion is to disperse the signal, rearranging the frequency components in time, while leaving the overall power spectrum invariant for all $|\omega| > \omega_*$. (Lower frequencies, $|\omega| < \omega_*$, are exponentially suppressed during propagation and are not observable at large distances.)

We now have a prescription for analytically propagating signals out to larger radii. Firstly, numerically evaluate the fast Fourier transform of the scalar profile on the extraction sphere; $\tilde{\sigma}(\omega;r_{\mathrm{ex}})$. Secondly, use Eq. (3.88) to obtain the Fourier domain signal at the target radius; $\tilde{\sigma}(\omega;r)$. Finally, numerically evaluate the inverse Fourier transform to obtain the desired signal; $\sigma(t;r)$.

3.4.3 Comparing the methods

As a simple test, consider a signal which, on the extraction sphere, is a cosine-Gaussian wavepacket,

$$\sigma(u;r_{\mathrm{ex}}) = \cos\left(\frac{2\pi(u-r_{\mathrm{ex}})}{T}\right)\exp\left(\frac{-(u-r_{\mathrm{ex}})^2}{18T^2}\right). \tag{3.89}$$

The parameter T is an overall timescale which is set to unity without loss of generality and the scalar field mass is chosen to be $\omega_* = 2/T$. The signal is propagated to larger radii using both of the methods described above and the results are summarized in Fig. 3.2. As can be seen in that figure, there is excellent qualitative agreement between

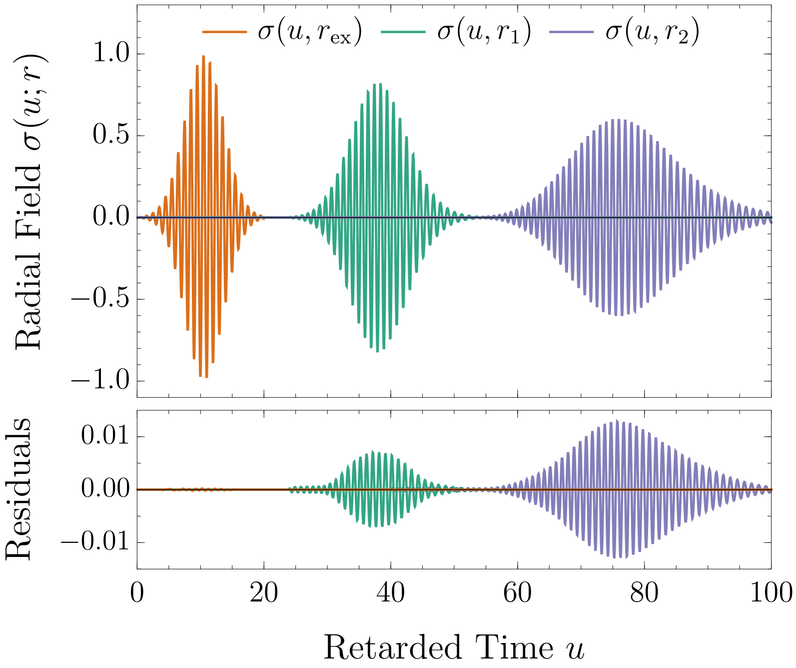

Fig. 3.2 The top panel shows the results of evolving an initially cosine-Gaussian waveform out to radii $r_1 = r_{\rm ex} + 500cT$ and $r_2 = r_{\rm ex} + 1200cT$ using the time domain numerical evolution of the wave equation (see Sec. 3.4.1). The evolution to large radii was also performed using the analytic Fourier domain approach (see Sec. 3.4.2) and the bottom panel shows the differences, or residuals, between the two methods.

the two methods. At the quantitative level there are small errors (generally $\lesssim 1\%$, as can be seen from the lower panel) which are due to numerical errors in the $1+1$ time domain evolution (this has been checked by verifying the scaling of the errors with grid resolution). As the signals propagate to larger radii the peak lags at later retarded times due to the subluminal wave propagation. Additionally, the variation in the group velocity between the different Fourier components of the wavepacket leads to a broadening of the peak; careful inspection of the $\sigma(u; r_2)$ profile reveals the beginnings of an *inverse chirp* profile (see Sec. 3.4.4) where the high frequencies arrive first, followed by the low frequencies.

Unfortunately, neither of the methods described (in their current form) is suitable for propagating the signal to astrophysically large distances (e.g. $r_{\rm ex} = 10\,\text{kpc}$). The unavoidable problem is that as the signal propagates further, the longer (more cycles) and more dispersively stretched out it becomes. This poses two problems for the time domain numerical integration: firstly, the evolution becomes increasingly expensive due to the large numerical grids required; and secondly, as can be seen from the bottom panel of Fig. 3.2, the numerical errors tend to grow as the signal is propagated to greater distances. The analytic frequency domain method can be pushed to somewhat larger radii; however, even this fails when the signal eventually becomes longer than the largest array for which the fast Fourier transform can be evaluated. The next section describes how the behaviour of the scalar field at very large distances may be studied.

3.4.4 Asymptotic behaviour: the inverse chirp

As the signal is stretched out it becomes ever more oscillatory, and the amplitude varies more slowly relative to the phase. Therefore, in the large distance limit the *stationary phase approximation* (SPA) may be used to evaluate the inverse Fourier transform in Eq. (3.87). It should be noted that the SPA *becomes* valid at large radii regardless of whether or not it was initially valid for the signal at the extraction radius. As will be shown below, dispersive signals tend to "forget" the details of their initial profile as they propagate over large distances and always tend to a generic "inverse chirp" profile.

As noted above, at large radii frequencies $|\omega| < \omega_*$ do not contribute because they decay exponentially with r. It will be convenient to write the time domain solution in Eq. (3.87) as an integral over positive frequencies only;

$$\sigma(t;r) = 2\Re\left\{ \int_{\omega_*}^{\infty} \frac{\mathrm{d}\omega}{2\pi}\, \mathcal{A}(\omega) \mathrm{e}^{\mathrm{i}\phi(\omega,t)} \right\} . \tag{3.90}$$

In this equation the initial signal at the extraction radius has been decomposed as $\tilde{\sigma}(\omega; r_{\mathrm{ex}}) = \mathcal{A}(\omega; r_{\mathrm{ex}})\mathrm{e}^{\mathrm{i}\Psi(\omega)}$, and the modified complex phase is defined as $\phi(\omega,t) \equiv \Psi(\omega) + k^{+}(r - r_{\mathrm{ex}}) - \omega t$. This phase has a stationary point when $\partial\phi(\omega,t)/\partial\omega = 0$ which is satisfied by

$$t = \frac{\mathrm{d}\Psi(\omega)}{\mathrm{d}\omega} + \frac{\omega(r - r_{\mathrm{ex}})}{\sqrt{\omega^2 - \omega_*^2}} . \tag{3.91}$$

Notice that the final term can be written as $(r - r_{\mathrm{ex}})/v_{\mathrm{group}}$. In the limit $r \gg r_{\mathrm{ex}}$ the final term in Eq. (3.91) becomes dominant and the $\mathrm{d}\Psi/\mathrm{d}\omega$ term can be neglected. In this approximation, it is straightforward to invert Eq. (3.91) which gives us the frequency of the signal at r as a function of time, $\omega = \Omega(t)$, where

$$\Omega(t) = \frac{\omega_*}{\sqrt{1 - \left(\frac{r - r_{\mathrm{ex}}}{t}\right)^2}} , \quad \text{for } \ t > r - r_{\mathrm{ex}} . \tag{3.92}$$

This frequency varies as an *inverse chirp* (see Fig. 3.3) with low frequencies arriving after high frequencies. The origin of the inverse chirp is easily understood as the

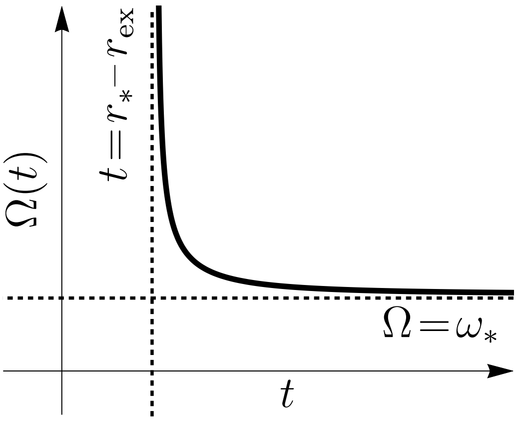

Fig. 3.3 A sketch plot showing the time-frequency structure of the "inverse chirp" in Eq. (3.92). The frequency decays over time; the high frequency components (traveling at almost the speed of light) arrive first, followed by the slower low frequency components. Frequencies below ω_* are exponentially suppressed and never reach large radii.

modes of each frequency arriving at a time corresponding to the group velocity of that frequency.

All that remains is to evaluate the amplitude as a function of time. This can also be done via the SPA. The integrand in Eq. (3.90) is highly oscillatory when $r - r_{\mathrm{ex}}$ is large, except for frequencies near $\Omega(t)$ which therefore dominate the result. Expanding the amplitude to zeroth order, and the phase to quadratic order about $\omega = \Omega(t)$ and substituting into Eq. (3.90) gives

$$\sigma(t;r) = 2\Re\left\{\mathcal{A}\big[\Omega(t)\big]\mathrm{e}^{\mathrm{i}\phi[\Omega(t),t]} \times \int_{\omega_*}^{\infty}\frac{\mathrm{d}\omega}{2\pi}\,\mathrm{e}^{\frac{\mathrm{i}}{2}[\omega-\Omega(t)]^2\phi''}\right\}, \tag{3.93}$$

where $\phi'' \equiv \partial^2\phi(\omega,t)/\partial\omega^2|_{\omega=\Omega(t)}$. The integrand in Eq. (3.93) is dominated by frequencies near $\omega = \Omega(t)$. At the current approximation order, the limits of integration can be changed to $\int_{\Omega(t)-a}^{\Omega(t)+b}\mathrm{d}\omega$ for any $a, b > 0$. Choosing $a, b \to \infty$, and changing variables to $u^2 = [\omega - \Omega(t)]\,\phi''$ gives

$$\sigma(t;r) = \Re\left\{\frac{\mathcal{A}\big[\Omega(t)\big]\mathrm{e}^{\mathrm{i}\phi[\Omega(t),t]}}{\sqrt{\pi^2\,|\phi''|}} \times \int_{-\infty}^{\infty}\mathrm{d}u\;\mathrm{e}^{\frac{\mathrm{i}}{2}u^2\mathrm{sign}(\phi'')}\right\}. \tag{3.94}$$

The integral in Eq. (3.94) is a standard Gaussian integral which may be readily evaluated to give

$$\sigma(t;r) = \Re\left\{\mathrm{Amp}(t;r)\,\mathrm{e}^{\mathrm{i}\,\mathrm{Phase}(t;r)}\right\}, \tag{3.95}$$

where

$$\begin{aligned}
\mathrm{Amp}(t;r) \quad &= \sqrt{\tfrac{2\left[\Omega^2(t)-\omega_*^2\right]^{3/2}}{\pi\omega_*^2(r-r_{\mathrm{ex}})}}\,\mathcal{A}\Big[\Omega(t)\Big]\,, && (3.96)\\
\mathrm{Phase}(t;r) \quad &= \Psi\Big[\Omega(t)\Big] + \sqrt{\Omega(t)^2-\omega_*^2}(r-r_{\mathrm{ex}}) - \Omega(t)t - \tfrac{\pi}{4}\,. && (3.97)
\end{aligned}$$

At each instant the signal is quasi monochromatic with a frequency $\Omega(t)$ and an amplitude, $\mathrm{Amp}(t;r)$, proportional to the square root of the power spectrum of the initial (extraction radius) signal evaluated at that frequency divided by a factor to account for the dispersive stretching of the signal.

The inverse chirp profile described by Eq. (3.97) (see Fig. 3.3) is an extremely robust prediction for the signal observed at large distances. The signal frequency as a function of time depends only on the distance to the source and the mass of the scalar field (and there is a near universal scaling behaviour with the scalar mass, as described in Chapter 5). The frequency as a function of time is completely independent of the details of the original signal near the source. The signal amplitude as a function of time does retain some information about the original source, through its dependence on the spectrum $A(\omega)$, although even this gets highly smeared out by the dispersion. The inverse chirp waveforms can be extremely long and highly oscillatory; for the scalar field masses and distances of interest here (i.e. $\mu \approx 10^{-14}\,\mathrm{eV}$ and $r_{\mathrm{ex}} \approx 10\,\mathrm{kpc}$) the signals can retain frequencies and amplitudes potentially detectable by LIGO/Virgo for centuries! These signals are best visualized by plotting the amplitude and frequency separately as functions of time (see Fig. 5.33 and the accompanying discussion in Sec. 5.8).

Chapter 4

Static profiles and models in massive Scalar Tensor Theory

In this chapter we study the stability of the static stellar models of massive ST theory as it predicts new branches of solutions as opposed to GR which can lead to further avenues of constraining the theory. In addition, understanding the structure of the solutions in the static case will provide important guidance for the analysis of the dynamic collapse scenarios studied in the next chapter.

This chapter is based on a paper in preparation and is the work of the author.

4.1 Introduction

The first detection of a neutron star (NS) by Jocelyn Bell Burnell [73] has opened new avenues of study and testing as well as confirming through direct detection the existence of one of the three types of compact objects (white dwarfs, NSs and BHs). Neutron stars are the result of a supernova explosion of a massive star. They are extremely compact objects: despite their mass being comparable to our Sun's mass, their radii are on the order of 10 km (for comparison, our Solar System's Sun has a radius of $\sim 7 \times 10^5$ km). They reach nuclear densities, making them excellent test-beds for strong gravity as well as for the supra-nuclear behaviour of matter. In Earth-based laboratories, such as particle accelerators, we can conduct experiments and test the behaviour of matter near nuclear density, but only at very high temperatures; for their behaviour at low temperatures we can only rely on astrophysical observations [74]. An excellent review of recent research into NSs and their formation can be found in [74]. ST theories lead to measurable deviations in extreme gravity scenarios; because of the no-hair theorems, we are limited in exploring ST theory using black holes, which makes NSs the preferred choice.

4.2 Equation of state

"It is probably not an exaggeration to state that there are more reviews and book chapters written on the equation of state of neutron stars than there are actual constraining measurements." (Nathalie Degenaar and Valery F. Suleimanov, Chapter 5, [74])

One of the main unknowns with regard to NSs is their equation of state (EOS) for densities larger than the nuclear density, which we approximate in this work by setting $\rho_{\text{nuc}} = 2 \times 10^{14}$ g/cm^3 [75]. In our study we shall employ a simple polytropic EOS for the static solutions and a cold hybrid EOS in the core collapse simulations which are discussed in more detail in the next chapter.

A polytropic equation of state gives a direct dependence between pressure and the baryon density

$$P(\rho) \;=\; K\rho^{\Gamma}, \tag{4.1}$$

where K is a constant and Γ the adiabatic index. For the polytropic equation of state we use Novak's EOS1 from [41, 42]. In these papers the EOS is written in terms of the baryon number density $\tilde{n}_B$, the baryon number density scale $\tilde{n}_0 = 0.1 fm^{-3}$ and the atomic mass unit $\tilde{m}_B = 1.66 \times 10^{-27}$ kg,

$$\tilde{p} = K\tilde{n}_0\tilde{m}_B\left(\frac{\tilde{n}_B}{\tilde{n}_0}\right)^{\Gamma}. \tag{4.2}$$

This can easily be rewritten in the form of Eq. (4.1) using the corresponding parameters:

$$K_{\text{cgs}} = 1.543446, \quad K_{c=G=M_\odot=1} = 1186.783, \quad \Gamma = 2.34. \tag{4.3}$$

If we consider the energy density ε and the internal energy ϵ, the first law of thermodynamics ($\varepsilon = \rho + \rho\epsilon$) leads to:

$$\epsilon \;=\; \frac{P}{(\Gamma-1)\,\rho}, \tag{4.4}$$

$$h \;=\; 1+\epsilon+\frac{P}{\rho} = 1+\frac{P}{(\Gamma-1)\rho}+\frac{P}{\rho}. \tag{4.5}$$

For the so-called hybrid EOS we use the version introduced by Janka, Zwerger and Monchmeyer in Ref. [76] that captures in closed analytic form the stiffening of the matter at nuclear densities and models the response of shocked material through a thermal pressure component; see also [77, 75] and [78, 79] for a comparison with modern finite temperature EOSs. The hybrid EOS consists of a cold and a thermal pressure component given by

$$P = P_{\mathrm{c}} + P_{\mathrm{th}}\,. \tag{4.6}$$

The cold component has piecewise polytropic form

$$P_{\mathrm{c}} = \begin{cases} K_1 \rho^{\Gamma_1} & \text{if} \quad \rho \le \rho_{\mathrm{nuc}} \\ K_2 \rho^{\Gamma_2} & \text{if} \quad \rho > \rho_{\mathrm{nuc}} \end{cases} \tag{4.7}$$

and the thermal contribution is given by

$$P_{\mathrm{th}} = (\Gamma_{\mathrm{th}} - 1)\, \rho\, (\epsilon - \epsilon_{\mathrm{c}})\,, \tag{4.8}$$

where ϵ_{c} follows from the first law of thermodynamics for adiabatic processes,

$$\epsilon_{\mathrm{c}} = \begin{cases} \frac{K_1}{\Gamma_1 - 1} \rho^{\Gamma_1 - 1} & \text{if} \quad \rho \le \rho_{\mathrm{nuc}} \\ \frac{K_2}{\Gamma_2 - 1} \rho^{\Gamma_2 - 1} + E & \text{if} \quad \rho > \rho_{\mathrm{nuc}} \end{cases}\,, \tag{4.9}$$

and E is a constant of integration determined by continuity at $\rho = \rho_{\mathrm{nuc}}$. Prior to core bounce, the flow is adiabatic which implies $\epsilon \approx \epsilon_{\mathrm{c}}$, but at core bounce the shocked material becomes non-adiabatical and thus subject to a non-negligible thermal pressure component.

The EOS given by Eqs. (4.6)-(4.9) is determined by the 5 parameters Γ_1, Γ_2, K_1, Γ_{th} and ρ_{nuc}, while K_2 follows from continuity of P_{c} at $\rho = \rho_{\mathrm{nuc}}$. We set the nuclear density $\rho_{\mathrm{nuc}} = 2 \times 10^{14}\ \mathrm{g\,cm^{-3}}$, following [75] and $K_1 = 4.9345 \times 10^{14}$ [cgs], as predicted for a relativistic degenerate gas of electrons with electron fraction $Y_{\mathrm{e}} = 0.5$ [80]. A gas of relativistic electrons has an adiabatic index of 4/3, but electron capture during the collapse phase reduces the effective adiabatic index Γ_1 to slightly lower values in the range $\Gamma_1 \approx 1.28$ to $\Gamma_1 \approx 1.32$ [78, 79, 81]. At densities $\rho > \rho_{\mathrm{nuc}}$, however, neutron degeneracy becomes dominant which leads to a larger adiabatic index Γ_2. Reference [79] find $\Gamma_2 \approx 2.5$ and $\Gamma_2 \approx 3$ to approxmate well the finite temperature EOSs of Lattimer–Swesty [82, 83] and Shen *et al* [84, 85], respectively. Finally, the thermal adiabatic index Γ_{th} models a mixture of relativistic and non-relativistic gas which leads to the bounds $4/3 < \Gamma_{\mathrm{th}} < 5/3$.

In summary, our hybrid EOS is determined by three parameters. Motivated by the above considerations, we select values $\Gamma_1 \in \{1.28,\ 1.3,\ 1.32\}$, $\Gamma_2 \in \{2.5,\ 3\}$ and $\Gamma_{\rm th} \in \{1.35,\ 1.5\}$ with $(\Gamma_1,\ \Gamma_2,\ \Gamma_{\rm th}) = (1.3,\ 2.5,\ 1.35)$ as our fiducial model. We have labeled the different combinations of parameters as pointed out in Table 4.1.

	EOS1	EOS2	EOS3	EOS5	EOS8	EOSa
Γ_1	1.30	1.28	1.32	1.30	1.30	1.28
Γ_2	2.50	2.50	2.50	3.00	2.50	3.00
$\Gamma_{\rm th}$	1.35	1.35	1.35	1.35	1.50	1.50

Table 4.1 Parameters for the different cold hybrid equations of state.

4.3 Static limit of the field equations

The equations governing static, spherically symmetric stars in massive ST theory are obtained by setting the time derivatives to zero in Eqs. (3.27)-(3.43). The line element in the Jordan frame takes on the same form,

$$\mathrm{d}s^2 = g_{\alpha\beta}\mathrm{d}x^\alpha \mathrm{d}x^\beta = -\nu^2\mathrm{d}t^2 + X^2\mathrm{d}r^2 + \frac{r^2}{F}\mathrm{d}\Omega^2\,, \tag{4.10}$$

but now $\nu,\ X, F$ are functions of r only.

In the static case there is no need to handle the formation of discontinuities and we work with the primitive rather than the conserved matter variables. Thus the evolution equations reduce to a set of five independent ordinary differential equations:

$$\begin{aligned}
\partial_r X &= \frac{4\pi r X^3}{F}(\rho h - P) + \frac{r X^3 \eta^2}{2} - \frac{X^3 F}{2r} + \frac{X}{2r} - \frac{\partial_\varphi F X^2 \eta}{2F} + X^3 F W r\,, && (4.11)\\
\partial_r \eta &= -\frac{3\eta}{2r} - \frac{2\pi X \partial_\varphi F}{F^2}(\rho h - 4P) - \frac{X^2 \eta F}{2r} - \frac{4X^2\eta\pi r P}{F} - \frac{X^2\eta^3 r}{2} \\
&\quad + \frac{X\eta^2\partial_\varphi F}{2F} + X^2\eta F W r + X F \partial_\varphi W\,, && (4.12)\\
\partial_r \Phi &= \frac{FX^2 - 1}{2r} + \frac{4\pi r P X^2}{F} + \frac{r X^2 \eta^2}{2} - W r X^2 F\,, && (4.13)\\
\partial_r \varphi &= X\eta\,, && (4.14)\\
\partial_r P &= -\rho h F X^2 \left(\frac{m}{r^2} + 4\pi r \frac{P}{F^2} + \frac{r}{2F}\eta^2 - rW\right) + \rho h \frac{\partial_\varphi F}{2F} X\eta\,. && (4.15)
\end{aligned}$$

These are completed by the equation of state that we choose. The boundary conditions (BCs) are given by

$$\begin{aligned} \eta\,(0) &= 0\,, \\ FX^2\,(0) &= 1\,, \\ \varphi\,(\infty) &= \varphi_0 = 0\,, \\ \Phi\,(\infty) &= 0\,, \\ \rho\,(\infty) &= 0\,. \end{aligned} \tag{4.16}$$

From Eq. (4.13) we see that Φ is unique up to a constant. We use this freedom to set $\Phi = 0$ at infinity so the time coordinate corresponds to the proper time of an observer situated at infinity. To the best of our knowledge translations of BCs at infinity to conditions at the stellar surface analogous to those used in Sec. 3.3 of Ref. [46] are not known. We therefore need to integrate all the way to infinity which is possible by compactifying the space outside the star. Instead of the radial coordinate and the variable η, we shall use for $r > r_S$ (where r_S is the surface radius of star)

$$y = \frac{1}{r}\,, \tag{4.17}$$

$$\hat{\eta} = \frac{1}{X}\partial_y \varphi\,. \tag{4.18}$$

We set $\rho = P = 0$ outside the star where there is no matter, which leads to the equations

$$\partial_y X = -\left(\frac{X^3\hat{\eta}^2 y}{2} - \frac{X^3 F}{2y} + \frac{X}{2y} + \frac{X^2\hat{\eta}\partial_\varphi F}{2F} + \frac{X^3 F W}{y^3}\right)\,, \tag{4.19}$$

$$\partial_y \Phi = -\left(\frac{FX^2 - 1}{2y} + \frac{X^2\hat{\eta}^2 y}{2} - \frac{WX^2F}{y^3}\right)\,, \tag{4.20}$$

$$\partial_y \hat{\eta} = -\frac{\hat{\eta}}{2y} + \frac{X^2\hat{\eta}F}{2y} + \frac{X^2\hat{\eta}^3 y}{2} + \frac{X\hat{\eta}^2\partial_\varphi F}{2F} - \frac{X^2\hat{\eta}FW}{y^3} + \frac{XF\partial_\varphi W}{y^4}\,, \tag{4.21}$$

$$\partial_y \varphi = X\hat{\eta}\,, \tag{4.22}$$

$$\partial_y P = 0\,. \tag{4.23}$$

Because of numerical difficulties at $y = 0$, we find it more convenient to use on the grid outside the star the mass function m (see Eq. (3.21)) instead of X, as $m \approx$

constant in the exterior. Thus, we rewrite Eq. (4.11)

$$\partial_r m = 4\pi r^2 \frac{\rho h - P}{F^2} + \frac{r^2 \eta^2}{2F} + r^2 W. \tag{4.24}$$

This form of the equations does not take into account the exponential Yukawa fall-off of the scalar field and the frequent divisions by y lead to divergences in the numerical solution near infinity where $y = 0$. In order to overcome this difficulty, we factor out the exponential behaviour from our φ variable. Asymptotic analysis shows that close to infinity the scalar field behaves as

$$\lim_{r\to\infty} \varphi \sim A_1 e^{-\mu r} + A_2 e^{\mu r} \,. \tag{4.25}$$

We want to suppress the exponentially growing mode and therefore require $A_2 = 0$. Numerically we enforce this by fixing $\varphi = 0$ at $y = 1/r = 0$. We incorporate the asymptotic behaviour of Eq. (4.25) by introducing rescaled variables

$$\sigma = \varphi e^{\mu/y} \quad \Longrightarrow \quad \varphi = \frac{\sigma}{e^{\mu/y}} \,, \tag{4.26}$$

$$\kappa = y^2 e^{\mu/y} \hat{\eta} \quad \Longrightarrow \quad \hat{\eta} = \frac{\kappa}{y^2 e^{\mu/y}} \,. \tag{4.27}$$

Substituting the new variables into Eqs. (4.19)-(4.23) leads to:

$$\begin{aligned}
\partial_y m &= -\frac{1}{2y^4 e^{2\mu/y}} \left(\frac{\kappa^2}{F} - \mu^2 \sigma^2 \right) \,, && (4.28)\\
\partial_y \Phi &= -\frac{m}{1-2my} - \frac{1}{2\,(1-2my)\, y^3 e^{2\mu/y}} \left(\frac{\kappa^2}{F} - \mu^2 \sigma^2 \right) \,, && (4.29)\\
\partial_y \sigma &= \frac{X\kappa - \mu\sigma}{y^2} \,, && (4.30)\\
\partial_y \kappa &= -\kappa \partial_y \Phi + \frac{F X \mu^2 \sigma + \kappa\,(2y - \mu)}{y^2} + \frac{X\kappa^2}{2y^2} \frac{F_{,\varphi}}{F} \,, && (4.31)\\
\partial_y P &= 0 \,. && (4.32)
\end{aligned}$$

For a star of radius r_S, we solve Eqs. (4.11)-(4.15) on an interior grid $r \in [0, r_\mathrm{S}]$ and Eqs. (4.28)-(4.32), on an exterior grid $y \in [0, 1/r_\mathrm{S}]$ subject to the boundary conditions

(4.16) and matching conditions

$$\begin{aligned}
\Phi(y = 1/r_{\rm S}) &= \Phi(r = r_{\rm S})\,,\\
m(y = 1/r_{\rm S}) &= m(r = r_{\rm S})\,,\\
P(y = 1/r_{\rm S}) &= P(r = r_S)\,,\\
\hat{\varphi}(y = 1/r_{\rm S}) &= \varphi(r_{\rm S})e^{\mu r_{\rm S}}\,,\\
\kappa(y = 1/r_{\rm S}) &= -\eta(r = r_{\rm S})e^{\mu r}\,,
\end{aligned} \qquad (4.33)$$

using a relaxation algorithm [86]. With a regular initial guess, this approach avoids any contamination from the exponentially growing modes. It also enables us to control the outer boundary explicitly.

Note that the stellar radius $r_{\rm S}$ is a free parameter in this approach and its value selects the specific stellar model that is computed. In shooting algorithms this role is usually played by the central density of the star which, in our case, is a product of the solution process instead.

4.4 Numerical implementation

4.4.1 Relaxation scheme

In order to numerically solve the system of equations presented in the previous section we have used a Newton-Raphson based relaxation code. Integrating the system of equations (with, for example, a fourth order Runge-Kutta scheme) from the centre of the star all the way to infinity through the compactified grid will pick up the exponentially growing modes and cause the code to crash. The relaxation algorithm starts from an initial guess and, keeping the BCS satisfied exactly, it iterates until it reaches an exact solution. This way it avoids the exponentially growing mode as it will not fit the boundary condition for φ at infinity.

4.4.2 Convergence test

In order to test the relaxation code we have calculated a strongly-scalarized static model with three interior resolutions $N_1 = 5000$ points, $N_2 = 10\ 000$ and $N_3 = 20\ 000$ points, respectively, for the low, medium and high resolution simulation; we matched the resolutions used in the exterior grid. A grid variable f converges at $n^{\rm th}$ order if

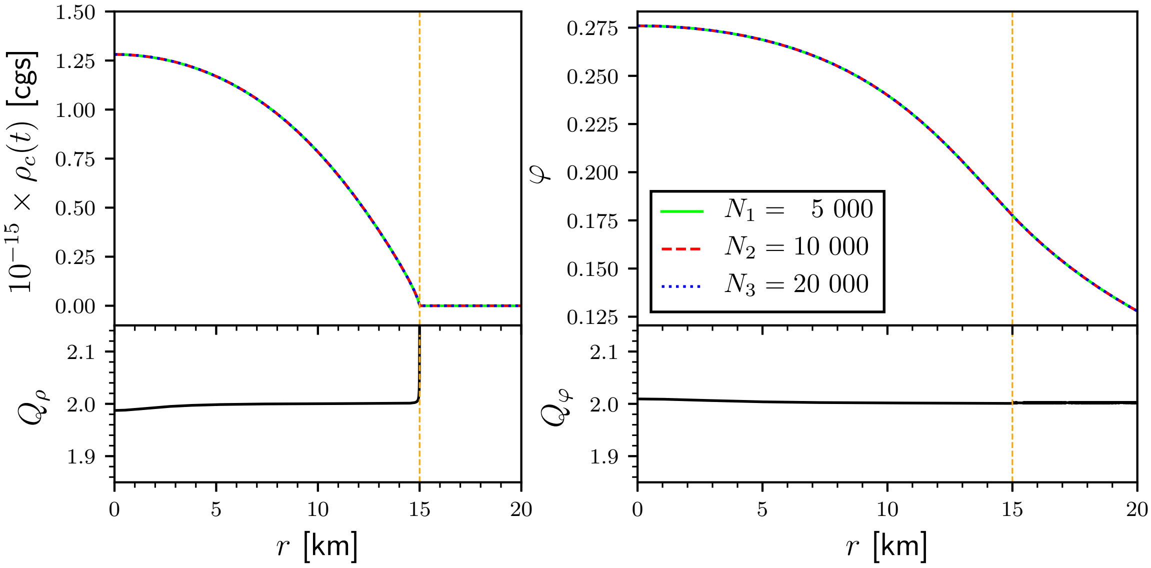

Fig. 4.1 Convergence of the baryon density field (left) and scalar field (right) for a scalarized solution of radius 15.0 km, using Novak's EOS1 and scalar field parameters $\mu = 4.8 \times 10^{-13}$ eV, $\alpha_0 = 10^{-4}$ and $\beta_0 = -15.0$. The vertical orange line represents the surface of the star.

the differences between low, medium and high resolutions scale according to

$$\frac{f_{N_1} - f_{N_2}}{f_{N_2} - f_{N_3}} = Q_n := \frac{(N_2/N_1)^n - 1}{1 - (N_2/N_3)^n} \,. \tag{4.34}$$

The scalar parameters used in the convergence test are $\mu = 4.8 \times 10^{-13}$ eV, $\alpha_0 = 10^{-4}$ and $\beta_0 = -15.0$. As we can see in Fig. 4.1 we observe first order convergence for the baryon mass and scalar field: the differences between high, medium and low resolution scale with $Q = 2$. This is below the expected second-order convergence; we believe this is due to the baryon density tending "slowly" to 0 at the star surface. A computer sometimes cannot distinguish well between a very small number and zero, so it might stop the iterations prematurely, when it reaches a threshold, creating an error of first order at the surface which transmits itself to the entire grid. We overcome this by using large grids.

As a further test we have verified that our models are in good agreement with the $M_b - R$ relations results obtained by *Gerosa et al* [46] and *Ramazanoğlu et al* [53].

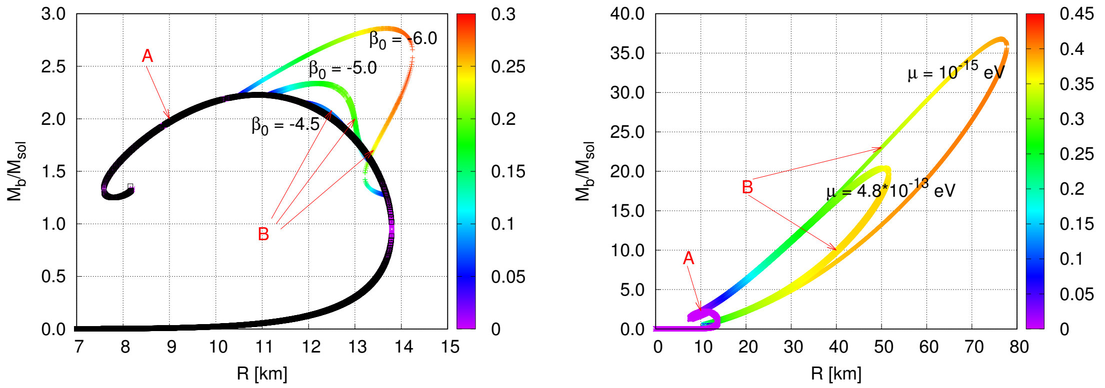

Fig. 4.2 $M_b - R$ plots for several β_0 values (left panel) and several μ values (right panel). The other scalar field parameters are $\mu = 4.8 \times 10^{-13}$ eV, $\alpha_0 = 10^{-4}$ (left) and $\beta_0 = -15$, $\alpha_0 = 10^{-4}$ (right). The color scale measures the central value of $|\varphi|$. The black points in the left panel represent GR solutions, i.e. we use $\alpha_0 = \beta_0 = 0$.

4.5 Results and discussion

For our exploration of static NS models in massive ST theory, we have computed spherically symmetric static solutions using the simple polytropic EOS with the parameters defined in Eq. (4.3).

In the following we shall often use as a diagnostic the baryon mass which is obtained from the baryon number density n_b and the mass per baryon m_b by

$$M_b = m_b \int d^3x \sqrt{-g} n_b u^t = 4\pi \int_0^{r_S} dr \left(r^2 \frac{\rho}{F^{3/2}\sqrt{1 - 2m/r}} \right) , \tag{4.35}$$

where we have used $\rho = m_b n_b$ and r_S is the radius of the star. We present the different branches of solutions in ST theory using mass versus radii ($M_b - R$) plots with the baryon mass M_b on the vertical axis and the Einstein frame radius R on the horizontal axis.

We define weakly scalarized solutions as NSs with scalar field magnitude $\varphi \sim O(\alpha_0)$, and strongly scalarized solutions NSs with magnitudes $\varphi \sim O(0.1)$.

In GR we find that this equation of state produces one branch of solutions parametrized by ρ_c with radii between 0 and 14 km and baryon masses between 0 and 2.25 $M_\odot$ (see black line in the left panel of Fig. 4.2). We encounter solutions of this branch in many of our ST cases, though the models are not identical to the GR solutions if $\alpha_0 \neq 0$; the departures from GR increase with α_0.

The introduction of a scalar field leads to extra branches of static spherically symmetric neutron star solutions which contain a non-trivial scalar field profile. The

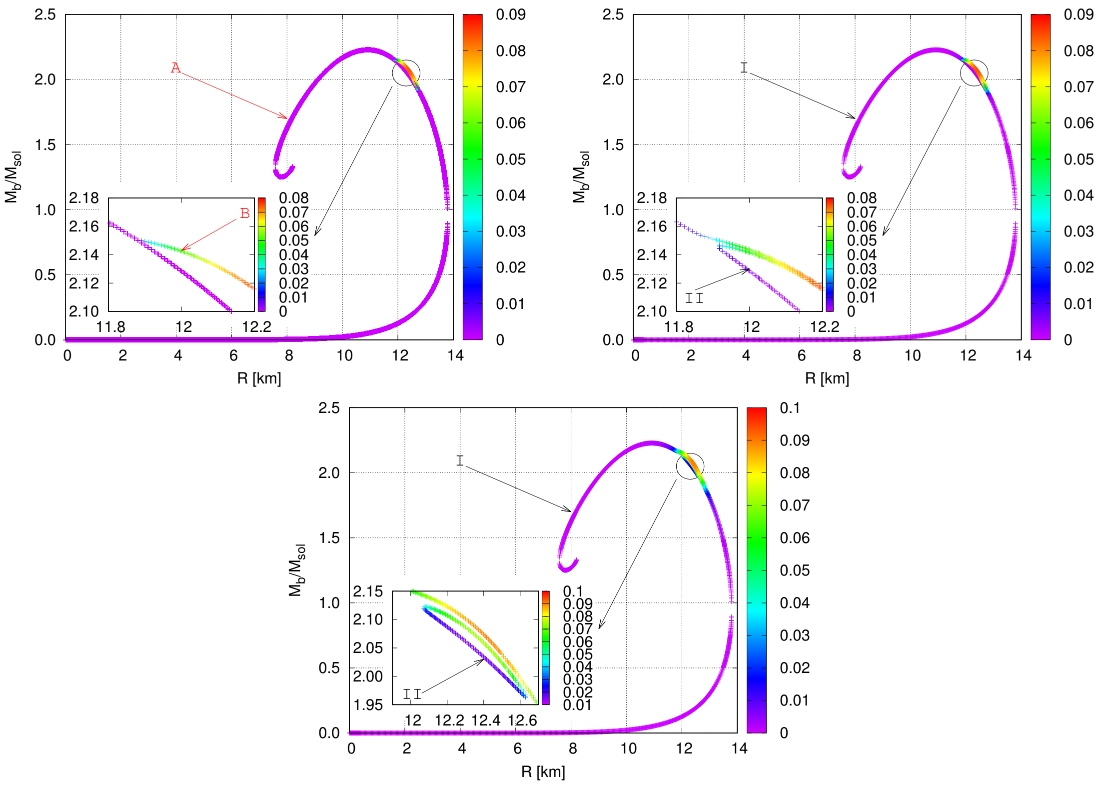

Fig. 4.3 $M_b - R$ plots for several α_0 values. The scalar field parameters are $\mu = 4.8 \times 10^{-13}$ eV, $\beta_0 = -4.5$ and $\alpha_0 = 0$ (top left), $\alpha_0 = 10^{-4}$ (top right) and $\alpha_0 = 10^{-3}$ (bottom). The color scale measures the central value of $|\varphi|$.

weakly scalarized solutions for radii smaller than 14 km nearly coincide with the GR branch of solutions and have a scalar field of the same magnitude $O(\alpha_0)$. The shape of the extra branches depends on the magnitude of the parameters α_0, β_0 and μ. To obtain the extra branch of scalarized solutions (i.e. see spontaneous scalarization) we confirm through our computations that β_0 needs to exceed a threshold value. This threshold depends on the equation of state used as well as on the other scalar parameters. As opposed to the GR case, these solutions are parametrized by two parameters, φ_c and ρ_c.

4.5.1 Dependence on μ

As indicated in Sec. 3.3.2, the scalar field mass weakens scalarization. When increasing the scalar mass and keeping the rest of the parameters the same, we obtain NS solutions of smaller masses and/or smaller radii. For example, for $\mu = 10^{-15}$ eV, we obtained NS stars with baryon mass larger than 35 $M_\odot$ and radii larger than 70 km, whereas

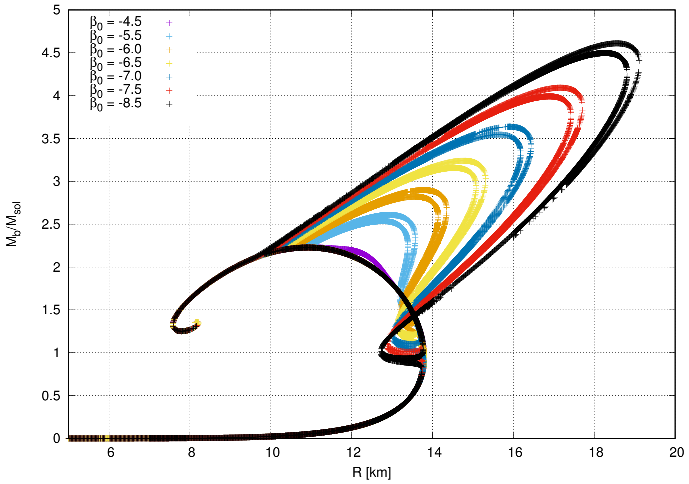

Fig. 4.4 $M_b - R$ plots when varying β_0 in the presence of a large α_0 parameter. The other scalar field parameters are $\mu = -4.8 \times 10^{-13}$ eV, $\alpha_0 = 10^{-2}$.

for a scalar mass $\mu = 4.8 \times 10^{-13}$ eV, we have no model with $M_b > 22\ M_\odot$ or $R > 55$ km (see right panel of Fig. 4.2). If we compare models of the same baryon mass and the largest possible radii from each case (these, as shall be argued in Sec. 4.5.4, are the stable solutions), for a larger scalar mass the radius of the star is smaller (i.e the star is more compact); we also note from the colorbar to the right of the plot that the central scalar field is smaller, supporting the hypothesis that the scalar field mass weakens scalarization.

In [53] the authors calculated NS static solutions with fixed ADM mass and varied scalar mass. As can be seen in their Fig. 2, a larger μ diminishes the scalar field to the point of killing it for values around $\sim 10^{-12}$ eV. In Fig. 3 they confirm that a smaller scalar mass allows for larger values of the ADM mass.

4.5.2 Dependence on α_0

When $\alpha_0 = 0$, Eqs. (4.11)-(4.15) are invariant under the transformation[1] $\varphi \to -\varphi$. As a consequence, there exist two strongly scalarized solutions which lie on the scalarized branch and they only differ by a minus sign in their scalar field profile. In addition to the strongly scalarized models, there is a third branch containing models with vanishing φ, i.e. models equal to the GR case.

If $\alpha_0 \neq 0$, the matter variables of the 2 strongly scalarized models differ from each other, in terms of macroscopic features such as their masses and radii. As a

---

[1] Recall that $\varphi \to -\varphi$ implies $\eta \to -\eta$ and $\psi \to -\psi$ which contain the terms $F_{,\varphi}$ and $W_{,\varphi}$ that are linear in φ when $\alpha_0 = 0$.

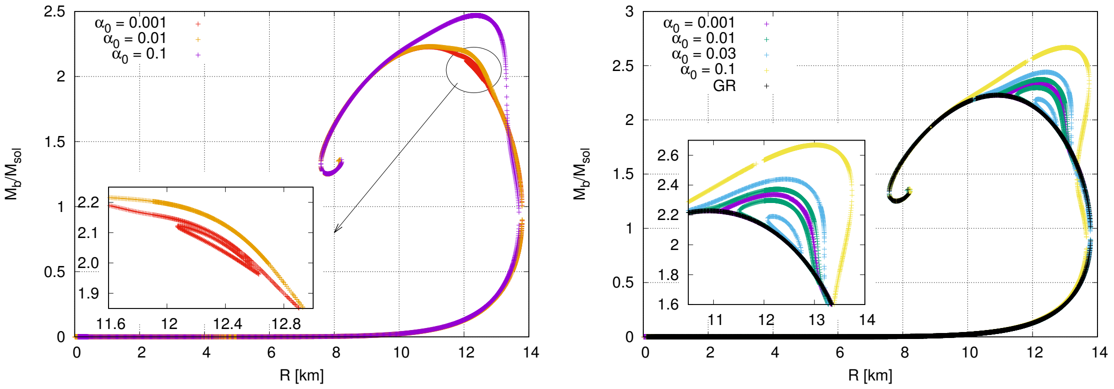

Fig. 4.5 $M_b - R$ plots for various α_0 values. The other scalar field parameters are $\mu = 4.8 \times 10^{-13}$ eV, $\beta_0 = -4.5$ (left) and $\beta_0 = -5.0$ (right).

consequence we see a split in the $M_b - R$ profile, even for small but finite values such as $\alpha_0 = 10^{-4}$, cf. the top left panel (for $\alpha_0 = 0$) and the top right panel ($\alpha_0 \neq 0$) of Fig. 4.3. The closed loop seems to follow the GR branch on one side and the scalarized arc on the other (cf. top right panel of Fig. 4.3), but close inspection shows the gap that exists at $R \sim 11.9$ km. We find this gap to be proportional to α_0, and independent of β_0. Thus, for small and non-zero values of α_0, we have 2 families of solutions: one that approximately follows the $M_b - R$ plot of GR for small and large central baryon density (which we refer to as branch I) and one separate family, contained on a closed loop (which we refer to as branch II). Note that in some plots we label the branches with A and B which is a classification based on different criteria which becomes clear in the next section.

Above a threshold value of α_0 we have not managed to obtain any solutions separate from branch I, suggesting that only one family of strongly scalarized solutions exists. At this point the $M_b - R$ plot shows just branch I, but with a clear deviation from the corresponding GR cases for intermediate ρ_c values. This is illustrated in Fig. 4.5, where $\alpha_0 = 10^{-1}$, $\beta_0 = -4.5$ (left panel, purple line) and $\beta_0 = -5$ (right panel, yellow line); here, the $M_b - R$ plots display only one branch of solutions, many of which are significantly heavier than their GR counterparts.

For small and nonzero α_0, we notice one feature about these two families of solutions: on the closed loop II we have $\varphi_c > 0$, whereas on branch I φ_c is mostly negative. In Figs. 4.6-4.7 we highlight the models with $\varphi_c < 0$ with orange and the ones with $\varphi_c > 0$ with black. We note that along branch I, the central baryon density strictly increases as we traverse it starting with $(M, R) = (0, 0)$. The central scalar field reaches positive, albeit small, values for large ρ_c.

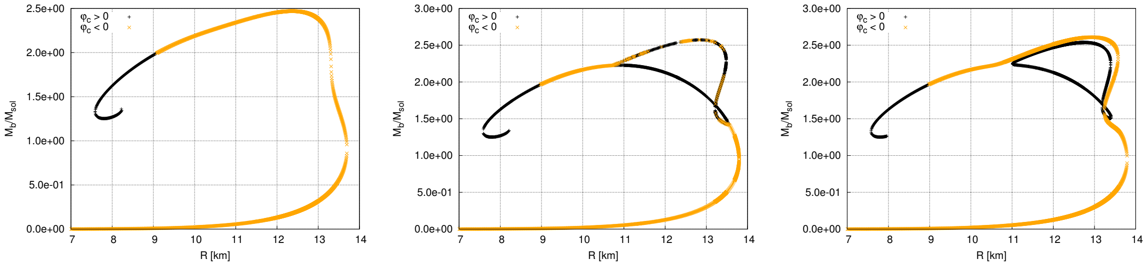

Fig. 4.6 Distribution of scalarized models based on the sign of φ_c in the M-R profiles for various α_0 values. The scalar parameters are $\mu = 4.8 \times 10^{-13}$ eV and $\alpha_0 = 10^{-1}$, $\beta_0 = -4.5$ (left panel), $\alpha_0 = 10^{-4}$, $\beta_0 = -5.5$ (middle panel), $\alpha_0 = 10^{-2}$, $\beta_0 = -5.5$. (right panel). The orange points represent models with $\varphi_c < 0$ whereas the black ones have $\varphi_c > 0$.

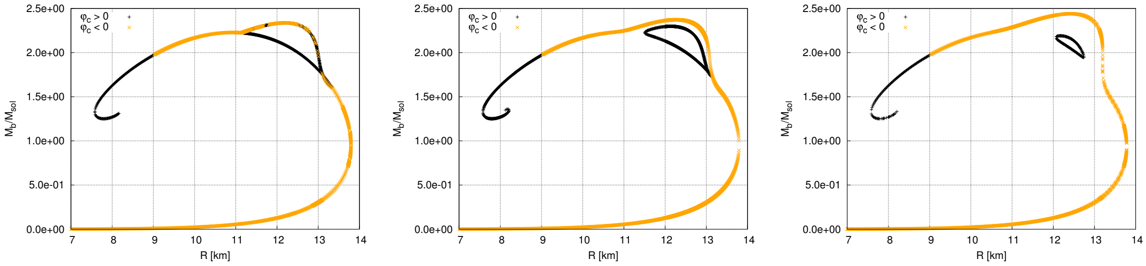

Fig. 4.7 Distribution of scalarized models based on the sign of φ_c in the $M_b - R$ plots for various α_0 values. The scalar parameters are $\mu = 4.8 \times 10^{-13}$ eV, $\beta_0 = -5$ and $\alpha_0 = 10^{-4}$ (first panel), $\alpha_0 = 10^{-2}$ (middle panel), $\alpha_0 = 3 \times 10^{-2}$ (right panel). The orange points represent models with $\varphi_c < 0$ whereas the black ones have $\varphi_c > 0$.

4.5.3 Dependence on β_0

In order to study the influence of β_0 we have chosen cases with $\alpha_0 = 10^{-4}$; the curves would barely differ for $\alpha_0 = 0$, but we require $\alpha_0 \neq 0$ to start nontrivial scalar dynamics. We refer to the portion of the $M_b - R$ plots that follow the GR case as branch A and the extra solutions as branch B. The NS models on branch A are weakly scalarized, whereas the solutions on branch B are strongly scalarized. As mentioned before, this is just a different classification, independent of I and II from the previous section, that will help us in studying β_0's influence on the models.

A more negative β_0 allows for larger values of the radius and baryon mass. As we can see in the left panel of Fig. 4.2 for the choice of $\mu = 4.8 \times 10^{-13}$ eV and $\alpha = 10^{-4}$ the extra branch for $\beta_0 \sim -4.5$ forms an "arc" splitting off the GR-like solutions between $12 - 13$ km. We have marked this section of the plot as branch B. The scalar field amplitude peaks at $\varphi_c \approx\sim -0.08$ for some of the stars on this branch. For $\beta_0 = -5$, arc B grows in size, with larger baryon masses being attained than possible in the GR

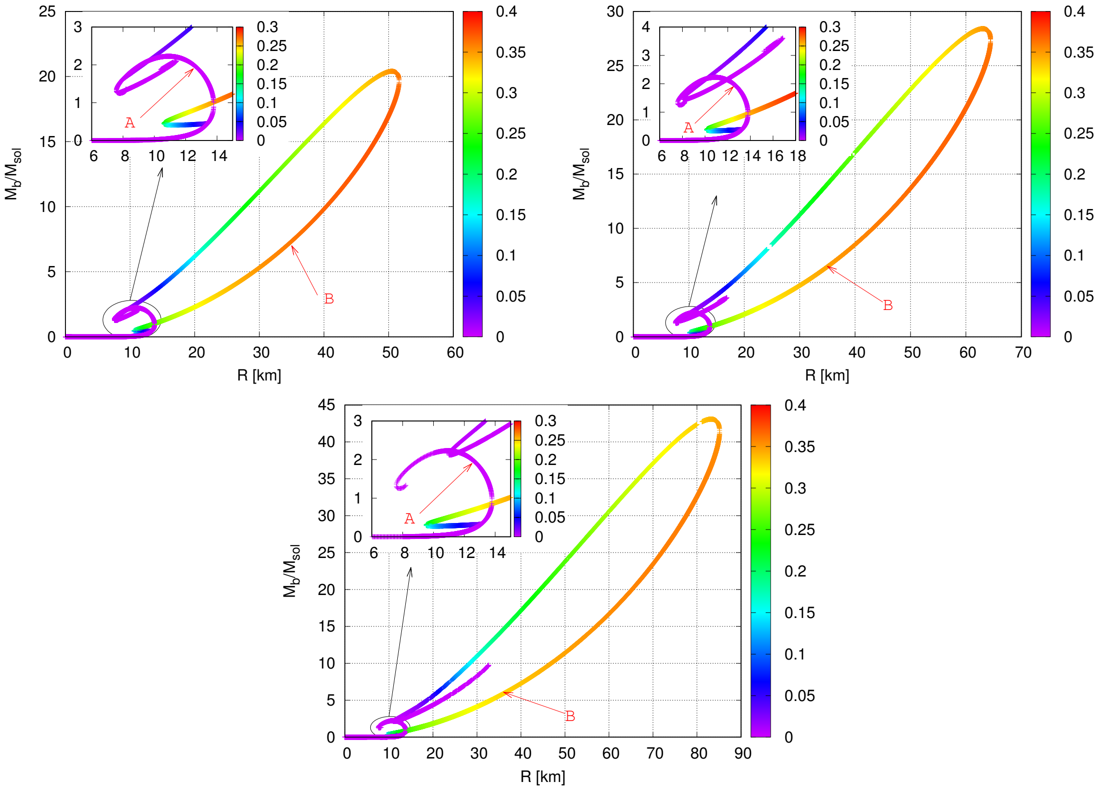

Fig. 4.8 $M_b - R$ plots for varying β_0 values. The other scalar field parameters are $\mu = 4.8 \times 10^{-13}$ eV, $\alpha_0 = 10^{-4}$ and $\beta_0 = -15$ (top left panel), $\beta_0 = -17$ (top right panel) and $\beta_0 = -20$ (bottom panel). The color scale measures the central value of $|\varphi|$.

cases and scalar fields with amplitudes of ~ 0.2. The branch now also extends below the GR-like solutions. For $\beta_0 = -6$ this additional feature becomes more pronounced and the entire scalarized branch B resembles an inverted "S". We have obtained models with baryon masses as large as $2.5 - 3.0\ M_{\odot}$, radii significantly larger than those encountered in GR, and scalar central field amplitudes of ~ 0.28.

In the left panel of Fig. 4.9 we plot the baryon mass and scalar field profiles of a few models from the scalarized branch B when $\beta_0 = -6$. Each different color represents a different model as marked on the $M_b - R$ plot in the bottom row. For the purpose of comparison we have selected the strongly scalarized models with positive φ_c. The other strongly scalarized solutions would have nearly the same matter fields and negative, but nearly equal in modulus scalar field. We see that along the scalarized branch B, the central baryon density increases monotonically as one traverses the branch from the "red" model (lowest mass) to the purple one; the scalar field also increases in amplitude as more massive models are encountered, reaching a peak on the branch section between the yellow and green cases, after which it decreases. Along the the

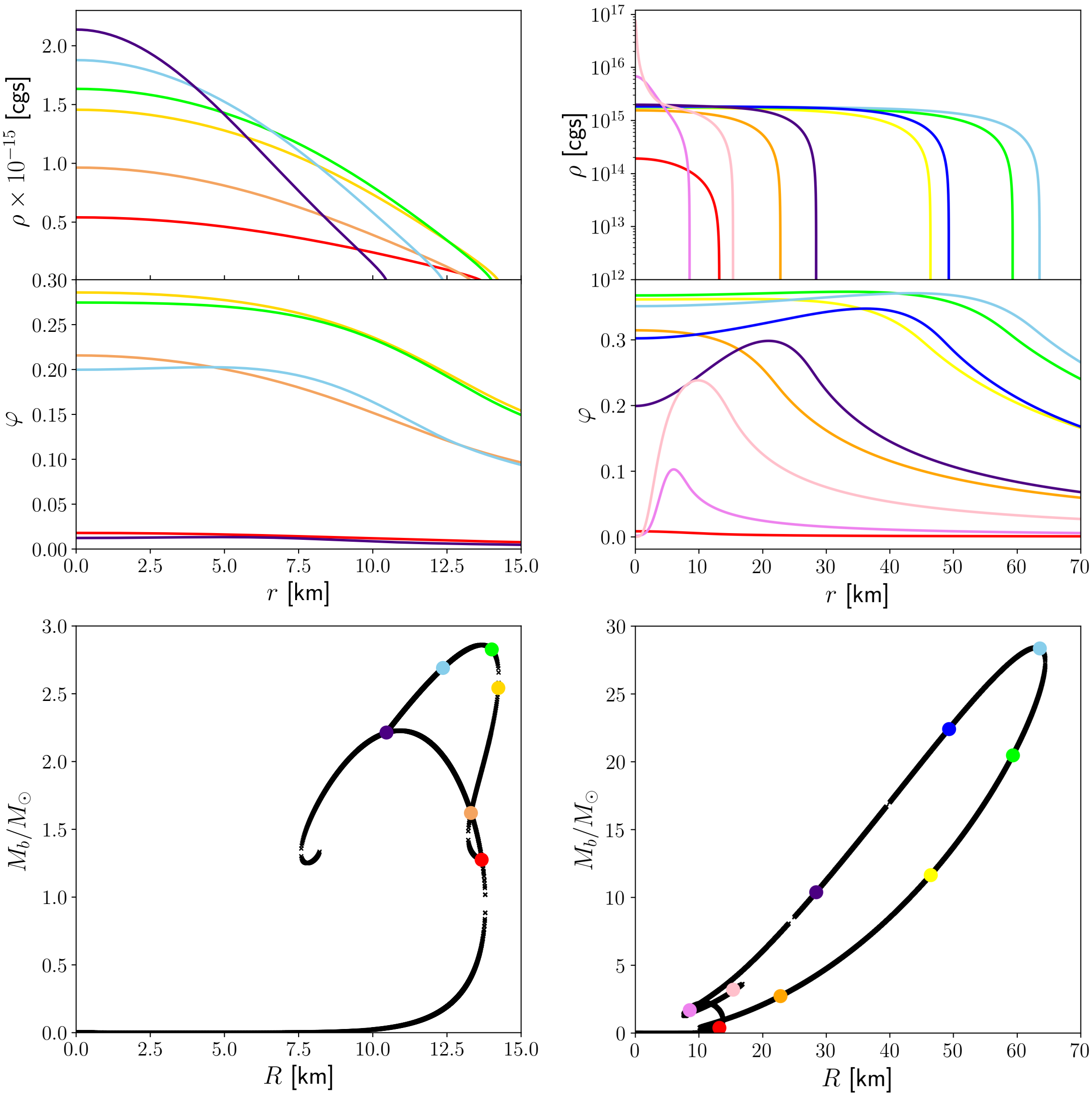

Fig. 4.9 *Top row:* Baryon density field profiles (top panels) and scalar field profiles (bottom panels) for several strongly scalarized models. The scalar field parameters are $\mu = 4.8 \times 10^{-13}$ eV, $\alpha_0 = 10^{-4}$ with $\beta_0 = -6$ (left) and $\beta_0 = -17$ (right). *Bottom row:* Representation of the NS models from the top row in the $M_b - R$ plane.

GR-like branch the central baryon density is strictly increasing starting from the point $(M_b, R) = (0, 0)$, similar to the GR case.

For very negative values of β_0 the strongly scalarized branch B "detaches" at one end from the GR-like one: as we can see in the three insets of Fig. 4.8, we start seeing a second branch plotted over where we expect the GR one and "curling" in a similar way for $\beta_0 = -15$. It becomes clearer that it is a second branch when we decrease β_0 even further and for β_0 between -20 and -25 the two branches A and B do not intersect a second time. In addition, the set of solutions found now reaches mass values of order 10 $M_\odot$ and radii larger than 50 km. The central scalar field amplitude saturates around $\sim 0.3 - 0.4$. The detached end of the scalarized branch B appears to be unscalarized, but the maximum scalar field amplitude for those models is not reached anymore at the centre. In the right panel of Fig. 4.9 we plot the baryon mass and scalar profiles of a few models from the scalarized branch B when $\beta_0 = -17$. We again chose as a strongly scalarized solution the one with positive φ_c. The same behaviour is found for solutions with negative φ_c. The central baryon density again increases monotonically along the branch, reaching values of $O(10^{17})$ [cgs]. As we move along this branch the scalar field exhibits an interesting behaviour: the maximum value of $|\varphi|$ starts moving away from the centre. We have already seen that the light blue model attains the maximum scalar field value at $r \sim 50$ km, rather close to its surface. It is for this reason that we distinguish between φ_c and the maximum value of the scalar field. As we reach the high density section of the branch (e.g. the pink model), most of the baryon mass is concentrated at the center and a "shell" of scalar field forms around it.

4.5.4 Stability of models

The stability of these neutron star models can be analysed by comparing the binding energy of models with the same baryon mass. Following that approach we interpret that the model with the lowest ADM mass, i.e. strongest binding energy, is stable. In Fig. (4.10) we show some examples for various β_0 values split into stable and unstable models: the green portions represent the stable models whereas unstable models are displayed in black color. This figure confirms theoretical predictions according to which the GR-like branch becomes unstable and the scalarized models become stable when spontaneous scalarization occurs [42]. In the figure we can see that the unscalarized branch is unstable when there is a choice between a scalarized and non-scalarized model (e.g. above ≈ 0.7 $M_\odot$ in the bottom right panel of Fig. 4.10). If there exist multiple scalarized models, the ones with larger radius are stable (as is typically also the case in GR). In Fig. 4.11 we display some models with different α_0 parameters that

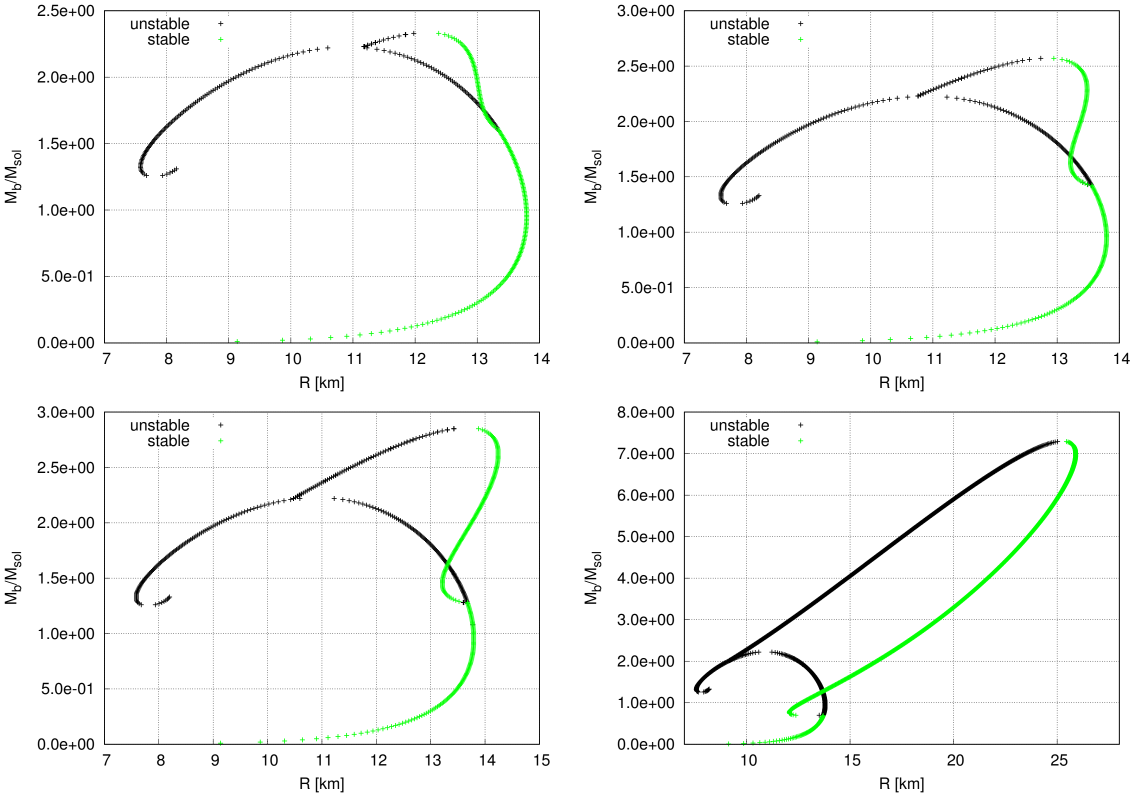

Fig. 4.10 Distribution of stable and unstable models in the M-R plane. The scalar parameters are $\mu = 4.8 \times 10^{-13}$ eV, $\alpha_0 = -10^{-4}$ and: $\beta_0 = -5$ (top left), $\beta_0 = -5.5$ (top right), $\beta_0 = -6$ (bottom left), $\beta_0 = -10$ (bottom right). The green points represent stable models whereas the black ones are unstable.

suggest that the models with negative central scalar field are the stable ones (compare with Figs. 4.6-4.7). Overall the solutions with a stronger scalar field are the stable ones. This is a uniform feature of all the models we have analysed.

4.6 Conclusions

In this chapter we have numerically computed solutions of spherically symmetric NSs in massive ST theories, discovering a richer phenomenology than initially predicted. For a certain section of the ST parameter space we obtain branches of static solutions that do not appear in GR. Larger values of α_0 and $-\beta_0$ lead to larger qualitative and quantitative differences from GR, whereas larger values of the scalar mass μ reduce these deviations.

For $\alpha_0 = 0$ we obtain a branch of solutions, named A in this chapter, identical to the GR ones (i.e. $\varphi = 0$ everywhere) and a second branch B of scalarized stars

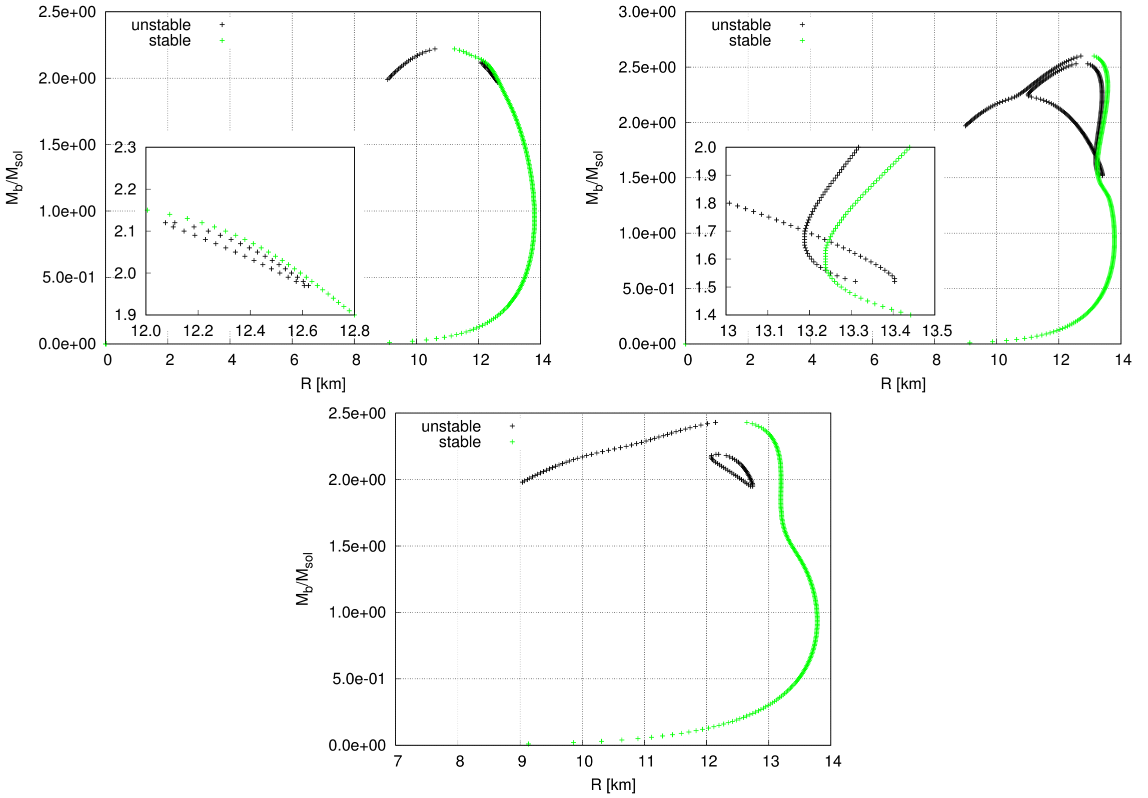

Fig. 4.11 Same as Fig. 4.10 using scalar parameters $\mu = 4.8 \times 10^{-13}$ eV, $\beta_0 = -5$ and: $\alpha_0 = 10^{-3}$, $\beta_0 = -4.5$ (top left), $\alpha_0 = 10^{-2}$, $\beta_0 = -5.5$ (top right), $\alpha_0 = 3 \times 10^{-2}$, $\beta_0 = -5$ (bottom).

containing two families of solutions differing only in the sign of the scalar field (in this case the system of equations is invariant under the transformation $\varphi \to -\varphi$). For more negative β_0, branch B reaches higher baryon masses and larger star radii. For $\alpha_0 \neq 0$, the two families of scalarized solutions start differing qualitatively and quantitatively, and we see the differences in the values of the macroscopic features of the stars. A nonzero α_0 leads to solutions with scalar fields of at least $O(\alpha_0)$. At this point we changed to a new classification system where we differentiate between the family of solutions with negative φ_c (branch I) and the ones with positive φ_c (branch II). For larger values of α_0, the latter dissapears. The behaviour with respect to the scalar parameters seems to be universal as we have encountered the same $M_b - R$ profile deviations with respect to GR for all other equations of state that we have studied. When the scalarized branches exist, the stable solution becomes the scalarized NS with the larger radius. For a nontrivial (and positive) α_0, the stable solutions have φ_c and most of the radial profile of the scalar field negative.

As pointed out in Sec. 4.5.3, for very negative β_0 values we obtained solutions where the maximum amplitude of the scalar field is attained away from the center of the star. In extreme cases, such as the pink model on the right of Fig 4.9, we obtain highly compact baryon cores surrounded by a scalar field "shell". This is reminiscent of the profiles obtained in Section V of [87] where the authors calculate stars in massles ST theory with a complex scalar field. Due to using only the massless theory, the authors were constrained in the parameter space they could use and studied large positive β_0 values instead. They obtain stationary solutions of stars with a scalar core, seen in Fig. 15 where they plot the amplitude of the scalar field and the fluid density. We note that in their case the maximum value of the baryon density is no longer located at the center of the star but at a finite radius and their solution is a scalar core surrounded by a "shell" of matter. The similarity of this behaviour (despite the variables in question switched from our case) and the fact that this was obtained for β_0 values from the unconstrained positive range, suggests the need for a study into the potential connection between these two cases and whether where is an underlying cause to this behaviour.

Chapter 5

Core-collapse in massive Scalar Tensor Theory

Another avenue of studying massive ST theory is by looking at its effects in the dynamical regime through the GWs that result from high energy events. ST theory allows for scalar radiation in the form of monopole waves which is missing in GR and would be smoking gun evidence of a deviation from GR. One setup that allows this is through the study of stellar core collapse. In this chapter we systematically explore the parameter space that characterizes the progenitor stars, the equation of state and the ST theory of the core collapse events. We identify a remarkably simple and straightforward classification scheme of the resulting collapse events.

This chapter and Appendix B is based on material published in [26] in collaboration with Ulrich Sperhake, Christopher J. Moore, Michalis Agathos, Davide Gerosa and Christian D. Ott, as well as a paper in preparation. The code was extended to massive ST theory by the author and U. Sperhake. The latter performed the simulations using progenitors of 12 solar mass with solar metallicity while the author covered the rest of the progenitor space together with the analysis on the influence of the different parameters. The theoretical analysis for the approximate scalar mass universality was performed by U. Sperhake and independently calculated by the author. The study of potential LIGO detections was performed by the author with C. Moore and M. Agathos.

5.1 Introduction

Gravitational collapse leading to the formation of NSs and BHs is the expected evolutionary end point of massive stars with zero age main sequence (ZAMS)[1] mass between $8 - 100\ M_{\odot}$. This is usually accompanied by a supernova (SN), one of the most powerful astrophysical phenomena, which releases an energy of $\sim 10^{53}$ erg [74]. Up to the point of collapse, the star fought gravity through radiative pressure due to the energy released in the nuclear fusion of its constituent particles, forming heavier elements. Before the collapse, the star's core is composed of mostly elements of the iron family which have the highest binding energy per nucleon and cannot further fuse. The star starts collapsing under the strength of gravity as it cannot produce any pressure to oppose it. When the core reaches nuclear density ρ_{nuc}, the equation of state stiffens, and the repulsive nature of nuclear degeneracy pressure leads the core to bounce. This bounce moves outwards against further infalling material as a hydrodynamic shock with an energy of a few $\sim 10^{51}$ ergs [80]. Inside/Behind this shock a proto-neutron star (PNS) is formed with a mass of $\sim 0.5\ M_{\odot}$. The shock soon stalls, due to nuclear dissociation and neutrino emission in the post-shock region. The shock in some cases is revived and continues towards the star surface, producing the SN explosion. The revival mechanism is still under debate; numerical simulations suggest the necessity of multidimensional scenarios as well as neutrino contribution in order to produce a SN [89, 90]. Supernova explosions leave behind compact remnants, such as NSs or BHs. An excellent synopsis of the recent research into core collapse SNe in GR, including numerical breakthroughs and future prospects, can be found in Chapter 1 of [74].

There have been few studies of the scalar radiation resulting from core collapse in ST theories. Matsuda and Niarai numerically simulated the gravitational collapse of a gaseous sphere in Brans-Dicke theory [91]. Scheel et al [39, 92], Shibata et al [93] and Harada et al [40] simulated Oppenheimer-Snyder collapse in Brans-Dicke theory. In addition Dimmelmeier explored the collapse of a fluid with a Γ law equation of state also in Brans-Dicke theory. Novak studied the NS transition to a scalarized state [42] and the collapse of NSs to BHs [41] in massless ST theory. Core collapse and GW emission in massless ST theory was first researched by Novak and Ibáñez [43] using pseudo-spectral methods and high-resolution shock-capturing schemes. Gerosa et al [46] simulated core collapse in massless ST theory for a variety of equations of state, using polytropic and realistic progenitors as initial data.

---

[1] Zero age main sequence is the moment a star starts burning hydrogen through nuclear fusion.

In this chapter we present the results of our spherically symmetric core collapse simulations in massive ST theory in which we explore a large parameter space. In our study we are interested in the breathing mode which is triggered by the compactification of the star; this mode together with dipole radiation are missing in GR because of conservation of mass and momentum. Because we simulate spherically symmetric scenarios, the breathing or radiative scalar mode is the only mode present. The star scalarizes when the core reaches nuclear density, just before the bounce. This abrupt change in the scalar field travels as a scalar wave towards the stellar surface, while the shock stalls behind it. As a consequence, we shall ignore in our simulations neutrino contributions.

5.2 Numerical implementation

5.2.1 Code

The computational framework for our core collapse simulations is based on the open source code GR1D [66] for modelling spherically symmetric fluids in GR with high-resolution shock capturing schemes. The discretization, grid and boundary treatment are identical to those described in detail in Sec. 3.2 of Ref. [46] where GR1D has been extended to ST gravity with a massless scalar field. We have further modified the code by adding the terms involving the potential as highlighted in Sec. 3.2.

In order to accurately capture the dynamics within and around the star, we use a uniform inner grid up to $r = 40$ km and a logarithmic outer one beyond this distance; the latter allows us to extract the scalar signal far away from the star to propagate it further while running the simulations for a reasonable amount of time. Our computational domain extends to 9×10^5 km so that the extraction radius (which, as argued in Sec. 5.2.5, we typically set at $r_{\text{ex}} = 3 \times 10^4$ km) is sufficiently far away from the boundary such that the signal is not affected by imperfections due to the Sommerfeld outer boundary condition (see Sec. 2.2 of [46]).

We characterize the resolutions used in the simulations by Δr (the spacing of the inner grid) and N (the total number of radial zones, from both the uniform and logarithmic grid). The number of zones corresponding to the several inner grid spacings we have used are listed in Table 5.1. We add 4 ghost cells at either end of the grid for the implementation of symmetry and boundary conditions. Unless stated otherwise, the simulations presented in this thesis employ a uniform inner grid with $\Delta r = 250$ m inside $r = 40$ km and a logarithmically increasing grid spacing up to the outer boundary at 9×10^5 km, comprising in total $N = 10\ 000$ radial zones (excluding the ghost cells).

Δr [m]	250.00	166.66	125.00	100.00	83.33	62.50	50.00	41.66
N_i	160	240	320	400	480	640	800	960

Table 5.1 Number of zones N_i of the inner grid for the corresponding zone width Δr.

5.2.2 Initial data

All simulations start with non-rotational models of the catalog of realistic pre-SN stars provided by Woosley and Heger [94]. The authors evolve Newtonian stars up to the moment of iron core collapse. They provide profiles for stars with zero-age-main-sequence (ZAMS) masses ranging from 10.8 to 75 solar masses and three different metallicities: solar (labelled from now on by s), 10^{-4} solar (labelled by u) and primordial (labelled by z). We initialize the scalar variables φ, ψ and η to 0. If $\alpha_0 = 0$, these Newtonian models lead to a collapse scenario similar to GR [46]. We only study cases with small but non-zero α_0 in this thesis, because for $\alpha_0 = 0$ the scalar remains zero at all times (cf. below).

For illustration we plot the baryon density profiles of some of the progenitor models we employ in the left panel of Fig. 5.1. To avoid instabilities arising from zero densities [66], we procede according to [46] and pad the Woosley-Heger profiles with a uniform atmosphere $\rho_{\text{atm}} = 1$ g cm^{-3} starting with points where the density drops below ρ_{thr}; the threshold value typically used is 3.57×10^3 g cm^{-3}. We discuss the negligible influence of the atmosphere on the results in Appendix B.1.

To test that we obtain a trivial scalar profile for $\alpha_0 = 0$, we have performed simulations using the 39 $M_\odot$ progenitors as initial data with three equations of state: EOS1, EOS3 and EOSa (see Table 4.1). We indeed obtain a zero scalar field, even when the other scalar parameters are non-zero.

We illustrate the qualitative behaviour of several collapsing models in the right panel of Fig. 5.1. We note the following features:

- The highly stiff equation of state EOSa leads to the formation of a neutron star after 56.27 ms (for solar metallicity), 67.18 ms (for 10^{-4} solar metallicity) and 68.02 ms (for primordial metallicity).

- For the softest equation of state EOS1 the star collapses to a neutron star after 73.13 ms (solar), 85.73 ms (10^{-4} solar) and 86.84 ms (primordial metalicity),

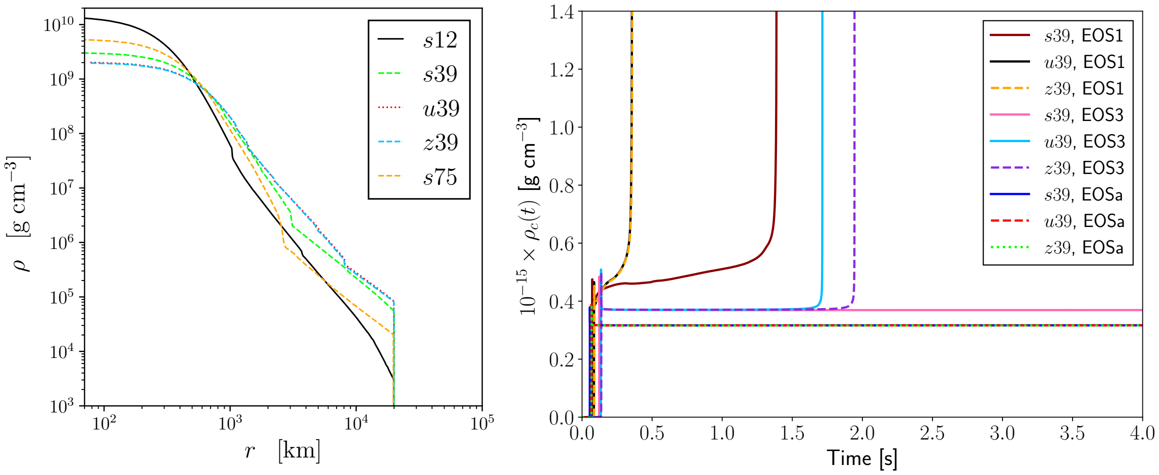

Fig. 5.1 *Left:* Baryon density profiles of initial data models $s12$ (black), $s39$ (green), $u39$ (red), $z39$ (blue) and $s75$ (orange) as obtained from [94]. *Right:* Evolution of the central baryon density for collapse in GR of 39 $M_\odot$ progenitors for solar (s), 10^{-4} solar (u) and primordial (z) metallicities for different EOSs. All three cases using EOSa (navy blue, red and green) as well as the solar metallicity progenitor with EOS3 (pink) lead to neutron star formation through one stage, while the other configurations (the brown, black, orange, light blue, purple) undergo a second collapse stage and form BHs.

but later on undergoes another collapse phase and forms a BH; the two lower metallicities result in a BH after only 0.35 s, whereas the solar metallicity model forms a BH after 1.388 s.

- EOS3 has intermediate stiffness and combines the features of the previous two cases: $s39$ leads to the formation of a neutron star after 122.82 ms; $u39$ collapses to a neutron star after 135.00 ms and after 1.71 s it forms a black hole; $z39$ collapses to a neutron star after 137.10 ms and after 1.94 s it forms a black hole.

5.2.3 Convergence test

Before discussing the physical properties of the various core collapse configurations in more detail, we discuss the numerical accuracy of our code. For this purpose we have repeated the convergence analysis displayed in Fig. 4.1 of [46] but now using a massive scalar field with $\mu = 10^{-14}$ eV and $\alpha_0 = 10^{-3}$ and $\beta_0 = -20$. We employ the $s12$ model as progenitor together with EOS1. The computational grid has uniform grid spacing in these simulations and extends to 2 000 km with $N_1 = 12\,000$, $N_2 = 18\,000$ and $N_3 = 24\,000$ points, respectively, for the low, medium and high resolution simulation.

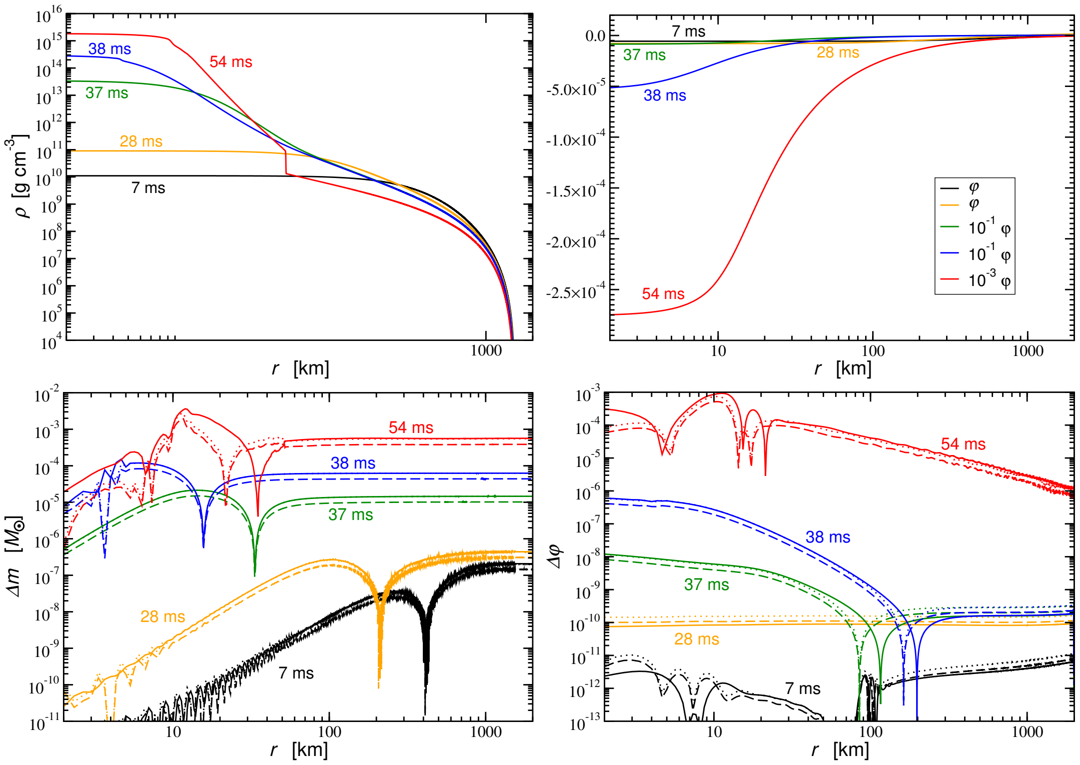

Fig. 5.2 Convergence analysis for stellar collapse in massive ST theory. A 12 $M_\odot$ star of solar metallicity and EOS1 collapses in a theory with $\alpha_0 = 10^{-3}$, $\beta_0 = -20$. *Upper panels:* Snapshots of the baryon density ρ (left) and the scalar field φ along the radius at different times of the evolution. For reference, core bounce occurs at 38 ms. Note that the scalar field at late times has been rescaled to allow for a comparison with the much smaller values at early times. *Bottom panels:* Difference in the mass function m (left) and the scalar field φ (right) obtained for N_1, N_2 and N_3 grid points. The solid curves show the differences obtained for N_1 and N_2 points. The dotted (dashed) curves are the difference for N_2 and N_3 points rescaled by the convergence factor $Q_2 = 2.86$ ($Q_1 = 2$) expected for second (first) order. If the solid line coincides with the dotted (dashed) curve, the code exhibits second (first) order convergence.

A grid variable f converges at n^{th} order if the differences between low, medium and high resolutions scale according to

$$\frac{f_{N_1} - f_{N_2}}{f_{N_2} - f_{N_3}} = Q_n := \frac{(N_2/N_1)^n - 1}{1 - (N_2/N_3)^n}\,. \tag{5.1}$$

In Fig. 5.2, we display the differences $f_{N_1} - f_{N_2}$ as a function of radius at different times in the evolution as solid lines. The high-resolution difference $f_{N_2} - f_{N_3}$ is rescaled for second (first) order convergence using $Q_2 = 2.86$ ($Q_1 = 2$) as dotted (dashed) curves. If the solid line overlaps with the dotted (dashed) curve, the code exhibits second (first)

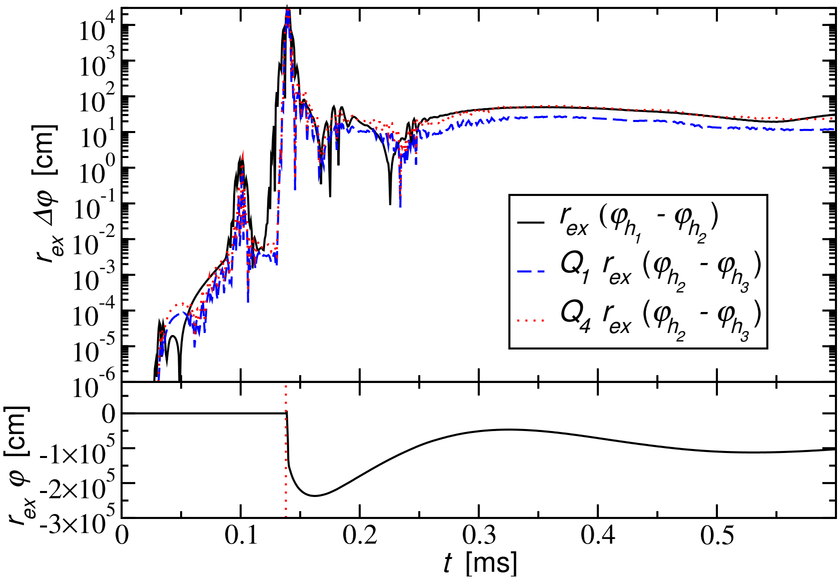

Fig. 5.3 Convergence of the wave signal at $r_{\rm ex} = 3\times10^4$ km from a typical, strongly scalarized collapse of the $s12$ profile with EOS1 and $\alpha_0 = 10^{-4}$, $\beta_0 = -20$, $\mu = 10^{-14}$ eV. The solid curve shows the difference of the coarse and medium resolution runs and is compared with that between medium and high resolution rescaled for first-order (dashed) and second-order (dotted curve) convergence factor. For reference, we show the signal $r_{\rm ex}\varphi$ in the bottom panel where the vertical dotted line at $t - r_{\rm ex} = 38\,{\rm ms}$ marks the core bounce.

order convergence. We observe the same convergence between first and second order, in agreement with the first and second order schemes used in the code. For reference, we also plot in the upper panels the profiles of the baryon density and the scalar field at the same moments in time. Following the second-order accurate initialization of the profiles, boundary effects lead to a drop in convergence to about first order after about one light crossing time $t\sim 7$ ms. As the dynamics picks up momentum, convergence is dominated by the smooth time evolution and approaches second order up to the core bounce at $t\sim 38$ ms when the first-order accurate shock capturing treatment sets in and the overall convergence properties result from a combination of first and second-order ingredients.

The pointwise convergence test requires us to employ a uniform grid while the production runs are performed with a non-uniform grid adapted to the high resolution requirements near the origin and the less demanding profiles propagating in the wave zone. In order to assess the accuracy of the waveforms generated, we have therefore performed a second convergence test starting from the $s12$ profile with the same EOS as in the first convergence study. The grid, however, is now of customized type using

$N_1 = 5\,000$, $N_2 = 10\,000$ and $N_3 = 20\,000$ points on a grid uniformly spaced with $\Delta r_1 = 250$ m, $\Delta r_2 = 125$ m and $\Delta r_3 = 62.5$ m up to $r = 40\,\text{km}$ and the remainder of the grid points logarithmically spaced from that point on to the outer edge at $r_{\text{out}} = 1.8 \times 10^5$ km. In contrast to the runs with a uniform grid, doubling the number of grid points does not lead to a decrease in the grid spacing by a factor 2 in the outer zone which complicates the convergence properties. We still expect the wave signal extracted at fixed radius (here $r_{\text{ex}} = 3 \times 10^4$ km) to exhibit convergence similar to the first or second-order behaviour seen above. As shown in Fig. 5.3, this is indeed the case. As before, we compare the low resolution differences with their high-resolution counterparts rescaled by $Q_1 = 2$ for first order (dashed curves) and $Q_4 = 4$ for second order. The figure shows that the gravitational waveform converges close to second order over most of the evolution. The error peaks at a retarded time of about $t - r_{\text{ex}} \approx 38$ ms corresponding to the bounce stage in the stellar evolution where the wave signal shows a steep gradient (cf. lower panel in Fig. 5.3). The good agreement between the solid and dotted curves demonstrates convergence close to second order and implies a discretization error of about 6 % (3 %) for coarse (medium) resolution. In the simulations from this thesis we use a range of resolutions, from $\Delta r = 250.00$ m to $\Delta r = 41.66$ m, but bear in mind the above numbers as conservative error estimates.

5.2.4 Spurious transients in the wave signal

The scalar dynamics are triggered because the initial profiles are Newtonian and as such not static solutions when $\alpha_0 \neq 0$. Similarly to Gerosa et al in Ref. [46], an initial transient phase causes the scalar field to settle to a non-trivial value before the collapse starts. One such case is highlighted in Fig. 5.4, where the physical scalar radiation is visible merely as a small "dent" compared to the spurious transient signal. This remains true for models that lead to BHs. Note however that these are weakly scalarized configurations with essentially zero GW signal. As we reach more negative values of β_0, the signal corresponding to the collapse of the star to supranuclear values becomes much stronger and completely dominates in amplitude over the noise from the transient. We can see this in Fig. 5.5 where there is a another peak in the waveforms at retarded time $t = 1.38$ s caused by the collapse to a BH and the descalarization of the star. The transient is completely negligible for all strongly scalarized cases.

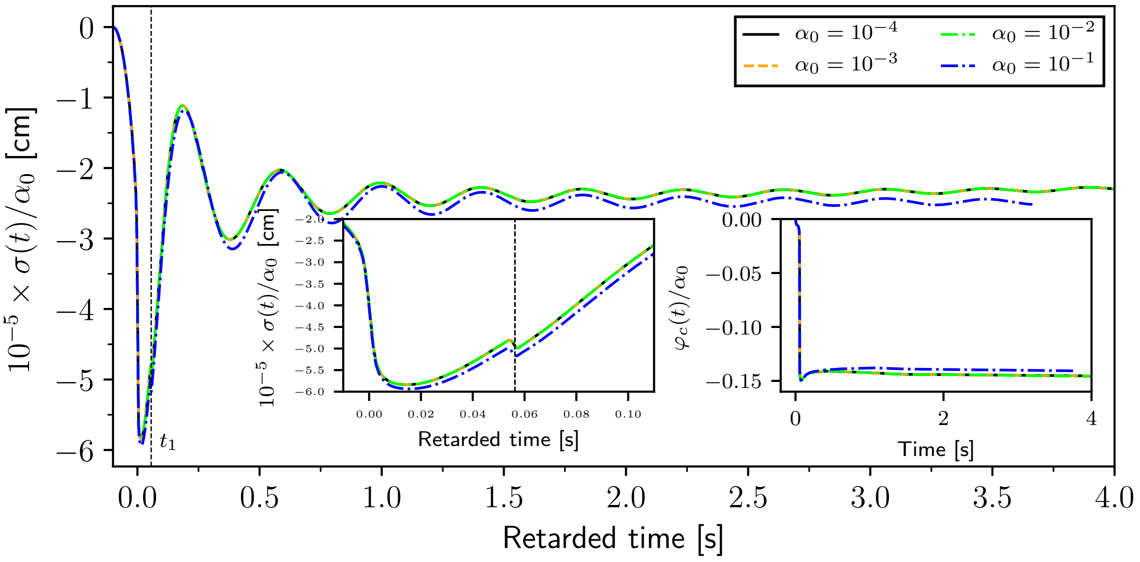

Fig. 5.4 The progenitor used is $s39$ with EOSa and the scalar parameters are $\beta_0 = -12$ and $\mu = 10^{-14}$ eV. We plot the waveforms, rescaled with α_0, extracted at $r_{\text{ex}} = 3 \times 10^4$ km, a zoom in (left inset plot) and the central scalar field (right inset plot). Core bounce occurs at $t_1 = 56$ ms and the physical signal from this collapse is the slight "dent" in the waveform at this time (observable in the left inset). The signal before t_1 is the pulse due to the transient.

5.2.5 Extraction radius

The GW signals we use in the previous figures and in the following analysis are extracted at 3×10^4 km. It is important that the extraction distance is large enough in order for the scalar field equation to be approximated by the flat space Klein-Gordon equation 3.67, in which case we can use the results from Sec. 3.4 to propagate the signal to LIGO distances. But, as the outer grid is logarithmic, the results are less accurate the further they are extracted from the star. We have checked whether $r_{\text{ex}} = 3 \times 10^4$ km is large enough in the following way: we have extracted a signal at r_{ex} and $r'_{\text{ex}} > r_{\text{ex}}$. We then propagate the former to r'_{ex} using the results from Sec. 3.4.2 and then we compare the result with the signal directly extracted at r'_{ex} .

In Fig. 5.6 we show gravitational waveforms resulting from the collapse of $u39$ at three different distances: 5×10^3 km (red), 3×10^4 km (green) and 9×10^4 km (black). We can see from the power spectrum of these signals in the upper right panel of the figure that the main difference arises at frequencies below $\omega_*/(2\pi)$, where the signal extracted at smaller radii (red) is stronger. This is reflected in the waveform by the drift (low frequency contributions) we see for the red signal. This feature is in agreement with the fact that low frequency modes decrease exponentially with

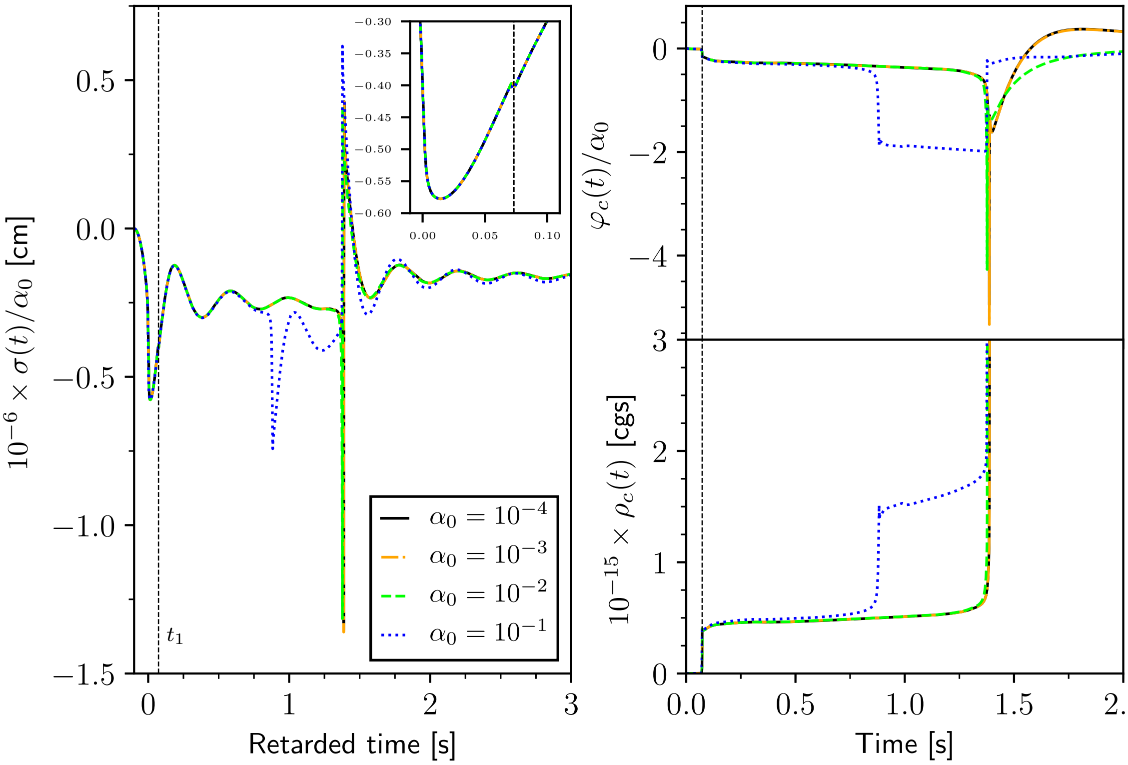

Fig. 5.5 The progenitor used is $s39$ with EOS1 and the scalar parameters are $\beta_0 = -4$ and $\mu = 10^{-14}$ eV. We plot the scaled waveforms extracted at $r_{\text{ex}} = 3 \times 10^4$ km (left panel), the central baryon density (bottom right panel) and the scaled central scalar field (top right panel). We see a qualitative difference for $\alpha_0 = 10^{-1}$ as there is an intermediate collapse stage into a high-compactness NS and later on it collapses into a BH. All simulations collapse to a NS after $t_1 = 73$ ms. The signal due to this can be seen in the inset of the left panel, where it can be barely registered as a dent. The signal before t_1 is the pulse due to the transient.

distance. When propagating our results to distances of the order of 10 kpc, modes with frequencies below $\omega_*/(2\pi)$ will be completely supressed. The power spectrums also shows differences for frequencies above 100 Hz, likely due to numerical inaccuracy, but the values here are several orders of magnitude smaller which makes their contribution to the signals negligible.

We then propagate the signals from 5×10^3 km, 3×10^4 km to 9×10^4 km and compare them to the signal directly extracted at 9×10^4 km (bottom panel). We see excellent agreement between all signals. This confirms that 3×10^4 km is an appropriate extraction radius. We have repeated this analysis for other progenitor masses and with different equations of state (see Fig. 5.7) and arrive at the same conclusion.

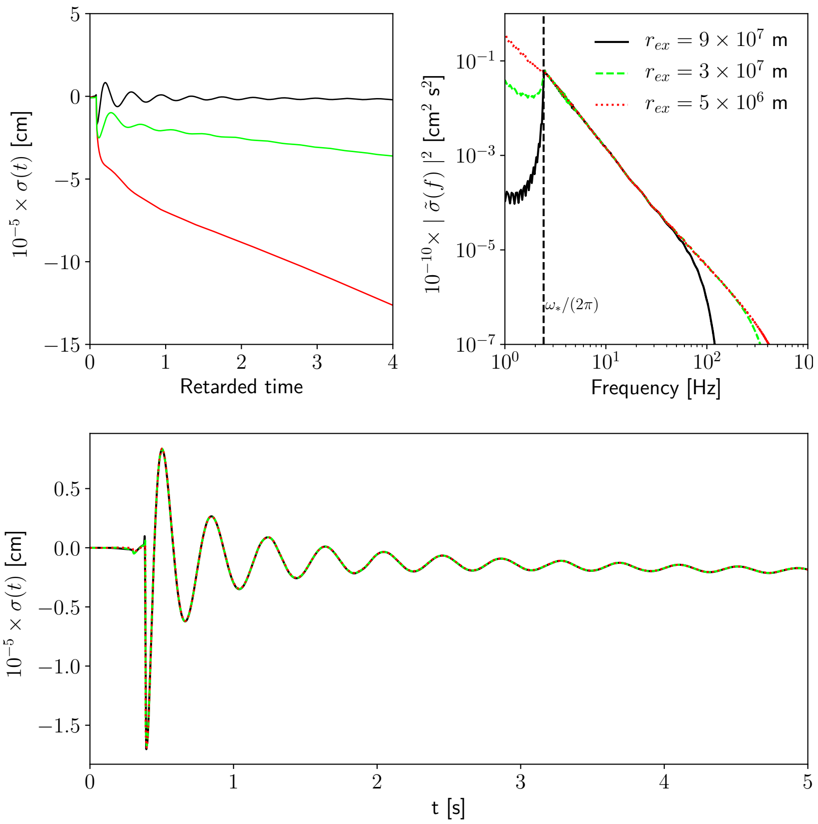

Fig. 5.6 Gravitational waveforms from the core collapse of $u39$ with EOS1 and scalar parameters $\alpha_0 = 10^{-2}$, $\beta_0 = -20$ and $\mu = 10^{-14}$ eV. In the top left panel we plot the waveforms extracted at 5×10^3 km, 3×10^4 km and 9×10^4 km and in the top right panel their corresponding power spectrum. We propagate the first two signals to a larger distance 9×10^4 km and plot the results in the bottom panel; they agree with high precision.

5.2.6 Freezing the matter evolution

Radial gauge and polar slicing are not ideal coordinates when the star approaches the Schwarzschild radius as the lapse function ν approaches 0. Following the method of Ref. [41, 46] we freeze the matter dynamics in this case, but continue the evolution of φ on the frozen background in order to propagate the signal to $r_{\rm ex}$. In practice we stop the matter dynamics either when the lapse function becomes smaller than a threshold value of our choice or at a specific time in the evolution.

We also use the freezing of the matter evolution to deal with another difficulty arising in a few simulations: close to the β_0 threshold for hyperscalarization we see a drop in density for insufficient numerical resolution. Such a scenario occurs, for example, when collapsing a $39\,M_\odot$ progenitor of primordial metallicity ($z39$) and equation of

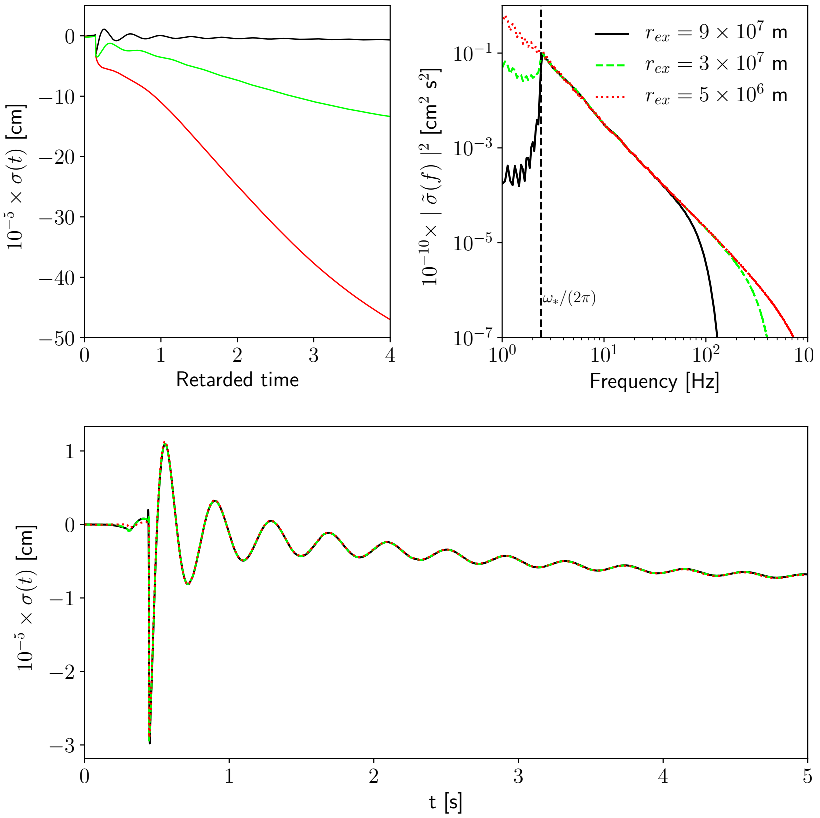

Fig. 5.7 Gravitational waveforms from the core collapse of $u75$ with EOS3 and scalar parameters $\alpha_0 = 10^{-2}$, $\beta_0 = -20$ and $\mu = 10^{-14}$ eV. In the top left panel we plot the waveforms extracted at 5×10^3 km, 3×10^4 km and 9×10^4 km and in the top right panel their corresponding power spectrum. Using the results from Sec. 3.4, we propagate the first two signals to 9×10^5 km and plot the results in the bottom panel.

state EOS3 using scalar parameters $\alpha_0 = 10^{-2}$, $\beta_0 = -8$ and $\mu = 10^{-14}$ eV; in the bottom left panel of Fig. 5.8, we plot the evolution of ρ_c as a function of time for four different resolutions. All our simulations suggest that the radial zone width Δr influences the results, whereas the number of radial zones N has little impact. As we increase the resolution, the drop in density happens later in time. This indicates that the drop is unphysical in the continuum limit, and we therefore freeze the matter evolution shortly before the drop.

As we can see in the bottom right panel of Fig. 5.8, φ_c mirrors the behaviour of ρ_c, such that a sudden drop in density causes a decrease in the scalar field amplitude. This sudden change in the scalar field propagates to the extraction radius and we see it as a second inverted peak in the waveform, similar to the ones caused by the descalarization of the stars due to BH formation. By freezing the matter evolution just before the drop happens, we eliminate this artifact. Of course this also prevents

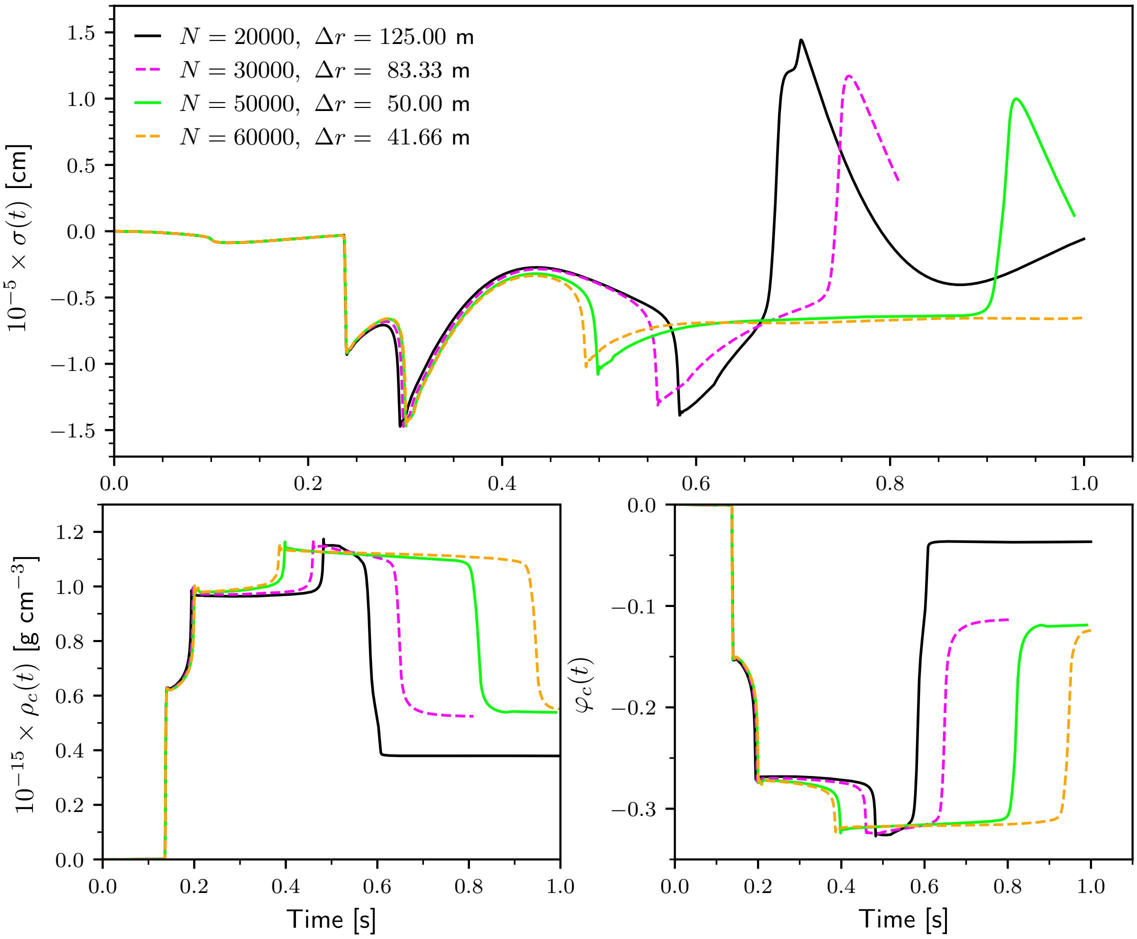

Fig. 5.8 Results for simulations using different resolutions. The progenitor used is $z39$ with EOS3 and the scalar parameters are $\alpha_0 = 10^{-2}$, $\beta_0 = -8$ and $\mu = 10^{-14}$ eV. We plot the waveforms extracted at 3×10^9 cm (top panel), the central baryon density (bottom left panel) and the central scalar field (bottom right panel).

any other dynamics from happening later (such as another jump in the density or full collapse into a BH) which could contribute to the strength of the signal. This applies to a set of measure zero in the parameter space. Freezing matter dynamics will provide us with a conservative estimate of the hyperscalarization.

5.3 Hyperscalarization

In this section we explore several equations of state for the lighter progenitor $s12$, as well as study the α_0, β_0 parameter space for models $s39$, $u39$ and $z39$ (heavy progenitors) where we focus on EOS1, EOS3 and EOSa.

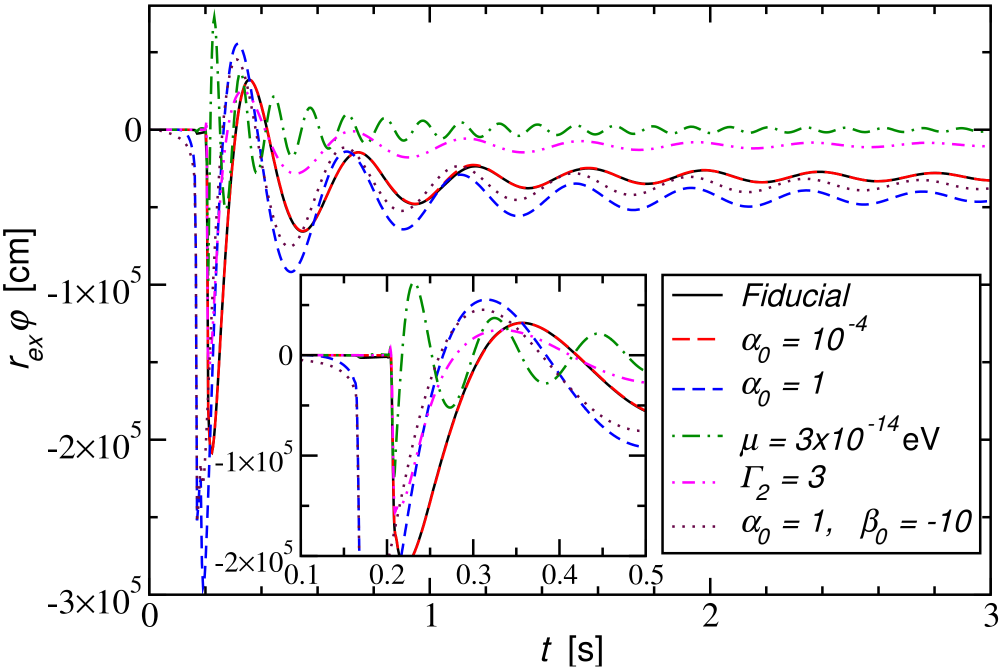

Fig. 5.9 Waveforms extracted at 5×10^4 km after the collapse of s12. The legend lists deviations from the fiducial parameters $\mu = 10^{-14}$ eV, $\alpha_0 = 10^{-2}$, $\beta_0 = -20$, $\Gamma_1 = 1.3$, $\Gamma_2 = 2.5$, $\Gamma_{\rm th} = 1.35$.

Our observations in these simulations can be summarized as follows: for sufficiently negative β_0 the scalar field reaches amplitudes of the order of unity, independent of the EOS. Even in the massless case $\mu = 0$, we observe this strong scalarization; the key impact of the massive field therefore lies in the weaker constraints on α_0, β_0 rather than a direct effect on the degree of scalarization of terms involving μ. For illustration, we plot in Fig. 5.9 the wave signal $r\varphi$ extracted at 5×10^4 km for various parameter combinations.

These waveforms are to be compared with those obtained for present observational bounds in the core collapse in massless ST theory as shown in Fig. 6 of Ref. [46]. The amplitudes observed here are larger by $\sim 10^4$ for neutron star formation from light progenitors and even exceed the strong signals in black hole formation from more massive progenitors by ~ 100. We refer to these extreme scalar values of the collapsing stars in massive ST theory (as compared with the more strongly constrained massless case) and the resulting substantially larger GW signals as *hyperscalarization*. By keeping all parameters fixed and varying β_0, we have searched for the values (from now on called *thresholds*) where hyperscalarization kicks in by looking at the value of the central scalar fields and the maximum amplitude of the gravitational waves extracted at a fixed radius, chosen here as $r_{\rm ex} = 3 \times 10^4$ km.

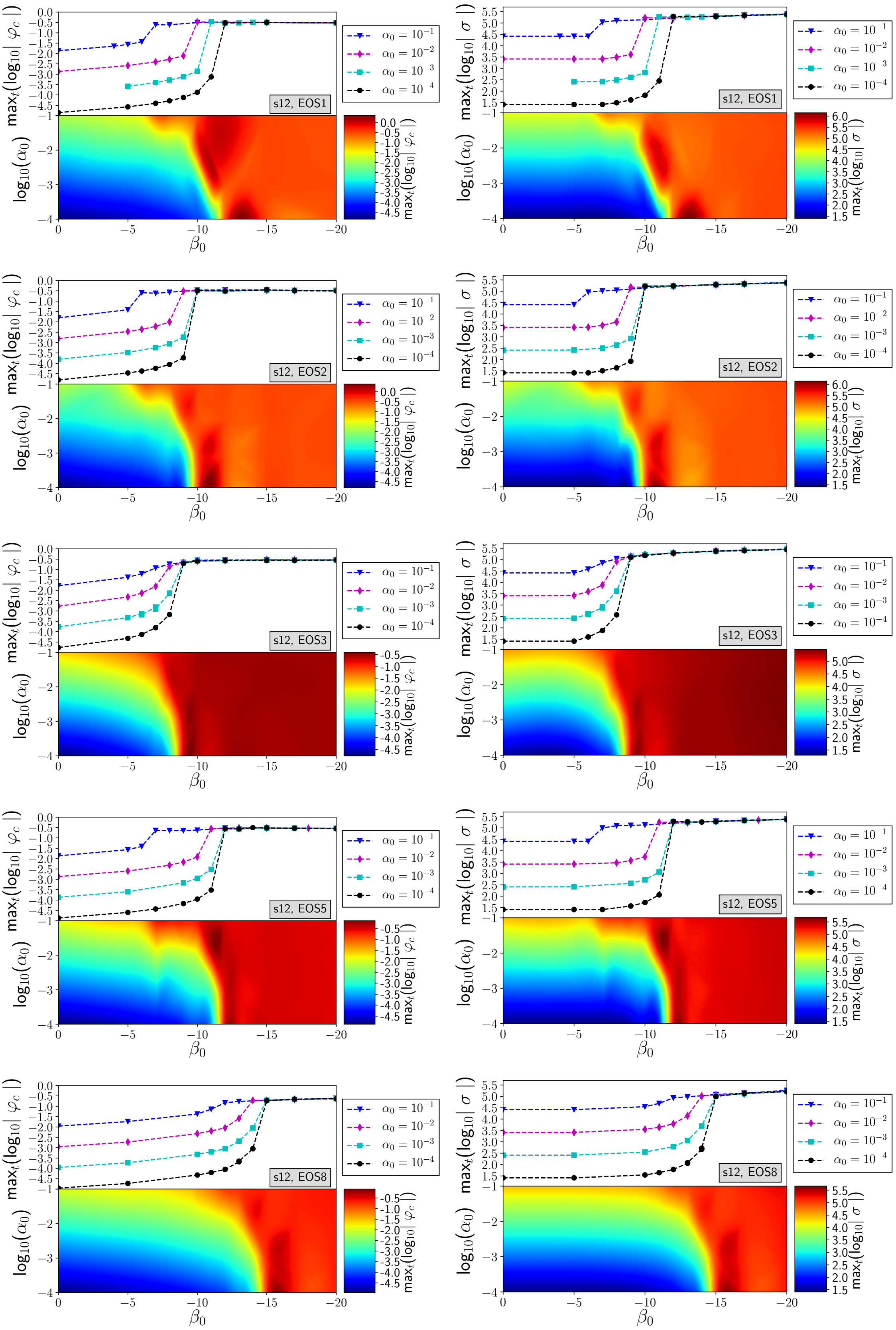

Fig. 5.10 Top: maximum amplitudes of the central scalar field (left) and the waveform extracted at $r_{\rm ex} = 3 \times 10^4$ km (right) as functions of β_0, for various α_0. Bottom: heatmaps created by interpolating the values from the top panels. Progenitors and EOSs are indicated by the grey labels.

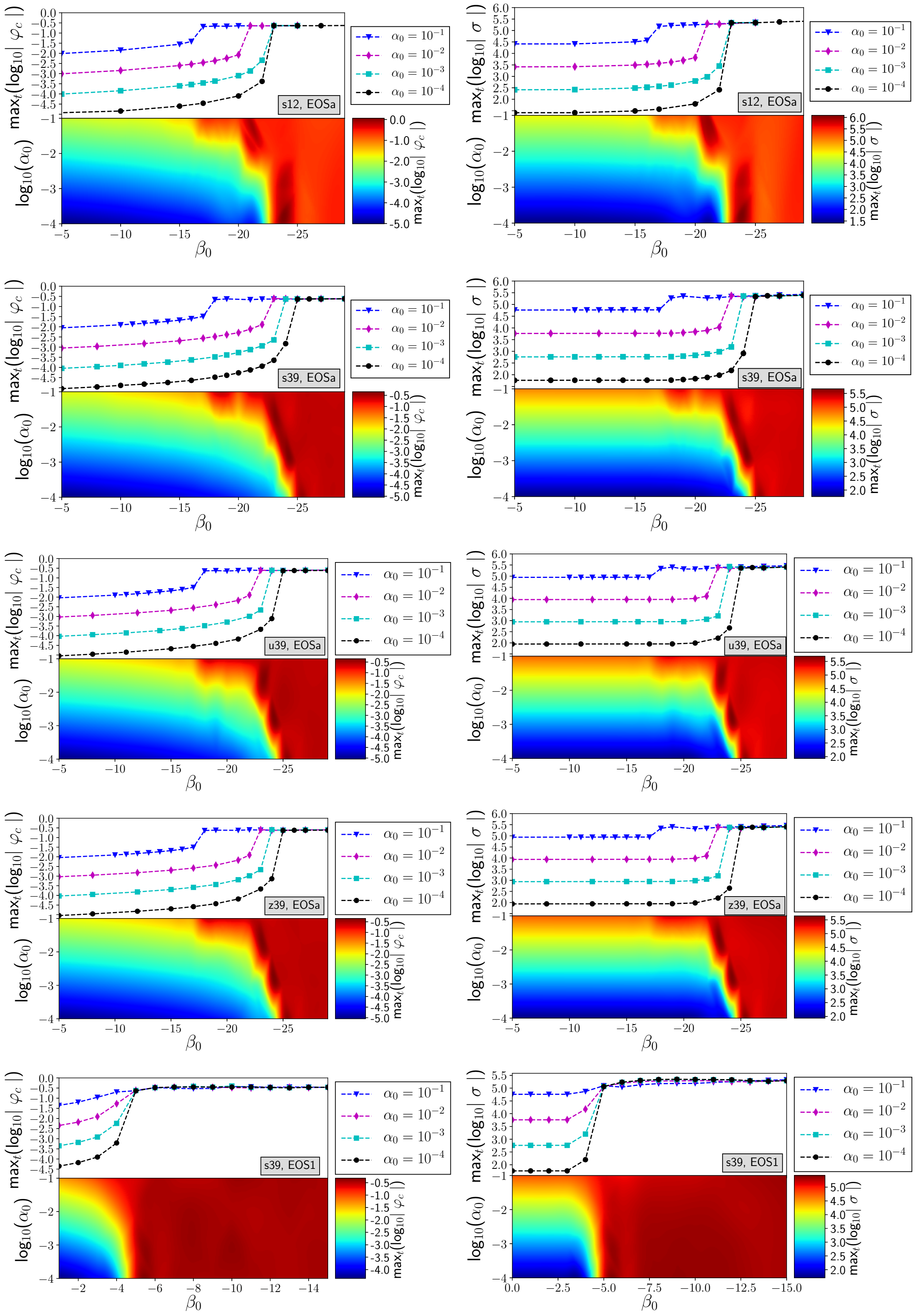

Fig. 5.11 Same as Fig. 5.10 for massive progenitors.

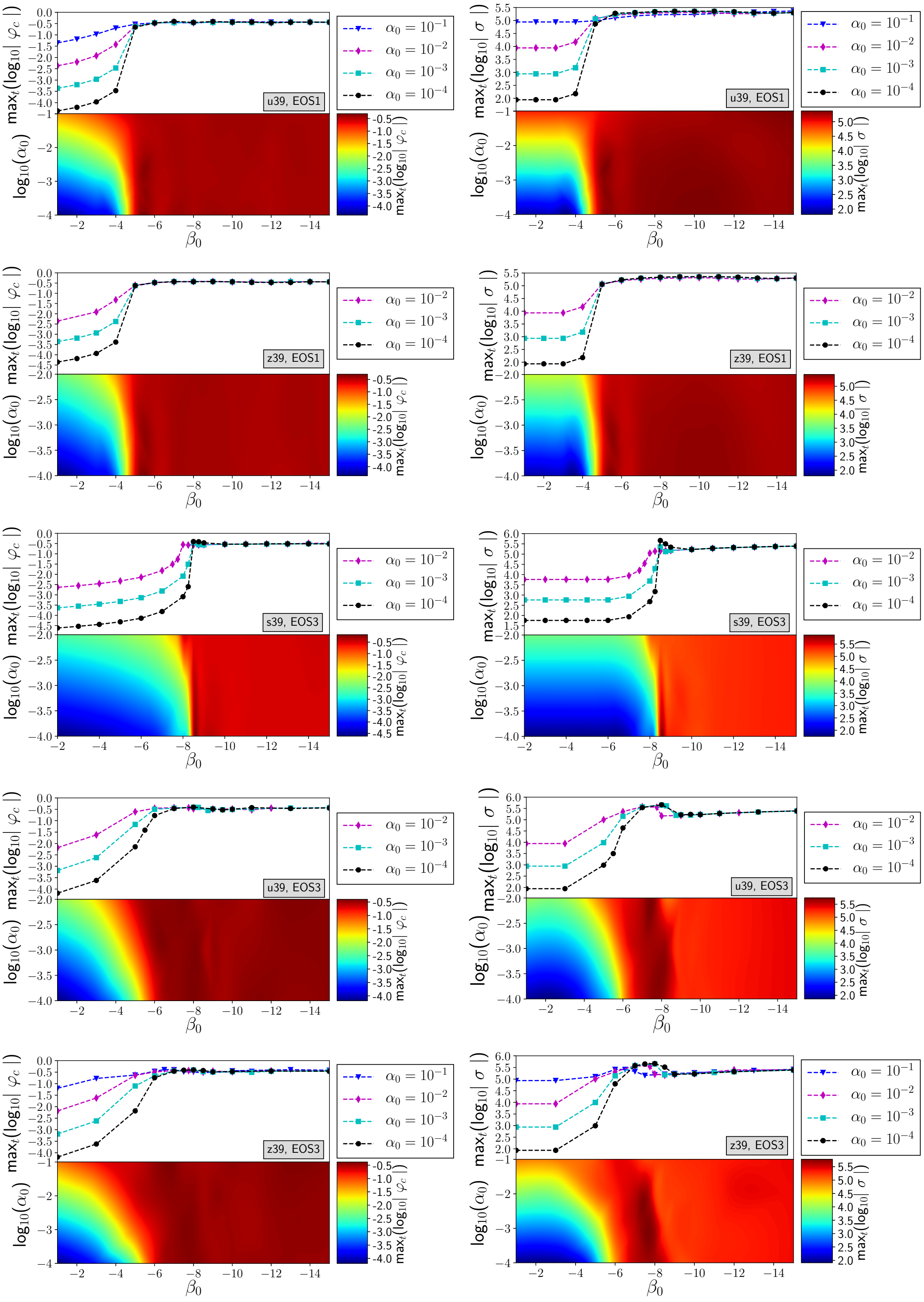

Fig. 5.12 Same as Fig. 5.10 for massive progenitors.

Our findings for the two quantities for $\mu = 10^{-14}$ eV, several progenitor models and EOSs in Figs. 5.10, 5.11, 5.12. To build these heatmaps (2D diagrams of the α_0, β_0 plane where each point represents a model and color is a measure of the scalarization) we have interpolated the maximal values for either φ_c or $r\varphi(r_{\text{ex}})$ from a discrete set of runs using the Python scipy.interpolate.griddata function with cubic splines. The left-hand columns contain the heatmaps corresponding to the central scalar field φ_c. The right-hand columns contain the heatmaps corresponding to the amplitudes of the waveforms extracted at $r_{\text{ex}} = 3 \times 10^4$ km.

The main conclusions we can draw from the heatmaps are:

- For β_0 values less negative than the threshold, the stars are weakly scalarized and φ_c and $r\varphi$ scale with α_0, as we can see from the top panels of the heatmaps where $\varphi_c \propto \alpha_0$. We can observe that this proportionality is maintained in time in Figs. 5.4, 5.5. The bottom right corner of the latter confirms that in this regime the baryon density is not affected for $\alpha_0 \leq 10^{-2}$. In Fig. 5.4, small differences appear for $\alpha_0 = 10^{-1}$ (blue line). In the heatmaps, φ_c shows a mild increase in amplitude, wheareas the waveform amplitude tends to remain constant as we vary β_0. This is due to the maximum being registered in the spurious signal due to the transient at the beginning of the simulation. The amplitude of φ_c is a better measure of scalarization (or lack of it) in this regime, as it continues decreasing as the baryon density increases.

- When β_0 is more negative than the threshold, φ_c reaches a value of $O(0.1)$ for all α_0. In this regime, the scalarization is driven by β_0.

Both heatmaps show the same thresholds for hyperscalarization, making either variable a suitable measure for strong scalarization. In our analysis care has been taken for those models that end up in black holes as sometimes such simulations crash before enough time has elapsed for the full signal to reach the extraction radius. In such situations the central scalar field is still a reliable measure for the degree of scalarization. For example, in Fig. 5.21 below we plot φ_c as a function of time for several stars that end up collapsing to a BH. For $\beta_0 = -3.25$ (blue line), the scalar field drops rapidly at ~ 1.20 as the star scalarizes and reaches a value of ~ -0.125 before starting to increase, as the star approaches a BH and descalarizes. Unfortunately, our simulation crashed when φ_c reached a value of about -0.050 and we could not extract a waveform corresponding to the descalarization, but the time evolution of φ_c demonstrates that $|\varphi_c|$ has reached its extreme value by the end of the simulation.

The middle range of values for β_0 is less definitive and these cases are most sensitive to the progenitors we use and the equation of state. We notice that for larger α_0 strong scalarization occurs for less negative β_0. One such example is plotted in Fig. 5.5 above for $s39$ with EOS1, $\beta_0 = -4$ and $\mu = 10^{-14}$ eV. For $\alpha_0 \leq 10^{-3}$, the waveform $r\varphi$ amplitude (left panel) scales with α_0 to high precision. The baryon density, on the other hand, barely changes with α_0 and the three stars collapse into a NS after 73 ms and into a BH after 1.38 s for $\alpha_0 \leq 10^{-3}$ and 1.37 s for $\alpha_0 = 10^{-2}$. Significant differences appear for the central scalar field φ_c (top right panel of Fig. 5.5), where the $\alpha_0 = 10^{-4}$ and $\alpha_0 = 10^{-3}$ cases agree, but the $\alpha_0 = 10^{-2}$ profile diverges (there is a 23% reduction in the amplitude of φ_c/α_0). For $\alpha_0 = 10^{-1}$ we encounter a different model altogether: before collapsing into a BH at $t = 1.37$ s, the star suffers an additional collapse at $t = 0.88$ s, forming a highly-compact NS. This is a strongly scalarized model $|\varphi_c|$ reaches the value of ≈ 0.2 and the scaling with α_0 no longer holds.

The β_0 thresholds for scalarization are highly dependent on the initial progenitors and equations of state, making it difficult to draw overall conclusions. The most negative values of the thresholds have been observed for EOSa (Fig. 5.11). One would expect that the adiabatic index Γ_2 of the inner core determines the star's resistance to strong scalarization, but the picture is more complicated as shown by comparing the results of model $s12$ for EOS5 and EOS8: the threshold for the fomer is around $\beta_0 \approx -11$ whereas for the latter it is $\beta_0 \approx -15$ even though EOS5 is a stiffer equation of state. Similarly, comparing EOS1 with EOS8 (first has $\Gamma_{\rm th} = 1.35$, whereas the second has $\Gamma_{\rm th} = 1.5$) shows again that one needs a more negative value of β_0 to induce strong scalarization. We suspect that the thermal component $\Gamma_{\rm th}$ of the pressure plays a significant role in these cases.

In all simulations φ is negative throughout the spatial domain with the exception of the stars forming BHs (during the descalarization, φ sometimes overshoots and reaches positive values). This is in agreement with our conclusion from Chapter 4 regarding to the stability of models with strong negative scalar field values.

5.4 Influence of the progenitor mass

We now study the influence of the progenitor's ZAMS mass ($M_{\rm ZAMS}$) on the degree of scalarization. For this purpose we have studied the onset of hyperscalarization for EOSa and $\alpha_0 = 10^{-2}$ for progenitor masses ranging from 10 $M_\odot$ to 75 $M_\odot$ for solar and 10^{-4} solar metallicity, and for masses in the interval $10 - 40$ $M_\odot$ for primordial metallicity. There are gaps in the catalogue of models provided in Ref. [94]; we have

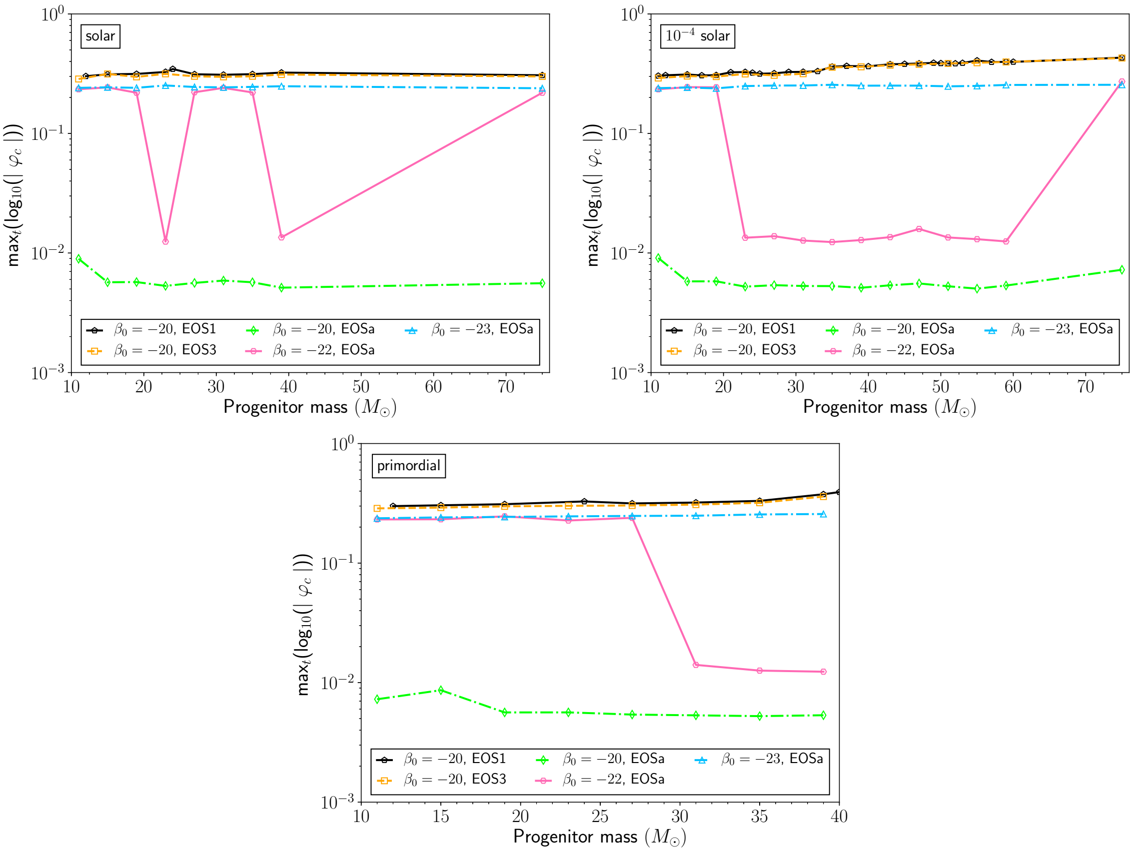

Fig. 5.13 Amplitude of φ_c for different progenitor masses used as initial data; each line is labelled by the equation of state and β_0 value used. The other scalar parameters are $\alpha_0 = 10^{-2}$ and $\mu = 10^{-14}$ eV. The metallicity used is solar (top left), 10^{-4} solar (top right) and primordial (bottom). Most simulations were done with higher resolutions.

studied all cases available. We have chosen this equation of state because no progenitor leads to BH formation. As we can see from the amplitudes of φ_c plotted in Fig. 5.13, we obtain weak scalarization for all M_{ZAMS} when $\beta_0 = -20$ (green line) and strong scalarization for all M_{ZAMS} when $\beta_0 = -23$ (blue line). For $\beta_0 = -22$ case, however, the situation is more complicated:

- Solar metallicity (top left panel of Fig. 5.13): 23 $M_\odot$ and 39 $M_\odot$ progenitors lead to week scalarization, whereas all other cases produce strong scalarization.
- 10^{-4} solar metallicity (top right panel of Fig. 5.13): progenitors with masses in the range $23 - 59$ $M_\odot$ lead to week scalarization, whereas lighter models and the case 75 $M_\odot$ produces strong scalarization.

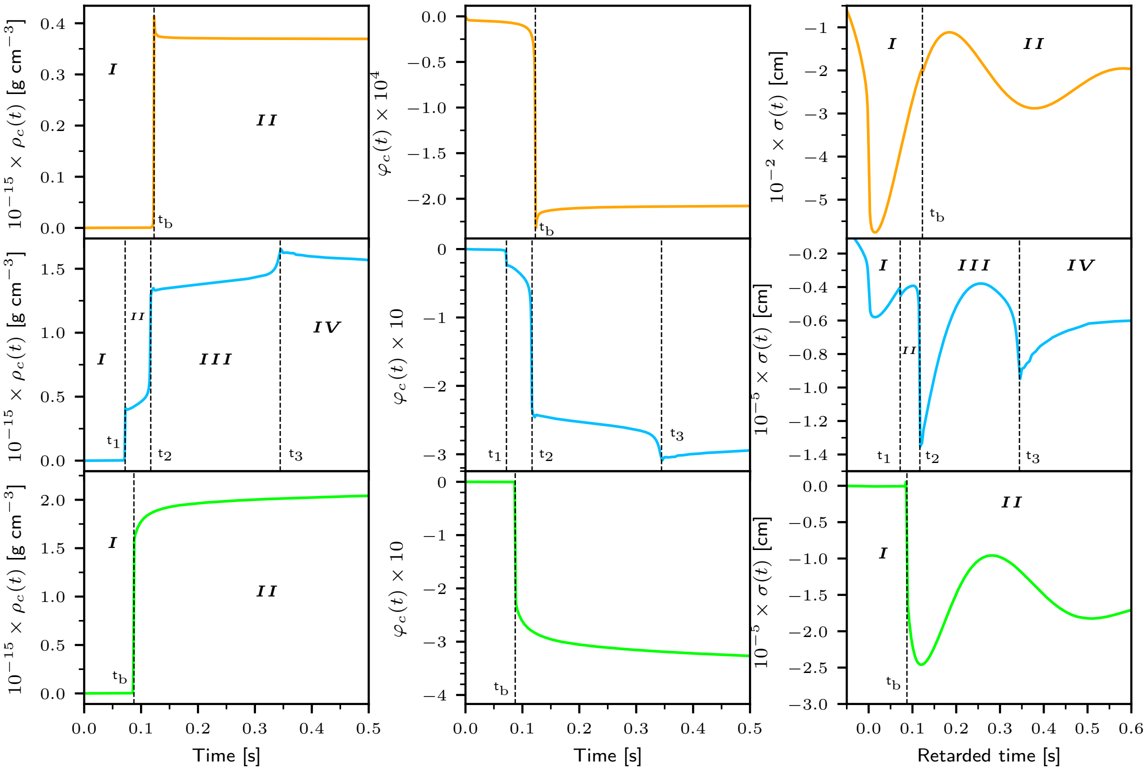

Fig. 5.14 Central baryon density (left column), central scalar field (middle column) and waveform extracted at $r_{\text{ex}} = 3 \times 10^4$ km (right column) as functions of time for the following NS models: top panels (orange curve) for $s39$, EOS3 with scalar parameters $\alpha_0 = 10^{-3}$, $\beta_0 = -2$, $\mu = 10^{-14}$, representing a prompt low-compactness NS, middle panels (blue curve) for $s39$, EOS1 with scalar parameters $\alpha_0 = 10^{-1}$, $\beta_0 = -7$, $\mu = 10^{-14}$, representing a multi-stage NS, bottom panels (green curve) for $z39$, EOS1 with scalar parameters $\alpha_0 = 10^{-3}$, $\beta_0 = -20$, $\mu = 10^{-14}$, representing a prompt high-compactness NS.

- Primordial metallicity (bottom panel of Fig. 5.13): massive progenitors ($M \geq 31\ M_{\odot}$) lead to weak scalarization, whereas lighter ones produce strong scalarization.

Clearly the outcome for $\beta_0 = -22$ sensitively depends on the progenitor. We believe this is due to the $\beta_0 = -22$ case for EOSa being close to the critical threshold of hyperscalarization.

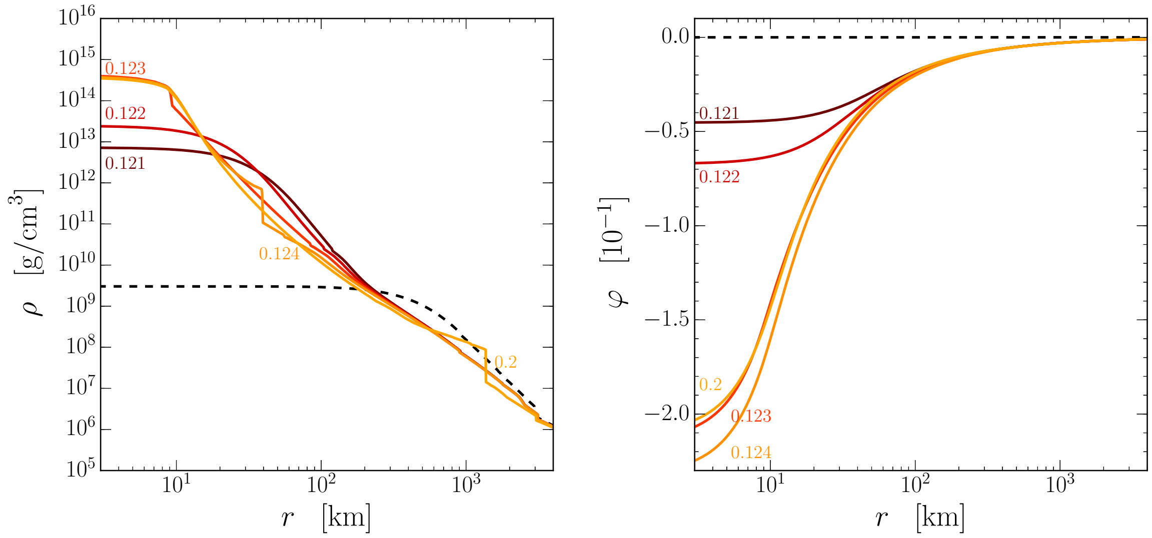

Fig. 5.15 Snapshots of the baryon density (left) and scalar field (right) profiles during the simulation of a prompt low-compactness NS. The progenitor used is $s39$ with EOS3 and the scalar parameters are $\alpha_0 = 10^{-3}$, $\beta_0 = -2$ and $\mu = 10^{-14}$ eV. The dotted black line respresents the initial profile.

5.5 Classification of the collapse scenarios

As we have seen in the previous examples, the behaviour of ρ_c varies with the scalar parameters. In this section we will try to classify the outcomes into different categories. We first discuss the qualitatively different outcomes we have obtained by providing an example for each case. In the next section we highlight which outcome is realized for which EOSs and scalar parameters.

For less negative and nonnegative β_0 values, independent of α_0, the collapse dynamics are similar to the corresponding scenario in GR: significant differences arise only in the scalar field profiles. Qualitative differences, such as delayed black hole formation, only appear when the scalar field reaches order unity values. For very negative β_0, independent of the initial data, the equation of state or α_0, all models collapse to a highly compact neutron star with the center attaining density values of order 10^{15} [cgs]. We have classified the models we obtain into five categories:

(i) prompt low-compactness NS,

(ii) multi-stage NS,

(iii) high-compactness NS,

(iv) 2-stage BH,

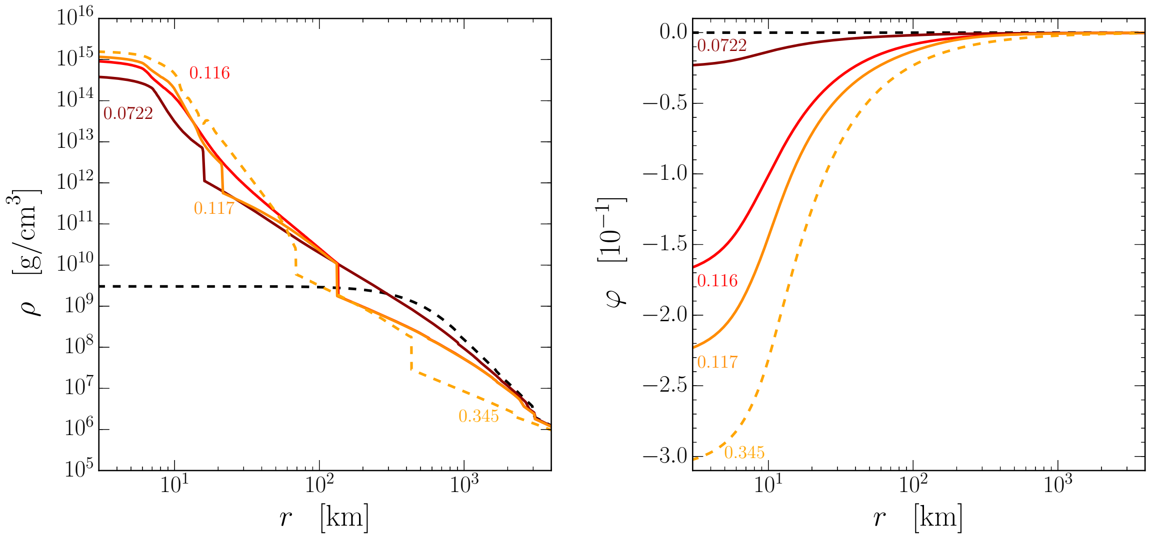

Fig. 5.16 Snapshots of the baryon density (left) and scalar field (right) profiles during the simulation of a multi-stage NS. The progenitor used is $s39$ with EOS1 and the scalar parameters are $\alpha_0 = 10^{-1}$, $\beta_0 = -7$ and $\mu = 10^{-14}$ eV. The dotted black line respresents the initial profile.

(v) multi-stage BH.

To determine the nature of a simulation it is often sufficient to consider the time evolution of ρ_c. Sometimes, however, the evolutions are more complicated and it becomes necessary to examine the whole density profile to determine the number of jumps in ρ_c. Each jump leads to an outward travelling shock that is easily identified in the time evolution of the density profile.

5.5.1 Prompt low-compactness NS

This scenario is realized for weakly negative β_0 values and for equations of state and progenitor models that collapse to a NS in GR.

As an example, we present the collapse of a 39 $M_\odot$ with solar metallicity and EOS3 and scalar parameters $\alpha_0 = 10^{-3}$, $\beta_0 = -2$ and $\mu = 10^{-14}$ eV. In the top row of Fig. 5.14 we plot the time evolution of φ_c and ρ_c as well as the waveform extracted at $r_{\rm ex} = 3 \times 10^4$ km. We clearly see one jump in ρ_c.

In Fig. 5.15 we plot snapshots of the density and scalar field profiles. After $t_b \sim 123$ ms the star collapses to a NS of compactness $m/r \sim 0.078$ (measured at ~ 10 km) and a shock forms which rapidly moves towards the surface of the star; it decelerates, but reaches ≈ 4000 km after ~ 0.4 s. The central baryon density peaks at 4.2×10^{14}

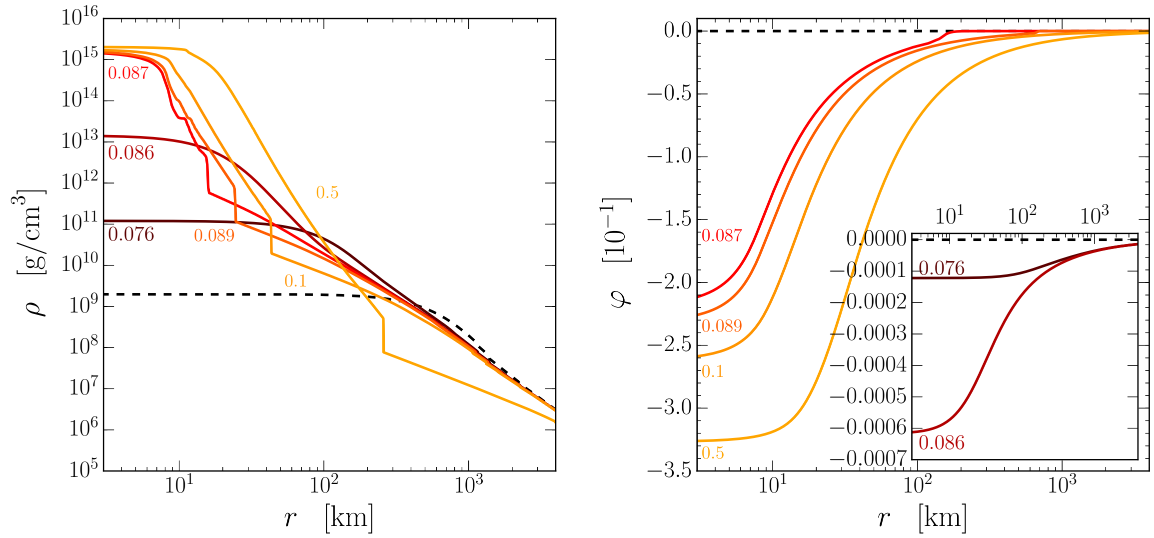

Fig. 5.17 Snapshots of the baryon density (left) and scalar field (right) profiles during the simulation of a prompt high-compactness NS. The progenitor used is $z39$ with EOS1 and the scalar parameters are $\alpha_0 = 10^{-3}$, $\beta_0 = -20$ and $\mu = 10^{-14}$ eV. The dotted black line respresents the initial profile.

[cgs] before settling to a smaller value $\sim 3.7 \times 10^{14}$ [cgs]. This behaviour is mirrored by the scalar field: the transient phase causes φ_c to reach -6.7×10^{-5}, it peaks at -2.3×10^{-4} just after the bounce, before relaxing to a smaller amplitude. The GW signal resulting from this model is very weak.

5.5.2 Multi-stage NS

This is an intermediate scenario arising for a narrow range of β_0 values as we decrease it beyond the range for low-compactness NS or multi-stage BH, but before the prompt high-compactness NS. It comprises at least two collapse phases which always lead to NSs and strong GW emission. This scenario is obtained in model E of [43] which shows a second collapse to another NS in Fig. 9.

As an example, we present the collapse of a 39 $M_\odot$ with solar metallicity, EOS1 and scalar parameters $\alpha_0 = 10^{-1}$, $\beta_0 = -7$ and $\mu = 10^{-14}$ eV. In the middle row of Fig. 5.14 we plot the evolutions of φ_c and ρ_c as well as the waveform extracted at $r_{\rm ex} = 3 \times 10^4$ km. In Fig. 5.16 we plot snapshots of the density and scalar field profiles. As we can see in Fig. 5.14, we observe three jumps in ρ_c (thus, this is a 3-stage simulation), but we cannot exclude more stages follow if the simulation were allowed to continue. The three jumps occur at $t_1 = 72.29$ ms, $t_2 = 116.70$ ms and $t_3 = 344.47$ ms. The shock formation and propagation is similar to the one described in Sec 5.5.5 for a multi-stage

BH before the final collapse. The neutron star that results after a collapse always has higher compactnerss, as m/r peaks at 0.05 for t_1, 0.117 for t_2 and 0.145 for t_3. More negative β_0 values diminish the jumps in value of ρ_c and cause the collapse to happen faster, determining an almost smooth transition towards the next model, as we shall see in Sec. 5.6.

5.5.3 Prompt high-compactness NS

This represents the collapse scenario for highly negative β_0 values. Here the outcome does not depend sensitively on the progenitors, equation of state or other scalar parameters.

As an example, we present the collapse of a 39 $M_\odot$ with primordial metallicity and EOS1 and scalar parameters $\alpha_0 = 10^{-3}$, $\beta_0 = -20$ and $\mu = 10^{-14}$ eV: in the bottom row of Fig. 5.14 we plot the evolution of φ_c and ρ_c as well as the waveform extracted at $r_{\text{ex}} = 3 \times 10^4$ km. As we can see in the bottom right panel of the figure, this model generates a strong GW wave signal.

In Fig. 5.17 we plot snapshots of the density and scalar field profiles. After 87 ms, the centre of the star reaches supranuclear baryon density, causing the equation of state to stiffen. At $t_b = 87.4$ we notice the inner core bounces and the shock starts moving outwards, but quickly stalls. The central baryon density reaches $\sim 2 \times 10^{15}$ [cgs] and continues increasing, whereas φ_c reaches ~ -0.3 and continues decreasing throughout our simulation which lasted 4 s. At t_b the compactness m/r reaches 0.0629 at $\sim$ 8 km; the star seems to accrete more matter and after 4 s, the inner core of the NS is larger, and m/r now reaches 0.1325 at $\sim$ 40 km. We do not rule out that for such negative β_0 values the stars ultimately form a BH (or that the multi-stage

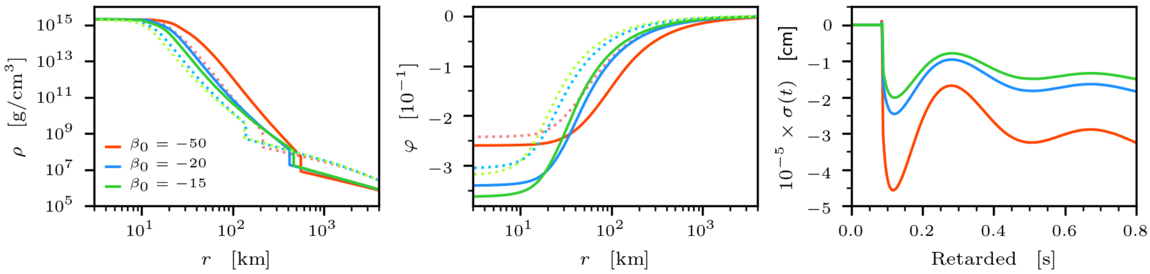

Fig. 5.18 Snapshots of the baryon density (left) and scalar field (centre) profiles during the simulation of prompt high-compactness NSs with varying β_0. The progenitor used is $z39$ with EOS1, the other scalar parameters are $\alpha_0 = 10^{-4}$ and $\mu = 10^{-14}$ eV and the profiles are from $t = 0.20$ s (dotted lines) and $t = 1.00$ s (full lines). In the right panel we plot the waveforms extracted at $r_{\text{ex}} = 3 \times 10^4$ km.

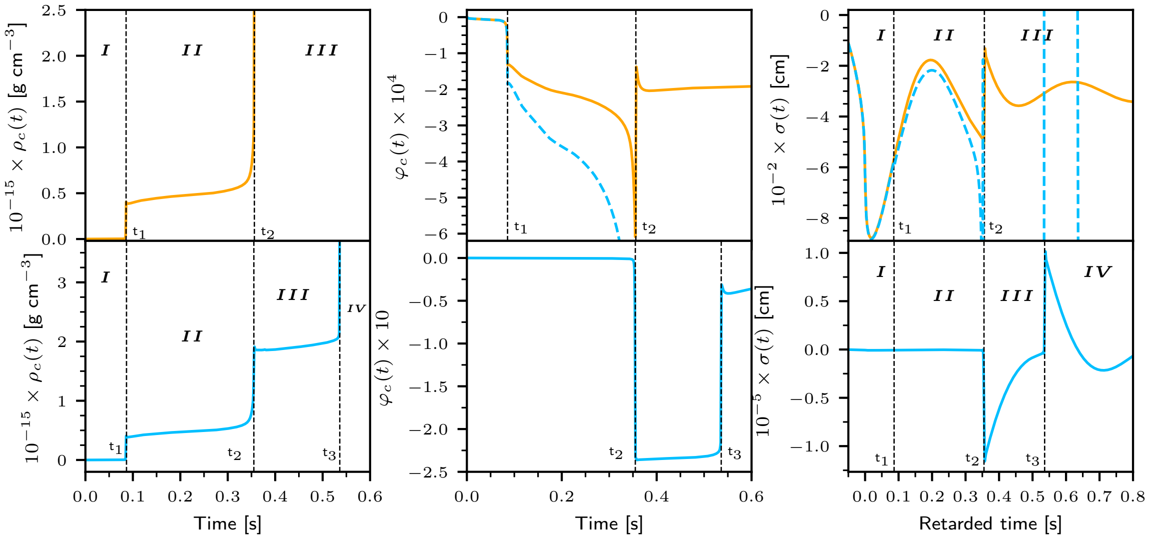

Fig. 5.19 Central baryon evolution (left column), central scalar field evolution (middle column) and waveform extracted at $r_{\mathrm{ex}} = 3 \times 10^4$ km (right column) as functions of time for the collapse of $u39$ with EOS1, $\alpha_0 = 10^{-3}$, $\mu = 10^{-14}$ and $\beta_0 = -2$ (orange) and $\beta_0 = -5$ (blue). The latter case was plotted in the upper panels as well, but with a doashed blue line; t_1 and t_2 coincide for the two cases.

NS scenario leads to a BH), but none of our simulations resulted in such an outcome. We have continued some runs for up to 20 s without seeing BH formation. But by that time numerical noise may have accumulated so that these runs need to be viewed with caution. For $\beta_0 = -50$, we obtain GW signals twice as strong than those for $\beta_0 = -20$, but the central scalar field amplitude φ_c decreases. We plot an example in Fig. 5.18: we compare three simulations with $\beta_0 = -15$ (green), -20 (blue) and -50 (red). For$\beta_0 = -15$, $|\varphi_c|$ peaks at 0.36, whereas for $\beta_0 = -50$ $|\varphi_c|$ peaks at 0.25. The compactness after $t = 1.0$ s attains values of 0.135 for $\beta_0 = -15$ and 0.057 for $\beta_0 = -50$. These results suggest that for more negative β_0 the stars become more massive (as infered from the baryon density profiles); the amplitude of the scalar field at a fixed point decreases, but, due to the larger volume over which $\varphi = O(0.1)$, the stars become *more scalarized* and the scalar GW is stronger.

5.5.4 2-stage BH

Similarly to the prompt low-compactness NS formation, this case occurs for less negative β_0 values and for equations of state and progenitors that collapse to a BH in GR. This case also includes the WH40 simulation studied in Ref. [46]. As an example, we present the collapse of $u39$ with EOS1 and scalar parameters $\alpha_0 = 10^{-3}$, $\beta_0 = -2$ and

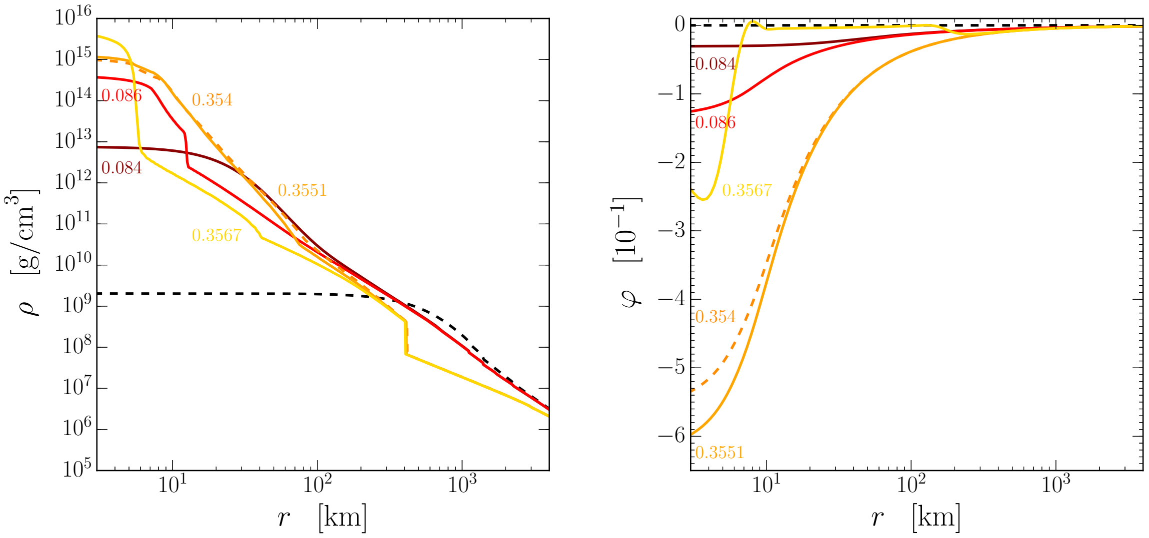

Fig. 5.20 Snapshots of the baryon density (left) and scalar field (right) profiles during the simulation of a 2-stage BH. The progenitor used is $u39$ with EOS1 and the scalar parameters are $\alpha_0 = 10^{-3}$, $\beta_0 = -2$ and $\mu = 10^{-14}$ eV. The dotted black line respresents the initial profile.

$\mu = 10^{-14}$ eV. In the top row of Fig. 5.19 we plot the evolution of φ_c and ρ_c as well as the waveform extracted at $r_{\mathrm{ex}} = 3 \times 10^4$ km (the $\beta_0 = -2$ case represents the orange line, the blue line from all panels is for $\beta_0 = -5$ which will be discussed in the next section). We can see in the top right panel of Fig. 5.19 the by now familiar spurious transient (zone $\boldsymbol{I}$) where φ_c reaches the value -5.6×10^{-5}. After $t_1 \sim 86$ ms from the beginning of the simulation the central density increases to values larger than ρ_{nuc}, the EOS stiffens which leads to the inner core bouncing. A proto-NS of compactness $m/r \sim 0.0516$ has formed, ρ_c peaks at 4.08×10^{14} [cgs], falls back to 3.86×10^{14} [cgs] after which it continues mildly increasing due to accretion. The central scalar field value drops to -1.32×10^{-4} and reflects the behaviour of ρ_c.

In Fig. 5.20 we plot snapshots of the density and scalar field profiles. After the first collapse phase, the shock starts travelling towards the surface of the star. It stalls due to nuclei dissociation which leads to a drop in thermal pressure behind the shock and comes to a halt at around 400 km before moving backwards at $t \sim 0.32$ s. At $t_2 = 0.36$ s after the start of the simulation, the lapse function ν has dropped to 10^{-8} and, just after, $|\varphi_c|$ has peaked at 6.1×10^{-4} before increasing towards 0. Because of the collapse of the lapse function we stopped the matter evolution, which leads to the star only partially descalarizing, as we can see in the upper middle panel of Fig. 5.19, where φ_c

settles around 2×10^{-4}. The compactness m/r peaks at the value 0.49, confirming that the simulation has approached a BH.

At $t \approx t_2$, the scalar field gradient rapidly grows, resulting in a peak value of $|\varphi_c|$, after which it decreases because of the descalarization as a BH is forming. In some cases we have seen that the descalarization leads to a stronger signal than the preceding scalarization of the NS. We believe this is the case when the descalarization occurs particularly abruptly leading to a stronger presence of high frequency modes. Whether or not this feature occurs depends on the details of the progenitor models and scalar parameters.

As we vary β_0 we noticed that the scalar field reaches larger amplitudes for more negative β_0 as shown in Fig. 5.21. At some threshold value, $\beta_0 = -3.75$ in the figure, we observe a brief phase where a highly compact NS is formed. For $\beta_0 = -3.75$ this is quickly followed by BH formation. For yet more negative β_0, this phase becomes more long lived and leads to the multi-stage BH formation discussed in the next section.

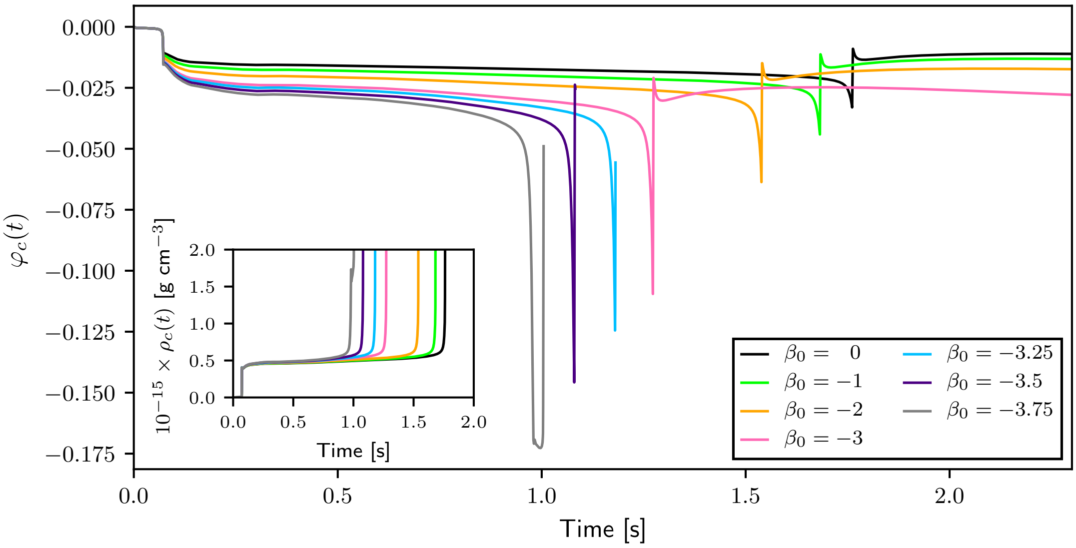

Fig. 5.21 Evolution in time of the central scalar field φ for different values of β_0. The progenitor used is $s39$ with EOS1 and the other scalar parameters are $\alpha_0 = 0.1$ and $\mu = 10^{-14}$ eV. The behaviour of the corresponding central baryon density value is plotted in the bottom left inset. Note that for $\beta_0 = -3.75$ the star does not immediately form a BH but briefly resides in the stage of a highly compact NS. This signals the onset of a third stage in the evolution of the compact core.

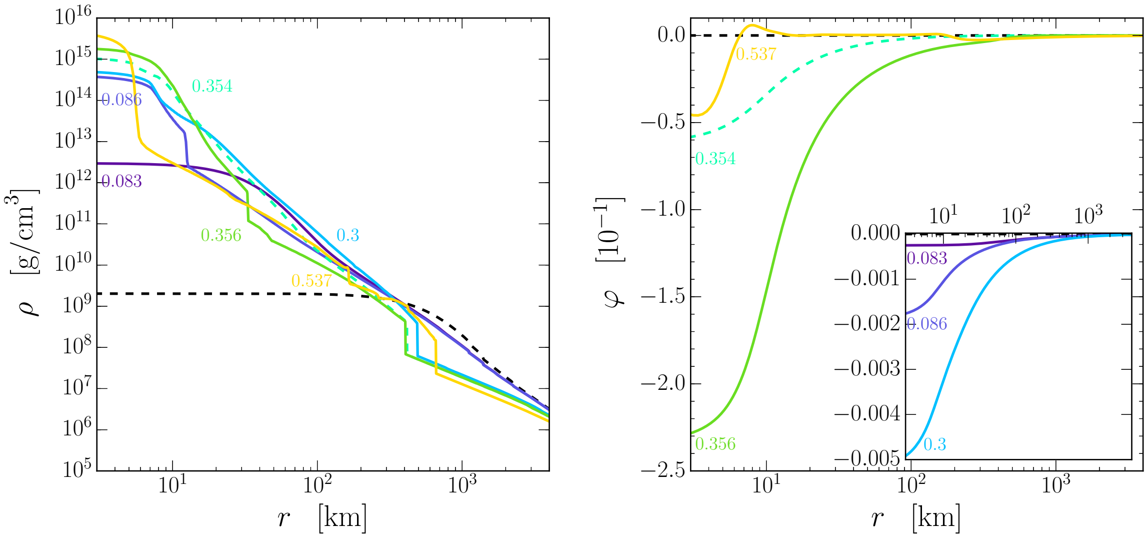

Fig. 5.22 Snapshots of the baryon density (left) and scalar field (right) profiles during the simulation of a multi-stage BH. The progenitor used is $u39$ with EOS1 and the scalar parameters are $\alpha_0 = 10^{-3}$, $\beta_0 = -5$ and $\mu = 10^{-14}$ eV. The dotted black line respresents the initial profile.

5.5.5 Multi-stage BH

As we have seen in the previous section, moderate values of β_0, lead to additional intermediate NS stages before the collapse to a BH.

As an example of such a multi-stage BH formation, we present the collapse of the same progenitor model as before, using again EOS1 and $\alpha_0 = 10^{-3}$. The only difference is that now $\beta_0 = -5$. In the bottom row of Fig. 5.19 we plot the evolutions of φ_c and ρ_c as well as the waveform extracted at $r_{\text{ex}} = 3 \times 10^4$ km. Note the descalarization at $t = t_3$ and the corresponding more complex wave signal. In Fig. 5.19 we see that the first and second collapse for the two models happen at the same time, but, for $\beta_0 = -5$, instead of forming a BH, the second collapse phase leads to a more compact neutron star.

In Fig. 5.22 we plot snapshots of the density and scalar field profiles. We observe in Fig. 5.22 the first bounce at $t_1 = 86.6$ ms, at which point φ_c attains the value -1.83×10^{-4}, m/r peaks at 0.0483 and $\rho_c = 3.9 \times 10^{14}$ [cgs]. The shock moves outwards, but stalls after ~ 300 ms and we see it going backwards towards the stellar centre. At $t_2 = 355$ ms we observe a second shock which also moves outwards and "meets" the first shock which results in a small pulse moving towards the center; this accounts for the slight jump in ρ_c after the collapse at $t = 377$ ms. The resulting star is strongly scalarized with $\varphi_c \approx -0.2361$), $\rho_c \sim 10^{15}$ [cgs] and compactness $m/r = 0.208$. At

$t = 537$ ms the lapse function drops to 1.1×10^{-5}, m/r reaches 0.4945 (measured at ~ 5.6 km) and the star descalarizes as it forms a BH. At this point we freeze the matter evolution and φ_c stays around ~ -0.03.

5.6 Systematic dependence on the equation of state

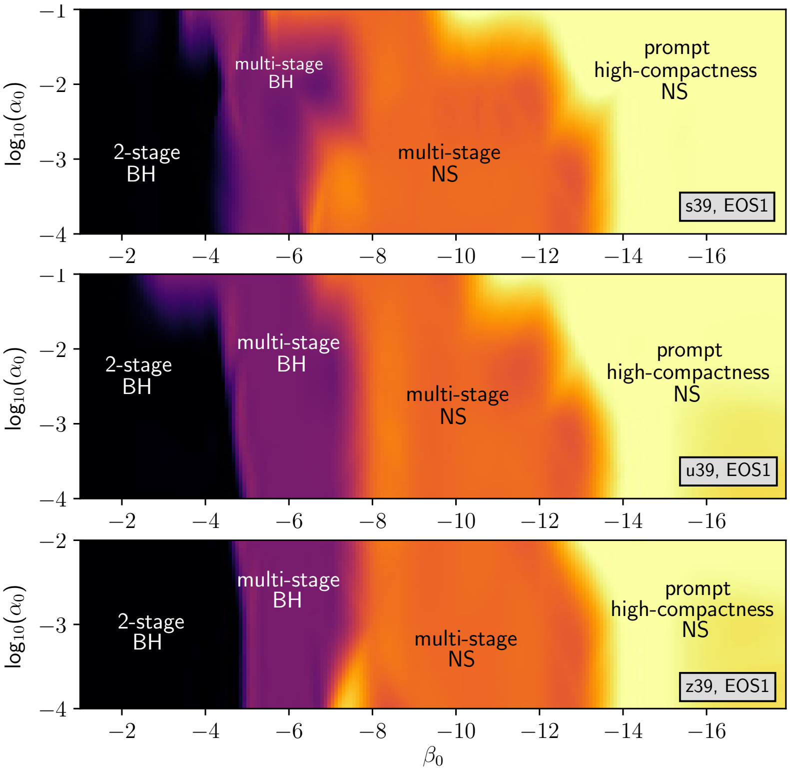

Fig. 5.23 Distribution of the collapse scenarios described in Sec. 5.5 for a 39 solar mass progenitor with EOS1 and solar (top), 10^{-4} solar (centre) and primordial (bottom) metallicity. The color coding is as follows: black (2-stage BH), purple (multi-stage BH), orange (multi-stage NS) and yellow (prompt high-compactness NS).

In this section we present the distribution of the various scenarios for equations of state EOS1 and EOS3 and all the 39 $M_\odot$ progenitor models, $s39$, $u39$, $z39$. We choose these particular models as initial data because they span all possible scenarios. We have documented the classification for each case in Appendix B.2 which we have used to build 2D maps of the distribution in Figs. 5.23 and 5.26. As before, we have employed the Python scipy.interpolate.griddata function with cubic spline for the interpolation. Since the progenitors for the primordial metallicity case and 10^{-4} case have similar baryon density profiles (see Fig. 5.1), the results for the two are very similar.

Throughout this section we refer to t_n as the collapse moment that marks the start of the n^{th} jump in ρ_c.

5.6.1 EOS1

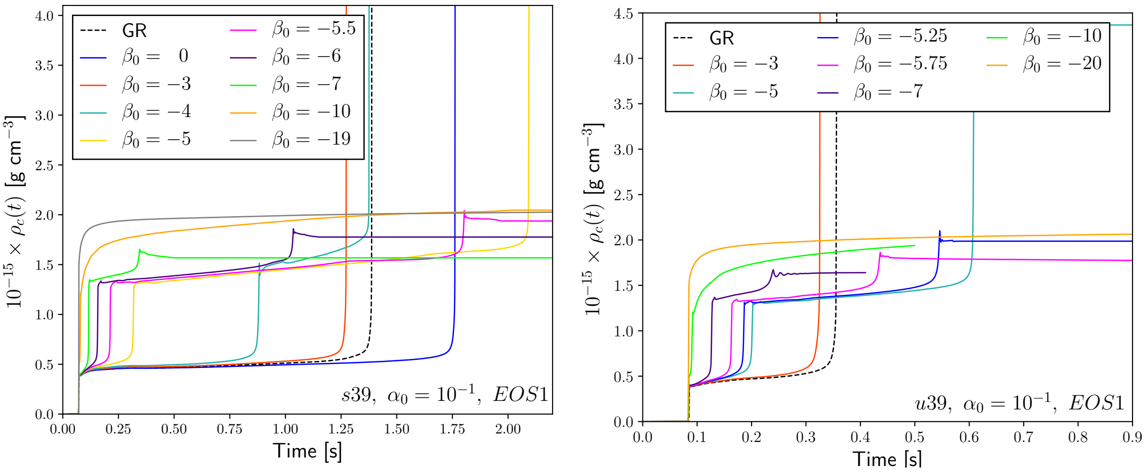

Fig. 5.24 Evolution in time of the central baryon density in GR (black dashed line) and in massive ST theory for different values of β_0 (solid lines). The progenitor used is $s39$ (left) and $u39$ (right) with EOS1 and the other scalar parameters are $\alpha_0 = 10^{-1}$ and $\mu = 10^{-14}$ eV.

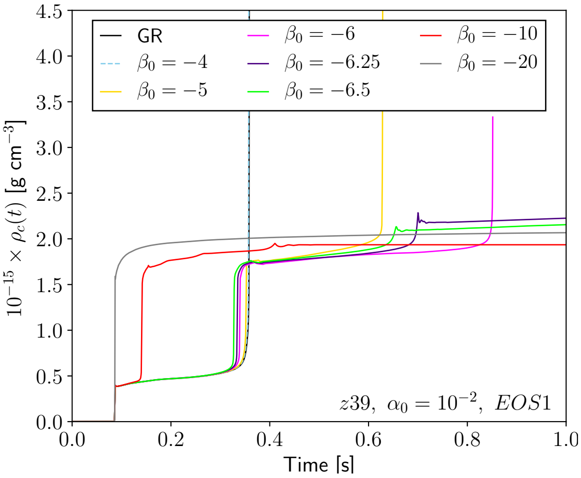

Fig. 5.25 Evolution in time of the central baryon density in GR (black line) and in massive ST theory for different values of β_0. The progenitor used is $z39$ with EOS1 and the other scalar parameters are $\alpha_0 = 10^{-2}$ and $\mu = 10^{-14}$ eV.

In this section we study the behaviour of stars with EOS1. To illustrate the general behaviour, we choose three cases: $s39$ and $\alpha_0 = 10^{-1}$ (Fig. 5.24), $u39$ and $\alpha_0 = 10^{-1}$

(Fig. 5.24) and $z39$ and $\alpha_0 = 10^{-2}$ (Fig. 5.25). We chose these three models because the jumps in ρ_c for the multi-stage NS scenario are particularly large. We plot the time evolution of ρ_c for β_0 values ranging from 0 to -20 in each case and we include the GR case (black line) for reference. We summarize the results as follows:

- As mentioned earlier, for weakly negative β_0 values the collapse proceeds similar to GR, in this case 2-stage BH formation. All models reach supranuclear densities at similar times (after ~ 73 ms for $s39$ and ~ 85 ms for $u39$ and $z39$) and ρ_c settles down to similar values around 4×10^{14} [cgs]. In addition, we notice for all metalicities that for $\alpha_0 \leq 10^{-2}$, the second collapse to a BH happens almost at the same time as in GR. This can be noticed in Fig. 5.25 where $\alpha_0 = 10^{-2}$: all cases with $\beta_0 \geq -4.75$ collapse to a BH after ~ 350 ms as opposed to the $\alpha_0 = 0.1$ case (top panels of Fig. 5.24), the time of BH formation varies mildly with β_0.

- When $\alpha_0 \lesssim 10^{-2}$, we encounter multi-stage BHs with three or more stages starting for $\beta_0 \lesssim -5$. For $\alpha_0 \sim 10^{-1}$ this happens for $\beta_0 \lesssim -3.5$. The collapse moment to a strongly scalarized NS (labelled as t_2 in the previous section) occurs earlier as we decrease β_0, but ρ_c always settles down to a similar value of order 10^{15} [cgs].

- For more negative β_0, the scalarization appears to obstruct the collapse to a BH and our simulations lead to finite densities $O(10^{15})$ [cgs], possibly following more than two jumps, but the magnitude of the jumps in ρ_c become smaller. The boundary between this set of models and the multi-stage BH one cannot be fully resolved in the β_0 space.

- For $\beta_0 \in [-14, -12]$ we started seeing prompt high-compactness NSs (for $\alpha_0 \leq 10^{-2}$). For $\alpha_0 = 10^{-1}$ this happens earlier.

In summary, as β_0 decreases from 0, we always have four scenarios in the same order: 2-stage BH, multi-stage BH, multi-stage NS, prompt high-compactness NS, with the β_0 transition boundaries varying mildly with α_0. The small oscillations seen in ρ_c, in particular after the third collapse (for example, for $\beta_0 = -7$ in the right panel of Fig. 5.24) were noticed by the authors of [43] who argue that they are specific to a star transitioning to a strongly scalarized state [42].

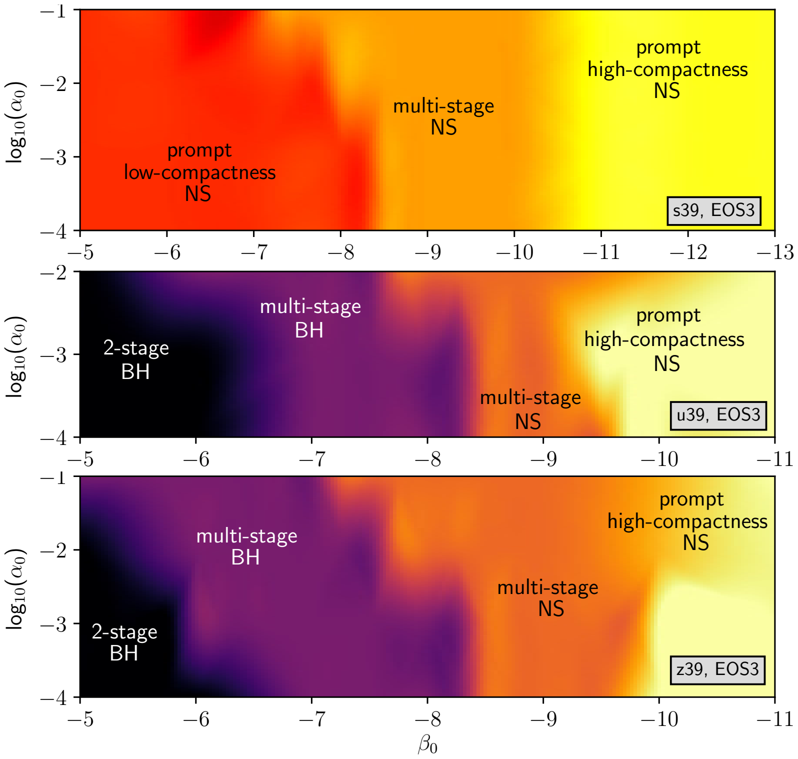

Fig. 5.26 Distribution of the collapse scenarios described in Sec. 5.5 for a 39 solar mass progenitor with EOS3 and solar (top), 10^{-4} solar (centre) and primordial (bottom) metallicity. The color coding is as follows: black (2-stage BH), purple (multi-stage BH), orange (multi-stage NS), yellow (prompt high-compactness NS) and red (prompt low-compactness NS).

5.6.2 EOS3

In this section we study the behaviour of stars with EOS3. To illustrate the general behaviour, we choose six cases: $s39$ and $\alpha_0 = 10^{-2}$, 10^{-4} (Fig. 5.27), $u39$ and $\alpha_0 = 10^{-2}$, $\alpha_0 = 10^{-4}$ (Fig. 5.28) and $z39$ and $\alpha_0 = 10^{-1}$, $\alpha_0 = 10^{-3}$ (Fig. 5.29). We plot the time evolution of ρ_c for β_0 values ranging from 0 to -20 in each case and we include the GR case (black line) for reference. We discuss the the results from progenitor $s39$ separately.

Progenitor $s39$

As noticed in Sec. 5.2.2, in GR this progenitor leads to the formation of a neutron star. The distribution of the different collapse scenarios is straightforward: for $\beta_0 \gtrsim -8.5$ we obtained prompt low-compactness NSs; for $\beta_0 \lesssim -10$ we obtain prompt high-compactness NSs, and in between there is a regime of multi-stage NSs. We plot the evolution of ρ_c for $\alpha_0 = 10^{-2}$, 10^{-4} and various β_0 in Fig. 5.27. All stars undergo

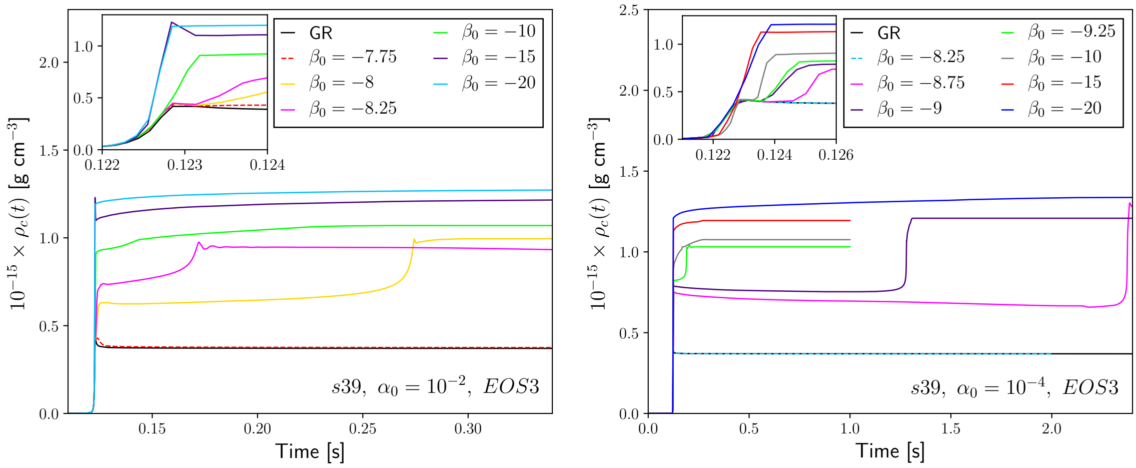

Fig. 5.27 Evolution in time of the central baryon density in GR (black line) and in massive ST theory for different values of β_0. The progenitor used is $s39$ with EOS3 and the other scalar parameters are $\mu = 10^{-14}$ eV, $\alpha_0 = 10^{-2}$ (left) and $\alpha_0 = 10^{-4}$ (right).

a first collapse at $t \sim 122$ ms. For prompt low-compactness NS, ρ_c settles down to $\sim 4 \times 10^{14}$ [cgs]. We can see in the top left insets of the plots that the more compact NSs actually undergo two collapse stages in rapid succession. Similarly to the models using EOS1, for more negative β_0 values the second jump in ρ_c becomes smaller and occurs sooner.

Progenitors $u39$ *and* $z39$

In GR these progenitors lead to a BH and their collapse scenario when varying β_0 is similar to that observed for EOS1, though the intervals in β_0 for each category are different. The range for which a BH is reached after several stages is smaller; the same applies to the multi-stage NS case. Several models with $\beta_0 \in [-8, -7]$ developed considerable numerical noise and could not be continued. We did not classify these cases which limits the resolution of the interpolation in the bottom two heatmaps in Fig. 5.26.

5.6.3 EOSa

None of our simulations for this equation of state has led to BH formation. Our study of the α_0, β_0 parameter space for 39 $M_\odot$ progenitors leads to similar conclusions (irrespective of metallicity) to the case of $s39$ with EOS3: prompt low-compactness NSs for large β_0 and high-compactness NSs for very negative β_0.

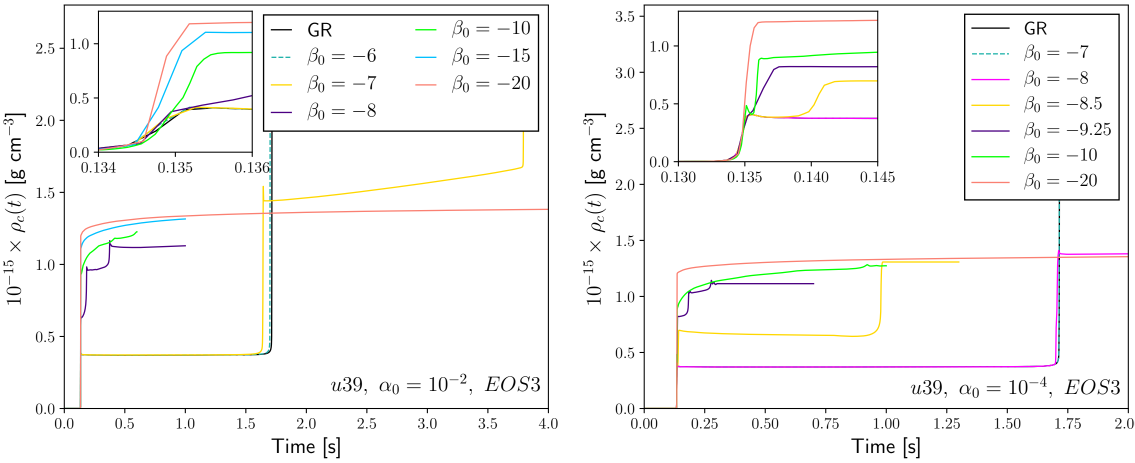

Fig. 5.28 Same as Fig. 5.27 for progenitor $z39$, EOS3 with $\alpha_0 = 10^{-2}$ (left) and $\alpha_0 = 10^{-4}$ (right).

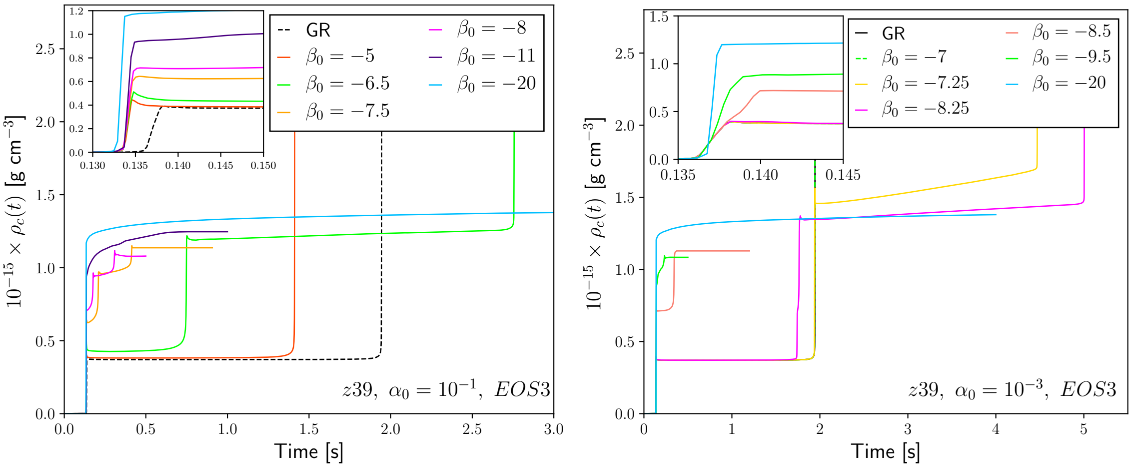

Fig. 5.29 Same as Fig. 5.27 for progenitor $z39$, EOS3 with $\alpha_0 = 10^{-1}$ (left) and $\alpha_0 = 10^{-3}$ (right).

5.7 Approximate universality under changes of the scalar mass

So far we have considered only simulations with scalar mass $\mu = 10^{-14}$ eV. In this section we discuss the impact of the scalar mass μ on the waveforms.

5.7.1 Theoretical considerations

The asymptotic behaviour of the wave signal under its dispersive propagation is determined by Eq. (3.92) for the frequency and Eq. (3.96) for the amplitude of the signal. The dependence of the propagated signal on the scalar mass μ and its associated frequency ω_* becomes clearer if we rewrite the solution in terms of dimensionless quantities. For this purpose, we define the rescaled frequency, radius and time by

$$\begin{aligned}\bar{\Omega} &= \frac{\Omega}{\omega_*}\,, & \bar{r}_{\rm ex} &= \omega_* r_{\rm ex}\,, \\ \bar{t} &= \omega_* t\,, & \bar{r} &= \omega_* r\,. \end{aligned} \tag{5.2}$$

With this notation, we can rewrite Eqs. (3.92), (3.97), (3.96) as

$$\begin{aligned}\bar{\Omega}(\bar{t},\bar{r}) &= \frac{1}{\sqrt{1-\frac{(\bar{r}-\bar{r}_{\rm ex})^2}{\bar{t}^2}}}\,, \\ \phi(\bar{t},\bar{r}) &= \sqrt{\bar{\Omega}^2-1}(\bar{r}-\bar{r}_{\rm ex}) - \bar{\Omega}\bar{t} - \frac{\pi}{4} + {\rm Arg}[\tilde{\sigma}(\Omega;r_{\rm ex})]\,, \\ A(\bar{t},\bar{r}) &= \sqrt{\frac{2}{\pi}}\frac{\omega_*(\bar{\Omega}^2-1)^{3/4}}{(\bar{r}-\bar{r}_{\rm ex})^{1/2}}{\rm Abs}[\tilde{\sigma}(\Omega;r_{\rm ex})]\,. \end{aligned} \tag{5.3}$$

We have thus been able to absorb much of the dependence on the scalar mass in terms of a simple rescaling of radius, time and frequency. But two issues remain: (i) a factor of ω_* is present in the amplitude $A(\bar{t},\bar{r})$ and (ii) the phase and amplitude implicitly depend on the scalar mass through the phase and amplitude of the Fourier transform $\tilde{\sigma}(\Omega, r_{\rm ex})$. Further progress requires information about the signal at $r_{\rm ex}$. More specifically, we can exploit two features that we find to be satisfied approximately in the generation of scalar radiation in stellar collapse in ST theory.

The first observation is that the scalar field at the centre of the star evolves largely independently of the scalar mass. Likewise, the scalar profile $\varphi(r)$ at late stages in the evolution is independent of the scalar mass (always assuming that the other parameters of the configuration are held fixed). This suggests that in the region of wave generation $\sigma(t,r)$ [rather than $\sigma(\bar{t},\bar{r})$] is approximately independent of the scalar mass. Let us take this as a working hypothesis and compute its implications.

From the definition of the Fourier transform we obtain

$$\begin{aligned}\tilde{\sigma}(\Omega;r_{\rm ex}) &= \int_{-\infty}^{\infty}\sigma(t;r_{\rm ex})e^{i\Omega t}dt \\ &= \frac{1}{\omega_*}\int_{-\infty}^{\infty}\sigma(\bar{t}/\omega_*;r_{\rm ex})e^{i\bar{\Omega}\bar{t}}d\bar{t}\,. \end{aligned} \tag{5.4}$$

Now we employ the second empirical observation. Near the star, the dynamics in the scalar field are dominated by the sudden transition from weak (or zero) to strong scalarization. The time dependence of the scalar field at a given radius is therefore approximated by a Heaviside function, $\sigma(t, r_{\rm ex}) \sim f(r_{\rm ex})H(t)$. The Heaviside function satisfies $H(t) = H(at)$ for $a = \text{const} \in \mathbb{R}$ and we can use $\sigma(\bar{t}/\omega_*; r_{\rm ex}) = \sigma(\bar{t}; r_{\rm ex})$ in Eq. (5.4), so that

$$\tilde{\sigma}(\Omega; r_{\rm ex}) = \frac{1}{\omega_*}\int_{-\infty}^{\infty} \sigma(\bar{t}; r_{\rm ex})e^{i\bar{\Omega}\bar{t}}d\bar{t} = \frac{1}{\omega_*}\tilde{\sigma}(\bar{\Omega}; r_{\rm ex})\,. \tag{5.5}$$

We thus acquire a factor $1/\omega_*$ in the amplitude of $\tilde{\sigma}(\Omega; r_{\rm ex})$ and no change in its phase and Eqs. (5.3) become

$$\begin{aligned}
\bar{\Omega}(\bar{t}, \bar{r}) &= \frac{1}{\sqrt{1 - \frac{(\bar{r}-\bar{r}_{\rm ex})^2}{\bar{t}^2}}}\,, \\
\phi(\bar{t}, \bar{r}) &= \sqrt{\bar{\Omega}^2 - 1}(\bar{r} - \bar{r}_{\rm ex}) - \bar{\Omega}\bar{t} - \frac{\pi}{4} + \mathrm{Arg}[\tilde{\sigma}(\bar{\Omega}; r_{\rm ex})]\,, \\
A(\bar{t}, \bar{r}) &= \sqrt{\frac{2}{\pi}\frac{(\bar{\Omega}^2 - 1)^{3/4}}{(\bar{r} - \bar{r}_{\rm ex})^{1/2}}}\mathrm{Abs}[\tilde{\sigma}(\bar{\Omega}; r_{\rm ex})]\,.
\end{aligned} \tag{5.6}$$

This gives us a universal expression for the wave signal which depends on the scalar mass ω_* only through the rescaling of time, radius and frequency according to Eq. (5.2). In other words, if we know the signal $[\Omega(t, r),\ \phi(t, r),\ A(t, r)]$ for a configuration with mass parameter $\omega_{*,1}$, we obtain the signal for the same configuration in ST theory with $\omega_{*,2}$ by replacing $t \to \lambda t$, $r \to \lambda r$, $\Omega \to \Omega/\lambda$, $(\phi, A) \to (\phi, A)$ with $\lambda = \omega_{*,1}/\omega_{*,2}$.

5.7.2 Results

The universality under changes in the scalar mass ω_* will only hold **approximately** for a number of reasons. (i) At least at small radii, the wave propagation will be governed by the field equations (3.31)-(3.33) rather than the Klein-Gordon equation underlying the calculations of this section. (ii) The time dependence of the scalar field near the source is only approximately of Heaviside shape. (iii) Especially for large scalar mass parameters, we expect the function $\sigma(t, r)$ no longer to be independent of the value ω_* as the Compton wavelength approaches the size of the stellar core. For example, a Compton wavelength $\lambda_{\rm c} < 1\,000$ km corresponds to a scalar mass $\mu > 1.97 \times 10^{-13}$ eV and frequency $\omega_* > 300\ {\rm s}^{-1}$. (Note that such large values of the scalar mass are no longer ideal for tests with GW observations as the contributions relevant for LIGO-Virgo partially fall inside the exponentially suppressed regime $\omega < \omega_*$).

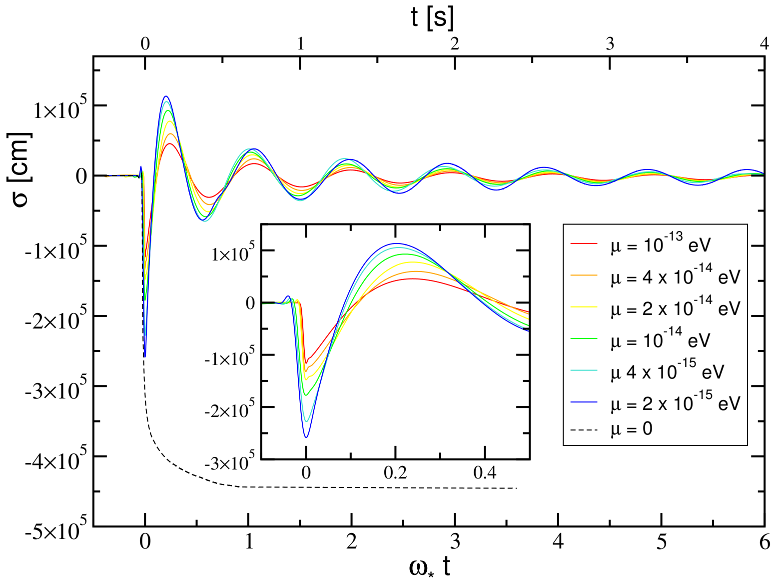

Fig. 5.30 GW signal $\sigma(t, r_{\rm ex})$ extracted from the collapse of $s12$ progenitor model with EOS5 at $\omega_* r_{\rm ex} = 5.07$ for different values of the scalar mass $\mu \in [2 \times 10^{-15}\ {\rm eV},\ 10^{-13}\ {\rm eV}]$. The overall amplitude increases monotonically with decreasing μ. For reference, we also show the wave signal obtained for $\mu = 0$ (dashed curve). In this case, we cannot rescale the time with ω_*; and instead measure time in seconds as labeled on the upper horizontal axis.

So how well is the universality predicted by Eqs. (5.6) satisfied in practice? To address this question we have numerically explored a range of configurations. For each of these, we have fixed α_0, β_0, the EOS and the progenitor model and then performed a one-parameter study varying μ in the range $2 \times 10^{-15}\ {\rm eV} \le \mu \le 10^{-13}\ {\rm eV}$. All of these cases exhibit the characteristic behaviour we illustrate in Figs. 5.30 and 5.31.

The wave amplitude σ in Fig. 5.30 has been extracted from the core collapse simulations at rescaled extraction radius $\bar{r}_{\rm ex} = 5.07 = (\mu/10^{-14}\ {\rm eV})^{-1} \times 10^5$ km. We have shifted the signals in time such that their peaks align at $\bar{t} = 0$. The main difference of the signals is a monotonic drop in amplitude as μ increases; the strongest signal (for $\mu = 2 \times 10^{-15}$ eV) exceeds the weakest one (for $\mu = 10^{-13}$ eV) by a factor of about 2.5. For scalar mass values $\mu < 2 \times 10^{-15}$ eV, simulations over several wave cycles become prohibitively costly (recall that the corresponding physical time scales $\propto 1/\mu$). We have, however, performed short simulations up to the first strong peak in the signal. This peak, shifted to $\bar{t} = 0$ in Fig. 5.30, corresponds to the core bounce at $t = \mathcal{O}(0.1)$ s and can be computed in shorter simulations lasting up to about $t \approx r_{\rm ex}$. We find the monotonic trend in the amplitude to continue with an upper bound given by the limiting case $\mu = 0$. The wave signal $\sigma(t)$ resulting from this limit can no longer be

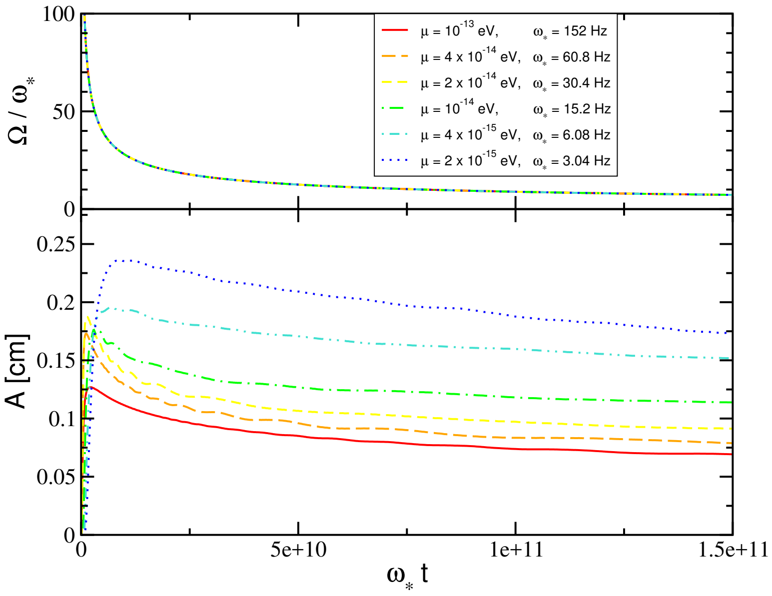

Fig. 5.31 The wave signals of Fig. 5.30 propagated according to Eqs. (3.92), (3.96) to $\omega_* r = 1.56 \times 10^{13} = (\mu/10^{-14}\,\text{eV})^{-1}$ 10 kpc. As expected, the curves for the rescaled frequency Ω/ω_* overlap in the upper panel. The amplitude in the lower panel shows a mild increase as we decrease the scalar mass μ.

rescaled according to Eq. (5.2) since $\omega_* = 0$; instead, we have included it in Fig. 5.30 (black dashed curve) as a function of physical time t denoted on the upper horizontal axis.

Amplitude and frequency of the corresponding waveforms propagated to $\omega_* r = 1.56 \times 10^{13} = (\mu/10^{-14}\,\text{eV})^{-1}$ 10 kpc are shown in Fig. 5.31. We find the same monotonic increase of the wave amplitude as μ decreases from 10^{-13} eV to 2×10^{-15} eV with, again, an overall factor of about 2.5 between the extreme cases. As expected from Eq. (5.6), the rescaled frequencies $\bar{\Omega}(\bar{r})$ agree exactly. We have explored in the same way other configurations differing from this case in the ST or EOS parameters or the mass of the stellar progenitor model. All cases show the same behaviour: the rescaled frequency is independent of the scalar mass μ when plotted as a function of rescaled time $\bar{t}$ whereas the amplitude shows a monotonic increase by an overall factor of about 1.5 to 3 as μ decreases from 2×10^{-15} eV to 10^{-13} eV.

Our result suggests an approximate universality of the wave signals when expressed in terms of rescaled frequency, time and radius $\bar{\Omega} = \Omega/\omega_*$, $\bar{t} = \omega_* t$, $\bar{r} = \omega_* r$. Whereas this result is rigorous (within the SPA) for the frequency, its validity for the amplitude has to be taken with a grain of salt; no matter how many configurations we test empirically, we can never exclude the possibility that configurations outside this test

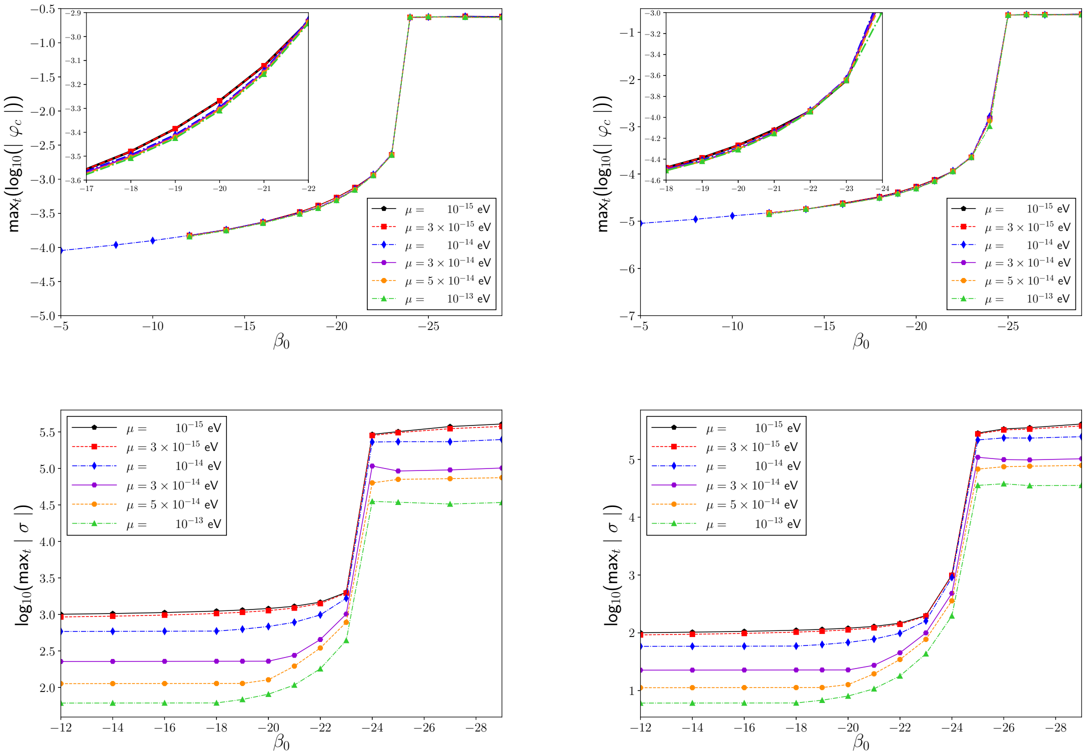

Fig. 5.32 Amplitudes of φ_c (top row) and σ (bottom row) for several β_0 and μ values. The simulations used $\alpha_0 = 10^{-3}$ (left panels) and $\alpha_0 = 10^{-4}$ (right panels). The progenitor used for these simulation was $s39$ with EOSa. The waveform amplitudes confirm the approximate scaling with the scalar mass μ for the entire tested β_0 range.

space depart from the observed pattern. Furthermore, the result for $\mu = 0$ in Fig. 5.30 indicates that for yet smaller masses, we may have to allow for an extra factor of a few in the amplitude scaling. A similar conclusion can be drawn when using a heavier progenitor and extracting at smaller radii; results for the collapse and rescaling of $u41$ with EOS1 are included in Appendix B.3 where we extract the signals at $\omega_* r_{\rm ex} = 0.91$ and $\omega_* r_{\rm ex} = 1.83$.

In summary, once we have computed a wave signal from a configuration for some value of μ, the signal for the (otherwise) identical configuration with a different scalar mass $\hat{\mu}$ can be obtained by a linear rescaling of the argument and result of the frequency $\Omega(t)$ while an approximate estimate of the amplitude $A(t)$ can be obtained by a rescaling of the time (but not of A). The frequency scaling is exact within the SPA whereas the amplitude scaling is approximate to within a factor of a few.

As a further check we have explored whether the onset of strong scalarization as shown in the heat maps in Figs. 5.10, 5.11, 5.12 depends on the scalar mass μ. The

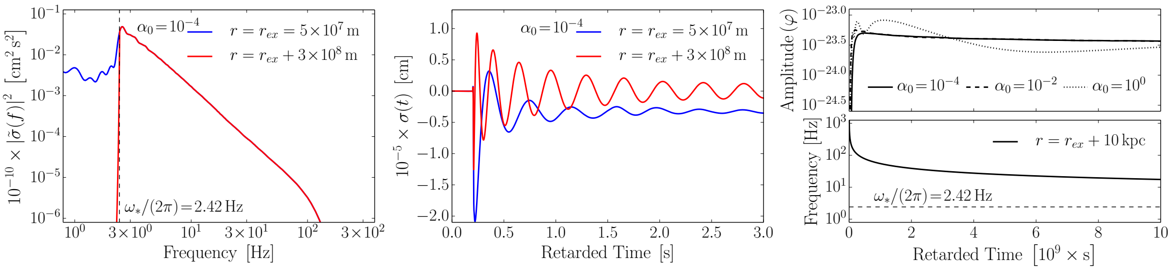

Fig. 5.33 *Left panel:* The frequency-domain power spectrum of the scalar field $\sigma \equiv r\varphi$ at the extraction sphere and 1 light second further out; the exponential decay of frequencies $f < \omega_*/(2\pi)$ can be clearly seen. This simulation was performed for a $s12$ with $\mu = 10^{-14}$ eV, $\alpha_0 = 10^{-4}$, and $\beta_0 = -20$. *Center panel:* The time-domain scalar field profiles for the two curves shown in the left panel; during the 1 s of propagation the signal becomes increasingly oscillatory, and the long-lived memory effect is exponentially suppressed. *Right panels:* The amplitude (top) and frequency (bottom) as functions of time for the scalar field φ from the same simulation as the other panels but at a distance of 10 kpc (it is not practical to plot the long, highly oscillatory time-domain signals at large distances). Also shown by the dotted and dashed curves are the amplitude profiles from other simulations using $\alpha_0 = 10^{-2}$ and $\alpha_0 = 10^0$; the amplitude of the scalar field depends relatively weakly on α_0. For the simulations shown here, the energy radiated in scalar GWs is $\sim 10^{-3}\, M_\odot$.

answer is *no* for all configurations we have tested (see Fig. 5.32); while the degree of strong scalarization mildly weakens for larger μ, the transition occurs at the same β_0 independent of the value of μ. Again, we cannot exclude the possibility of exceptions from this rule outside our test space.

5.8 LIGO detections

5.8.1 Classification

GW signals from stellar collapse in ST theory may show up in several ways in existing LIGO-Virgo searches. In each case there is, in principle, a *smoking gun* which allows the signal to be distinguished from other types of sources. Here, it is argued that a new dedicated program to search for ST core collapse signals is not needed; however, the results of this work should be kept in mind in analyzing results from existing searches.

Monochromatic searches – The highly dispersed signal [described by Eq. (3.96), see right panels in Fig. 5.33] at large distances can last for many years and is nearly monochromatic on time scales of $\lesssim 1$ month. Quasimonochromatic GWs with slowly evolving frequency may also be generated by rapidly rotating nonaxisymmetric neutron stars; the scalar signals described in this Chapter can be distinguished from neutron stars by the scalar polarization content and the highly characteristic frequency evolution described in Eq. (3.92).

These signals may be detected by existing monochromatic searches and allow for the determination of the scalar mass from the frequency change $\dot{f}$. The signals may show up in *all-sky* searches; however, greater sensitivities can be achieved via *directed* searches at known nearby supernovae (all-sky searches achieved sensitivities that constrain $h \lesssim 9.7 \times 10^{-25}$ [95], whereas model-based, directed searches at a supernova remnant have achieved sensitivities of $h \lesssim 2.3 \times 10^{-25}$ [96] at frequencies $\sim 150\,\mathrm{Hz}$). Methods to detect signals of any polarization content have been presented in Ref. [97]; note that interferometers are a factor ~ 2 less sensitive to scalar than tensor GWs. A directed search should begin within a few months to years of the supernova observation and may last for decades with sensitivity improving as time$^{-1/2}$ (see the amplitude as a function of time in Fig. 5.33). In fact, the amplitude can remain at detectable levels for so long that directed searches aimed at historical nearby supernovae (e.g. SN1987A[2]) may be worthwhile; a nondetection from such a search can place the most stringent constraints to date on certain regions of the massive ST parameter space, (μ, α_0, β_0).

In any monochromatic search there would be two smoking gun features indicating an origin of hyperscalarized core collapse in massive ST theory: the scalar polarization content, and the long signal duration with gradual frequency evolution according to Eq. 3.92. Our simulations suggest that the intrinsic amplitude of the scalar field is insensitive to α_0, β_0, and μ over wide parameter ranges. However, the GW strain scales linearly with the coupling; $h \propto \alpha_0 \varphi$. Extrapolating the results in Fig. 5.33 suggests that if a supernova at 10 kpc were to be observed and followed up by a directed monochromatic search by aLIGO at design sensitivity, the coupling could be constrained to $\alpha_0 \lesssim 3 \times 10^{-4}$ (assuming no signal was in fact observed) which compares favorably with the impressive Cassini bound in the massless case [52].

Stochastic searches – As shown above, stellar core collapse in massive ST theory can generate large amplitude signals, allowing them to be detected at greater distances. However, the signals propagate dispersively, spreading out in time and developing a sharp spectral cutoff at the frequency of the scalar mass. The long duration signals from distant sources can overlap to form a stochastic background of scalar GWs with a characteristic spectral shape around this frequency.

Burst searches – If the scalar field is light ($\mu \lesssim 10^{-20}$eV) then signals originating within the galaxy will not be significantly dispersed [e.g. the spread in arrival times across the

---

[2] For $\mu = 10^{-14}\,\mathrm{eV}$, for example, we obtain for SN1987A a frequency $\Omega/(2\pi) \approx 128\,\mathrm{Hz}$ and rate of change $\dot{\Omega}/(2\pi) \approx 2\,\mathrm{Hz/yr}$, using distance $D := r - r_{\mathrm{ex}} = 51.2\,\mathrm{kpc}$ and time $t - D = 30\,\mathrm{yr}$.

LIGO bandwidth, $(10-10^3)\,\mathrm{Hz}$, for a source at $10\,\mathrm{kpc}$ is $\lesssim 1\,\mathrm{s}$]. These short-duration, burstlike scalar GW signals may be detected using strategies similar to those used to search for standard core collapse supernovae in GR. However, for these light scalar fields the observational constraints on the coupling constants α_0 and β_0 rule out the hyperscalarized signals shown in Fig. 5.9 and the amplitudes are similar to those reported in Ref. [46].

5.8.2 Potential scalar waveforms observations

Any GW detector, small compared to the GW wavelength $\lambda = 1/f$, measures the *electric* components of the Riemann tensor R_{0i0j} [5]. The symmetries of the tensor suggest 6 independent components which are related to the 6 components of the spatial metric tensor. A gravitational wave propagating in the z-direction can be expressed in terms of 6 possible polarizations:

$$h_{ij} = \begin{pmatrix} h_B + h_+ & h_\times & h_{V_1} \\ h_\times & h_B - h_+ & h_{V_2} \\ h_{V_1} & h_{V_2} & h_L \end{pmatrix} . \tag{5.7}$$

The detector(s) will output a total signal

$$s(t) = n(t) + h(t) \,, \tag{5.8}$$

where $n(t)$ represents the noise in the interferometer.

The contribution for each polarization is weighted by angular pattern functions F_i (eqs. (131)-(132) from [5]):

$$h = F_+ h_+ + F_\times h_\times + F_B h_B + F_L h_L + F_{V_1} h_{V_1} + F_{V_2} h_{V_2} \,. \tag{5.9}$$

We characterize the noise contribution to the output using the one-sided noise power spectral density $S_n(f)$ [98]:

$$\langle \tilde{n}(f) \tilde{n}^*(f') \rangle = \frac{1}{2} \delta(f - f') S_n(f) \,, \tag{5.10}$$

where $\langle\cdot\rangle$ represents the expectation of the noise. For the Fourier transform we again use the convention:

$$\tilde{h}\,(f,r) \;=\; \int_{-\infty}^{+\infty} h\,(t,r)\, e^{2\pi i f t} dt\,, \tag{5.11}$$

$$h\,(t,r) \;=\; \int_{-\infty}^{+\infty} \tilde{h}\,(f,r)\, e^{-2\pi i f t} df\,, \tag{5.12}$$

where $\tilde{h}(f)$ is the Fourier transform of $h(t)$. Thus, the signal to noise ratio (SNR) squared takes the form:

$$\rho^2 = \int_0^{\infty} df \frac{4|\tilde{h}(f)|^2}{S_n(f)}\,. \tag{5.13}$$

The Jordan frame metric perturbation is determined by the scalar field φ (the tensorial GW degrees of freedom vanish in spherical symmetry). In massless ST theory, the R_{0i0j} 3-tensor is transverse to the GW wave vector, $R_{0i0j}\propto\delta_{ij}-k_ik_j$. This is called a *breathing* mode and its strain amplitude is given by [15]:

$$h_B(t) = \frac{2}{D}\alpha_0 r\,(\varphi-\varphi_0)\;, \tag{5.14}$$

where r is the extraction radius, φ is the scalar field evaluated at r, D is the distance between the detector and the source and α_0 determines the coupling between the scalar field and the detector. In massive ST theory, there is an additional *longitudinal* mode, $R_{0i0j}\propto k_ik_j$, with suppressed amplitude $h_{\rm L}=(\omega_*/\omega)^2 h_{\rm B}$ [5]. A GW interferometer responds identically (up to a sign) to both of these polarizations meaning they cannot be distinguished [5]; henceforth we refer to the overall measurable *scalar* signal with amplitude

$$h = F_B h_B + F_L h_L\,. \tag{5.15}$$

The angular pattern functions for the breathing and longitudinal mode are:

$$F_L = -F_B = \frac{1}{2}\sin^2\theta\cos 2\phi\,. \tag{5.16}$$

The observation period in our computation is of the order of a few months, during which the Earth (and the detector) will be rotating; as a consequence we consider the average detector response:

$$\bar{F}^2_{L,B} = \frac{1}{4\pi}\int_0^{\pi}\sin\theta d\theta\int_0^{2\pi}d\phi\left(\frac{1}{2}\sin^2\theta\cos 2\phi\right)^2 = \frac{1}{15}\,. \tag{5.17}$$

This leaves us with the signal:

$$h = \frac{1}{2}\sin^2\theta\cos2\phi \times \frac{2\alpha_0 r\varphi}{D}\left(\left(\frac{\omega_*}{\omega}\right)^2 - 1\right) = \frac{2\alpha_0 r\varphi}{\sqrt{15}D}\left(\left(\frac{\omega_*}{\Omega}\right)^2 - 1\right). \tag{5.18}$$

The duration of a burst-like signal is short, in which case we should calculate the SNR as defined in Eq. (5.13). But, as deduced in Sec. 3.4.4, after its propagation over a long distance, the signal can be written as $\sigma(t;r) = r\varphi = \Re\left\{\mathrm{Amp}(t;r)\,\mathrm{e}^{\mathrm{i\,Phase}(t;r)}\right\}$, with Ω, Amp and Phase defined in Eqs. (3.92),(3.96)-(3.97). Since $\Omega/\dot{\Omega} \gg$ observation period (T), the signal is quasimonochromatic and $\sigma \sim \mathrm{Amp} \times \cos\Omega t$.

This simplifies the signal seen by the intereferometer to:

$$h = \frac{2\alpha_0}{\sqrt{15}D}\mathrm{Amp} \times \cos(\Omega t)\left(\left(\frac{\omega_*}{\Omega}\right)^2 - 1\right), \tag{5.19}$$

where the new amplitude and frequency is quasi-constant during the observation period.

Returning to Eq. (5.13), we may rewrite it as:

$$\rho^2 = \frac{2}{S_n\left(\frac{\Omega}{2\pi}\right)}\int_{-\infty}^{\infty} df|\tilde{h}(f)|^2. \tag{5.20}$$

We can now apply Parseval's theorem and obtain:

$$\rho^2 = \frac{2}{S_n\left(\frac{\Omega}{2\pi}\right)}\int_{-\infty}^{\infty} dt|h(t)|^2. \tag{5.21}$$

The observation period is finite, though, so that

$$\rho^2 = \frac{2}{S_n\left(\frac{\Omega}{2\pi}\right)}\int_{0}^{T} dt|h(t)|^2. \tag{5.22}$$

Using Eq. (5.19), we find

$$\rho^2 = \frac{2}{S_n\left(\frac{\Omega}{2\pi}\right)}\int_{0}^{T} dt\left[\frac{2\alpha_0}{\sqrt{15}D}\mathrm{Amp} \times \cos(\Omega t)\left(\left(\frac{\omega_*}{\Omega}\right)^2 - 1\right)\right]^2. \tag{5.23}$$

As mentioned before, Amp and Ω are quasi-constant during the observation period so we are left with integrating $\cos^2(\Omega t)$.

$$\int_0^T \cos^2(\Omega t)dt = \left(\frac{2\Omega t + \sin(2\Omega t)}{4\Omega}\right)_0^T = \frac{T}{2} + \frac{\sin(2\Omega T)}{4\Omega}. \tag{5.24}$$

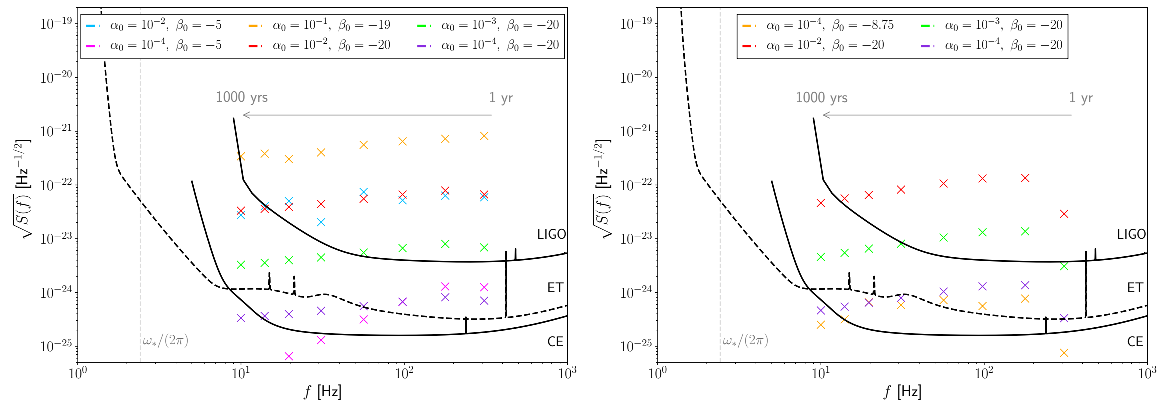

Fig. 5.34 $\sqrt{S_o}$ for quasimonochromatic GWs emitted during stellar collapse for several $(\alpha_0,\ \beta_0)$ values and $\mu = 10^{-14}$ eV using progenitor $s39$ with EOS1 (left) and EOS3 (right). We consider an observation period of $T = 2$ months of a signal from a source placed at $D = 10$ kpc from the detector. The different points mark the SNR obtained when starting the observation period at different time intervals after the collapse: from 1 year (the points furthest to the right, corresponding to the highest frequency) to 1000 years (the point furthest to the left, corresponding to the lowest frequency). The exact moments considered are: $t =\ 1,\ 3,\ 10,\ 30,\ 100,\ 250,\ 500,\ 1000$ years. We compare $\sqrt{S_o}$ to the expected sensitivity curves of LIGO, the Einstein Telescope and Cosmic Explorer.

As the observation period is of the order of a few months, the second term is negligibile relative to the first and the integral is $\simeq T/2$, which gives us

$$\rho = \sqrt{\frac{T}{S_n\left(\frac{\Omega}{2\pi}\right)}} \times \frac{2\alpha_0}{\sqrt{15}D} \times \left(1 - \left(\frac{\omega_*}{\Omega}\right)^2\right) \times \text{Amp}\,. \tag{5.25}$$

5.8.3 Results

In this section we are using Eq. 5.25 to calculate optimal SNRs. These are applicable to targeted, directed and all-sky searches, though different monochromatic searches have different thresholds.

The root of the noise power spectral density $S_n(f)$ together with the analogous quantity

$$\sqrt{S_h(f)} = 2\sqrt{f}|\tilde{h}(f)| \tag{5.26}$$

are the most frequently plotted quantities in literature [98]. We use the latter quantity integrated over the observation period as measurement of the strength of our signals

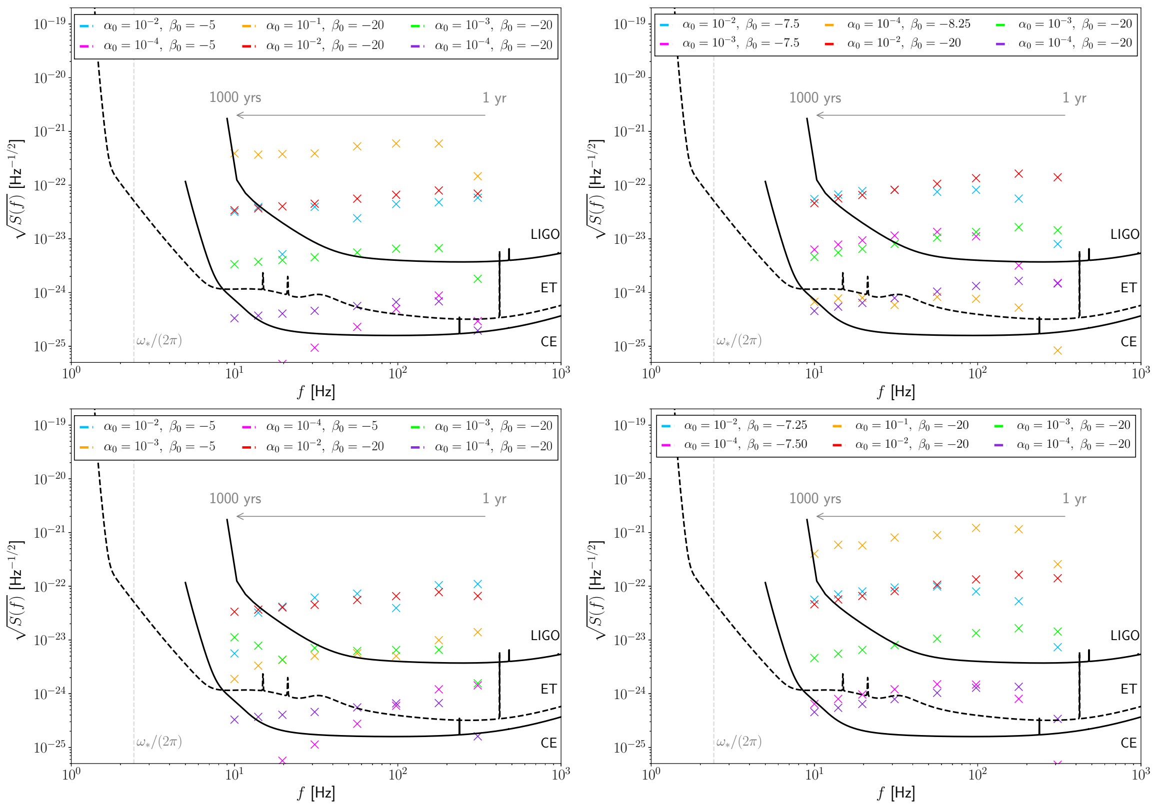

Fig. 5.35 $\sqrt{S_o}$ for quasimonochromatic GWs emitted during stellar collapse for several $(\alpha_0,\ \beta_0)$ pairs and $\mu = 10^{-14}$ eV. The left column represents EOS1 and the right column EOS3. The top row represents $u39$ and the bottom row $z39$. The source distance and time intervals are the same as in Fig. 5.34.

and denote it

$$\sqrt{S_o(\Omega/2\pi)} = \sqrt{T} \times \frac{2\alpha_0}{\sqrt{15}D} \times \left(1 - \left(\frac{\omega_*}{\Omega}\right)^2\right) \times \mathrm{Amp}\,. \tag{5.27}$$

We plot $\sqrt{S_o}$ $(\rho\sqrt{S_n(\Omega/2\pi)})$ for a detection period of $T = 2$ months from sources placed at $D = 10$ kpc from the detector. We consider several $\alpha_0,\ \beta_0$ parameters with $\mu = 10^{-14}$ eV and progenitors: $s39$ with EOS1, EOS3 (Fig. 5.34), $u39$ with EOS1, EOS3 (top row panels of Fig. 5.35) and $z39$ with EOS1, EOS3 (bottom row panels of Fig. 5.35). We have selected strongly scalarized models which form prompt highly-compact NSs as well as a handful of parameters near the β_0 threshold for hyperscalarization which produces strong signals. For EOSa, we have chosen only strongly scalarized cases for all 39 $M_\odot$ progenitors which we plot in Fig. 5.36 and in the left panel of Fig. 5.37. We assume the observation starts at time t after the star collapse occurs, where for t we consider the following values: 1, 3, 10, 30, 100, 250, 500 and 1000 years. For all cases

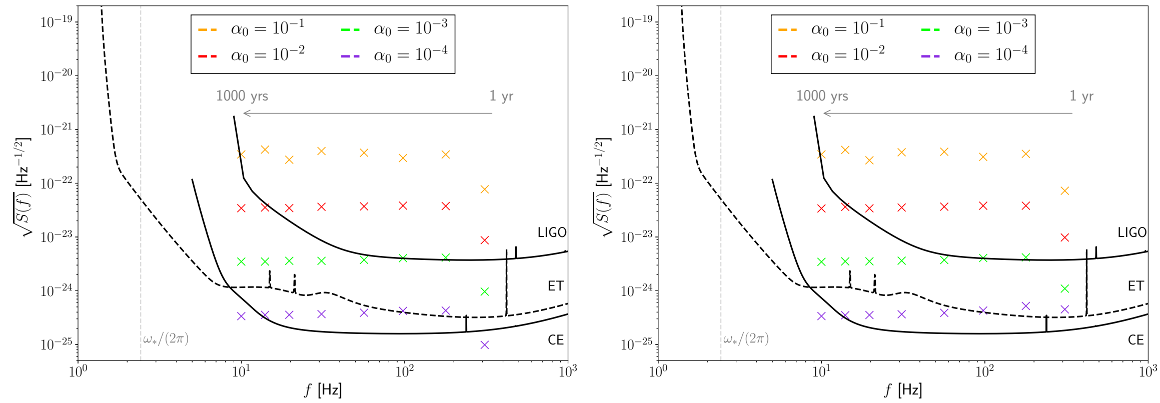

Fig. 5.36 $\sqrt{S_o}$ for quasimonochromatic GWs emitted during stellar collapse for various α_0 values using progenitors $u39$ (left panel) and $z39$ (right panel) with EOSa. The other ST parameters are $\beta_0 = -29$ and $\mu = 10^{-14}$ eV. The source distance and time intervals are the same as in Fig. 5.34.

we consider an observation period of $T = 2$ months. We compare our results to the expected sensitivity curves of LIGO, Einstein Telescope and Cosmic Explorer.

Our analysis suggests that with current LIGO capabilities we should be able to detect signals up to 30 years after we observe a Supernova, provided $\alpha_0 \gtrsim 10^{-3}$. When Cosmic Explorer will be in operation, we may see signals even 1000 years after such an event, meaning we can rely on historic observations. On the other hand, a lack of scalar radiation from a SN will allow us to constrain the coupling $\alpha_0 < 10^{-4}$, which is considerably stronger than the Cassini bound in the massless case. A more negative β_0 (we plot $\sqrt{S_o}$ for $\beta_0 = -50$ in the right panel of Fig. 5.37) leads to improved chances of detection, providing us with an avenue to constrain this parameter as well.

5.9 Conclusions

In this Chapter we have performed the first extensive study of spherically symmetric core-collapse in massive ST theory in which we cover a wide range of equations of state and progenitor models, as well as a vast section of the scalar parameter space centred around the threshold for hyperscalarization. A stronger scalar field delays gravitational collapse to the point of impeding BH formation.

For mildly negative values of the quadratic coefficient β_0 in the conformal factor, we recover the two well-known collapse scenarios in GR, the formation of a neutron star (NS) and the formation of a black hole (BH) resulting from continued accretion onto a proto NS. For sufficiently negative values of β_0, we encounter three collapse scenarios

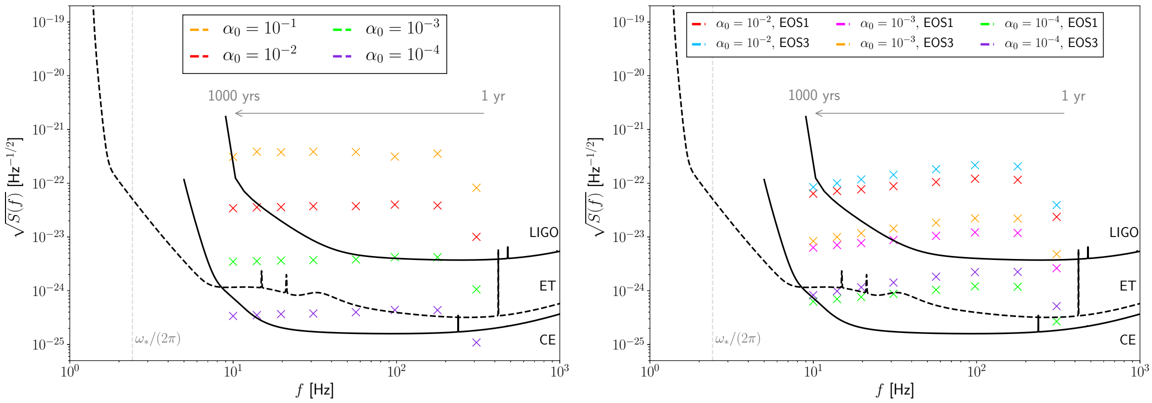

Fig. 5.37 $\sqrt{S_o}$ for quasimonochromatic GWs emitted during stellar collapse for various α_0 values using progenitor $s39$ with EOSa and $\beta_0 = -29$ (left panel) and EOS1, EOS3 with $\beta_0 = -50$ (right panel). The scalar mass used is $\mu = 10^{-14}$ eV. The source distance and time intervals are the same as in Fig. 5.34.

qualitatively different from those in GR, the formation of a BH following multiple NS stages, the multi-stage formation of a strongly scalarized NS and the prompt formation of a strongly scalarized NS.

The fate of a progenitor (with fixed equation of state) in GR dictates the distribution of these five collapse scenarios as we vary the scalar parameters. As we change β_0 from zero towards negative values, only two possible successions of collapse scenarios are possible. The first sequence is: 2-stage BH formation, multi-stage BH formation, multi-stage formation of a strongly scalarized NS, prompt formation of a strongly scalarized NS. The second sequence is prompt formation of a low-compactness weakly scalarized NS, multi-stage formation of a strongly scalarized NS, prompt formation of a strongly scalarized NS. The boundaries between the different classes can vary with the equation of state, the metalicity or the mass of the progenitor, but for every progenitor we encounter either or the other sequence, depending on whether the star forms a BH or a NS in GR.

The different scenarios are reflected in the scalar field (which mirrors the matter density evolution) and, as a consequence, in the scalar radiation. The scalar mass causes the GW signal to disperse as it propagates and by the time it would reach a detector the signal will retain little information with regard to its source, but it carries a highly characteristic imprint of the massive ST theory. Over a wide range of massive ST theory parameters, we find that the resulting gravitational-wave signals will be strong enough to reach SNRs $\gtrsim 20$ over long periods of time, even up to several centuries. This implies potential detection through the study of historical supernovae or, through non-detection, the most stringent constraints on the (α_0, β_0) parameter space of massive ST theory.

Chapter 6

Scalar Tensor Theory with self-interacting potential

The main purpose of this chapter is to perform a systematic exploration of the impact of higher-order terms in the scalar potential and test the robustness of the *inverse-chirp* signals found in massive ST theory.

This chapter and Appendix C is based on material published in [99], authored together with Christopher Moore, Michalis Agathos and Ulrich Sperhake. The theoretical analysis of the toy model was covered by C. Moore. The numerical integration of the non-linear Klein Gordon equation was implemented by U. Sperhake. The author generalised the core collapse code to include self-interacting potentials and performed the simulations and analysis for up to and including the octic term.

6.1 Introduction

In the previous chapter, we have computed the GW signals in massive ST gravity and demonstrated how the gravitational collapse of stellar cores leads to highly characteristic signals, stretched out over years or even centuries by the dispersive nature of the mass term, that would show up in existing LIGO-Virgo searches. Most recently, a first exploration of stellar collapse in ST theory with a mass *and* a quartic self-interaction term has identified the possibility of a weakening effect of the self-interaction term on the magnitude of the GW signal [100]. As we will demonstrate in this section, the generation of the inverse-chirp signals in massive ST theory, their amplitude and propagation is astonishingly robust to modifications of the potential.

We study how the gravitational wave signal from stellar collapse in scalar-tensor gravity varies under the influence of scalar self-interaction. To this end, we extract the gravitational radiation from numerical simulations of stellar collapse for a range of potentials with higher-order terms in addition to the quadratic mass term. Our study includes collapse to neutron stars and black holes and we find the strong inverse-chirp signals obtained for the purely quadratic potential to be exceptionally robust under changes in the potential at higher orders; quartic and sextic terms in the potential lead to noticeable differences in the wave signal only if their contribution is amplified, implying a relative fine-tuning to within 5 or more orders of magnitude between the mass and self-interaction parameters.

6.2 Formalism

The formalism for this class of ST theories is the same as described in Sec. 3.2, the key difference arising in the scalar potential formulation:

$$W(\varphi) = \frac{\mu^2\varphi^2}{2\hbar^2}\left(1 + \lambda_1\frac{\varphi^2}{2} + \lambda_2\frac{\varphi^4}{3} + \ldots + \lambda_n\frac{\varphi^{2n}}{n+1}\right)\,, \quad \text{with} \;\; \lambda_n > 0\,. \tag{6.1}$$

Here, the scalar mass μ introduces a characteristic frequency

$$\omega_* = 2\pi f_* = \frac{\mu}{\hbar}\,. \tag{6.2}$$

In this chapter we set $\mu = 10^{-14}\,\mathrm{eV}$ corresponding to $\omega_* = 15.2\,\mathrm{s}^{-1}$ or $f_* = 2.42\,\mathrm{Hz}$. Note that all λ_i in Eq. (6.1) are dimensionless and that we recover the massive but not self-interacting case of Chapter 5 by setting $\lambda_i = 0$, and the massless case by setting $\mu = 0$.

Let us conclude this section with a summary of the free parameters in our ST theory. The conformal factor is described by α_0 and β_0 and we have n further parameters describing the self-interaction of the scalar field. In this chapter we restrict our attention to the case $n = 2$ giving a total of four free parameters, $\alpha_0,\ \beta_0,\ \lambda_1,\ \lambda_2$, additionally to the four fixed parameters $\mu = 10^{-14}\,\mathrm{eV}$, $\Gamma_1 = 1.3$, $\Gamma_2 = 2.5$, $\Gamma_{\mathrm{th}} = 1.35$ for the scalar mass and the EOS.

6.3 Models and results

The computational framework for our core collapse simulations is again based on the open source code which we modify such that the scalar potential is now given by Eq. (6.1). As initial data for our simulations here we focus on two stellar models

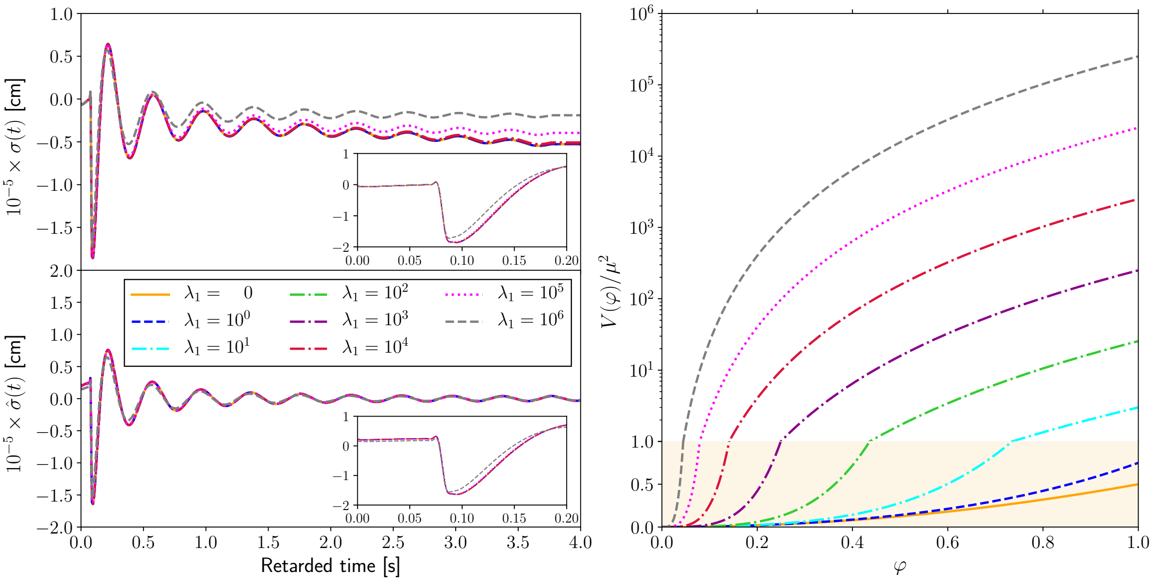

Fig. 6.1 The effect of varying the quartic, λ_1, term of the scalar field potential. Top-left panel: the scalar field signal at the extraction radius 7×10^4 km. Bottom-left panel: the band-passed scalar field signal at the extraction radius 7×10^4 km; modes with frequencies less than ω_* are set to 0. Right panel: the scalar field potential. The progenitor used is a 41 $M_\odot$ star of 10^{-4} solar metallicity and the scalar parameters are $\alpha_0 = 10^{-2}$, $\beta_0 = -20$.

with 10^{-4} times solar metalicity and $M_{\text{ZAMS}} = 39\, M_\odot$ and $41\, M_\odot$. We have studied a wider range of initial models and also tested the effect of varying the EOS parameters; the impact of the self-interaction terms λ_i on the GW generation exhibits a universal character in all these simulations which is fully encapsulated by the models presented in this section. Additional results can be found in Appendix C.

The one common feature of all our simulations is that they result in strong scalarisation of the compact stars formed during the collapse and, thus, lead to a large GW signal for ST theory without self-interaction, i.e. for $\lambda_i = 0$. Let us first consider the collapse of a 41 $M_\odot$ progenitor model with 10^{-4} solar metallicity with ST parameters $\alpha_0 = 10^{-2}$, $\beta_0 = -20$. For $\lambda_i = 0$, the collapse of the baryon matter leads to core bounce at $t \simeq 0.07$ s which generates a scalar wave signal $\sigma = r_{\text{ex}}\varphi$ of $O\left(10^5\right)$ at extraction radius $r_{\text{ex}} = 7 \times 10^4$ km. This signal is shown as the solid (orange) curve in Fig. 6.1. During the collapse, the scalar field at the centre of the star rapidly increases before levelling off at a magnitude of 0.38.

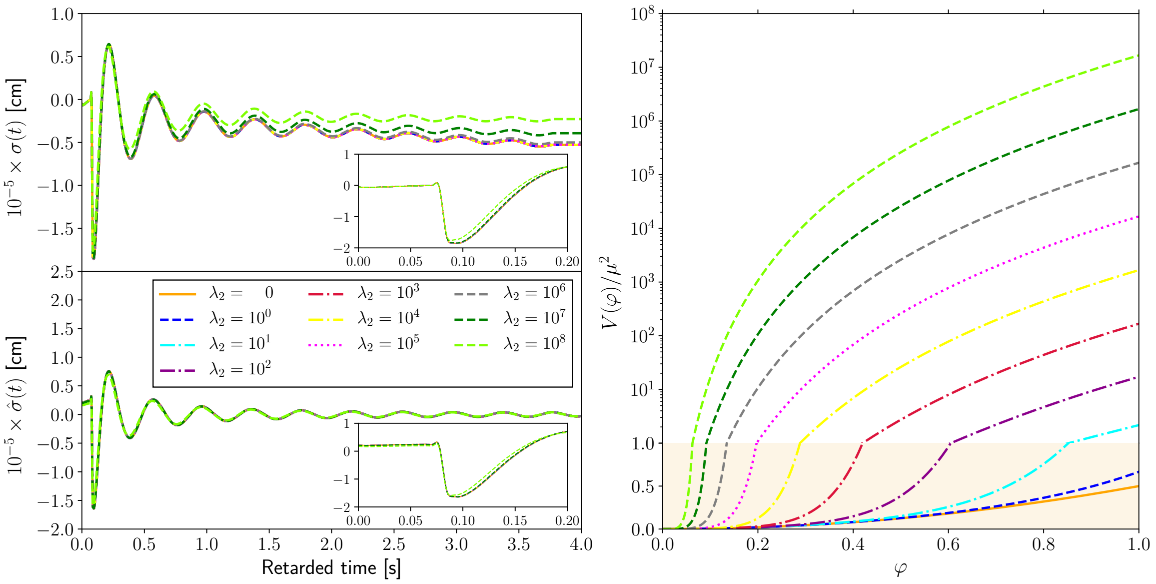

Fig. 6.2 The effect of varying the sextic, λ_2, term of the scalar field potential. Top-left panel: the scalar field signal at the extraction radius 7×10^4 km. Bottom-left panel: the band-passed scalar field signal at the extraction radius 7×10^4 km; modes with frequencies less than ω_* are set to 0. Right panel: the scalar field potential. The progenitor used is a 41 $M_\odot$ star of 10^{-4} solar metallicity and the scalar parameters are $\alpha_0 = 10^{-2}$, $\beta_0 = -20$.

Next, we repeat this collapse simulation for non-zero λ_1 but keeping all $\lambda_i = 0$ for $i \geq 2$. Even though the potential changes dramatically as we increase λ_1 (see the right panel of Fig. 6.1), up to $\lambda_1 = 10^4$, we observe no modifications in the scalar wave signals (see upper left panel of Fig. 6.1) and the peak value of the scalar field at the stellar centre remains 0.38. For $\lambda_1 \gtrsim 10^5$, we start seeing a mild deviation of the signal in the form of a slow drift. The low frequency modes associated with this drift, however, will be screened during the propagation of the signals to large distances: all modes with frequencies below ω_* – 2.42 Hz in this case – decay exponentially at large radii (Sec. 3.4). In the context of LIGO-Virgo observations, these modes are therefore irrelevant. In order to asses the observationally relevant impact of λ_1, we band pass the signals by suppressing modes below ω_*. The result is shown in the bottom left panel of Fig. 6.1 and demonstrates excellent agreement of all waveforms up to $\lambda_1 \approx 10^6$. Increasing λ_1 beyond this magnitude leads to a gradual reduction in the amplitude of the scalar radiation.

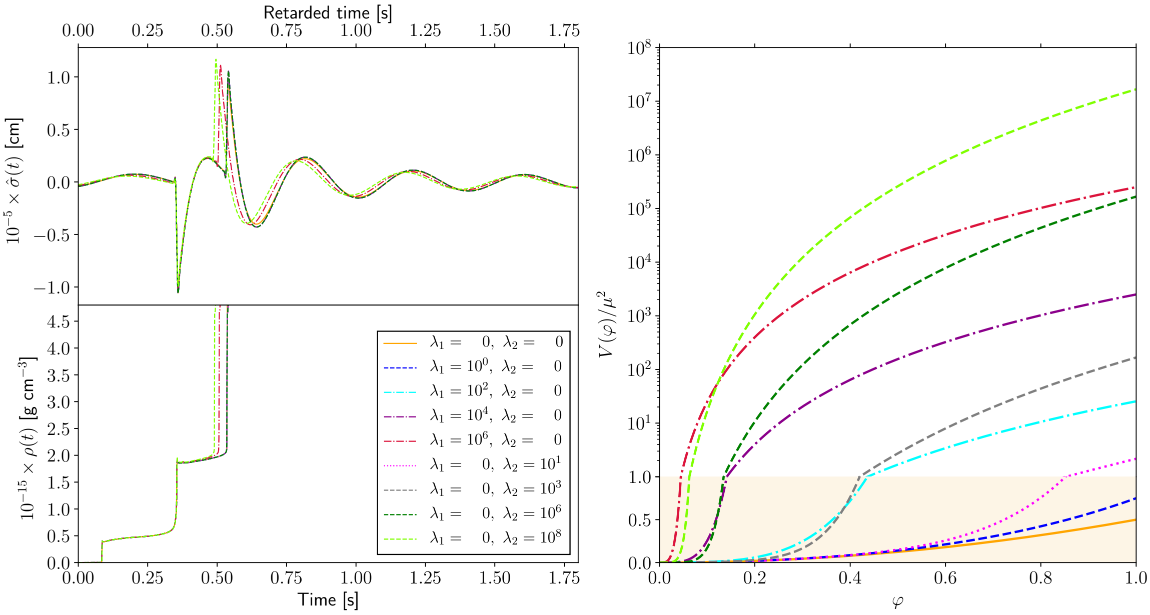

Fig. 6.3 The effect of varying the λ_1 and λ_2 parameters for models that lead to BH formation. Top-left panel: the band-passed scalar field signal at the extraction radius 7×10^4 km; modes with frequencies less than ω_* are set to 0. Bottom-left panel: the central density until a BH is reached. Right panel: the scalar field potential. The progenitor used is a 39 $M_\odot$ star of 10^{-4} solar metallicity and the scalar parameters are $\alpha_0 = 10^{-3}$, $\beta_0 = -5$.

In Fig. 6.2, we have repeated the same analysis but now varying λ_2 while keeping all other $\lambda_i = 0$. The observations are the same as for λ_1 except that the sextic term only exhibits visible deviations for $\lambda_2 \gtrsim 10^7$ (instead of $\lambda_1 \gtrsim 10^5$ for the quartic term). This quantitative difference is not surprising given the additional suppression in the sextic term by a factor $\sim \varphi^2$. We have obtained similar results when varying λ_3: we observe no significant deviation up to values of $\lambda_3 \approx 10^8$ but a reduction of the GW amplitudes above this value. For $\lambda_3 = 10^{12}$, for example, we see a drop by about 50% relative to the non-self-interacting case.

The scenario discussed so far represents a straightforward collapse of a low-density star to a compact neutron star. Especially for high M_{ZAMS} progenitor models, however, the outcome can reveal a more complex behaviour. The collapse may first form a weakly scalarised neutron star which, through continued accretion, later migrates to the strongly scalarised branch or the collapse may form a BH instead of a neutron star. We now consider a model that exhibits all these features in one collapse. This model consists of a 39 $M_\odot$ progenitor with 10^{-4} solar metallicity collapsing in ST theory with $\alpha_0 = 10^{-3}$, $\beta_0 = -5$. For $\lambda_i = 0$, this star initially forms a weakly scalarised compact core, as indicated by the first jump in the central density at $t \simeq 0.09\,\mathrm{s}$ in the bottom left panel of Fig. 6.3. Through accretion, the core becomes more massive and eventually migrates to the strongly scalarised branch at $t \simeq 0.35\,\mathrm{s}$. This change in scalarisation – the central value of the scalar field increases from nearly zero to 0.24 – generates the first peak in the scalar wave signal in the upper left panel of Fig. 6.3. As the core continues accreting and becomes yet more massive, ultimately a BH is formed and the star descalarises in accordance with the no-hair theorems for BHs [101, 102]. From the viewpoint of GW generation, this process is, in essence, a reversal of the original scalarisation and, correspondingly, leads to a second peak at $t \simeq 0.53\,\mathrm{s}$ resembling a mirror image of the first peak. This scenario remains largely unchanged when increasing λ_1 up to 10^5 or, alternatively, λ_2 up to 10^7. For larger values, we eventually see a shift in the time of collapse to a BH: $t \simeq 0.50\,\mathrm{s}$ for $\lambda_1 = 10^6$ and at $t \simeq 0.49\,\mathrm{s}$ for $\lambda_2 = 10^8$. For even larger values of the quartic and sextic parameters, the scalarisation is weakened in accordance with our observations in the above cases. Furthermore, the strongly scalarised stage becomes shorter; for $\lambda_1 = 10^7$ or $\lambda_2 = 10^9$ this stage disappears and the star collapses directly into a BH at $t \simeq 0.35\,\mathrm{s}$. This observation indicates that strong scalarisation tends to delay BH formation.

Qualitatively, one may interpret an increase in the parameter λ_i at fixed β_0 has an effect similar to decreasing β_0 for zero λ_i; as for example moving right to left in the heatmaps in Fig. 5.23.

6.4 Self-interaction and wave propagation

The GW signal we may observe from a stellar collapse event in massive ST gravity is affected by self-interaction terms in the potential in two ways: (i) the scalarisation of the star and the corresponding local generation of a GW signal, and (ii) the propagation of this signal from source to detector. In the previous section, we have addressed item (i); GW generation is affected by the self-interaction terms only for enormous values of the dimensionless coefficients λ_1 and λ_2. In this section we will discuss item (ii). We begin by reviewing the case without self-interaction.

In ST theories with $\lambda_i = 0$, the GW signals at astrophysically large distances, d, tend to a predictable *inverse chirp* (Sec. 3.4); at each instant in time the signal is quasi-monochromatic with instantaneous frequency

$$\Omega(t) = \omega_* / \sqrt{1 - (d/t)^2} \quad \text{for } t > d\,, \tag{6.3}$$

and an amplitude which varies as a function of time according to

$$A(t) = \sqrt{\frac{2}{\pi}} \frac{(\Omega^2 - \omega_*^2)^{3/4}}{\omega_* d^{1/2}} \left| \tilde{\sigma} \left[\Omega(t) \right] \right| . \tag{6.4}$$

Here, $\sigma(t) \equiv r_{\rm ex} \varphi(t; r_{\rm ex})$ is the rescaled scalar field signal extracted at a radius $r_{\rm ex}$ in the wave zone of a strong-field simulation (e.g. as obtained from our numerical simulations at 7×10^4 km), and a tilde denotes a Fourier transform. Note that the scalar profile near the source only enters into the expression for the amplitude of the signal at large distances (not the frequency), and even then only through the modulus of its Fourier transform (or power spectrum).

6.4.1 A toy model

The structure of the inverse chirp is due, almost entirely, to the dispersive nature of the wave propagation, and not to any internal dynamics of the neutron star. To emphasise this point let us consider the following toy model.

At large distances, the dynamics of the non-self-interacting scalar field are governed by the flat-space Klein-Gordon equation,

$$\left(\partial_t^2 - \nabla^2 \right) \varphi + \mu^2 \varphi = 4\pi \varrho \, , \tag{6.5}$$

where ϱ is the source for the scalar field. Although this flat-space equation is only expected to hold at large radii, in our toy model it will be used throughout spacetime. Before the neutron star has scalarised there is no source term; however, after scalarisation the field is sourced by a small, static neutron star. We approximate this scenario with a source function given by

$$\varrho(t; \vec{x}) = \varphi_* \, W_\tau(t) \delta^{(3)}(\vec{x}) \, , \quad \text{where } \; W_\tau(t) = \begin{cases} \frac{2}{\pi} \arctan\left(\frac{t}{\tau}\right) & \text{if } t \geq 0 \\ 0 & \text{if } t < 0 \end{cases} , \tag{6.6}$$

where $\varphi_*(x)$ parameterises the magnitude of the scalarisation, and τ is the typical timescale over which scalarisation occurs. The field equation for our toy model, Eq. (6.5), is linear and may be solved using a retarded Green's function;

$$\varphi(x) = \int \mathrm{d}^4 x \; G(x, x') \varrho(x') \, , \tag{6.7}$$

where $G(x,x')$ is given explicitly by [103]

$$G(x,x') = \left[\delta(\chi) - \frac{\mu}{\sqrt{-2\chi}} J_1(\mu\sqrt{-2\chi})\theta(-\chi)\right] \quad \text{if } t-t' \geq 0 \quad \text{else } 0\,, \tag{6.8}$$

with $\chi(x,x') = \frac{1}{2}\eta_{\mu\nu}(x-x')^\mu(x-x')^\nu$ and J_α denoting the Bessel functions of the first kind. Evaluating the integral in Eq. (6.7) with the source in Eq. (6.6) gives

$$\varphi(t;r) = \varphi_* \left[\frac{W_\tau(t-r)}{r} - \int_0^{t-r} \mathrm{d}t' \, \frac{\mu J_1\left(\mu\sqrt{(t-t')^2 - r^2}\right) W_\tau(t')}{\sqrt{(t-t')^2 - r^2}}\right] \quad \text{if } t \geq r \quad \text{else } 0. \tag{6.9}$$

This is the solution (written in terms of an integral to be evaluated numerically) for the scalar field in our toy model; the first term is the familiar result for a massless field, whilst the second "tail" term depends on μ and accounts for the dispersive nature of the wave propagation. The result in Eq. (6.9) is plotted as a function of retarded time $t-r$ at several fixed radii in Fig. 6.4. Obviously our simple toy model has neglected all of the interesting physics in the region surrounding the scalarising neutron star (for example, it neglects the dynamical space-time curvature, the magneto-hydrodynamics of the collapsing baryons, and the finite size and internal structure of the remnant).

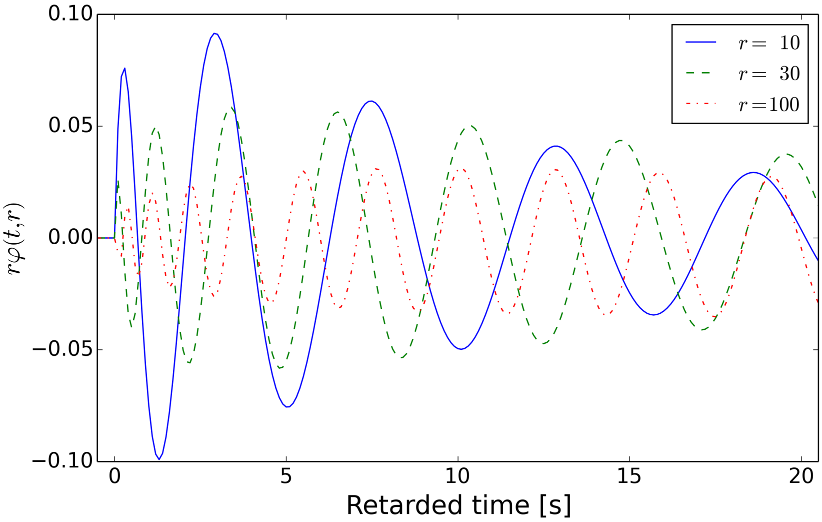

Fig. 6.4 The scalar field as a function of retarded time in the toy model [Eq. (6.9)] at three different distances from the origin: $r = 10$, 30, and 100. The other model parameter values are $\mu = \varphi_* = \tau = 1$, and $\lambda_i = 0$. As described in Sec. 3.4, the signal becomes increasingly oscillatory at greater distances; the $r = 10$ curve has five maxima in the plot range, the $r = 30$ curve has seven, whilst the $r = 100$ curve has ten.

Nevertheless, the scalar profiles plotted in Fig. 6.4 bear a close resemblance to the results of the full numerical simulation reported in Fig. 5.9 as well as the profiles for the self-interacting scalar fields in Figs. 6.1 and 6.2. The fact that the qualitative features of the true signal can be recovered by a simple toy model based solely on the massive wave equation (6.7) serves to emphasise the point that, for non-self-interacting scalar fields, the core collapse GW signal observed at large distances is determined almost entirely by the dispersive nature of the wave propagation in flat space-time, and not by the internal dynamics of the GW source.

We now turn our attention to self-interacting scalar fields [i.e. $n > 0$ in Eq. (6.1)]. The above analysis of our toy model cannot be repeated for this case because the flat space wave equation is now non-linear and does not admit a solution using Green's functions;

$$\left(\partial_t^2 - \nabla^2\right)\varphi + \mu^2\varphi\left(1 + \lambda_1\varphi^2 + \lambda_2\varphi^4 + \ldots + \lambda_n\varphi^{2n}\right) = 4\pi\varrho\,. \tag{6.10}$$

However, the non-linear terms in this equation are only significant near the origin where $\lambda_k\varphi^{2k} \sim 1$; at large distances the scalar field decays as $\varphi \lesssim 1/r$ (or faster). Therefore, the propagation of the signal from the origin to some intermediate radius r_{ex} where $\lambda_1\varphi^2 \ll 1$ is governed by the full non-linear equation. However, the subsequent propagation from r_{ex} out to the astrophysical distances d relevant for LIGO/Virgo observations is once again governed, to an excellent approximation, by the linear Eq. (6.5). Therefore, we expect that at very large distances the signal will still be an inverse chirp as described by Eqs. (6.3) and (6.4).

6.4.2 Numerical integration of the non-linear Klein-Gordon equation

The expectation from the above discussion is that higher-order effects in the potential should not significantly affect the propagation of the gravitational wave signal provided a sufficiently large r_{ex} is chosen. We test this hypothesis by numerically solving the three dimensional Klein-Gordon equation (6.10) with $\varrho = 0$; here we do not source a signal through some model function ϱ, but instead inject a genuine core collapse waveform at $r = r_{\mathrm{ex}}$ and propagate it further outwards to $r = d$ with the homogeneous Klein-Gordon equation. Writing this equation in terms of the variable $\sigma = r\varphi$ (and restoring factors of $\hbar$), we obtain a one-dimensional wave equation that we evolve in characteristic coordinates $(u := t - r, r)$ in the form of the first-order system

$$\begin{aligned} \partial_r \sigma &= \eta\,, \qquad \varphi = \frac{\sigma}{r}\,, \\ \partial_u \eta &= \frac{1}{2}\partial_r \eta - \frac{1}{2}\sigma \frac{\mu^2}{\hbar^2}\left(1 + \lambda_1 \varphi^2 + \lambda_2 \varphi^4 + \ldots + \lambda_n \varphi^{2n}\right)\,. \end{aligned} \tag{6.11}$$

The specific injected signal in our case is given by the waveform $\sigma(t, r_{\rm ex})$ extracted at $r_{\rm ex} = 7 \times 10^4\,$km from the collapse of a $12\,M_\odot$ progenitor in non-self-interacting ST gravity with $\alpha_0 = 10^{-2}$, $\beta_0 = -17$. This is a representative example of a waveform generated for a strongly scalarising star, but it here only serves as a common starting signal for the Klein-Gordon evolutions; what we are interested in is how the propagation of this signal from $r_{\rm ex}$ to d changes for different choices of the λ_i while setting all other $\lambda_i = 0$ and fixing $\mu = 10^{-14}\,$eV.

The signal propagated to $d = 3 \times 10^7\,$km with $\lambda_1 = 0$ and $\lambda_1 = 10^{10}$, respectively, is shown by the two curves in the top row of Fig. 6.5. For $\lambda_1 = 10^6$ and $\lambda_1 = 10^8$ the curves would be indistinguishable from the $\lambda_1 = 0$ case in this plot and we therefore do not include them. The differences in the propagated signals for all self-interacting cases relative to the $\lambda_1 = 0$ signal are shown in the three remaining rows of Fig. 6.5; note that this deviation increases linearly with λ_1 but remains well below the percent level even for $\lambda_1 = 10^8$.

Even within the relatively simple framework of the characteristic Klein-Gordon equation, it is not feasible to compute the propagation of the signal to distances of the order of 10 kpc, typical for galactic LIGO sources. We have, however, repeated the above numerical analysis for $d = 6 \times 10^7\,$km to assess how our findings change with extraction radius. We find no significant difference; the analogous plot for $d = 6 \times 10^7\,$km is barely distinguishable from Fig. 6.5. In conclusion, the propagation of the wave signal in ST theory with higher-order self-interaction terms remains essentially unchanged relative to the massive case studied in Chapter 5, provided $\lambda_1 \lesssim 10^8$. For larger values of λ_1, significant quantitative deviations arise but do not change the "inverse-chirp" character nor the oscillatory pattern of the signal. This result is in agreement with a rough estimate of the accumulation of deviations in the self-interacting case: Over a distance d, the leading extra terms in the potential are of order $\mathcal{O}(d^{-2})$ and the total accumulated deviation is dominated by the contributions at *small* distance from the source. From Figs. 6.1-6.3, we see that the scalar field reaches values of the order of 10^{-5} at $r_{\rm ex} = 7 \times 10^4\,$km, so that $\lambda_1 \varphi^2 \sim 1$ for $\lambda_1 = 10^{10}$, which is precisely the magnitude of λ_1 where deviations in the scalar wave propagation become significant.

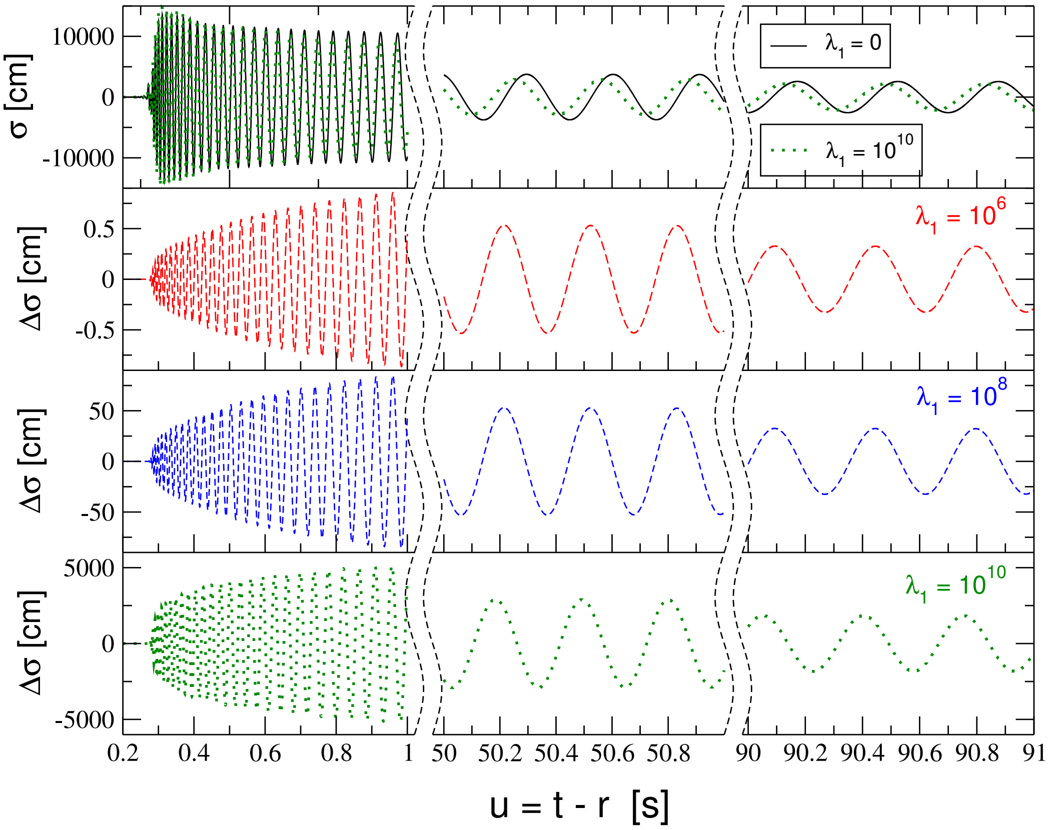

Fig. 6.5 A representative scalar wave signal is injected at $r_{\text{ex}} = 7 \times 10^4$ km and then propagated according to Eq. (6.11) to $d = 3 \times 10^7$ km for $\lambda_1 = 0$, 10^6, 10^8 and 10^{10}, respectively. The top row shows the signals thus obtained at $d = 3 \times 10^7$ km; the waveforms for $\lambda_1 = 10^6$ and $\lambda_1 = 10^8$ would be indistinguishable from the $\lambda_1 = 0$ curve and are not included to avoid confusion. Note that it would be impossible to resolve the long and highly oscillatory signal over its entire duration in this figure and we instead display 3 segments of length 1 s each around u=0, 50 and 90 s. The three following rows respectively show the difference of the three signals propagated with self-interacting potential from the $\lambda_1 = 0$ case. Note that the deviation grows linearly with λ_1 and is negligible up to about $\lambda_1 = 10^8$.

For the sixth-order and higher terms in the potential, the same argument holds even more emphatically: The λ_2 term in the potential falls of with d^{-4} and has even less impact on the wave propagation than the quartic terms and likewise for λ_3 etc.

6.5 Conclusions

Scalar-tensor theories are perhaps the theoretically most well understood of all possible modifications to the general theory of relativity. In such theories compact objects, such as neutron stars, can undergo *spontaneous scalarization* [15], where the scalar field inside the star grows rapidly to large values of order $\mathcal{O}(1)$. This process, and the accompanying GW signal produced, has been studied dynamically during the core collapse process by a number of authors [40–46, 92].

If the scalar is endowed with a mass (i.e. a quadratic potential) a much wider range of the theory's parameter space is compatible with present observational constraints, allowing for a significantly enhanced magnitude of the scalarization, and the GW signal gets distorted by the effects of dispersion and tends to a universal *inverse-chirp* profile.

In this Chapter we have investigated the effects of self-interaction in the scalar field (i.e. a more complicated potential including several higher-order terms). Our results should be compared with those of Ref. [100] where the case of the quartic potential was studied and it was found that self-interaction can suppress the scalarisation effect. Our results are consistent with this conclusion, but we note that such suppression requires a great deal of fine-tuning of the parameters of the potential. For example, when including a quartic φ^4 term, the dimensionless coefficient must be artificially set to a factor of $\gtrsim 10^5$ larger than the leading quadratic term before there is any noticeable effect (see Fig. 6.1). The main conclusion of our study is that the scalarisation phenomenon is incredibly robust against the effects of scalar self-interaction.

We have also demonstrated that the important features of the wave propagation are unaffected by the presence of self-interaction in the scalar potential. In particular, the observed signal still tends to the same universal inverse-chirp profile at large distances.

This apparent insensitivity to the detailed shape of the potential may be both a blessing and a curse. On the one hand it allows a very simple and robust prediction of the expected GW signal to be made. However, if such a signal should ever be detected it will make it very difficult to observationally study any details of physics in the scalar sector, beyond measuring the scalar field mass.

Chapter 7

Superkicks from eccentric binary BH collisions

In this chapter we study BH binaries in General Relativity, specifically eccentric merging BHs with initially antiparallel spins lying in the orbital plane. Binary eccentricity boosts the recoil of the merger remnant by up to 25% which might have important consequences for the retention of stellar-mass black holes in star clusters and supermassive black holes in galactic hosts. There is no symmetry in this scenario, thus we need to use the full numerical three-dimensional approximation of Einstein equations, as described in Sec. 2.2.3.

This chapter is based on material published in [104] in collaboration with Ulrich Sperhake, Davide Gerosa and Emanuele Berti. The simulations were performed by U. Sperhake and the author. The results analysis was performed by all authors.

7.1 Introduction

According to Einstein's theory of GR, gravitational waves carry energy, angular momentum and linear momentum. In a binary BH system the emission of energy and angular momentum causes the orbit to shrink, eventually leading to the merger of the two BHs. The emission of linear momentum imparts a recoil (or *kick*) to the merger remnant [105–107].

Calculations based on post-Newtonian (PN) theory found BH recoil speeds[1] of $\mathcal{O}(100)$ km/s [108–110]. Numerical relativity (NR) simulations, however, show that BH recoils can be more than an order of magnitude larger. This is because the vast

---

[1] Speeds are dimensionless in natural units ($c = G = 1$). Therefore, the recoil imparted to a BH does not depends on the total mass of the system.

majority of the linear momentum is emitted during the last few orbits and merger, where spin interactions are particularly prominent and analytic descriptions within the PN framework become inaccurate. In particular, in 2007 several groups realized that binary BHs with spins lying in the orbital plane and anti-parallel to each other might receive *superkicks* as large as ~ 3500 km/s [111–113]. Subsequent studies found that even larger kicks, up to ~ 5000 km/s, can be reached by further fine-tuning the spin directions [114, 115]. Large kicks strongly affect the dominant mode of gravitational waveforms [116–118], and therefore it should be possible to directly measure their effect with future GW observations [119, 120]. Further studies targeted hyperbolic encounters [121] and ultrarelativistic collisions (which are not expected to occur in astrophysical settings) [122], where kicks can reach 10^4 km/s. We refer to [123–125] for more extensive reviews on the phenomenology of BH recoils.

The occurrence of superkicks has striking astrophysical consequences for both stellar-mass and supermassive BHs. In particular, BH recoils predicted by NR simulations should be compared to the escape speeds of typical astrophysical environments [126].

The stellar-mass BH binaries observed by LIGO and Virgo may form dynamically in globular clusters [127], which present escape velocities in the range 10-50 km/s. These values are smaller even than typical recoil velocities of nonspinning BH binaries [128], which implies that a large fraction of stellar-mass BHs merging in those environments is likely to be ejected [129] (see [130] for a complementary study on intermediate-mass BHs in globular clusters). This may not be the case for environments with larger escape speeds such as nuclear star clusters [131] or accretion disks in active galactic nuclei [132, 133], which might therefore retain a majority of their merger remnants. If able to pair again, the BHs in such an environment can form “second generation” GW events detectable by LIGO and Virgo [134].

The supermassive BH mergers targeted by LISA and pulsar-timing arrays (PTAs) may also be significantly affected by large recoils. Superkicks of $\mathcal{O}(1000)$ km/s exceed the escape speed of even the most massive elliptical galaxies in our Universe. If supermassive BHs are efficiently ejected from their galactic hosts, this decreases their occupation fraction [135] and, consequently, LISA event rates [136, 137]. Spin-alignment processes of both astrophysical [138–141] and relativistic [142, 143] nature are commonly invoked to mitigate this effect.

Recoils are driven by asymmetries in the merging binary [144, 145]: no kick can be imparted if linear momentum is emitted isotropically in all directions.

For instance, an equal-mass nonspinning binary does not recoil by symmetry. Unequal masses or misaligned spins, however, introduce asymmetries in the GW

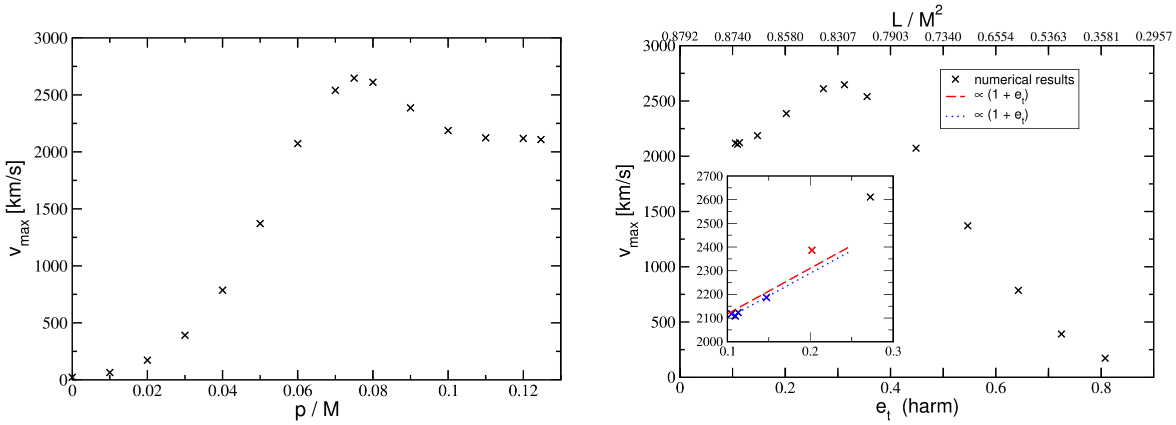

Fig. 7.1 Superkicks for eccentric binary BHs with equal masses and spins of magnitude $\chi_1 = \chi_2 = 0.596 \simeq 0.6$. *Left*: The maximum kick velocity $v_{\max}$ as a function of the linear momentum parameter. The largest kicks correspond to moderate eccentricity and exceed the quasicircular value by about 25 %. *Right*: The maximum kick velocity $v_{\max}$ as a function of the eccentricity parameter e_t estimated in harmonic gauge. Labels on the upper horizontal axis display the corresponding initial orbital angular momentum L/M^2 of the binaries. The inset zooms in on the low-eccentricity regime and shows linear fits $v_{\text{kick}} \propto (1 + e_t)$ obtained from the first 4, blue data points (dotted curve) and also including the 5th, red data point (dashed curve). The increase of the recoil for small eccentricity is compatible with the $(1 + e)$ scaling from close-limit calculations [146].

emission. Orbital eccentricity is a further natural ingredient to enhance the asymmetry of the binary and, consequently, the kick. Early PN estimates show that, for low eccentricities $e \lesssim 0.1$, the kick imparted to nonspinning BHs increases by about $\sim 10\%$, with a scaling proportional to $1 + e$ [146].

In this chapter, we investigate how superkicks are affected by binary eccentricity using NR simulations of the merger. For this purpose, we consider equal-mass binaries with $M_1 = M_2 \equiv M/2$ with BH spins of equal magnitude pointing in opposite directions inside the orbital plane, $\boldsymbol{S}_1 = -\boldsymbol{S}_2$. Fixing the dimensionless spin $\chi_i \equiv |\boldsymbol{S}_i|/M_i^2$ to $\chi_1 = \chi_2 = 0.596$, we generate a sequence of increasing eccentricity by gradually reducing the initial orbital angular momentum L at fixed binding energy from the quasi-circular value to the head-on limit $L = 0$; in practice, we vary for this purpose the initial tangential momentum parameter p of each BH. For a given eccentricity (i.e. fixed L), the kick is known to depend sinusoidally on the initial angle of the two spins relative to the line connecting the BHs. The maximum value of this sine function is the kick reported in Fig. 7.1 as a function of the linear momentum and of the eccentricity. The significant increase of the maximum kick from about 2100 km/s for approximately quasi circular binaries to 2600 km/s for moderate eccentricities $e_t\sim 0.3$ is the main finding of our study (where e_t is the eccentricity parameter of Ref. [147, 148]). We furthermore show that such an increase holds over a wider range of spin magnitudes and correspondingly raises the maximum superkick in BH binaries to about 4200 km/s, larger than the maximum of ~ 3700 km/s for negligible eccentricity.

7.2 Computational framework and set of simulations

7.2.1 Numerical-relativity setup

The BH binary simulations reported in this work have been performed with the Lean code [149], which is based on the Cactus computational toolkit [150, 151]. The Einstein equations are implemented in the form of the Baumgarte-Shapiro-Shibata-Nakamura-Oohara-Kojima (BSSNOK) formulation [22–24] using the method of lines with fourth-order Runge-Kutta differencing in time and sixth-order stencils in space for improved phase accuracy [152]. The wide range of lengthscales is accommodated through adaptive mesh refinement provided by Carpet [153, 154] and we compute apparent horizons with AHFinderDirect [155, 156]. We start our simulations with puncture [157] data of Bowen-York [158] type computed with Ansorg's spectral solver [159] inside Cactus' TwoPuncture thorn. The gravitational wave signal is extracted in the form of the Newman-Penrose scalar Ψ_4 computed from the grid variables [149].

7.2.2 Black-hole binary configurations

In this study we consider equal-mass BH binaries in the *superkick* configuration, i.e. the BHs have spins of equal magnitude pointing in opposite directions in the orbital plane.[2] In practice, we do not compute the dimensionless spins χ_i directly from the Bowen-York spin, because some angular momentum and energy is contained in the spurious radiation of the conformally flat initial data. This energy and momentum is partly accreted onto the BHs and partly radiated to infinity, leading to a brief period of spin adjustment. While negligible for slowly rotating BHs, this effect increases for larger spin parameters and ultimately leads to a saturation at $\chi\sim 0.928$ [160, 161]. In order to obtain a more accurate estimate of χ_i, we monitor the BH spins $\boldsymbol{S}_i$ using the method

---

[2] We define here the orbital plane as the plane spanned by the initial position vector connecting the BHs and their initial linear momentum – in our case this is the xy plane, and the z axis points in the direction perpendicular to this plane.

described in Ref. [162] and compute the irreducible mass $m_{\rm ir}$ from the apparent horizon during the evolution. The dimensionless spin χ_i can then be computed according to [163]

$$M_i^2 = m_{{\rm ir},i}^2 + \frac{|\boldsymbol{S}_i|^2}{4m_{{\rm ir},i}^2}\,, \qquad \chi_i = \frac{|\boldsymbol{S}_i|}{M_i^2}\,. \tag{7.1}$$

As expected from the above description, we observe a brief transient period in all simulations during which χ_i mildly decreases. Throughout this work we report the initial spin as the value at time $t_\chi = 20M$ measured from the beginning of the simulation. By this time χ_i has reached a nearly stationary value, so that the precise value of t_χ does not affect the results. We distinguish this estimate for the initial spin from the value directly obtained from the Bowen-York parameters, which we denote by $\chi_{{\rm BY},i}$. The relation between χ_i and $\chi_{{\rm BY},i}$ is shown in the fourth and fifth columns of Table 7.1. All simulations presented in this paper have $\chi_1 = \chi_2$.

The net spin is zero in the superkick configurations, resulting in dynamics rather similar to those of nonspinning BH binaries; the main difference is a periodic motion of the orbital plane in the orthogonal (in our case z) direction. This motion of the binary orthogonal to the orbital plane results in a periodic blue and red shift of the gravitational radiation and the net effect of this beaming leads to asymmetric GW emission, especially in the $(\ell, m) = (2, 2)$ and $(2, -2)$ multipoles and, hence, net emission of linear momentum and the ensuing recoil of the post-merger remnant [116, 117]. For fixed initial position $(\pm x_0,\ 0,\ 0)$ of the BH binary, the periodic nature of the blue and red shifting of the gravitational radiation furthermore manifests itself in a sinusoidal dependence of the actual kick magnitude on the initial orientation of the spins in the orbital plane [116, 164]. We quantify this orientation in terms of the angle α between the initial spin of the BH starting at $x > 0$ and the x axis, i.e. this BH has initial spin $\boldsymbol{S}_1 = S\,(\cos\alpha,\ \sin\alpha,\ 0)$ while the BH at $x < 0$ is initialized with $\boldsymbol{S}_2 = -\boldsymbol{S}_1$ [116, 125].

In order to assess the impact of the orbital eccentricity on the magnitude of the gravitational recoil, we have constructed a set of binary configurations guided by the second sequence of equal-mass, nonspinning BH binaries in Table I of Ref. [147]. This sequence starts with a quasicircular binary with initial separation $D/M = 7$ and a tangential linear momentum $p/M = 0.1247$ for each BH, resulting in an orbital angular momentum $L/M^2 = 0.8729$. These parameters determine the binding energy of the binary through $E_{\rm b} \equiv M_{\rm ADM} - M$, where $M_{\rm ADM}$ is the Arnowitt-Deser-Misner (ADM) mass [21] of the binary spacetime. We construct a sequence of configurations with increasing eccentricity by gradually reducing the initial linear momentum parameter while keeping the binding energy fixed at $E_b/M = -0.012$. For this choice, the gradual reduction of initial kinetic energy for larger eccentricity implies a larger initial separation, i.e. correspondingly less negative potential energy, and, thus, ensures an inspiral phase of comparable duration irrespective of the eccentricity.

The variation in the initial separation of the BHs requires a minor change in the setup of the computational grid for low- and high-eccentricity binaries. In the notation of Ref. [149] we employ a grid setup given in units of M by

$$\begin{aligned} &\{(256,\, 128,\, 64,\, 32,\, 16,\, 8) \times (2,\, 1),\; h\}\,, \\ &\{(256,\, 128,\, 64,\, 32,\, 16) \times (4,\, 2,\, 1),\; h\}\,, \end{aligned} \tag{7.2}$$

respectively, for binaries with $p/M \geq 0.8$ and those with $p/M < 0.8$. Unless stated otherwise, we use a resolution $h = M/64$ on the innermost refinement level.

In order to accommodate the above mentioned sinusoidal variation of the kick velocity with the initial spin orientation α, we have performed for each value of the linear momentum parameter p a subset of 6 runs with $\alpha \in [0,\, 180°)$. Due to the symmetry of the superkick configuration under a shift of the azimuthal angle $\phi \to \phi + 180°$, the recoil will always point in the z direction with $v_x = v_y = 0$ [144, 145]. Furthermore, two binaries with initial spin orientations α and $\alpha + 180°$ will generate kicks of equal magnitude but opposite direction, i.e. $v_z(\alpha) = -v_z(\alpha + 180°)$ [116]. Kick velocities for $\alpha \geq 180°$ can therefore be directly inferred through this symmetry from the simulations performed. For a few selected cases, we have performed additional simulations with $\alpha \geq 180°$; the symmetry is confirmed with accuracy of $\mathcal{O}(0.1)$ % or better.

7.2.3 Measuring the eccentricity

Our sequence of simulations is characterized by the variation of the orbital angular momentum at fixed binding energy. As discussed in detail in Ref. [147], there is no unambiguous way to assign an eccentricity parameter to BH binaries in the late stages of the inspiral. Motivated by the close similarity of the orbital dynamics of (equal-mass) superkick binaries and nonspinning binaries, we follow here the procedure used in [147] to obtain a PN estimate for nonspinning binaries. Specifically, we use Eqs. (20), (25) of Ref. [148], which provide the PN eccentricity parameter e_t for nonspinning binaries. This estimate needs to be taken with a grain of salt as it is only an approximation at the small binary separation during the last orbits before merger, and it ignores the effect of BH spins. Furthermore e_t exhibits an infinite gradient near the quasicircular limit when plotted as a function of the orbital angular momentum, leading to limited precision for values $e_t \lesssim 0.1$. Similarly, in the head-on limit the vanishing of L leads to a formal divergence of the eccentricity parameter and a Newtonian interpretation ceases to be valid (values $e_t > 1$ are possible in this regime). Nevertheless, e_t provides us with a rough estimate to quantify deviations from the quasicircular case and distinguish low-, moderate- and high-eccentricity configurations.

For all simulations, we have computed the following diagnostic variables. The energy, linear and angular momentum radiated in GWs are computed on extraction spheres of coordinate radius $r_{\rm ex}/M = 30, 40, \ldots, 90$ from the Newman-Penrose scalar according to the standard methods described, for example, in [165]. For the physical radiation reported in Table 7.1 we exclude the spurious radiation inherent in the initial data by considering only the wave signal starting at retarded time $u \equiv t - r_{\rm ex} = 50\ M$. We also compute the dimensionless spin of the post-merger BH from the apparent horizon [166]. We have confirmed these values using also conservation of energy and angular momentum, which yields agreement to within 0.5 % or better.

7.2.4 Numerical accuracy

Our numerical results for the GW emission and the recoil velocities are affected by two main sources of uncertainty: the discretization error and the finite extraction radii for the Newman-Penrose scalar.

We address the latter by extrapolating the GW signal to infinity using a Taylor series in $1/r$ as in Ref. [167]. The results reported are those extrapolated at linear order in $1/r$, and we estimate the error through the difference with respect to a second-order extrapolation. The magnitude of this error is $\sim 2\,\%$ or less.

In order to assess the error due to finite differencing, we have performed additional simulations of the configuration $p/M = 0.1247$, $\chi_i = 0.596$, $\alpha = 150°$ using grid resolutions $h = M/48$ and $h = M/80$. Figure 7.2 shows convergence between fourth and fifth order resulting in a discretization error of about $2\,\%$ for the radiated linear momentum. A similar behavior is observed for the radiated energy $E_{\rm rad}$. We use this value as an error estimate, but note that this is a conservative estimate for the *maximum* kick velocity at fixed eccentricity. The reason is that a considerable part of the numerical error consists in the inaccuracy of the inspiral phase of the binary. This phase error significantly affects the angle α_0 in Eq. (7.3) below, but has weaker repercussions on the maximum kick $v_{\max}$ In other words, at lower resolution, we will obtain the maximum kick at a “wrong” phase angle α_0, but still measure this maximum with decent precision. We have verified this expectation by generating a

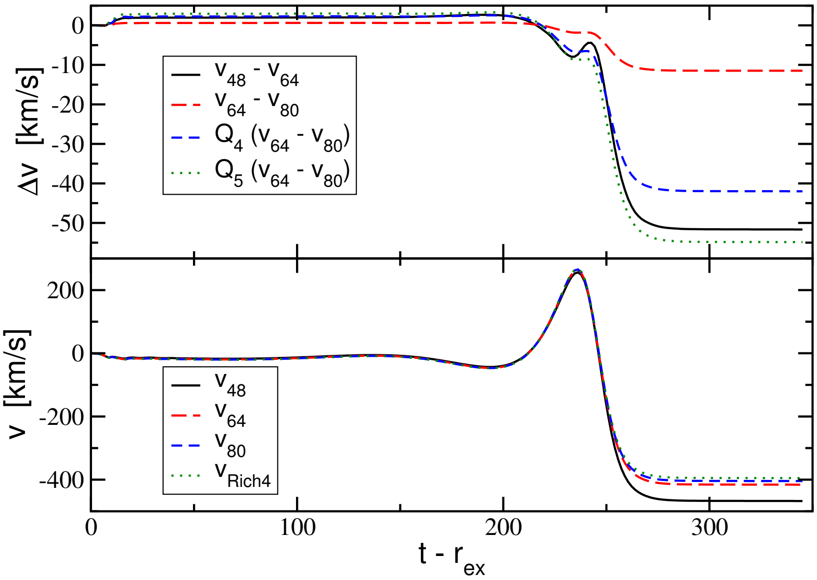

Fig. 7.2 Convergence analysis for the linear momentum radiated from a binary with $p/M = 0.1247$, $\chi_i = 0.596$, $\alpha = 150°$. The linear momentum obtained for resolutions $h = M/48$, $h = M/64$ and $h = M/80$ is shown in the form of the kick velocity accumulated up to retarded time $u = t - r_{\rm ex}$ in the bottom panel. The upper panel shows differences between various resolutions, together with rescaling according to fourth- and fifth-order convergence. We estimate the uncertainty from the more conservative fourth-order Richardson extrapolation, and we obtain a numerical error estimate of about 2 % for our standard resolution $h = M/64$.

complete sequence for $p/M = 0.1247$, $\chi_i = 0.596$ at low, medium and high resolution. Applying the fit (7.3) to each of these gives us $v_{\rm max} = 2098.1, 2108.3$, and 2109.7 km/s, respectively, for $h/M = 1/48$, 1/64, and 1/80. Since we cannot entirely rule out fortuitous cancellation of errors in this excellent agreement, we keep in the remainder of this work the more conservative 2 % estimate from Fig. 7.2. Combined with the extrapolation procedure to $r_{\rm ex} \to \infty$, we estimate our total error budget as $\sim 4\,\%$.

7.3 Numerical results

The main results of our study are summarized in Table 7.1. For each sequence with prescribed linear momentum p, we list there the initial separation D, orbital angular momentum L, the initial BH spin χ_i, eccentricity estimates e_t obtained in ADMTT and harmonic gauge according to Eqs. (20), (25) of Ref. [148], the mean radiated energy E_0, the maximum kick velocity $v_{\rm max}$ and the dimensionless spin χ_0 of the merger remnant.

p/M	D/M	L/M^2	$\chi_1 = \chi_2$	e_t(ADMTT)	e_t(harm)	$10^2\, E_0/M$	$v_{\max}$ [km/s]	χ_0
0.1247	7.000	0.8729	0.596	0.1095	0.1096	3.687	2108	0.6815
0.12	7.278	0.8734	0.596	0.1049	0.1052	3.678	2118	0.6810
0.11	7.932	0.8725	0.596	0.1130	0.1130	3.664	2123	0.6798
0.10	8.678	0.8678	0.596	0.1480	0.1472	3.757	2187	0.6808
0.09	9.529	0.8576	0.596	0.2040	0.2020	3.862	2387	0.6884
0.08	10.493	0.8394	0.596	0.2758	0.2725	3.656	2611	0.6999
0.075	11.018	0.8264	0.596	0.3166	0.3124	3.368	2647	0.7010
0.07	11.571	0.8100	0.596	0.3608	0.3555	3.069	2540	0.7021
0.06	12.754	0.7652	0.596	0.4567	0.4485	2.258	2073	0.6905
0.05	14.013	0.7007	0.596	0.5603	0.5467	1.452	1371	0.6539
0.04	15.288	0.6115	0.596	0.6681	0.6428	0.833	786	0.5862
0.03	16.487	0.4946	0.596	0.7835	0.7247	0.429	391	0.4839
0.02	17.488	0.3498	0.596	1.0122	0.8078	0.203	172	0.3467
0.01	18.162	0.1816	0.596	3.0771	2.0975	0.100	64	0.1813
0	18.398	0	0.596	∞	∞	0.071	22	0
0.075	11.018	0.8264	0.596	0.3166	0.3124	3.368	2647	0.7010
0.075	11.018	0.8264	0.645	0.3166	0.3124	3.383	2849	0.7002
0.075	11.018	0.8264	0.694	0.3166	0.3124	3.368	3019	0.6990
0.075	11.018	0.8264	0.742	0.3166	0.3124	3.386	3166	0.6969
0.075	11.018	0.8264	0.789	0.3166	0.3124	3.330	3479	0.6976
0.075	11.018	0.8264	0.834	0.3166	0.3124	3.233	3583	0.6960
0.075	11.018	0.8264	0.876	0.3166	0.3124	3.167	3776	0.6950

Table 7.1 Each sequence of simulations is characterized by the linear momentum parameter p and the initial BH separation D (which determine the orbital angular momentum L and the eccentricity of the binary), as well as the initial spins, given here in the form of the horizon estimate χ_i. The remaining columns list: estimates of the eccentricity e_t obtained from PN relations in the ADMTT and harmonic gauge, respectively; the mean radiated GW energy E_0; the maximum kick velocity $v_{\max}$; and the mean spin χ_0 of the remnant BH.

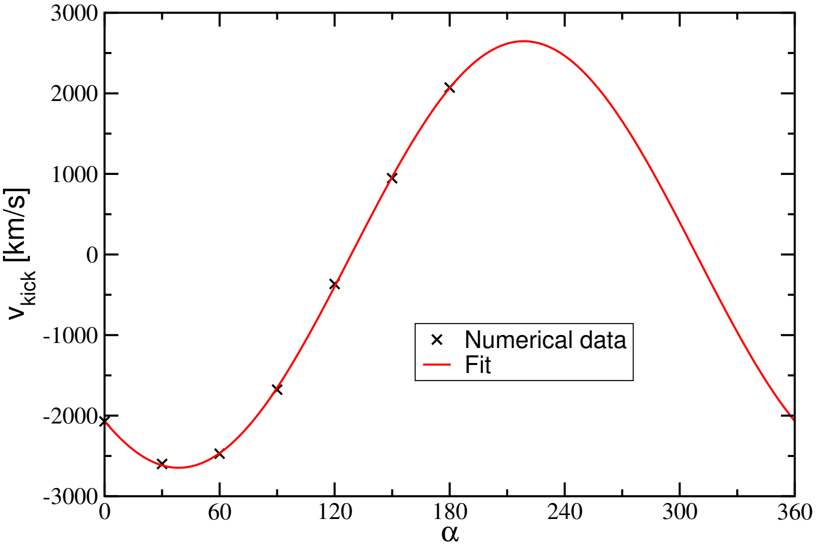

Fig. 7.3 The recoil velocity computed numerically from the GW signal for $p = 0.075$ is shown as × symbols for different values of the spin orientation α. The red curve represents the fit obtained from these data according to Eq. (7.3). Only data for $\alpha < 180°$ are needed to determine the fitting coefficients, due to the symmetry of the superkick configurations.

7.3.1 Impact of the orbital eccentricity

The sinusoidal dependence of the kick magnitude on the initial spin orientation α is illustrated in Fig. 7.3 for the case $p/M = 0.075$, $\chi_i = 0.596$. The data are reproduced with high precision by a fit of the form

$$v_{\mathrm{kick}} = v_{\mathrm{max}} \times \cos(\alpha - \alpha_0)\,, \tag{7.3}$$

where, for this specific series, $v_{\mathrm{max}} = 2647$ km/s and $\alpha_0 = 218.7°$. The radiated energy E_{rad} and the final spin, in contrast, vary only mildly (within the numerical uncertainties) with the angle α; we report average values for these quantities. More specifically, we fit $E_{\mathrm{rad}} = E_0 + E_1 \sin(2\alpha + \alpha_0)$ and report E_0 (and likewise χ_0).

The variation of the kick velocity with eccentricity is visualized in the left panel of Fig. 7.1, which shows v_{max} as a function of the linear momentum p. We clearly see that the largest kicks are not realized for quasicircular binaries but for moderate eccentricities. A similar effect is apparent for the radiated energy values of Table 7.1, which closely resembles the observation in Table I of Ref. [147] for the nonspinning case. The increase in the recoil velocity, however, is much stronger: for $p/M = 0.075$, the maximum kick exceeds the quasicircular value by about 25 % while the largest energy represents a meager 5 % increase relative to the quasicircular case. This discrepancy shows that the enhanced kick is not merely due to increased radiation, but also to a higher degree of asymmetry in eccentric binaries.

An increase in the recoil at small eccentricities has already been noticed in the close limit calculations of Ref. [146, 168], which find a $(1+e)$ proportionality for eccentricities $e \lesssim 0.1$. In the right panel of Fig. 7.1, we plot the maximum kick velocity as a function of the eccentricity parameter e_t in harmonic gauge (the ADMTT version of e_t would result in virtually the same figure). Due to the diverging gradient of e_t with respect to the orbital angular momentum [147], our data points are limited to $e_t \gtrsim 0.1$, but as shown in the inset of the figure, the data are compatible with the linear growth $\propto (1+e_t)$ of the close-limit approximation. The two fits shown in the inset have been obtained using either the first 4 or the first 5 data points with the expression $v_{\text{max}} = v_0(1+e_t)$. The numerical results suggest that above $e_t \approx 0.2$, v_{max} increases even more strongly with e_t before reaching the maximum at $e_t \approx 0.3$, and then decreases for yet higher eccentricity.

7.3.2 Impact of the spin magnitudes

The gravitational recoil in superkick configurations is known to increase approximately linearly with the spin magnitudes χ_i. Extrapolating numerical results to maximal spin $\chi_i = 1$ results in a maximal superkick of about 3680 km/s [164] for quasicircular binaries. We will now investigate to what extent nonzero eccentricity can increase this upper limit. In order to keep the computational costs manageable, we focus for this purpose on the $p/M = 0.075$ sequence which maximizes the recoil in our eccentricity analysis for $\chi_i = 0.596$. We cannot rule out that the "optimal" eccentricity maximizing recoil depends on the spin magnitude, so that our analysis should be regarded as a conservative estimate; the largest possible superkick in eccentric binaries may even exceed the value resulting from the analysis below.

We vary the initial spin magnitude χ_i while keeping all other parameters, including the eccentricity e_t, fixed. A convergence analysis for $\chi_i = 0.9$ yields a similar order as in Fig. 7.2, but demonstrates that higher resolution is needed for these configurations. We use $h = M/80$ for the simulations discussed in this subsection, which results in a discretization error of about 4 %. As before, we cover the range of the initial spin orientation by evolving 6 binaries with $\alpha \in [0, 180°)$ for each value of χ_i and fit the resulting v_{kick} according to the sinusoidal function of Eq. (7.3). The results for these simulations are listed in the lower block of Table 7.1. As expected, the maximum recoil velocity v_{max} increases with the spins χ_i. We display v_{max} as a function of χ_i in Fig. 7.4, together with a linear fit to model the leading-order dependence of the

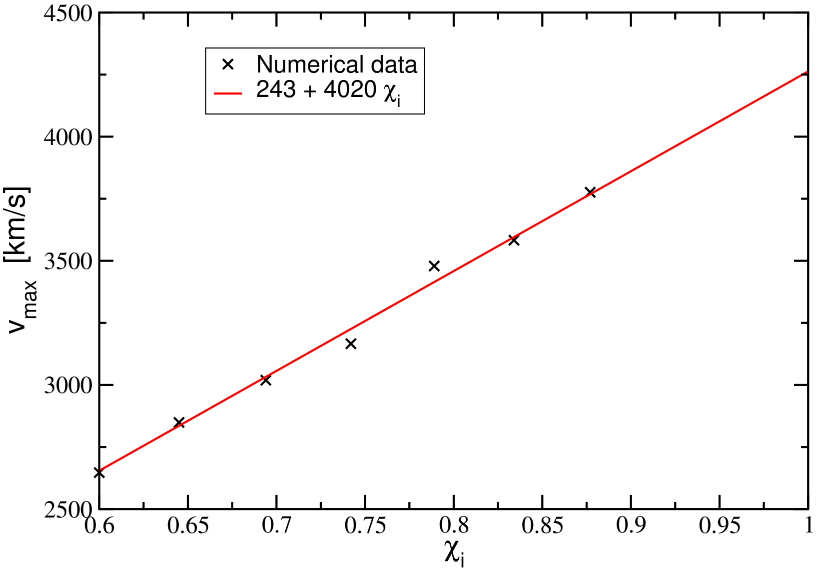

Fig. 7.4 The maximum recoil velocity v_{max} for $p/M = 0.075$ as a function of the initial spin magnitude χ_i. The curve represents the linear fit (7.4).

maximum recoil velocity v_{max} on the spin magnitude χ_i [112, 164]. This fit is given by

$$v_{\mathrm{max}} = \Big[(243 \pm 122) \;+\; (4020 \pm 163)\,\chi_i\Big]\ \mathrm{km/s}\,, \tag{7.4}$$

and predicts a maximum kick of 4263 ± 285 km/s for extremal spins $\chi_i = 1$. This value exceeds the maximal superkick for quasicircular binaries of about 3680 km/s [112, 164] by about 16 %, but falls short of the 5000 km/s maximum for the hang-up kicks reported in Ref. [114]. To the best of our knowledge, the effect of eccentricity on these hang-up kicks has, not yet been explored. The results reported here and the findings of Ref. [146] hint that yet larger recoils may be possible in bound BH binary systems.

7.4 Conclusions

Orbital eccentricity amplifies superkicks. We have presented an extensive series of numerical simulations of merging BHs with spin vectors of magnitude ~ 0.6 in the orbital plane and initially antialigned with each other. We then vary the initial linear momentum of the holes for fixed binding energy, which is equivalent to modifying the initial eccentricity. We find that orbital eccentricity can boost the final recoil by up to $\sim 25\%$. The binaries that receive the largest kick of ~ 2600 km/s have moderate eccentricity $e_t \sim 0.3$ [147, 148]. For comparison, the maximal kick imparted to a quasicircular binary with the same parameters is ~ 2100 km/s. Our results suggest that the enhanced radiation of linear-momentum is mainly due to the more pronounced asymmetry in the binary's GW emission rather than the mere consequence of a larger energy flux.

An additional series of simulations with fixed eccentricity and varying spin magnitudes allows us to extrapolate these results to maximally rotating BHs. We predict a maximum superkick of at least ~ 4300 km/s, compared to the quasicircular result ~ 3700 km/s. We stress that this estimate is conservative because (i) we did not explore the optimal value of the eccentricity as a function of the spin magnitude, and (ii) we constrain the spins to the orbital plane; partial alignment is known to generate larger recoils [114, 115]. The impact of orbital eccentricity on these *hang-up* kicks with partial spin alignment is a complex task that we leave for future work: the recoil has a more complicated dependence on the eccentricity and the initial spin orientations because of spin precession.

The amplification of superkicks due to orbital eccentricity may have important consequences for the modeling of GW sources. For the stellar-mass BHs targeted by ground-based interferometers, a nonnegligible eccentricity at merger would be a powerful signature of strong and recent interactions with external bodies (cf. e.g. [169–171, 170, 172–174]). If BH binaries coalescing in dynamical environments are indeed eccentric, our findings further limit the ability of stellar cluster to retain their merger remnants [134]. For instance, Refs. [175, 176] found that dynamical interactions in globular clusters are a viable formation mechanism to explain multiple generations of eccentric BH mergers. The calculation of the retention fraction, however, does not take into account the significant kick enhancement due to eccentricity that we have found in this work. Given the low escape speed of globular clusters, this amplification may considerably reduce the predicted number of second-generation BH mergers.

For the case of supermassive BH binaries, eccentric sources are commonly invoked to explain current PTA limits. Orbital eccentricity shifts some of the emitted power to higher frequencies, causing a turnover in the predicted spectrum [177–180]. The presence of this feature allows current astrophysical formation models calibrated on galaxy counts to more easily accommodate the measured upper limits. Our work highlights that kicks may be higher than currently assumed, further reducing the merger rate and the predicted stochastic GW background.

Numerical relativity simulations now provide a thorough understanding of the properties of the BH remnants left behind following mergers of BHs on quasicircular orbits. Efficient and accurate models for final mass, spin, and kick are available and routinely implemented in astrophysical predictions. For eccentric orbits, the additional dimensionality of the parameter space increases the computational resources required to accurately predict waveforms and remnant properties. Comparatively few numerical studies have focused on the eccentric regime in the past [147, 181, 182], but more recently systematic efforts in GW modeling have expanded into the eccentric regime [183]. We hope that our findings have further demonstrated the fertile ground of this class of binaries and that they will spark future work in this direction.

Chapter 8

Conclusions

In this Thesis we have provided source modelling for General Relativity and massive Scalar Tensor theory through the use of numerical simulations.

We have studied the stability of our NS solutions by comparing the binding energy of models with the same baryon mass. In agreement with the literature, we observe that GR like solutions are unstable if scalarized solutions with the same baryon mass exist. We also deduce that when there are several scalarized solutions, the model with the larger radius is stable.

We have performed core collapse simulations of stars and have studied the phenomenology of the scalarization over the astrophysically plausible range of stellar progenitor masses and metallicities, as well as a large part of the parameter space of the class of modified theories of gravity. There are several potential smoking gun signatures of a departure from general relativity associated with this process. These signatures could show up within existing LIGO-Virgo searches.

We have identified a remarkably simple and straightforward classification scheme of the resulting collapse events. For any given set of parameters, the collapse leads to one of three end states, a weakly scalarized neutron star, a strongly scalarized neutron star or a black hole, possibly formed in multiple stages. The latter two end states can lead to strong gravitational-wave signals that may be detectable in present continuous-wave searches with ground-based detectors. We have obtained qualitatively different collapse scenarios from those occuring in GR, such as delayed black hole formation and multi-stage collapse into neutron stars. We have identified a very sharp boundary in the parameter space that separates events with strong gravitational-wave emission from those with negligible radiation.

The dispersive nature of wave propagation for massive fields leads to a characteristic inverse chirp signal, where low frequency modes arrive after high frequency modes. We have obtained and verified numerically a semi-analytic formula for the amplitude and frequency of the GWs at large distances from the source. We have predicted that signals would be long-lived and their amplitudes large enough to justify searches directed at historical nearby supernovae. Using this formula we have studied the propagation of the signals resulting from core collapse to distances comparable to those between the interferometers and the sources of gravitational waves. We have also considered the scope for observing the resulting scalar GWs with present and future GW detectors.

Next we have expanded the scalar potential to include self-interacting terms and studied how these additional parameters influence the GWs. To this end, we have extracted the gravitational radiation from numerical simulations of stellar collapse for a range of potentials with higher-order terms in addition to the quadratic mass term. Our study includes cases of collapse to neutron stars and black holes and we find the strong inverse-chirp signals obtained for the purely quadratic potential to be exceptionally robust under changes in the potential at higher orders; quartic and sextic terms in the potential lead to noticeable differences in the wave signal only if their contribution is amplified, implying a relative fine-tuning to within five or more orders of magnitude between the mass and self-interaction parameters.

Finally, we have performed numerical-relativity simulations of eccentric merging black holes with initially antiparallel spins lying in the orbital plane (the so-called superkick configuration). Binary eccentricity boosts the recoil of the merger remnant by up to 25%. The increase in the energy flux is much more modest, and therefore this kick enhancement is mainly due to asymmetry in the binary dynamics. Our findings might have important consequences for the retention of stellar-mass black holes in star clusters and supermassive black holes in galactic hosts.

The work presented in this thesis suggests various directions for future research. Despite covering a wide range of EOSs in our simulations so far by using piece-wise polytropes that mimic in closed analytic form the stiffening of the core of the star when it reaches nuclear densities and the thermal effects of the hydrodynamic shock passing through the star, it is important to also explore modern finite temperature EOSs. Furthermore, we can relax the spherical symmetry by considering rotating solutions: there has been an abundance of studies of the stationary solutions for slowly and rapidly rotating stars, but the dynamical formation of compact objects through core collapse remained largely unexplored. As previously mentioned, the GW signals propagate dispersively, spreading out in time; long-lived signals from different sources can overlap to form a stochastic background of scalar GWs with a characteristic spectral shape around the frequency of the scalar mass. A study of these potential backgrounds would benefit LIGO-VIRGO searches in this direction.

In recent years, phenomena akin to spontaneous scalarization have been highlighted in the case of other modified gravity theories, such as spontaneous growth of vector fields (or “spontaneous vectorization”) and spontaneous scalarization of charged black holes. It thus appears that spontaneous scalarization or vectorization is a particular case of a more general phenomenon that appears in modified theories of gravity. It would be interesting to explore how generic this phenomenon is among modified gravity theories, and whether smoking gun signatures such as those generated by stellar collapse in massive ST gravity might in fact be more common for a wider range of theories and physical systems.

Through this study of some of the predictions of GR and deviations from those predictions in alternative theories of gravity, we have filled a small but significant gap in the cavern that represents our ignorance with regards to the laws governing the Universe. This effort should help researchers as a community be closer to a unified theory, one infinitesimal step at a time.

References

[1] Albert Einstein. The field equations of gravitation. *Sitzungsber. Preuss. Akad. Wiss. Berlin (Math. Phys.)*, 1915:844–847, 1915.

[2] Albert Einstein. Approximative integration of the field equations of gravitation. *Sitzungsber.Preuss.Akad.Wiss.Berlin (Math.Phys.)*, pages 688–696, 1916.

[3] Albert Einstein. The foundation of the general theory of relativity. *Annalen Phys.*, 49(7):769–822, 1916.

[4] Albert Einstein. Explanation of the perihelion motion of mercury from the general theory of relativity. *Sitzungsber.Preuss.Akad.Wiss.Berlin (Math.Phys.)*, pages 831–839, 1915.

[5] Clifford M Will. The confrontation between general relativity and experiment. *Living Rev. Relativ.*, 17(1):4, June 2014.

[6] Dimitrios Psaltis. Probes and tests of Strong-Field gravity with observations in the electromagnetic spectrum. *Living Rev. Relativ.*, 11(1):9, November 2008.

[7] Justin Alsing, Emanuele Berti, Clifford M Will, and Helmut Zaglauer. Gravitational radiation from compact binary systems in the massive Brans-Dicke theory of gravity. *Phys. Rev. D*, 85(6):064041, March 2012.

[8] David N Spergel. The dark side of cosmology: dark matter and dark energy. *Science*, 347(6226):1100–1102, March 2015.

[9] Emanuele Berti, Enrico Barausse, Vitor Cardoso, Leonardo Gualtieri, Paolo Pani, Ulrich Sperhake, Leo C Stein, Norbert Wex, Kent Yagi, Tessa Baker, and Others. Testing general relativity with present and future astrophysical observations. *Classical Quantum Gravity*, 32(24):243001, 2015.

[10] LIGO Scientific Collaboration and Virgo Collaboration. Observation of gravitational waves from a binary black hole merger. *Phys. Rev. Lett.*, 116(6):061102, February 2016.

[11] Ligo Scientific Collaboration and Virgo Collaboration. Tests of general relativity with GW150914. *Phys. Rev. Lett.*, 116(22):221101, June 2016.

[12] Nicolás Yunes, Kent Yagi, and Frans Pretorius. Theoretical physics implications of the binary black-hole mergers GW150914 and GW151226. *Phys. Rev. D*, 94(8):084002, October 2016.

[13] Thibault Damour and Gilles Esposito-Farese. Tensor-multi-scalar theories of gravitation. *Classical Quantum Gravity*, 9(9):2093, 1992.

[14] Yasunori Fujii and Kei-Ichi Maeda. *The Scalar-Tensor Theory of Gravitation.* Cambridge University Press, January 2003.

[15] T Damour and G Esposito-Farèse. Nonperturbative strong-field effects in tensor-scalar theories of gravitation. *Phys. Rev. Lett.*, 70(15):2220–2223, April 1993.

[16] Frans Pretorius. Evolution of binary black hole spacetimes. July 2005.

[17] M Campanelli, C O Lousto, P Marronetti, and Y Zlochower. Accurate evolutions of orbiting Black-Hole binaries without excision. November 2005.

[18] John G Baker, Joan Centrella, Dae-Il Choi, Michael Koppitz, and James van Meter. Gravitational wave extraction from an inspiraling configuration of merging black holes. November 2005.

[19] Miguel Alcubierre. *Introduction to 3+1 Numerical Relativity.* OUP Oxford, April 2008.

[20] Robert M Wald. *General Relativity.* University of Chicago Press, 1984.

[21] R Arnowitt, S Deser, and C W Misner. The dynamics of general relativity. May 2004.

[22] Takashi Nakamura, Kenichi Oohara, and Yasufumi Kojima. General relativistic collapse to black holes and gravitational waves from black holes. *Progr. Theoret. Phys.*, 90:1–218, January 1987.

[23] M Shibata and T Nakamura. Evolution of three-dimensional gravitational waves: Harmonic slicing case. *Phys. Rev. D Part. Fields*, 52(10):5428–5444, November 1995.

[24] Thomas W Baumgarte and Stuart L Shapiro. On the numerical integration of einstein's field equations. October 1998.

[25] Eric Gourgoulhon. 3+1 formalism and bases of numerical relativity. March 2007.

[26] Ulrich Sperhake, Christopher J Moore, Roxana Rosca, Michalis Agathos, Davide Gerosa, and Christian D Ott. Long-Lived inverse chirp signals from Core-Collapse in massive Scalar-Tensor gravity. *Phys. Rev. Lett.*, 119(20):201103, November 2017.

[27] The LIGO Scientific Collaboration. Advanced LIGO. *Classical Quantum Gravity*, 32(7):074001, March 2015.

[28] F Acernese, M Agathos, K Agatsuma, and others. Advanced virgo: a second-generation interferometric gravitational wave detector. *Classical Quantum Gravity*, 32(2):024001, December 2014.

[29] LIGO Scientific Collaboration and Virgo Collaboration. Tests of general relativity with the binary black hole signals from the LIGO-Virgo catalog GWTC-1. March 2019.

[30] LIGO Scientific Collaboration and Virgo Collaboration. Tests of general relativity with GW170817. *Phys. Rev. Lett.*, 123(1):011102, July 2019.

[31] Giuseppe Papallo. *Causality and the initial value problem in Modified Gravity.* PhD thesis, University of Cambridge, 2019.

[32] Térence Delsate, David Hilditch, and Helvi Witek. Initial value formulation of dynamical Chern-Simons gravity. *Phys. Rev. D*, 91(2):024027, January 2015.

[33] Giuseppe Papallo and Harvey S Reall. On the local well-posedness of lovelock and horndeski theories, 2017.

[34] Gwyneth Allwright and Luis Lehner. Towards the nonlinear regime in extensions to GR: assessing possible options. *Classical Quantum Gravity*, 36(8):084001, April 2019.

[35] Richard Brito, Alexandra Terrana, Matthew Johnson, and Vitor Cardoso. The nonlinear dynamical stability of infrared modifications of gravity. September 2014.

[36] Maria Okounkova, Leo C Stein, Mark A Scheel, and Daniel A Hemberger. Numerical binary black hole mergers in dynamical Chern-Simons gravity: Scalar field. *Phys. Rev. D*, 96(4):044020, August 2017.

[37] Maria Okounkova, Leo C Stein, Mark A Scheel, and Saul A Teukolsky. Numerical binary black hole collisions in dynamical Chern-Simons gravity. June 2019.

[38] Helvi Witek, Leonardo Gualtieri, Paolo Pani, and Thomas P Sotiriou. Black holes and binary mergers in scalar Gauss-Bonnet gravity: Scalar field dynamics. *Phys. Rev. D*, 99(6):064035, March 2019.

[39] M A Scheel, S L Shapiro, and S A Teukolsky. Collapse to black holes in Brans-Dicke theory. i. horizon boundary conditions for dynamical spacetimes. *Phys. Rev. D Part. Fields*, 51(8):4208–4235, April 1995.

[40] Tomohiro Harada, Takeshi Chiba, Ken-Ichi Nakao, and Takashi Nakamura. Scalar gravitational wave from Oppenheimer-Snyder collapse in scalar-tensor theories of gravity. *Phys. Rev. D*, 55(4):2024–2037, February 1997.

[41] Jérôme Novak. Spherical neutron star collapse toward a black hole in a tensor-scalar theory of gravity. *Phys. Rev. D*, 57(8):4789–4801, April 1998.

[42] Jérôme Novak. Neutron star transition to a strong-scalar-field state in tensor-scalar gravity. *Phys. Rev. D*, 58(6):064019, August 1998.

[43] Jérôme Novak and José M Ibáñez. Gravitational waves from the collapse and bounce of a stellar core in Tensor-Scalar gravity. *ApJ*, 533(1):392, December 2008.

[44] Carlos Palenzuela, Enrico Barausse, Marcelo Ponce, and Luis Lehner. Dynamical scalarization of neutron stars in scalar-tensor gravity theories. *Phys. Rev. D*, 89(4):044024, February 2014.

[45] Carlos Palenzuela and Steven L Liebling. Constraining scalar-tensor theories of gravity from the most massive neutron stars. *Phys. Rev. D*, 93(4):044009, February 2016.

[46] Davide Gerosa, Ulrich Sperhake, and Christian D Ott. Numerical simulations of stellar collapse in scalar-tensor theories of gravity. *Classical Quantum Gravity*, 33(13):135002, May 2016.

[47] Laura Bernard. Dynamics of compact binary systems in scalar-tensor theories: Equations of motion to the third post-newtonian order, 2018.

[48] Laura Bernard. Dynamics of compact binary systems in scalar-tensor theories. II. center-of-mass and conserved quantities to 3PN order, 2019.

[49] Paulo C C Freire, Norbert Wex, Gilles Esposito-Farèse, Joris P W Verbiest, Matthew Bailes, Bryan A Jacoby, Michael Kramer, Ingrid H Stairs, John Antoniadis, and Gemma H Janssen. The relativistic pulsar-white dwarf binary PSR J1738 0333 - II. the most stringent test of scalar-tensor gravity, 2012.

[50] John Antoniadis, Paulo C C Freire, and Et al Wex. A massive pulsar in a compact relativistic binary. *Science*, 340(6131):448, 1233232, April 2013.

[51] Norbert Wex. Testing relativistic gravity with radio pulsars. February 2014.

[52] B Bertotti, L Iess, and P Tortora. A test of general relativity using radio links with the cassini spacecraft. *Nature*, 425(6956):374–376, September 2003.

[53] Fethi M Ramazanoğlu and Frans Pretorius. Spontaneous scalarization with massive fields. *Phys. Rev. D*, 93(6):064005, March 2016.

[54] T Damour and G Esposito-Farèse. Tensor-scalar gravity and binary-pulsar experiments. *Phys. Rev. D Part. Fields*, 54(2):1474–1491, July 1996.

[55] Marcelo Salgado. The cauchy problem of scalar–tensor theories of gravity. *Classical Quantum Gravity*, 23(14):4719, July 2006.

[56] Marcelo Salgado, David Martínez-del Río, Miguel Alcubierre, and Darío Núñez. Hyperbolicity of scalar-tensor theories of gravity. *Phys. Rev. D*, 77(10):104010, May 2008.

[57] Daniela D Doneva and Stoytcho S Yazadjiev. Rapidly rotating neutron stars with a massive scalar field—structure and universal relations. *J. Cosmol. Astropart. Phys.*, 2016(11):019, November 2016.

[58] Stoytcho S Yazadjiev, Daniela D Doneva, and Dimitar Popchev. Slowly rotating neutron stars in scalar-tensor theories with a massive scalar field. *Phys. Rev. D*, 93(8):084038, April 2016.

[59] Daniela D Doneva, Stoytcho S Yazadjiev, Nikolaos Stergioulas, and Kostas D Kokkotas. Differentially rotating neutron stars in scalar-tensor theories of gravity, 2018.

[60] Michael Horbatsch, Hector O Silva, Davide Gerosa, Paolo Pani, Emanuele Berti, Leonardo Gualtieri, and Ulrich Sperhake. Tensor-multi-scalar theories: relativistic stars and 3 1 decomposition, 2015.

[61] Fethi M Ramazanoğlu. Spontaneous growth of vector fields in gravity. *Phys. Rev. D*, 96(6):064009, September 2017.

[62] Fethi M Ramazanoğlu. Spontaneous tensorization from curvature coupling and beyond. *Phys. Rev. D*, 99(8):084015, April 2019.

[63] Daniela D Doneva and Stoytcho S Yazadjiev. Topological neutron stars in tensor-multi-scalar theories of gravity. November 2019.

[64] Peter G Bergmann. Comments on the scalar-tensor theory. *Int. J. Theor. Phys.*, 1(1):25–36, May 1968.

[65] Robert V Wagoner. Scalar-Tensor theory and gravitational waves. *Phys. Rev. D*, 1(12):3209–3216, June 1970.

[66] Evan O'Connor and Christian D Ott. A new Open-Source code for Spherically-Symmetric stellar collapse to neutron stars and black holes. December 2009.

[67] Thibault Damour. Binary systems as Test-Beds of gravity theories. In Monica Colpi, Piergiorgio Casella, Vittorio Gorini, Ugo Moschella, and Andrea Possenti, editors, *Physics of Relativistic Objects in Compact Binaries: From Birth to Coalescence*, pages 1–41. Springer Netherlands, Dordrecht, 2009.

[68] Irwin I Shapiro. Solar system tests of general relativity: Recent results and present plans. In *General relativity and gravitation, 1989*. 1990.

[69] James G Williams, Slava G Turyshev, and Dale H Boggs. Progress in lunar laser ranging tests of relativistic gravity. November 2004.

[70] Tomohiro Harada. Neutron stars in scalar-tensor theories of gravity and catastrophe theory. January 1998.

[71] Manuel Hohmann, Laur Jarv, Piret Kuusk, and Erik Randla. Post-Newtonian parameters gamma and beta of scalar-tensor gravity with a general potential. August 2013.

[72] Saul A Teukolsky. On the stability of the iterated Crank-Nicholson method in numerical relativity. September 1999.

[73] A Hewish, S J Bell, J D H Pilkington, P F Scott, and R A Collins. Observation of a rapidly pulsating radio source, 1968.

[74] Luciano Rezzolla, Pierre Pizzochero, David Ian Jones, Nanda Rea, and Isaac Vidaña. *The Physics and Astrophysics of Neutron Stars*. Springer, 2018.

[75] H Dimmelmeier, J A Font, and E Müller. Relativistic simulations of rotational core collapse II. collapse dynamics and gravitational radiation. *Astron. Astrophys. Suppl. Ser.*, 393(2):523–542, 2002.

[76] H T Janka, T Zwerger, and others. Does artificial viscosity destroy prompt type-II supernova explosions? *Astronomy*, 1993.

[77] T Zwerger and E Mueller. Dynamics and gravitational wave signature of axisymmetric rotational core collapse. *Astron. Astrophys.*, 1997.

[78] H Dimmelmeier, C D Ott, H-T Janka, A Marek, and E Müller. Generic gravitational-wave signals from the collapse of rotating stellar cores. *Phys. Rev. Lett.*, 98(25):251101, June 2007.

[79] Harald Dimmelmeier, Christian D Ott, Andreas Marek, and Hans-Thomas Janka. The gravitational wave burst signal from core collapse of rotating stars. June 2008.

[80] Stuart L Shapiro and Saul A Teukolsky. *Black Holes, White Dwarfs, and Neutron Stars: The Physics of Compact Objects*. John Wiley & Sons, November 2008.

[81] H Shen, H Toki, K Oyamatsu, and K Sumiyoshi. Relativistic equation of state for Core-Collapse supernova simulations. *ApJS*, 197(2):20, November 2011.

[82] J M Lattimer, C J Pethick, D G Ravenhall, and D Q Lamb. Physical properties of hot, dense matter: The general case. *Nuclear Physics, Section A*, 432(3):646–742, 1985.

[83] James M Lattimer and Douglas F Swesty. A generalized equation of state for hot, dense matter. *Nucl. Phys. A*, 535:331–376, December 1991.

[84] Hong Shen, Hiroshi Toki, Kazuhiro Oyamatsu, and Kohsuke Sumiyoshi. Relativistic equation of state of nuclear matter for supernova explosion. *Progr. Theoret. Phys.*, 100(5):1013–1031, November 1998.

[85] H Shen, H Toki, K Oyamatsu, and K Sumiyoshi. Relativistic equation of state of nuclear matter for supernova and neutron star. May 1998.

[86] William T Vetterling, Saul A Teukolsky, William H Press, and Brian P Flannery. *Numerical recipes in C: the art of scientific computing*. Cambridge university press, 1999.

[87] Richard Brito, Vitor Cardoso, Caio F B Macedo, Hirotada Okawa, and Carlos Palenzuela. Interaction between bosonic dark matter and stars. December 2015.

[88] Richard Brito, Vitor Cardoso, and Hirotada Okawa. Accretion of dark matter by stars. August 2015.

[89] Marcella Ugliano, H Thomas Janka, Andreas Marek, and Almudena Arcones. Progenitor-Explosion connection and remnant birth masses for Neutrino-Driven supernovae of Iron-Core progenitors. May 2012.

[90] A Burrows, L Dessart, E Livne, C D Ott, and J Murphy. Simulations of magnetically driven supernova and hypernova explosions in the context of rapid rotation. *ApJ*, 664(1):416, December 2008.

[91] Takuya Matsuda and Hidekazu Nariai. Hydrodynamic calculations of spherical gravitational collapse in the Scalar-Tensor theory of gravity. *Progr. Theoret. Phys.*, 49(4):1195–1204, April 1973.

[92] M A Scheel, S L Shapiro, and S A Teukolsky. Collapse to black holes in Brans-Dicke theory. II. comparison with general relativity. *Phys. Rev. D Part. Fields*, 51(8):4236–4249, April 1995.

[93] Masaru Shibata, Kenichi Nakao, and Takashi Nakamura. Scalar-type gravitational wave emission from gravitational collapse in Brans-Dicke theory: Detectability by a laser interferometer, 1994.

[94] Stellar evolution. https://2sn.org/stellarevolution/. Accessed: NA-NA-NA.

[95] LIGO Scientific Collaboration and Virgo Collaboration. Comprehensive all-sky search for periodic gravitational waves in the sixth science run LIGO data. *Phys. Rev. D*, 94(4):042002, August 2016.

[96] LIGO Scientific Collaboration and Virgo Collaboration. Upper limits on gravitational waves from scorpius X-1 from a Model-Based Cross-Correlation search in advanced LIGO data. June 2017.

[97] Maximiliano Isi, Matthew Pitkin, and Alan J Weinstein. Probing dynamical gravity with the polarization of continuous gravitational waves. *Phys. Rev. D*, 96(4):042001, August 2017.

[98] C J Moore, R H Cole, and C P L Berry. Gravitational-wave sensitivity curves. *Classical Quantum Gravity*, 32(1):015014, December 2014.

[99] Roxana Rosca-Mead, Christopher J Moore, Michalis Agathos, and Ulrich Sperhake. Inverse-chirp signals and spontaneous scalarisation with self-interacting potentials in stellar collapse. *Classical Quantum Gravity*, 36(13):134003, June 2019.

[100] Patrick Chi-Kit Cheong and Tjonnie Guang Feng Li. Numerical studies on core collapse supernova in self-interacting massive scalar-tensor gravity, 2019.

[101] S W Hawking. Black holes in the Brans-Dicke. *Commun. Math. Phys.*, 25(2):167–171, June 1972.

[102] Kip S Thorne and John J Dykla. Black holes in the Dicke-Brans theory of gravity. *Astrophys. J.*, 166:L35, 1971.

[103] Eric Poisson. The motion of point particles in curved spacetime. *Living Rev. Relativ.*, 7(1):6, May 2004.

[104] U Sperhake, R Rosca-Mead, D Gerosa, and E Berti. Amplification of superkicks in black-hole binaries through orbital eccentricity. October 2019.

[105] W B Bonnor, M A Rotenberg, and Louis Rosenhead. Transport of momentum by gravitational waves: the linear approximation. *Proc. R. Soc. Lond. A Math. Phys. Sci.*, 265(1320):109–116, December 1961.

[106] Asher Peres. Classical radiation recoil. *Phys. Rev.*, 128(5):2471–2475, December 1962.

[107] Jacob D Bekenstein. Gravitational-Radiation recoil and runaway black holes. *Astrophys. J.*, 183:657–664, July 1973.

[108] M J Fitchett. The influence of gravitational wave momentum losses on the centre of mass motion of a newtonian binay system. *Mon. Not. R. Astron. Soc.*, 203:1049–1062, June 1983.

[109] Marc Favata, Scott A Hughes, and Daniel E Holz. How black holes get their kicks: Gravitational radiation recoil revisited. February 2004.

[110] Luc Blanchet, Moh'd S S Qusailah, and Clifford M Will. Gravitational recoil of inspiralling Black-Hole binaries to second Post-Newtonian order. July 2005.

[111] J A Gonzalez, M D Hannam, U Sperhake, B Brugmann, and S Husa. Supermassive recoil velocities for binary black-hole mergers with antialigned spins. February 2007.

[112] Manuela Campanelli, Carlos O Lousto, Yosef Zlochower, and David Merritt. Maximum gravitational recoil. February 2007.

[113] Wolfgang Tichy and Pedro Marronetti. Binary black hole mergers: large kicks for generic spin orientations. March 2007.

[114] Carlos O Lousto and Yosef Zlochower. Hangup kicks: Still larger recoils by partial Spin/Orbit alignment of Black-Hole binaries. August 2011.

[115] Carlos O Lousto and Yosef Zlochower. Nonlinear gravitational recoil from the mergers of precessing Black-Hole binaries. November 2012.

[116] Bernd Bruegmann, Jose Gonzalez, Mark Hannam, Sascha Husa, and Ulrich Sperhake. Exploring black hole superkicks. July 2007.

[117] Frans Pretorius. Binary black hole coalescence. October 2007.

[118] Jeremy D Schnittman, Alessandra Buonanno, James R van Meter, John G Baker, William D Boggs, Joan Centrella, Bernard J Kelly, and Sean T McWilliams. Anatomy of the binary black hole recoil: A multipolar analysis. July 2007.

[119] Davide Gerosa and Christopher J Moore. Black hole kicks as new gravitational wave observables. June 2016.

[120] Juan Calderón Bustillo, James A Clark, Pablo Laguna, and Deirdre Shoemaker. Tracking black hole kicks from gravitational wave observations. June 2018.

[121] James Healy, Frank Herrmann, Ian Hinder, Deirdre M Shoemaker, Pablo Laguna, and Richard A Matzner. Superkicks in hyperbolic encounters of binary black holes. July 2008.

[122] Ulrich Sperhake, Emanuele Berti, Vitor Cardoso, Frans Pretorius, and Nicolas Yunes. Superkicks in ultrarelativistic encounters of spinning black holes. November 2010.

[123] Joan M Centrella, John G Baker, Bernard J Kelly, and James R van Meter. Black-hole binaries, gravitational waves, and numerical relativity. October 2010.

[124] Ulrich Sperhake. Gravitational recoil and astrophysical impact, 2015.

[125] Davide Gerosa, François Hébert, and Leo C Stein. Black-hole kicks from numerical-relativity surrogate models. February 2018.

[126] David Merritt, Milos Milosavljevic, Marc Favata, Scott A Hughes, and Daniel E Holz. Consequences of gravitational radiation recoil. February 2004.

[127] Matthew J Benacquista and Jonathan M B Downing. Relativistic binaries in globular clusters. October 2011.

[128] Jose A Gonzalez, Ulrich Sperhake, Bernd Bruegmann, Mark Hannam, and Sascha Husa. Total recoil: the maximum kick from nonspinning black-hole binary inspiral. October 2006.

[129] J Morawski, M Giersz, A Askar, and K Belczynski. MOCCA-SURVEY database i: Assessing GW kick retention fractions for BH-BH mergers in globular clusters. February 2018.

[130] Kelly Holley-Bockelmann, Kayhan Gultekin, Deirdre Shoemaker, and Nico Yunes. Gravitational wave recoil and the retention of intermediate mass black holes. July 2007.

[131] Fabio Antonini and Frederic A Rasio. Merging black hole binaries in galactic nuclei: implications for advanced-LIGO detections. June 2016.

[132] Nicholas C Stone, Brian D Metzger, and Zoltan Haiman. Assisted inspirals of stellar mass black holes embedded in AGN disks: Solving the “final AU problem”. February 2016.

[133] Imre Bartos, Bence Kocsis, Zoltán Haiman, and Szabolcs Márka. Rapid and bright stellar-mass binary black hole mergers in active galactic nuclei. February 2016.

[134] Davide Gerosa and Emanuele Berti. Escape speed of stellar clusters from multiple-generation black-hole mergers in the upper mass gap. *Phys. Rev. D*, 100(4):041301, August 2019.

[135] Davide Gerosa and Alberto Sesana. Missing black holes in brightest cluster galaxies as evidence for the occurrence of superkicks in nature. May 2014.

[136] Laura Blecha and Abraham Loeb. Effects of gravitational-wave recoil on the dynamics and growth of supermassive black holes. May 2008.

[137] A Sesana. Extreme recoils: impact on the detection of gravitational waves from massive black hole binaries. July 2007.

[138] Tamara Bogdanovic, Christopher S Reynolds, and M Coleman Miller. Alignment of the spins of supermassive black holes prior to coalescence. March 2007.

[139] Giuseppe Lodato and Davide Gerosa. Black hole mergers: do gas discs lead to spin alignment? November 2012.

[140] M Coleman Miller and Julian H Krolik. Alignment of supermassive black hole binary orbits and spins. July 2013.

[141] Davide Gerosa, Benedetta Veronesi, Giuseppe Lodato, and Giovanni Rosotti. Spin alignment and differential accretion in merging black hole binaries. March 2015.

[142] Michael Kesden, Ulrich Sperhake, and Emanuele Berti. Relativistic suppression of black hole recoils. March 2010.

[143] Emanuele Berti, Michael Kesden, and Ulrich Sperhake. Effects of post-newtonian spin alignment on the distribution of Black-Hole recoils. March 2012.

[144] Latham Boyle, Michael Kesden, and Samaya Nissanke. Binary black hole merger: symmetry and the spin expansion. September 2007.

[145] Latham Boyle and Michael Kesden. The spin expansion for binary black hole merger: new predictions and future directions. December 2007.

[146] Carlos F Sopuerta, Nicolas Yunes, and Pablo Laguna. Gravitational recoil velocities from eccentric binary black hole mergers. November 2006.

[147] U Sperhake, E Berti, V Cardoso, J A Gonzalez, B Bruegmann, and M Ansorg. Eccentric binary black-hole mergers: The transition from inspiral to plunge in general relativity. October 2007.

[148] Raoul-Martin Memmesheimer, Achamveedu Gopakumar, and Gerhard Schäfer. Third post-newtonian accurate generalized quasi-keplerian parametrization for compact binaries in eccentric orbits. July 2004.

[149] Ulrich Sperhake. Binary black-hole evolutions of excision and puncture data. June 2006.

[150] G Allen, T Goodale, J Masso, and E Seidel. The cactus computational toolkit and using distributed computing to collide neutron stars. In *Proceedings. The Eighth International Symposium on High Performance Distributed Computing (Cat. No.99TH8469)*, pages 57–61, August 1999.

[151] Cactus code. http://cactuscode.org/. Accessed: 2019-11-13.

[152] Sascha Husa, Jose A Gonzalez, Mark Hannam, Bernd Bruegmann, and Ulrich Sperhake. Reducing phase error in long numerical binary black hole evolutions with sixth order finite differencing. June 2007.

[153] Erik Schnetter, Scott H Hawley, and Ian Hawke. Evolutions in 3D numerical relativity using fixed mesh refinement. October 2003.

[154] Carpet — AMR for cactus. https://carpetcode.org/. Accessed: 2019-11-13.

[155] Jonathan Thornburg. Finding apparent horizons in numerical relativity. August 1995.

[156] Jonathan Thornburg. A fast Apparent-Horizon finder for 3-dimensional cartesian grids in numerical relativity. June 2003.

[157] Steven Brandt and Bernd Bruegmann. A simple construction of initial data for multiple black holes. March 1997.

[158] Jeffrey M Bowen and James W York. Time-asymmetric initial data for black holes and black-hole collisions. *Phys. Rev. D*, 21(8):2047–2056, April 1980.

[159] Marcus Ansorg, Bernd Bruegmann, and Wolfgang Tichy. A single-domain spectral method for black hole puncture data. April 2004.

[160] G B Cook and J W York, Jr. Apparent horizons for boosted or spinning black holes. *Phys. Rev. D Part. Fields*, 41(4):1077–1085, February 1990.

[161] S Dain, C O Lousto, and R Takahashi. New conformally flat initial data for spinning black holes. January 2002.

[162] Manuela Campanelli, Carlos O Lousto, Yosef Zlochower, Badri Krishnan, and David Merritt. Spin flips and precession in Black-Hole-Binary mergers. December 2006.

[163] Demetrios Christodoulou. Reversible and irreversible transformations in Black-Hole physics. *Phys. Rev. Lett.*, 25(22):1596–1597, November 1970.

[164] Manuela Campanelli, Carlos O Lousto, Yosef Zlochower, and David Merritt. Large merger recoils and spin flips from generic Black-Hole binaries. January 2007.

[165] Milton Ruiz, Miguel Alcubierre, Dario Nunez, and Ryoji Takahashi. Multipole expansions for energy and momenta carried by gravitational waves. July 2007.

[166] William G Cook, Diandian Wang, and Ulrich Sperhake. Orbiting black-hole binaries and apparent horizons in higher dimensions. August 2018.

[167] Ulrich Sperhake, Bernd Bruegmann, Doreen Mueller, and Carlos F Sopuerta. Black-hole binaries go to eleven orbits. December 2010.

[168] Carlos F Sopuerta, Nicolas Yunes, and Pablo Laguna. Gravitational recoil from binary black hole mergers: the Close-Limit approximation. August 2006.

[169] Fabio Antonini and Hagai Perets. Secular evolution of compact binaries near massive black holes: gravitational wave sources and other exotica. March 2012.

[170] Johan Samsing, Abbas Askar, and Mirek Giersz. MOCCA-SURVEY database i: Eccentric black hole mergers during Binary-Single interactions in globular clusters. December 2017.

[171] László Gondán, Bence Kocsis, Péter Raffai, and Zsolt Frei. Eccentric black hole Gravitational-Wave capture sources in galactic nuclei: Distribution of binary parameters. November 2017.

[172] Michael Zevin, Johan Samsing, Carl Rodriguez, Carl-Johan Haster, and Enrico Ramirez-Ruiz. Eccentric black hole mergers in dense star clusters: The role of Binary-Binary encounters. October 2018.

[173] Giacomo Fragione and Abraham Loeb. Black hole–neutron star mergers from triples. *Mon. Not. R. Astron. Soc.*, 486(3):4443–4450, July 2019.

[174] Johan Samsing, Daniel J D'Orazio, Kyle Kremer, Carl L Rodriguez, and Abbas Askar. Gravitational-wave captures of single black holes in globular clusters. July 2019.

[175] Carl L Rodriguez, Pau Amaro-Seoane, Sourav Chatterjee, and Frederic A Rasio. Post-Newtonian dynamics in dense star clusters: Highly-Eccentric, Highly-Spinning, and repeated binary black hole mergers. December 2017.

[176] Carl L Rodriguez, Michael Zevin, Pau Amaro-Seoane, Sourav Chatterjee, Kyle Kremer, Frederic A Rasio, and Claire S Ye. Black holes: The next generation—repeated mergers in dense star clusters and their gravitational-wave properties. *Phys. Rev. D*, 100(4):043027, August 2019.

[177] Motohiro Enoki and Masahiro Nagashima. The effect of orbital eccentricity on gravitational wave background radiation from supermassive black hole binaries. September 2006.

[178] A Sesana. Self consistent model for the evolution of eccentric massive black hole binaries in stellar environments: implications for gravitational wave observations. June 2010.

[179] E A Huerta, Sean T McWilliams, Jonathan R Gair, and Stephen R Taylor. Detection of eccentric supermassive black hole binaries with pulsar timing arrays: Signal-to-noise ratio calculations. April 2015.

[180] S R Taylor, E A Huerta, J R Gair, and S T McWilliams. Detecting eccentric supermassive black hole binaries with pulsar timing arrays: Resolvable source strategies. May 2015.

[181] Ian Hinder, Birjoo Vaishnav, Frank Herrmann, Deirdre Shoemaker, and Pablo Laguna. Circularization and final spin in eccentric binary black hole inspirals. October 2007.

[182] Ian Hinder, Frank Herrmann, Pablo Laguna, and Deirdre Shoemaker. Comparisons of eccentric binary black hole simulations with post-newtonian models. June 2008.

[183] Antoni Ramos-Buades, Sascha Husa, Geraint Pratten, Héctor Estellés, Cecilio García-Quirós, Maite Mateu, Marta Colleoni, and Rafel Jaume. A first survey of spinning eccentric black hole mergers: numerical relativity simulations, hybrid waveforms, and parameter estimation. September 2019.

Appendix A

Scalar Tensor Theory conformal transformation

In this section we present summary of the algebra for the conformal transformation from the Jordan frame to the Einstein frame. We start with the Jordan frame action:

$$S = \int dx^4 \sqrt{-g}\left[\frac{F(\phi)}{16\pi G}R - \frac{1}{2}g^{\mu\nu}(\partial_\mu\phi)(\partial_\nu\phi) - V(\phi)\right] + S_m(\psi_m, g_{\mu\nu}). \tag{A.1}$$

A general conformal transformation is defined as:

$$\bar{g}_{\mu\nu} = \Omega^2\left(x\right) g_{\mu\nu}\,, \tag{A.2}$$

where $\Omega\left(x\right)$ is an arbitrary function of the space-time coordinate, x^α. This is equivalent to transforming the line element according to

$$d\bar{s}^2 = \Omega^2\left(x\right) ds^2\,. \tag{A.3}$$

Here we limit ourselves to transformations that preserve the signature of the metric,i.e. we have $\Omega^2 > 0$. From Eq.(A.2) we conclude

$$g^{\mu\nu} = \Omega^2\bar{g}^{\mu\nu}\,, \tag{A.4}$$

$$\sqrt{-g} = \Omega^{-4}\sqrt{-\bar{g}}\,. \tag{A.5}$$

The Jordan frame Christoffel symbol,

$$\Gamma^\mu_{\nu\lambda} = \frac{1}{2}g^{\mu\rho}\left(\partial_\nu g_{\rho\lambda} + \partial_\lambda g_{\rho\nu} - \partial_\rho g_{\nu\lambda}\right)\,, \tag{A.6}$$

can be written in terms of the Christoffel symbol of the conformal frame

$$\Gamma^{\mu}_{\nu\lambda} = \bar{\Gamma}^{\mu}_{\nu\lambda} - \left(f_{\nu}\delta^{\mu}_{\nu} - \bar{f}^{\mu}\bar{g}_{\nu\lambda}\right) \tag{A.7}$$

where

$$f = \ln\left(\Omega\right) \,, \tag{A.8}$$

$$f_{\nu} = \frac{\partial_{\nu}\left(\Omega\right)}{\Omega} = \partial_{\nu} f \,, \tag{A.9}$$

$$\bar{f}^{\mu} = \bar{g}^{\mu\nu} f_{\nu} \,. \tag{A.10}$$

After some algebra (see Appendix G of [14]), one obtains

$$R = \Omega^{2}\left(\bar{R} + 6\bar{\Box} f - 6\bar{g}^{\mu\nu} f_{\mu} f_{\nu}\right) \,, \tag{A.11}$$

where the d'Alambertian operator ($\Box \equiv g^{\mu\nu}\nabla_{\mu}\nabla_{\nu}$) in the conformal metric is

$$\bar{\Box} f = \frac{1}{\sqrt{-\bar{g}}}\partial_{\mu}\left(\sqrt{-\bar{g}}\bar{g}^{\mu\nu}\partial_{\nu} f\right) \tag{A.12}$$

These are all the terms that appear in the Lagrangian, so we can apply the conformal transformation to the action as well:

$$\mathcal{L} = \sqrt{-g}\left[\underbrace{\frac{F(\phi)R}{16\pi G}}_{\mathcal{L}_1} - \underbrace{\frac{1}{2} g^{\mu\nu}\left(\partial_{\mu}\phi\right)\left(\partial_{\nu}\phi\right)}_{\mathcal{L}_2} - V(\phi) + L_{\text{matter}}\right] \tag{A.13}$$

$$\mathcal{L}_1 = \sqrt{-g}\frac{F(\phi)}{16\pi G} = \Omega^{-4}\sqrt{-\bar{g}} \times \frac{F(\phi)}{16\pi G} \times \Omega^{2}\left(\bar{R} + 6\bar{\Box} f - 6\bar{g}^{\mu\nu} f_{\mu} f_{\nu}\right) \tag{A.14}$$

$$\Longrightarrow \mathcal{L}_1 = \sqrt{-\bar{g}} \times \frac{\Omega^{-2}F(\phi)}{16\pi G}\left(\bar{R} + 6\bar{\Box} f - 6\bar{g}^{\mu\nu} f_{\mu} f_{\nu}\right) \tag{A.15}$$

We want to use the conformal transformation to rewrite the action as the Einstein-Hilbert action with a scalar field, so want to be left with only $\sqrt{-\bar{g}}\bar{R}$ in $\mathcal{L}$; Ω is an arbitrary function, so we chose $\Omega^{-2}F(\phi) = 1$. This implies

$$\Omega = F^{\frac{1}{2}} \,. \tag{A.16}$$

The term

$$\bar{\Box} f = \frac{1}{\sqrt{-\bar{g}}}\partial_{\mu}\left(\sqrt{-\bar{g}}\bar{g}^{\mu\nu}\partial_{\nu} f\right) \,. \tag{A.17}$$

can be eliminated through integration by parts.

$$f_\mu = \frac{\partial_\mu \Omega}{\Omega} = \frac{\partial_\mu F^{\frac{1}{2}}}{F^{\frac{1}{2}}} = \frac{1}{2}\frac{\partial_\mu F}{F} = \frac{F'}{2F}\partial_\mu \phi, \text{ where } F' \equiv \frac{dF}{d\phi} \tag{A.18}$$

Thus

$$\begin{aligned} \mathcal{L}_1 &= \sqrt{-\bar{g}}\frac{1}{16\pi G}\left(\bar{R} - 6\bar{g}^{\mu\nu}\frac{1}{4}\times\left(\frac{F'}{F}\right)^2 \partial_\mu\phi\partial_\nu\phi\right), &(A.19)\\ \mathcal{L}_2 &= \sqrt{-g}\left(-\frac{1}{2}g^{\mu\nu}(\partial_\mu\phi)(\partial_\nu\phi)\right) - \frac{1}{2}\sqrt{-\bar{g}}\times\frac{1}{F}\times\bar{g}^{\mu\nu}\partial_\mu\phi\partial_\nu\phi\,. &(A.20)\end{aligned}$$

Bearing in mind that

$$\sqrt{-g}V(\phi) \longrightarrow \sqrt{-\bar{g}}\times\frac{1}{F^2}V(\phi) \tag{A.21}$$

we obtain

$$\begin{aligned}\mathcal{L} = \sqrt{-\bar{g}}\Bigg[\frac{\bar{R}}{16\pi G} - \frac{1}{16\pi G}\times\frac{3}{2}\left(\frac{F'}{F}\right)^2\times\bar{g}^{\mu\nu}\partial_\mu\phi\partial_\nu\phi - \frac{1}{2F}\bar{g}^{\mu\nu}\partial_\mu\phi\partial_\nu\phi- \\ -\frac{16\pi G}{F^2}V(\phi) + \frac{1}{F^2}L_{\text{matter}}\Bigg]\end{aligned} \tag{A.22}$$

or, more concisely,

$$\begin{aligned}\mathcal{L} = \frac{1}{16\pi G}\sqrt{-\bar{g}}\Bigg[\bar{R} - 2\left(\frac{3}{4}\left(\frac{F'}{F}\right)^2 + \frac{4\pi G}{F}\right)\bar{g}^{\mu\nu}\partial_\mu\phi\partial_\nu\phi - \frac{16\pi G}{F^2}V(\phi)- \\ +\frac{1}{F^2}L_{\text{matter}}\Bigg]\end{aligned} \tag{A.23}$$

Next we define

$$\Delta = \frac{3}{4}\left(\frac{F'}{F}\right)^2 + \frac{4\pi G}{F}\,. \tag{A.24}$$

If $\Delta < 0$, the sign in front of the kinetic term $\propto \bar{g}^{\mu\nu}\partial_\mu\varphi\partial_\nu\varphi$ is positive, meaning φ is a ghost field. We want to avoid this and impose that the field have a positive energy, i.e. $\Delta > 0$.

If $\Delta > 0$, consider $\varphi(x)$ that satisfies

$$\frac{d\varphi}{d\phi} = \sqrt{\Delta} = \sqrt{\frac{3}{4}\left(\frac{F_{,\varphi}}{F}\right)^2 + \frac{4\pi G}{F}} \tag{A.25}$$

$$\Longrightarrow \sqrt{\Delta}\partial_\mu\phi = \frac{d\varphi}{d\phi}\partial_\mu\phi = \partial_\mu\varphi \tag{A.26}$$

With this result we can rewrite Eq. (A.23) as

$$\mathcal{L} = \frac{1}{16\pi G}\sqrt{-\bar{g}}\left[\bar{R} - 2\bar{g}^{\mu\nu}\partial_\mu\varphi\partial_\nu\varphi - \frac{16\pi G}{F^2}V(\phi) + \bar{L}_{\text{matter}}\right] \tag{A.27}$$

With the definition

$$W = \frac{4\pi G V}{F^2} \tag{A.28}$$

we obtain

$$\mathcal{L} = \frac{1}{16\pi G}\sqrt{-\bar{g}}\left[\bar{R} - 2\bar{g}^{\mu\nu}\partial_\mu\varphi\partial_\nu\varphi - 4W(\varphi)\right] + \mathcal{L}_{\text{matter}} \tag{A.29}$$

Using

$$F_{,\phi} = F_{,\varphi}\frac{\partial\varphi}{\partial\phi} \tag{A.30}$$

we can invert Eq. A.25

$$\Longrightarrow \left(\frac{\partial\varphi}{\partial\phi}\right)^2 = \frac{3}{4} \times \frac{1}{F^2} \times F_{,\varphi}^2\left(\frac{\partial\varphi}{\partial\phi}\right)^2 + \frac{4\pi G}{F} \tag{A.31}$$

$$\Longrightarrow \left(\frac{\partial\varphi}{\partial\phi}\right)^2 \left[4F^2 - 3(F_{,\varphi})^2\right] = 16\pi G F \tag{A.32}$$

$$\Longrightarrow \left(\frac{\partial\phi}{\partial\varphi}\right)^2 = \frac{4F^2 - 3(F_{,\varphi})^2}{16\pi G F} \Longrightarrow \frac{\partial\phi}{\partial\varphi} = \sqrt{\frac{4F^2 - 3(F_{,\varphi})^2}{16\pi G F}}\,. \tag{A.33}$$

Appendix B

Core collapse in massive Scalar Tensor Theory

B.1 Influence of atmosphere

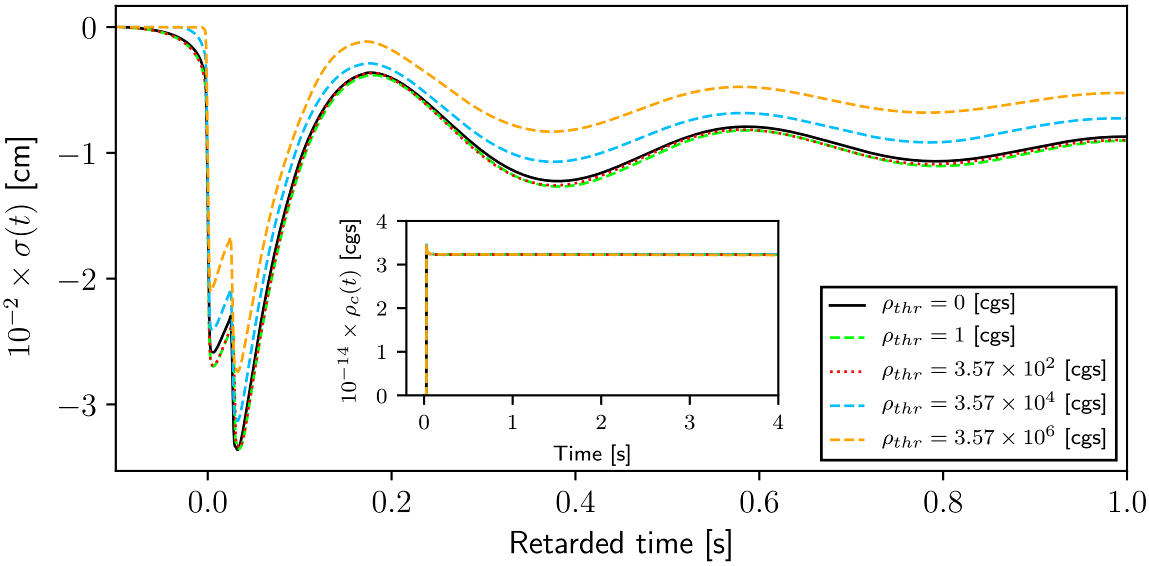

Fig. B.1 Waveforms extracted at 3×10^4 km from the collapse of $s12$ with EOSa for several atmosphere threshold values at which we set the baryon density to 1 [cgs]. The scalar paramaters are $\alpha_0 = 10^{-3}$, $\beta_0 = -16$ and $\mu = 10^{-14}$ eV. The inset contains the central baryon density as a function of time.

To avoid simulation difficulties arising from zero densities ([46, 66]) we pad the initial data profiles with a constant atmosphere density by setting the baryon density below a ρ_{thr} to the value $\rho_{\text{atm}} = 1$ [cgs]. This effectively truncates the initial profiles

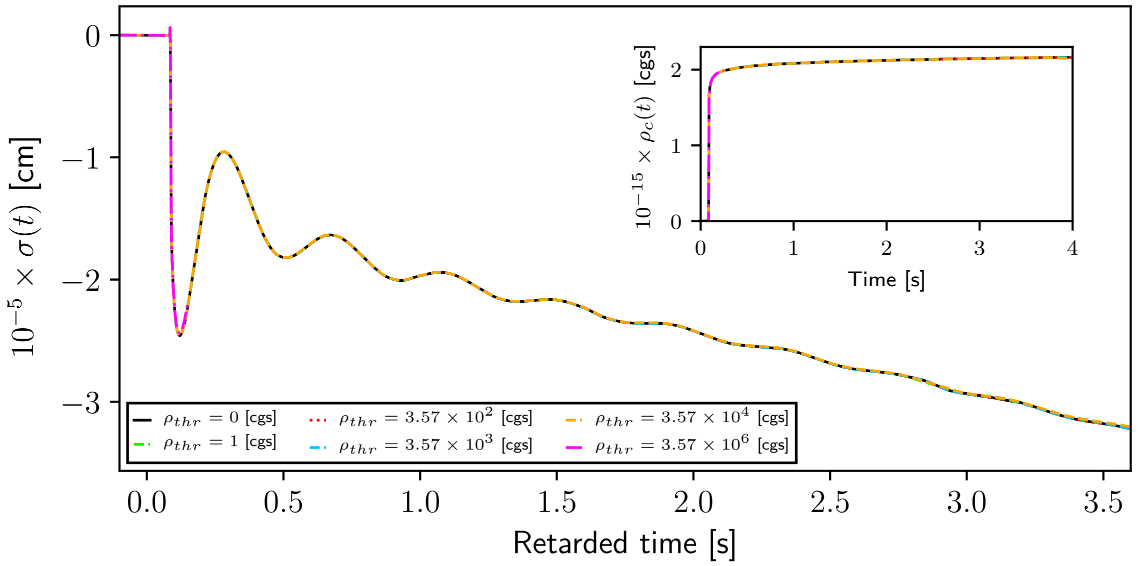

Fig. B.2 Waveforms extracted at 3×10^4 km from the collapse of $z39$ with EOS1 for several atmosphere threshold values at which we set the baryon density to 1 [cgs]. The scalar paramaters are $\alpha_0 = 10^{-4}$, $\beta_0 = -20$ and $\mu = 10^{-14}$ eV. The inset contains the central baryon density as a function of time.

after the $\rho_{\rm thr}$ value is reached at a certain point, but guarantees non-zero values. In addition, larger thresholds determine the simulations to proceed faster as many subroutines and calculations are cut short. We have tested different $\rho_{\rm thr}$ values ranging from 0 g cm^{-3} to 3.57×10^6 g cm^{-3} for a weakly scalarized model (progenitor $s12$ with EOSa and scalar parameters $\alpha_0 = 10^{-3}$, $\beta_0 = -16$ and $\mu = 10^{-14}$) and a strongly scalarized case (progenitor $z39$ with EOS1 and scalar parameter s$\alpha_0 = 10^{-4}$, $\beta_0 = -20$ and $\mu = 10^{-14}$). The results from the former are plotted in Fig. B.1: we observe no difference in the central baryon density, whereas when truncating earlier the initial data, we see a reduction in the waveform amplitude (consistent with less matter being around the star). The amplitude of the waveform drops visibly for $\rho_{\rm thr} = 3.57 \times 10^4$ g cm^{-3} by $\Delta h/h = 6.84\%$ and for $\rho_{\rm thr} = 3.57 \times 10^{-6}$ g cm^{-3} it drops by 18.46%. The strongly scalarized case shows no difference in the waveform, but the simulation with the threshold set at 3.57×10^6 g cm^{-3} crashed after 0.24 s.

For the simulations presented in this thesis we have used $\rho_{\rm thr}$ values in the range $3.57 - 3.57 \times 10^3$ g cm^{-3}.

B.2 Collapse scenario distribution for α_0 and β_0

In this section we present the results used to produce the heatmaps in Figs. 5.23 and 5.26. We include the classification of the collapse scenario of the different parameters used in our simulations in Tables B.1-B.6.

Unless otherwise noted, our results have been obtained the case for $N = 10\,000$, $\Delta r = 250$ m. The first multi-stage NS cases in each configuration were concluded to not lead to BHs if at least the $\Delta r = 166.66$ and 250 m cases failed to form BHs, usually by the central density dropping abruptly as described in Sec. 5.2.6. The exact boundary between multi-stage NS and prompt high-compactness NS can also be hard to pinpoint as the sudden increases in ρ_c during a collapse stage are smaller; the results should be taken cautiously so should be taken cautiously. Empty cells mean the cases were not simulated. We in general varied β_0 in increments of 1 and included intermediate values ony in order to determine the boundary beween different collapse models.

In addition we plot the respective qualitative color maps together with the corresponding heat maps that reflect the level of scalarization through the maximum value of the central scalar field; the latter correspond to Figs. 5.10-5.12. Furthermore we include the scenario classification for the collapse of the $s12$ progenitor with several equations of state in Fig. B.4.

Table B.1 Evolution models for simulations using $s39$, EOS1 and $\mu = 10^{-14}$ eV.

α_0 β_0	10^{-1}	10^{-2}	10^{-3}	10^{-4}
0	2-stage BH	2-stage BH	2-stage BH	2-stage BH
-1	2-stage BH	2-stage BH	2-stage BH	2-stage BH
-2	2-stage BH	2-stage BH	2-stage BH	2-stage BH
-3	2-stage BH	2-stage BH	2-stage BH	2-stage BH
-3.25	2-stage BH			
-3.50	multi-stage BH			
-3.75	multi-stage BH			
-4	multi-stage BH	2-stage BH	2-stage BH	2-stage BH
-4.25		2-stage BH		
-4.50		multi-stage BH		
-4.75		multi-stage BH		
-5	multi-stage BH	multi-stage BH	multi-stage BH	multi-stage BH
-5.25	multi-stage BH			
-5.50	multi-stage NS	multi-stage BH	multi-stage BH	multi-stage BH
-5.75	multi-stage NS	multi-stage BH	multi-stage BH	
-6	multi-stage NS	multi-stage BH	multi-stage BH	multi-stage BH
-6.25				multi-stage BH
-6.50				multi-stage NS
-6.75				multi-stage NS
-7	multi-stage NS	multi-stage BH	multi-stage NS	multi-stage BH
-8	multi-stage NS	multi-stage NS	multi-stage NS	multi-stage NS
-9	multi-stage NS	multi-stage NS	multi-stage NS	multi-stage NS
-10	prompt high-comp. NS	multi-stage NS	multi-stage NS	multi-stage NS
-11	prompt high-comp. NS	multi-stage NS	multi-stage NS	multi-stage NS
-12	prompt high-comp. NS	multi-stage NS	multi-stage NS	multi-stage NS
-13	prompt high-comp. NS	prompt high-comp. NS	multi-stage NS	multi-stage NS
-14	prompt high-comp. NS	prompt high-comp. NS	prompt high-comp. NS	prompt high-comp. NS
-15	prompt high-comp. NS	prompt high-comp. NS	prompt high-comp. NS	prompt high-comp. NS
-16	prompt high-comp. NS	prompt high-comp. NS	prompt high-comp. NS	prompt high-comp. NS
-17	prompt high-comp. NS	prompt high-comp. NS	prompt high-comp. NS	prompt high-comp. NS

Table B.2 Evolution models for simulations using $u39$, EOS1 and $\mu = 10^{-14}$ eV.

α_0 β_0	10^{-1}	10^{-2}	10^{-3}	10^{-4}
-1	2-stage BH	2-stage BH	2-stage BH	2-stage BH
-2	2-stage BH	2-stage BH	2-stage BH	2-stage BH
-3	multi-stage BH	2-stage BH	2-stage BH	2-stage BH
-4	multi-stage BH	2-stage BH	2-stage BH	2-stage BH
-4.25		2-stage BH	2-stage BH	2-stage BH
-4.50		multi-stage BH	2-stage BH	2-stage BH
-4.75		multi-stage BH	multi-stage BH	2-stage BH
-5	multi-stage BH	multi-stage BH	multi-stage BH	multi-stage BH
-5.25				multi-stage BH
-5.50				multi-stage BH
-5.75	multi-stage BH			multi-stage BH
-6	multi-stage BH	multi-stage BH	multi-stage BH	multi-stage BH
-6.25		multi-stage BH	multi-stage BH	multi-stage BH
-6.50		multi-stage BH	multi-stage BH	multi-stage BH
-6.75		multi-stage BH	multi-stage BH	multi-stage BH
-7	multi-stage NS	multi-stage BH	multi-stage BH	multi-stage BH
-8	multi-stage NS	multi-stage NS	multi-stage NS	multi-stage NS
-9	multi-stage NS	multi-stage NS	multi-stage NS	multi-stage NS
-10	multi-stage NS	multi-stage NS	multi-stage NS	multi-stage NS
-11	prompt high-comp. NS	multi-stage NS	multi-stage NS	multi-stage NS
-12	prompt high-comp. NS	multi-stage NS	multi-stage NS	multi-stage NS
-13	prompt high-comp. NS	prompt high-comp. NS	multi-stage NS	multi-stage NS
-14	prompt high-comp. NS	prompt high-comp. NS	prompt high-comp. NS	prompt high-comp. NS
-15	prompt high-comp. NS	prompt high-comp. NS	prompt high-comp. NS	prompt high-comp. NS
-20	prompt high-comp. NS	prompt high-comp. NS	prompt high-comp. NS	prompt high-comp. NS

Table B.3 Evolution models for simulations using $z39$, EOS1 and $\mu = 10^{-14}$ eV.

β_0 \ α_0	10^{-2}	10^{-3}	10^{-4}
-1	2-stage BH	2-stage BH	2-stage BH
-2	2-stage BH	2-stage BH	2-stage BH
-3	2-stage BH	2-stage BH	2-stage BH
-4	2-stage BH	2-stage BH	2-stage BH
-4.25	2-stage BH	2-stage BH	2-stage BH
-4.50	2-stage BH	2-stage BH	2-stage BH
-4.75	multi-stage BH	2-stage BH	2-stage BH
-5	multi-stage BH	multi-stage BH	multi-stage BH
-5.25			multi-stage BH
-5.50			multi-stage BH
-5.75			multi-stage BH
-6	multi-stage BH	multi-stage BH	multi-stage BH
-6.25	multi-stage BH	multi-stage BH	multi-stage BH
-6.50		multi-stage BH	multi-stage BH
-6.75	multi-stage BH	multi-stage BH	multi-stage BH
-7	multi-stage BH	multi-stage BH	multi-stage NS
-8	multi-stage NS	multi-stage NS	multi-stage NS
-9	multi-stage NS	multi-stage NS	multi-stage NS
-10	multi-stage NS	multi-stage NS	multi-stage NS
-11	multi-stage NS	multi-stage NS	multi-stage NS
-12	multi-stage NS	multi-stage NS	multi-stage NS
-13	prompt high-comp. NS	multi-stage NS	multi-stage NS
-14	prompt high-comp. NS	prompt high-comp. NS	prompt high-comp. NS
-15	prompt high-comp. NS	prompt high-comp. NS	prompt high-comp. NS
-20	prompt high-comp. NS	prompt high-comp. NS	prompt high-comp. NS

Table B.4 Evolution models for simulations using $s39$, EOS3 and $\mu = 10^{-14}$ eV.

β_0 \ α_0	10^{-1}	10^{-2}	10^{-3}	10^{-4}
-2		prompt low-comp. NS	prompt low-comp. NS	prompt low-comp. NS
-3		prompt low-comp. NS	prompt low-comp. NS	prompt low-comp. NS
-4		prompt low-comp. NS	prompt low-comp. NS	prompt low-comp. NS
-5	prompt low-comp. NS	prompt low-comp. NS	prompt low-comp. NS	prompt low-comp. NS
-6	prompt low-comp. NS	prompt low-comp. NS	prompt low-comp. NS	prompt low-comp. NS
-7	prompt low-comp. NS	prompt low-comp. NS	prompt low-comp. NS	prompt low-comp. NS
-7.25	multi-stage NS			
-7.50	multi-stage NS			
-7.75	multi-stage NS	prompt low-comp. NS		
-8	multi-stage NS	multi-stage NS	prompt low-comp. NS	prompt low-comp. NS
-8.25	multi-stage NS	multi-stage NS	prompt low-comp. NS	prompt low-comp. NS
-8.50	multi-stage NS	multi-stage NS	multi-stage NS	multi-stage NS
-8.75	multi-stage NS	multi-stage NS	multi-stage NS	multi-stage NS
-9	multi-stage NS	multi-stage NS	multi-stage NS	multi-stage NS
-9.25	multi-stage NS	multi-stage NS	multi-stage NS	multi-stage NS
-9.50	multi-stage NS	multi-stage NS	multi-stage NS	multi-stage NS
-9.75	multi-stage NS	prompt high-comp. NS	multi-stage NS	multi-stage NS
-10	multi-stage NS	prompt high-comp. NS	prompt high-comp. NS	prompt high-comp. NS
-11	prompt high-comp. NS	prompt high-comp. NS	prompt high-comp. NS	prompt high-comp. NS
-12	prompt high-comp. NS	prompt high-comp. NS	prompt high-comp. NS	prompt high-comp. NS
-13	prompt high-comp. NS	prompt high-comp. NS	prompt high-comp. NS	prompt high-comp. NS
-14		prompt high-comp. NS	prompt high-comp. NS	prompt high-comp. NS
-15		prompt high-comp. NS	prompt high-comp. NS	prompt high-comp. NS
-20		prompt high-comp. NS	prompt high-comp. NS	prompt high-comp. NS

Table B.5 Evolution models for simulations using $u39$, EOS3 and $\mu = 10^{-14}$ eV.

α_0 β_0	10^{-2}	10^{-3}	10^{-4}
-1	2-stage BH	2-stage BH	2-stage BH
-3	2-stage BH	2-stage BH	2-stage BH
-4	2-stage BH		
-4.25	2-stage BH		
-4.50	2-stage BH		
-4.75	2-stage BH		
-5	2-stage BH	2-stage BH	2-stage BH
-5.25		2-stage BH	2-stage BH
-5.50		2-stage BH	2-stage BH
-5.75		2-stage BH	2-stage BH
-6	multi-stage BH	2-stage BH	2-stage BH
-6.50	multi-stage BH		
-6.75	multi-stage BH		
-7	multi-stage BH	multi-stage BH	multi-stage BH
-7.25			multi-stage BH
-7.50	multi-stage BH		
-7.75	multi-stage NS		
-8	multi-stage NS	multi-stage BH	
-8.25	multi-stage NS	multi-stage BH	multi-stage BH
-8.50	multi-stage NS	multi-stage NS	multi-stage NS
-8.75	multi-stage NS	multi-stage NS	multi-stage NS
-9	multi-stage NS	multi-stage NS	multi-stage NS
-10	multi-stage NS	prompt high-comp. NS	prompt high-comp. NS
-11	prompt high-comp. NS	prompt high-comp. NS	prompt high-comp. NS
-12	prompt high-comp. NS		
-13		prompt high-comp. NS	prompt high-comp. NS
-15	prompt high-comp. NS	prompt high-comp. NS	prompt high-comp. NS
-20	prompt high-comp. NS	prompt high-comp. NS	prompt high-comp. NS

Table B.6 Evolution models for simulations using $z39$, EOS3 and $\mu = 10^{-14}$ eV.

α_0 β_0	10^{-1}	10^{-2}	10^{-3}	10^{-4}
-1	2-stage BH	2-stage BH	2-stage BH	2-stage BH
-3	2-stage BH	2-stage BH	2-stage BH	2-stage BH
-4	2-stage BH	2-stage BH		
-5	multi-stage BH	2-stage BH	2-stage BH	2-stage BH
-5.25	multi-stage BH		2-stage BH	2-stage BH
-5.50	multi-stage BH		2-stage BH	2-stage BH
-5.75			2-stage BH	2-stage BH
-6	multi-stage BH	multi-stage BH	multi-stage BH	2-stage BH
-6.25	multi-stage BH	multi-stage BH		
-6.50	multi-stage BH	multi-stage BH		
-6.75	multi-stage BH	multi-stage BH		
-7	multi-stage BH	multi-stage BH	multi-stage BH	multi-stage BH
-7.25	multi-stage NS		multi-stage BH	multi-stage BH
-7.50	multi-stage NS	multi-stage BH		
-7.75	multi-stage NS	multi-stage NS		
-8	multi-stage NS	multi-stage NS	multi-stage BH	multi-stage BH
-8.25	multi-stage NS	multi-stage NS	multi-stage BH	multi-stage BH
-8.50	multi-stage NS	multi-stage NS	multi-stage NS	multi-stage NS
-8.75	multi-stage NS	multi-stage NS	multi-stage NS	multi-stage NS
-9	multi-stage NS	multi-stage NS	multi-stage NS	multi-stage NS
-10		prompt high-comp. NS	prompt high-comp. NS	prompt high-comp. NS
-11	prompt high-comp. NS		prompt high-comp. NS	
-12		prompt high-comp. NS	prompt high-comp. NS	prompt high-comp. NS
-13	prompt high-comp. NS			
-15	prompt high-comp. NS	prompt high-comp. NS	prompt high-comp. NS	prompt high-comp. NS
-17	prompt high-comp. NS			
-18		prompt high-comp. NS	prompt high-comp. NS	prompt high-comp. NS
-19	prompt high-comp. NS			
-20	prompt high-comp. NS	prompt high-comp. NS	prompt high-comp. NS	prompt high-comp. NS

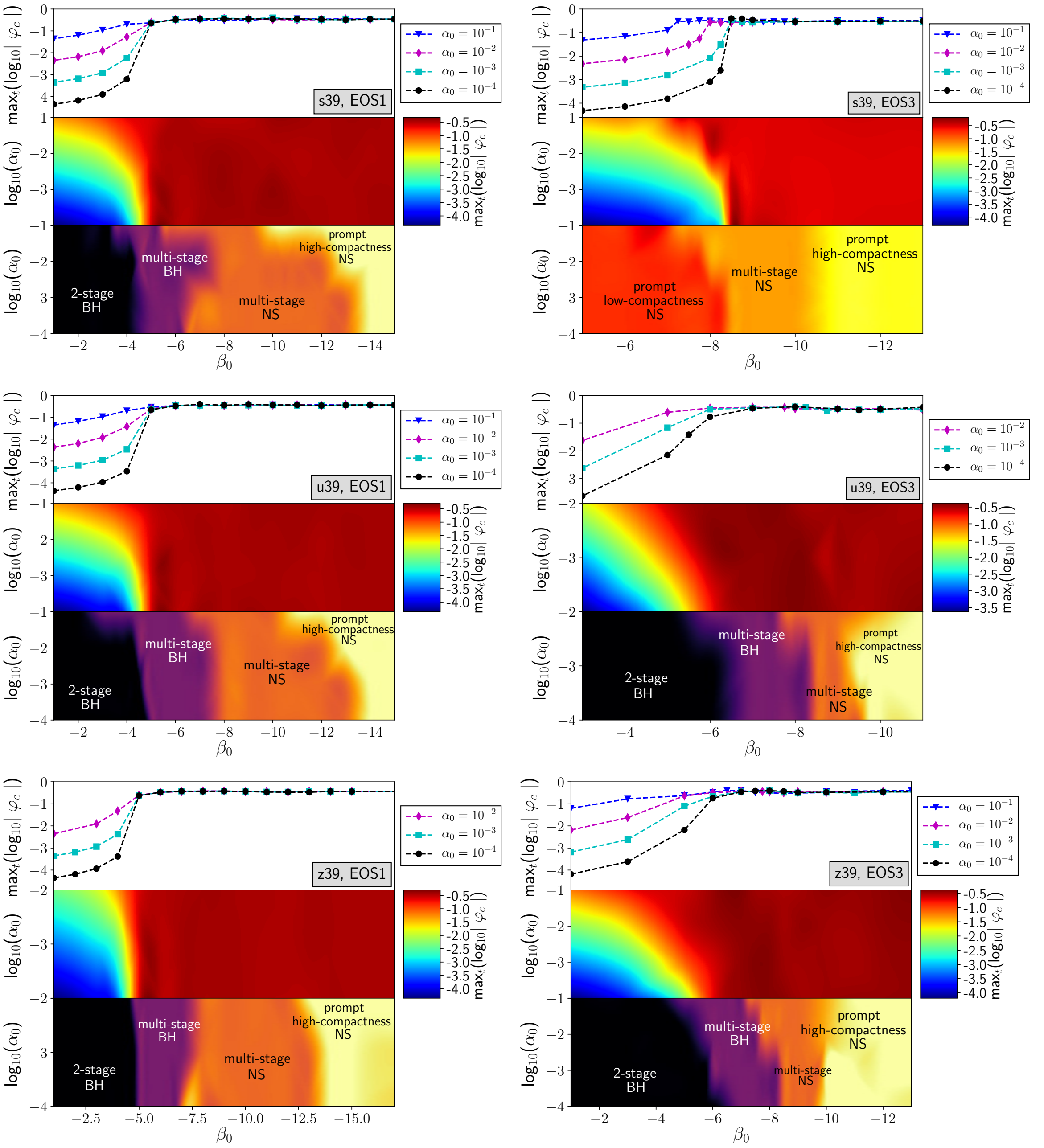

Fig. B.3 We consider a fixed progenitor star with ZAMS mass 39 $M_\odot$, equation of state EOS1 (left column) and EOS3 (right column), and fix the scalar mass at $\mu = 10^{-14}$ eV. The progenitor and equation of state used are marked in the top panels. Top row: For selected values of α_0, we plot the maximal scalarization of the collapsing star as a function of β_0. The middle rows provide a color (or "heat") map of the same quantity in the (α_0, β_0) plane; "Red" = strong scalarization, "Blue" = weak scalarization. The bottom row presents a color code of the five qualitatively different collapse scenarios listed in Sec. 5.5.

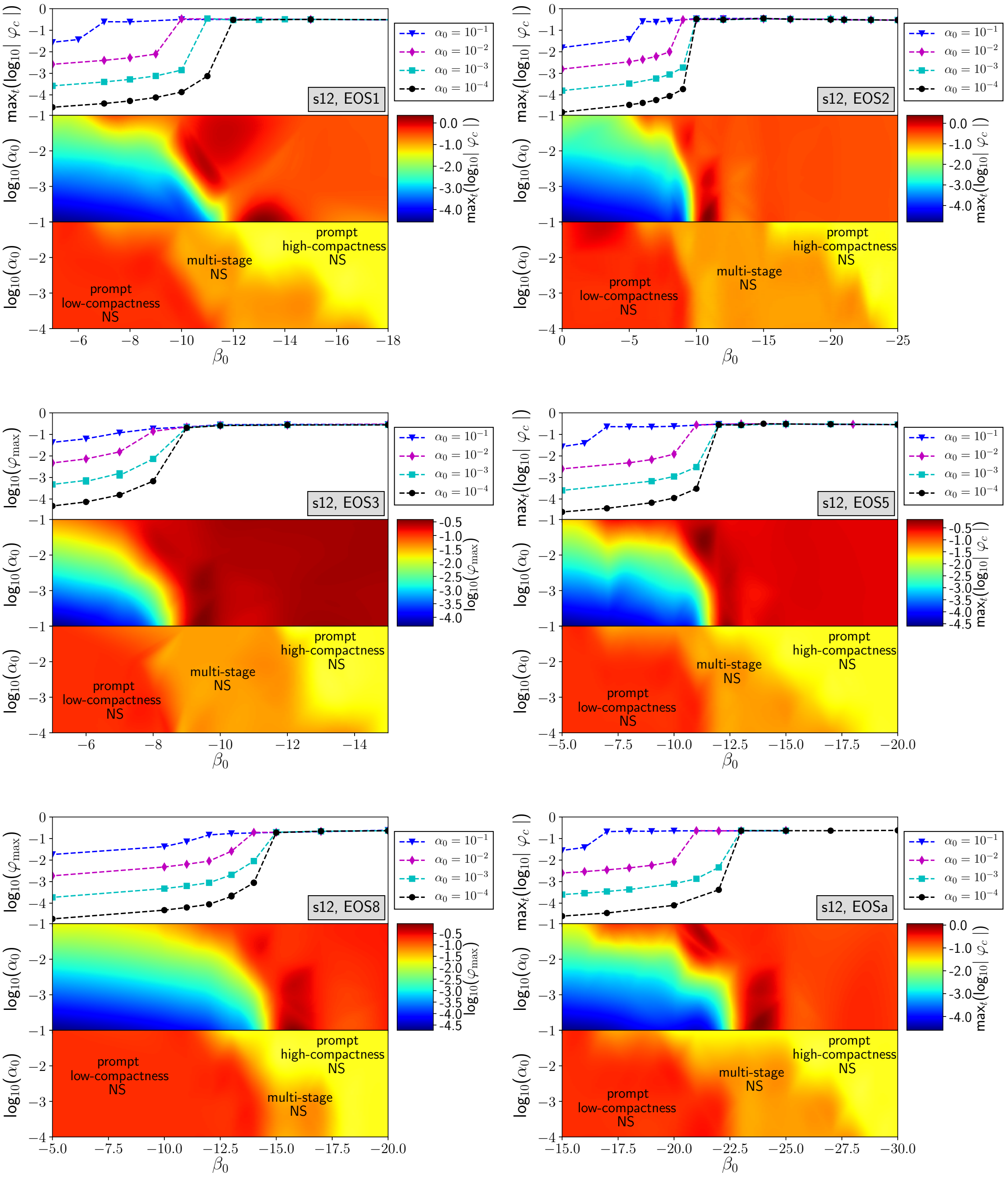

Fig. B.4 Similarly to Fig. B.3, for each panel we consider a fixed progenitor star with ZAMS mass 12 $M_\odot$, solar metallicity and several equations of state of Table 4.1. Top rows: For selected values of α_0, we plot the maximal scalarization of the star as a function of β_0. The middle rows provide a color (or "heat") map of the same quantity in the (α_0, β_0) plane; "Red" = strong scalarization, "Blue" = weak scalarization. The bottom rows present a color code of the five qualitatively different collapse scenarios listed in Sec. 5.5.

B.3 Approximate μ universality for $u41$

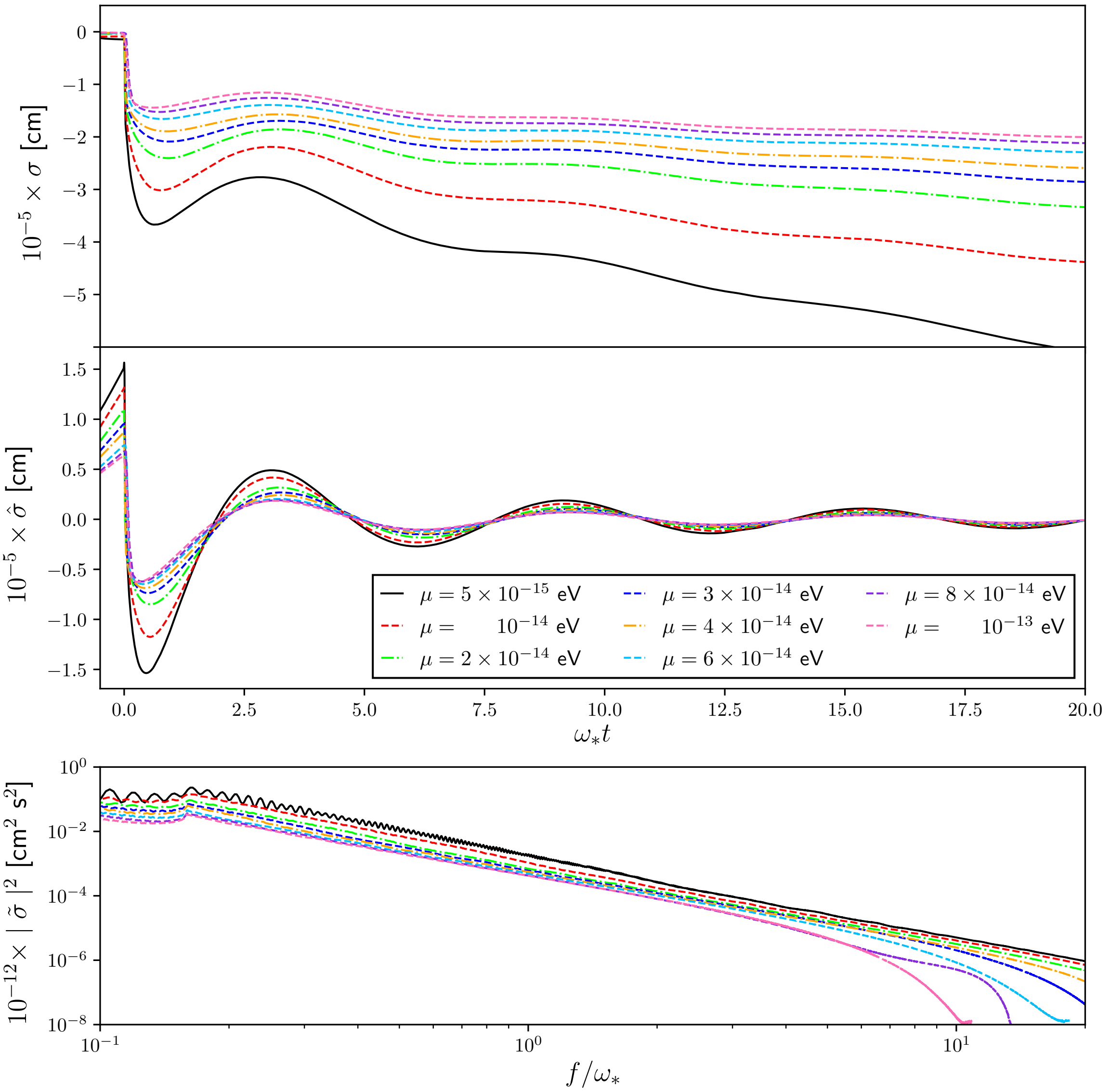

Fig. B.5 GW signal $\sigma(t, r_{\text{ex}})$ extracted from the collapse of $u41$ with EOS1 and parameters $\alpha_0 = 10^{-2}$, $\beta_0 = 20$ at $\omega_* r_{\text{ex}} = 0.91$ for different values of the scalar mass $\mu \in [5\times10^{-15}\text{ eV},\ 10^{-13}\text{ eV}]$. The overall amplitude increases monotonically with decreasing μ. *Top panel*: signals as obtained from the simulations at the scaled extraction radii. *Middle panel*: we band-pass the signal by suppressing modes below ω_* in order to eliminate the drift. *Bottom panel*: Power spectrum of the band-passed signal $\hat{\sigma}$.

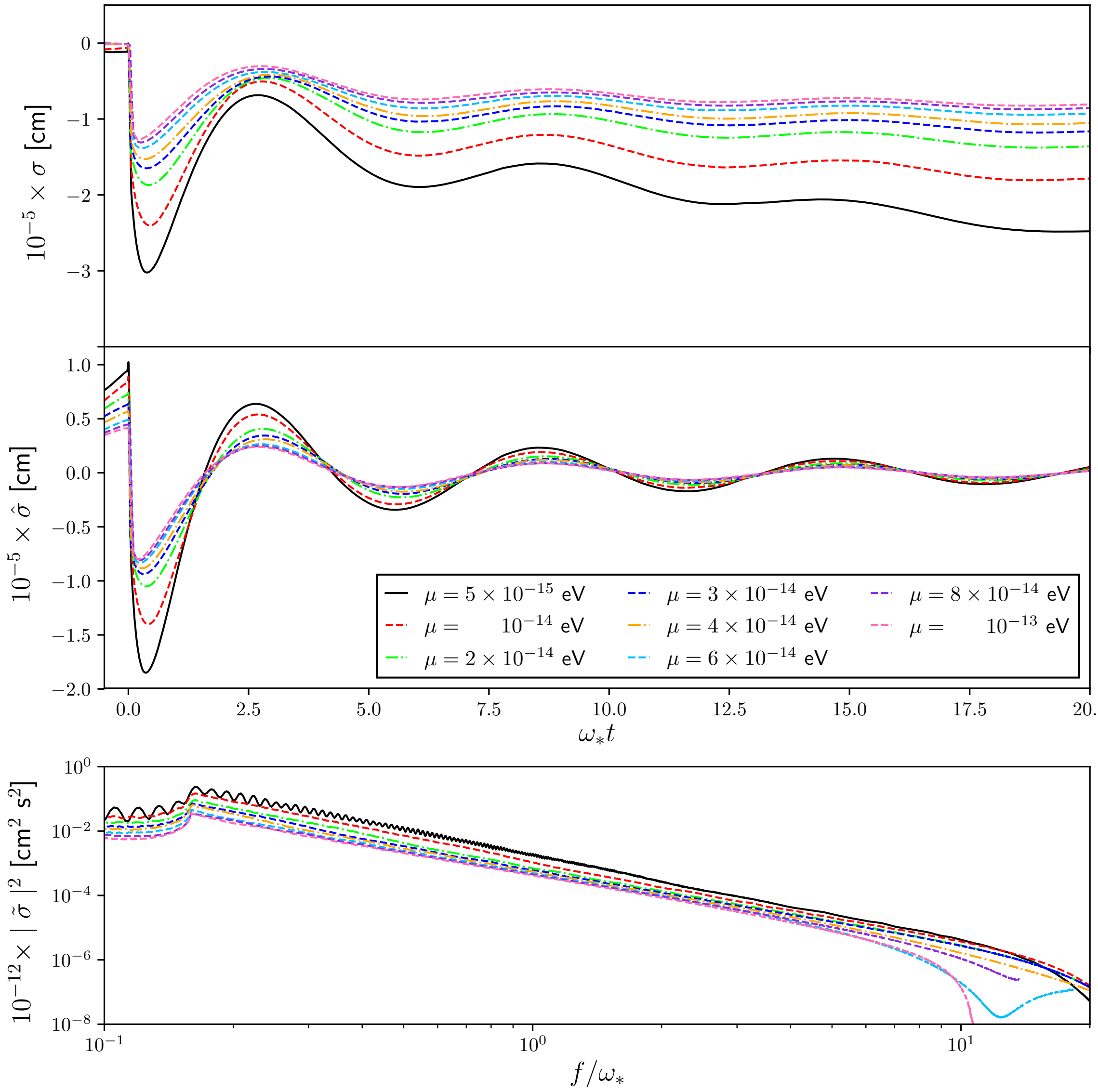

Fig. B.6 GW signal $\sigma(t, r_{\rm ex})$ extracted from the collapse of $u41$ with EOS1 and parameters $\alpha_0 = 10^{-2}$, $\beta_0 = 20$ at $\omega_* r_{\rm ex} = 1.83$ for different values of the scalar mass $\mu \in [5 \times 10^{-15}\ \text{eV},\ 10^{-13}\ \text{eV}]$. The overall amplitude increases monotonically with decreasing μ. *Top panel*: signals as obtained from the simulations at the scaled extraction radii. *Middle panel*: we band-pass the signal by suppressing modes below ω_* in order to eliminate the drift. *Bottom panel*: Power spectrum of the band-passed signal $\hat{\sigma}$.

Appendix C

Scalar Tensor Theory with self-interacting potential - additional results

We present here a handful more of cases, including a series where we vary the quartic, sextic and octic terms of the potential expressed in Eq. (6.1). The scalar mass for all runs is $\mu = 10^{-14}$ eV. As we increase the λ_i values, our simulations lead to BH formation, which need higher resolutions in order to continue for long enough such that a full signal can be extracted. The intermediate range of λ values lead to the cimulations crashing even for higher resolutions. As a consequence some cases are missing in the figures. In the plots, we include band-passed versions of the waveforms in the second row and, in order to test the agreement for small values of λ. We split our cases between the two columns in the figures (usually cases that lead to NSs (left) and BHs (right)).

All simulations done reinforce the conclusions from Chapter 6.

C.1 Core collapse with varying λ_1

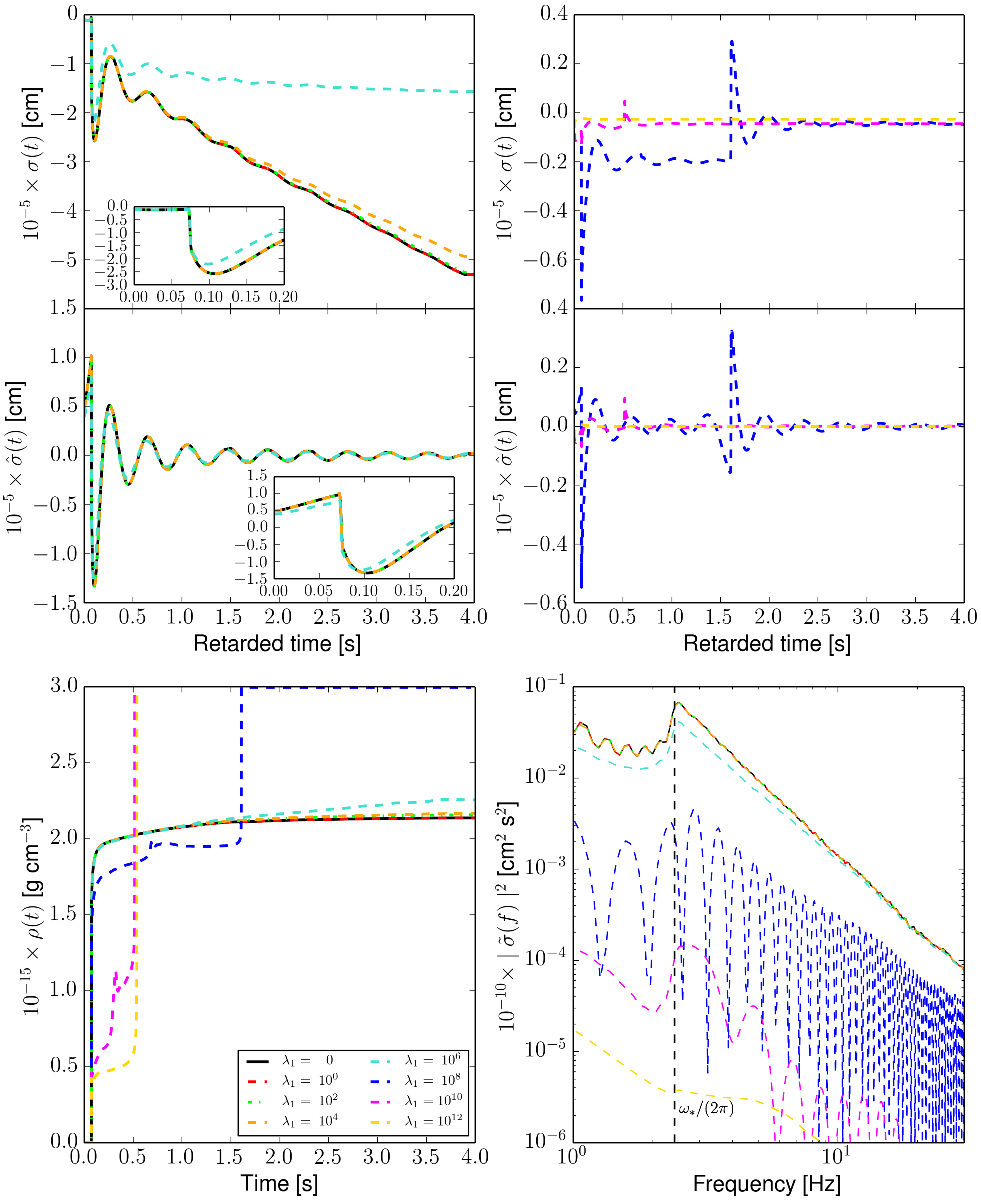

Fig. C.1 The effect of varying the λ_1 term of the scalar field potential using progenitor $u50$ with EOS1 and scalar parameters $\lambda_{2,3} = 0,\ \alpha_0 = 10^{-2},\ \beta_0 = -20$. *Top panels:* the scalar field signal at the extraction radius 3×10^4 km. *Middle panels:* the band-passed scalar field signal at the extraction radius 3×10^4 km; modes with frequencies below ω_* are set to 0. *Bottom left panel:* the central density evolution. *Bottom right panel:* power spectrum of waveforms extracted at 3×10^4 km. Higher resolution was used for $\lambda_1 = 10^6,\ 10^{10}$ $(N = 20\,000,\ \Delta r = 125$ m$)$.

C.2 Core collapse with varying λ_2

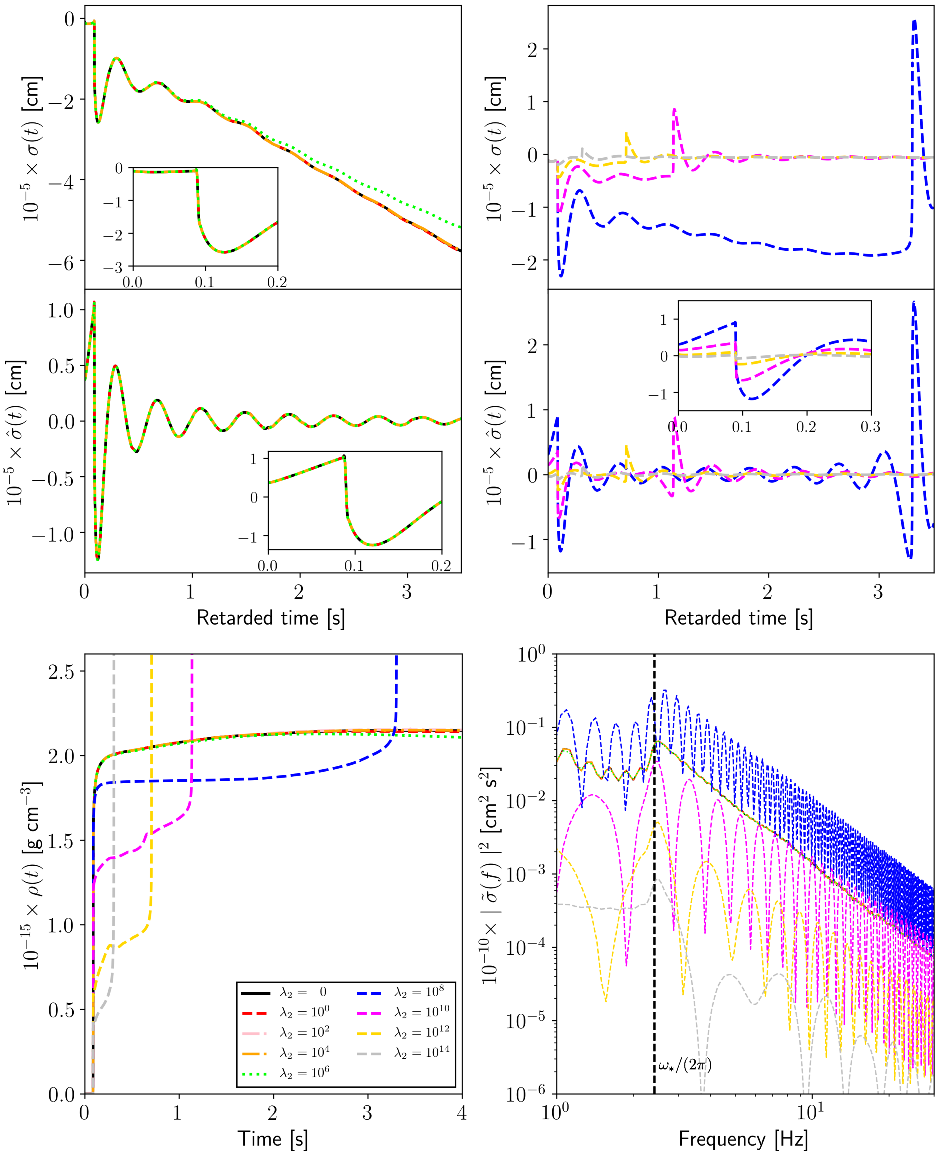

Fig. C.2 The effect of varying the λ_2 term of the scalar field potential using progenitor $u60$ with EOS1 and scalar parameters $\lambda_{1,3} = 0,\ \alpha_0 = 10^{-2},\ \beta_0 = -20$. *Top panels:* the scalar field signal at the extraction radius 3×10^4 km. *Middle panels:* the band-passed scalar field signal at the extraction radius 3×10^4 km; modes with frequencies below ω_* are set to 0. *Bottom left panel:* the central density evolution. *Bottom right panel:* power spectrum of waveforms extracted at 3×10^4 km. Higher resolution was used for $\lambda_2 = 10^8$ ($N = 25\ 000,\ \Delta r = 100$ m), $\lambda_2 = 10^{10}$ ($N = 20\ 000,\ \Delta r = 125$ m), $\lambda_2 = 10^{12}$ ($N = 30\ 000,\ \Delta r = 83.33$ m) and $\lambda_2 = 10^{14}$ ($N = 15\ 000,\ \Delta r = 166.66$ m).

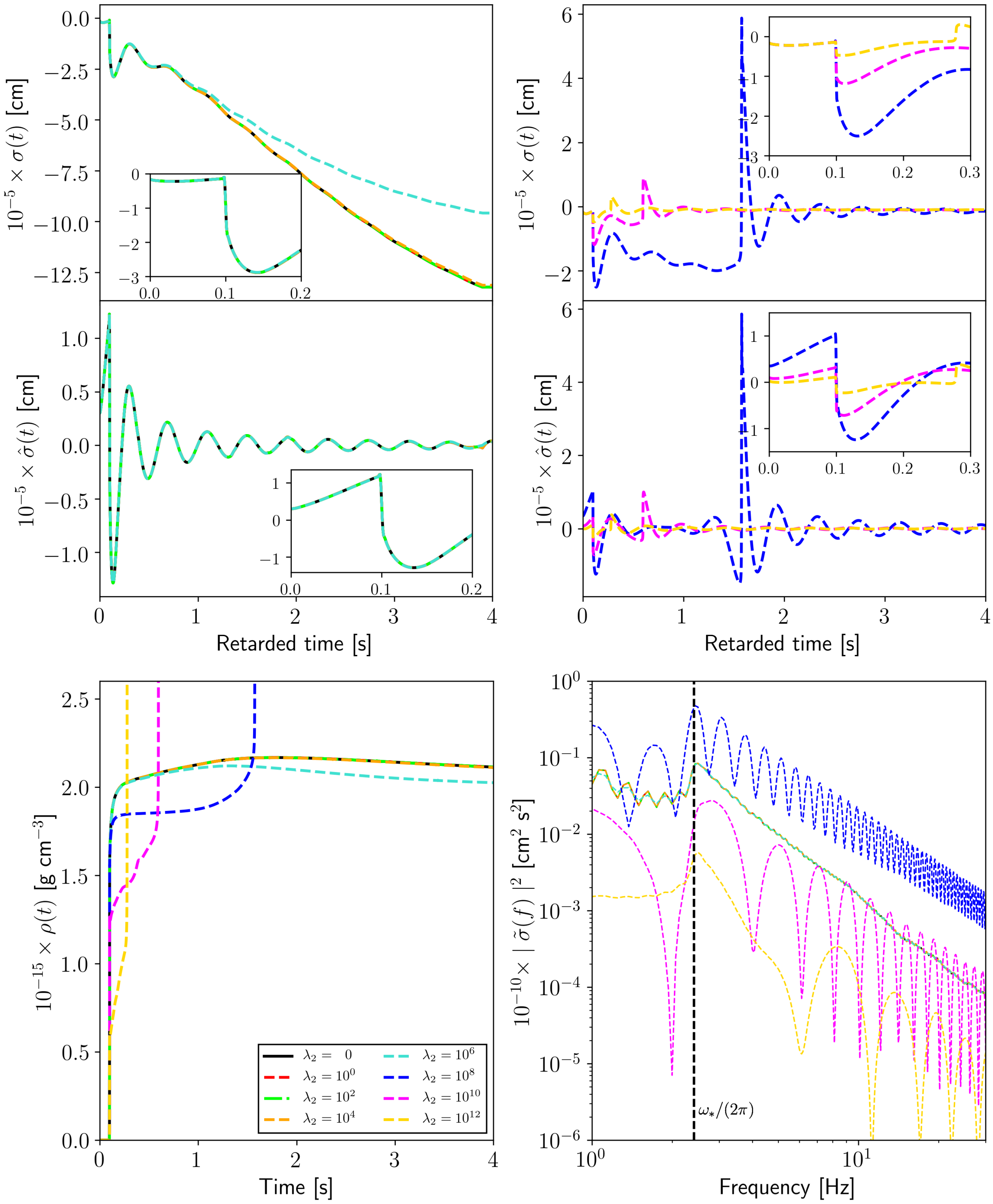

Fig. C.3 The effect of varying the λ_2 term of the scalar field potential using progenitor $u75$ with EOS1 and scalar parameters $\lambda_{1,3} = 0$, $\alpha_0 = 10^{-2}$, $\beta_0 = -20$. *Top panels:* the scalar field signal at the extraction radius 3×10^4 km. *Middle panels:* the band-passed scalar field signal at the extraction radius 3×10^4 km; modes with frequencies below ω_* are set to 0. *Bottom left panel:* the central density evolution. *Bottom right panel:* power spectrum of waveforms extracted at 3×10^4 km. Higher resolution was used for $\lambda_2 = 10^8$, 10^{12} ($N = 20\,000$, $\Delta r = 125$ m) and $\lambda_2 = 10^{10}$ ($N = 25\,000$, $\Delta r = 100$ m).

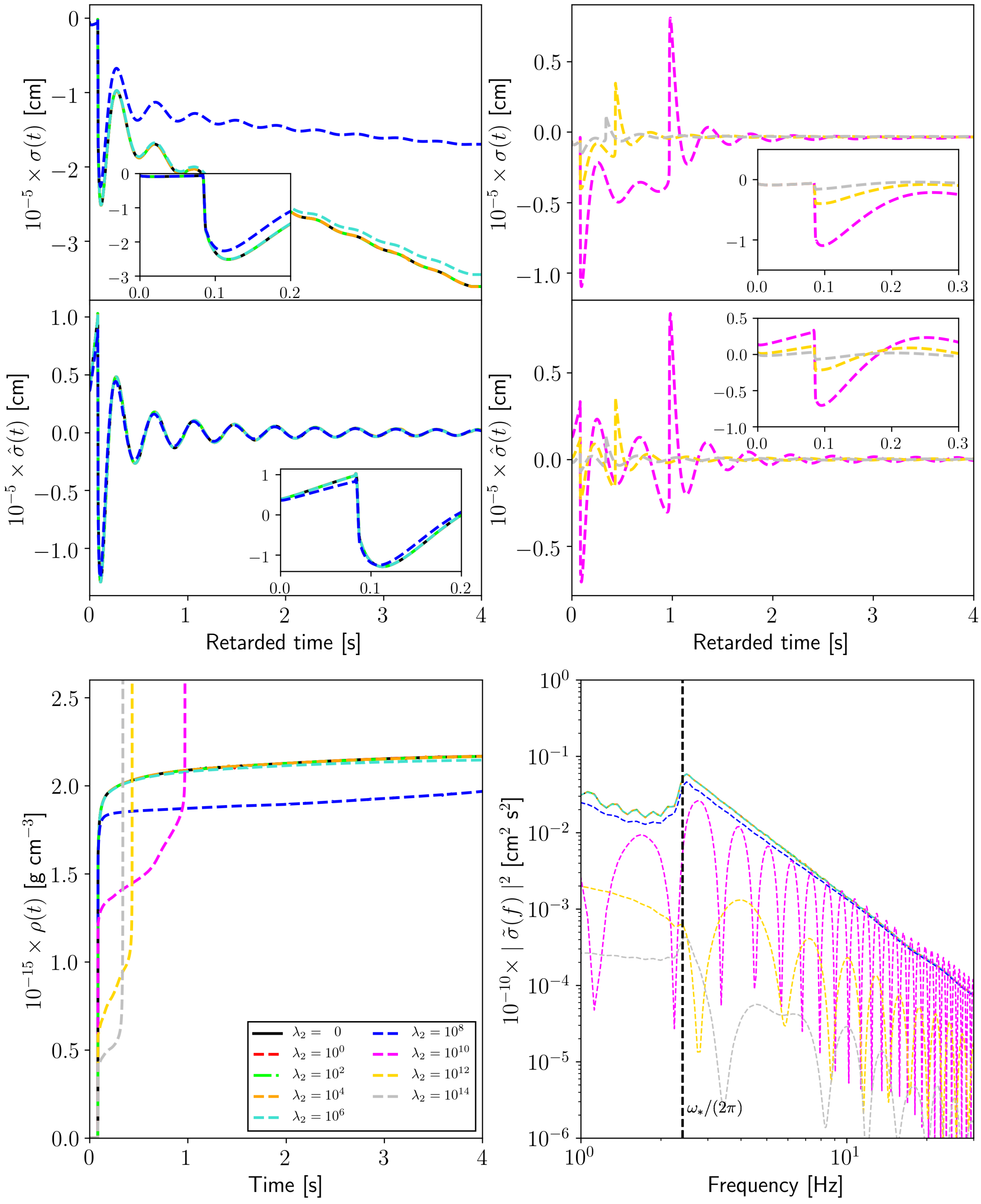

Fig. C.4 The effect of varying the λ_2 term of the scalar field potential using progenitor $z40$ with EOS1 and scalar parameters $\lambda_{1,3} = 0,\ \alpha_0 = 10^{-2},\ \beta_0 = -20$. *Top panels:* the scalar field signal at the extraction radius 3×10^4 km. *Middle panels:* the band-passed scalar field signal at the extraction radius 3×10^4 km; modes with frequencies below ω_* are set to 0. *Bottom left panel:* the central density evolution. *Bottom right panel:* power spectrum of waveforms extracted at 3×10^4 km. Higher resolution was used for $\lambda_2 = 10^{10},\ 10^{12}$ ($N = 15\,000,\ \Delta r = 166.66$ m).

C.3 Core collapse with varying λ_3

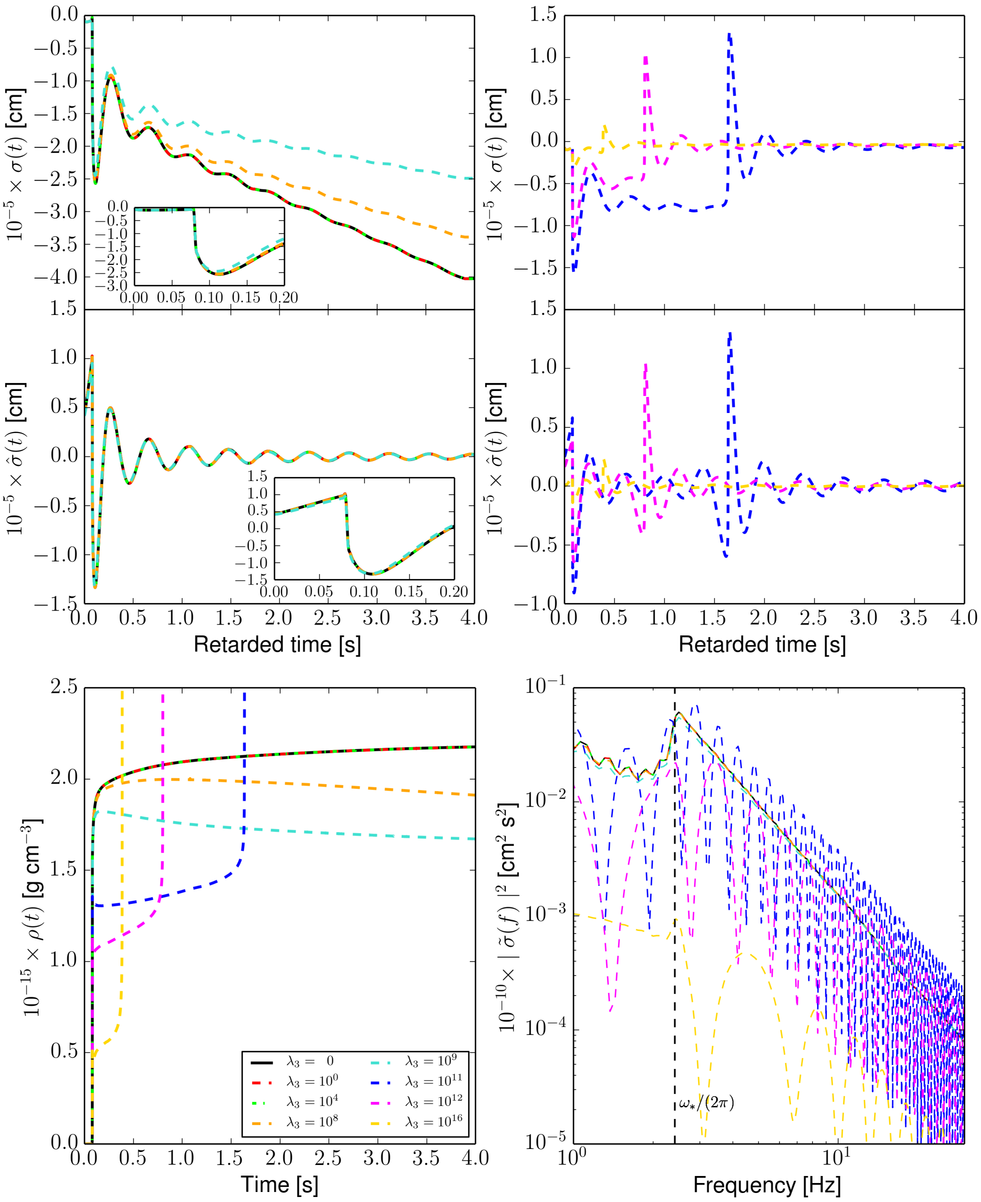

Fig. C.5 The effect of varying the λ_3 term of the scalar field potential using progenitor $u41$ with EOS1 and scalar parameters $\lambda_{1,2} = 0,\ \alpha_0 = 10^{-2},\ \beta_0 = -20$. *Top panels:* the scalar field signal at the extraction radius 3×10^4 km. *Middle panels:* the band-passed scalar field signal at the extraction radius 3×10^4 km; modes with frequencies below ω_* are set to 0. *Bottom left panel:* the central density evolution. *Bottom right panel:* power spectrum of waveforms extracted at 3×10^4 km. Higher resolution was used for $\lambda_3 = 10^{11},\ 10^{12}$ ($N = 20\,000,\ \Delta r = 125$ m) and $\lambda_3 = 10^{16}$ ($N = 15\,000,\ \Delta r = 166.66$ m).

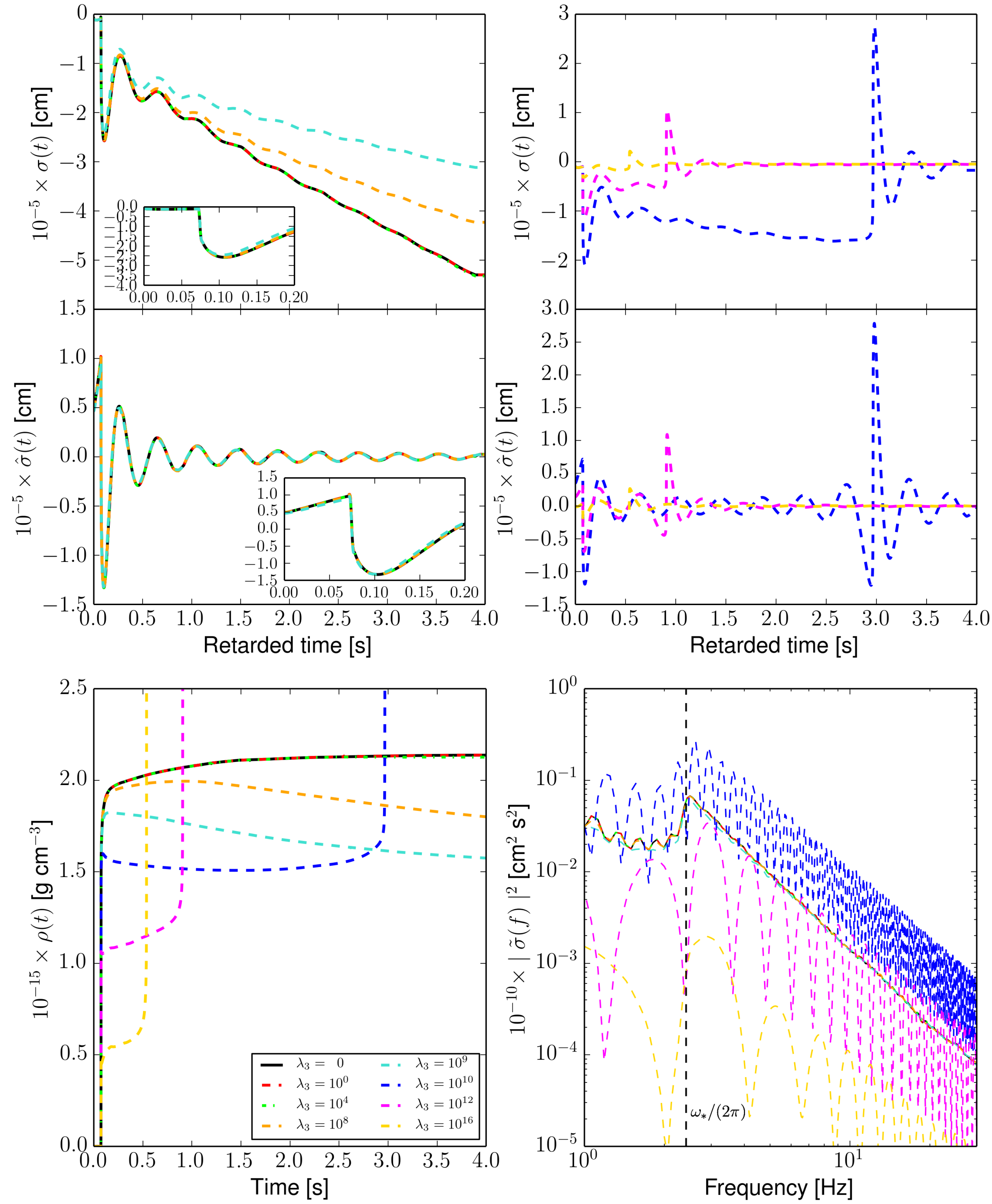

Fig. C.6 The effect of varying the λ_3 term of the scalar field potential using progenitor $u50$ with EOS1 and scalar parameters $\lambda_{1,2} = 0,\ \alpha_0 = 10^{-2},\ \beta_0 = -20$. *Top panels:* the scalar field signal at the extraction radius 3×10^4 km. *Middle panels:* the band-passed scalar field signal at the extraction radius 3×10^4 km; modes with frequencies below ω_* are set to 0. *Bottom left panel:* the central density evolution. *Bottom right panel:* power spectrum of waveforms extracted at 3×10^4 km. Higher resolution was used for $\lambda_3 = 10^{10},\ 10^{12}$ ($N = 25\ 000,\ \Delta r = 100$ m) and $\lambda_3 = 10^{16}$ ($N = 15\ 000,\ \Delta r = 166.66$ m).

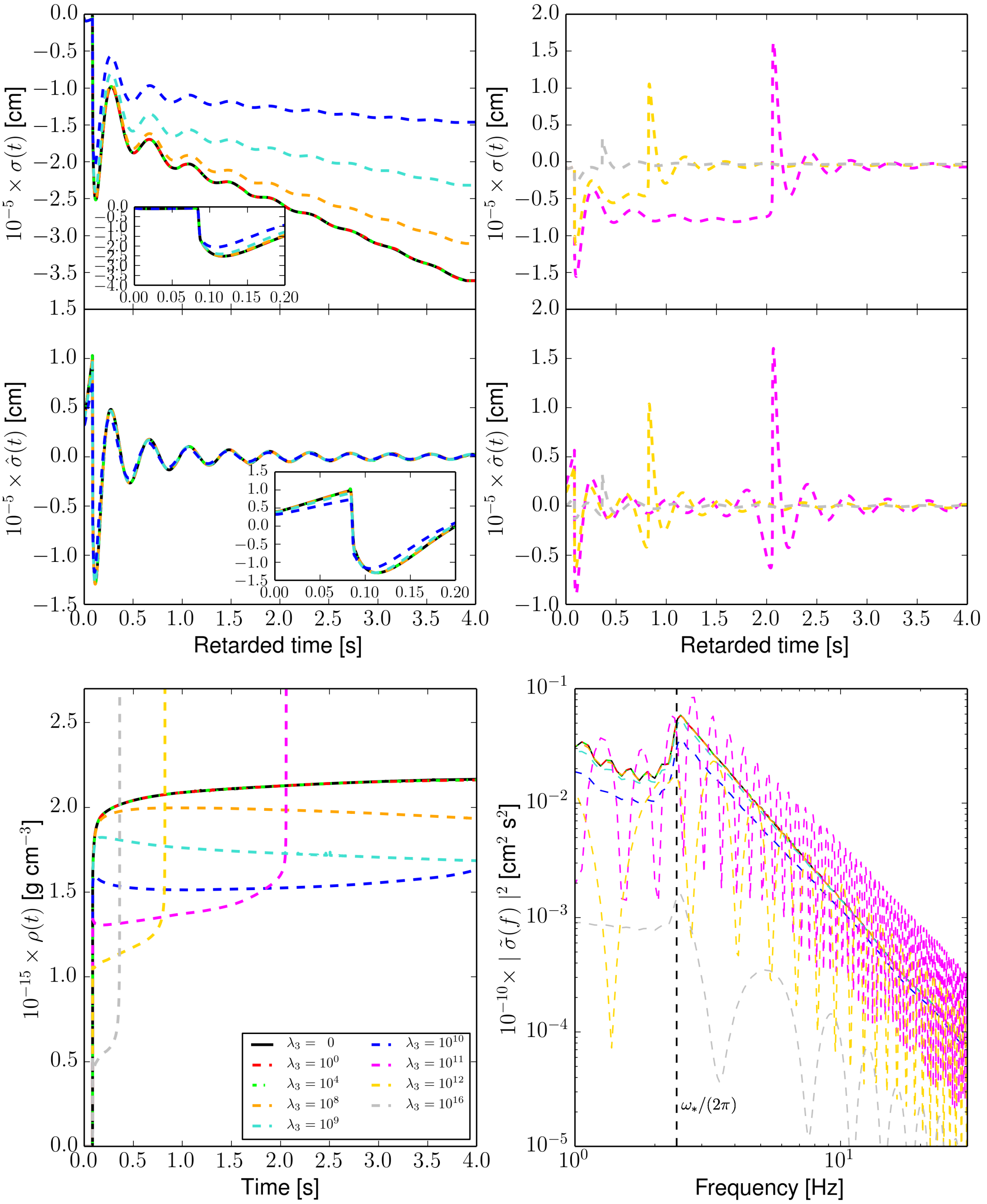

Fig. C.7 The effect of varying the λ_3 term of the scalar field potential using progenitor $z40$ with EOS1 and scalar parameters $\lambda_{1,2} = 0,\ \alpha_0 = 10^{-2},\ \beta_0 = -20$. *Top panels:* the scalar field signal at the extraction radius 3×10^4 km. *Middle panels:* the band-passed scalar field signal at the extraction radius 3×10^4 km; modes with frequencies below ω_* are set to 0. *Bottom left panel:* the central density evolution. *Bottom right panel:* power spectrum of waveforms extracted at 3×10^4 km. Higher resolution was used for $\lambda_3 = 10^{11}$ ($N = 25\ 000,\ \Delta r = 100$ m), $\lambda_3 = 10^{12}$ ($N = 15\ 000,\ \Delta r = 166.66$ m) and $\lambda_3 = 10^{16}$ ($N = 20\ 000,\ \Delta r = 125$ m).

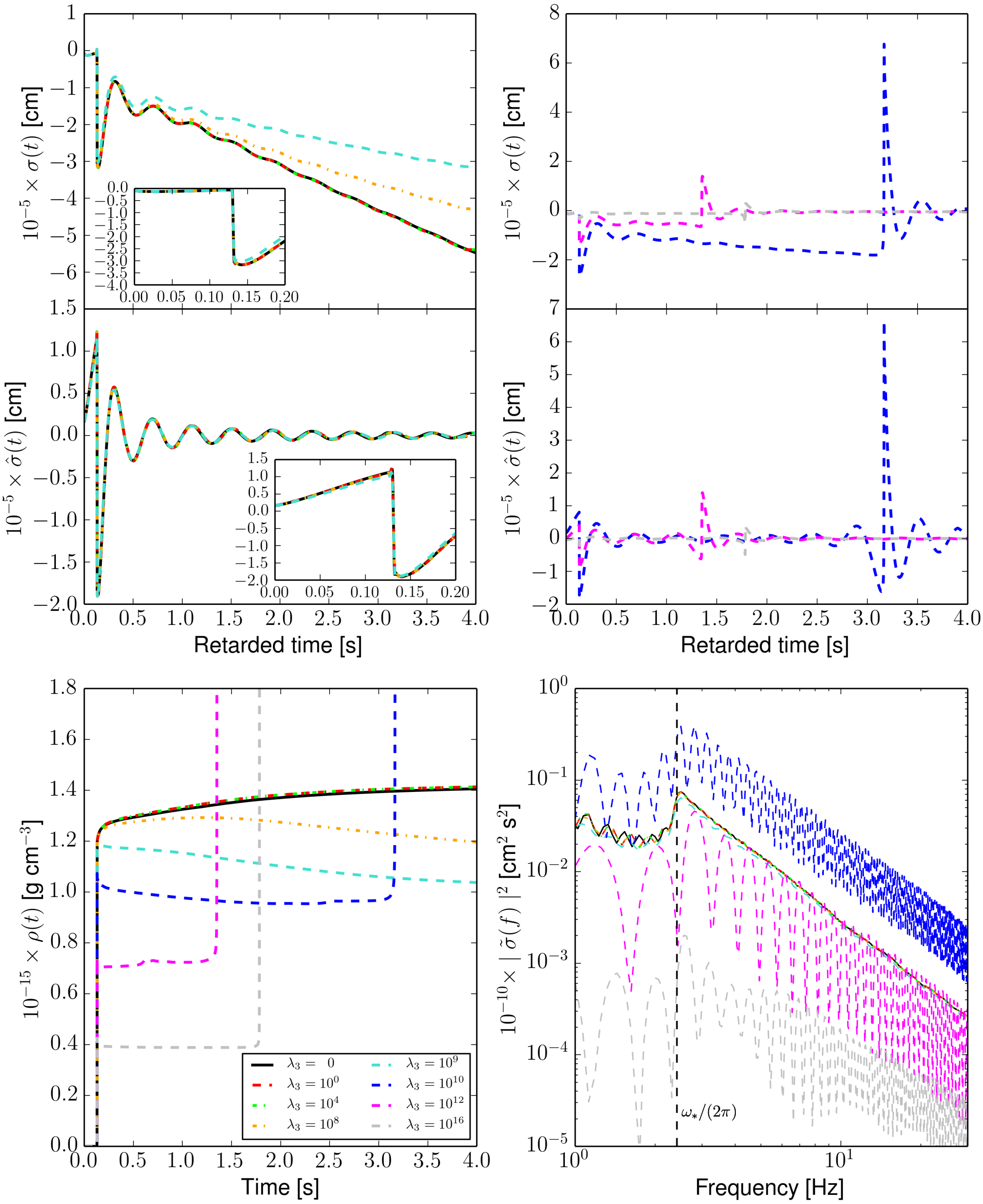

Fig. C.8 The effect of varying the λ_3 term of the scalar field potential using progenitor $u55$ with EOS3 and scalar parameters $\lambda_{1,2} = 0,\ \alpha_0 = 10^{-2},\ \beta_0 = -20$. *Top panels:* the scalar field signal at the extraction radius 3×10^4 km. *Middle panels:* the band-passed scalar field signal at the extraction radius 3×10^4 km; modes with frequencies below ω_* are set to 0. *Bottom left panel:* the central density evolution. *Bottom right panel:* power spectrum of waveforms extracted at 3×10^4 km. Higher resolution was used for $\lambda_3 = 10^{10},\ 10^{12}$ ($N = 30\ 000,\ \Delta r = 83.33$ m).